Process Extension from Embryonic Stem Cell-Derived Motor Neurons through Synthetic Extracellular Matrix Mimics

by

Daniel Devaud McKinnon

B.A., University of Colorado, 2009

M.S., University of Colorado, 2012

A thesis submitted to the

Faculty of the Graduate School of the

University of Colorado in partial fulfillment

of the requirements for the degree of

Doctor of Philosophy

Department of Chemical & Biological Engineering

2014

This thesis entitled:
Process Extension from Embryonic Stem Cell-Derived Motor Neurons through Synthetic Extracellular Matrix Mimics
written by Daniel Devaud McKinnon
has been approved for the Department of Chemical & Biological Engineering

_____

Kristi Anseth

_____

Professor Joel Kaar

Date _____

The final copy of this thesis has been examined by the signatories, and we find that both the content and the form meet acceptable presentation standards of scholarly work in the above mentioned discipline.

McKinnon, Daniel Devaud (Ph.D., Chemical & Biological Engineering)

Process Extension from Embryonic Stem Cell-Derived Motor Neurons through Synthetic Extracellular Matrix Mimics

Thesis directed by Distinguished Professor Kristi Anseth

This thesis focuses on studying the extension of motor axons through synthetic poly(ethylene glycol) PEG hydrogels that have been modified with biochemical functionalities to render them more biologically relevant. Specifically, the research strategy is to encapsulate embryonic stem cell-derived motor neurons (ESMNs) in synthetic PEG hydrogels crosslinked through three different chemistries providing three mechanisms for dynamically tuning material properties. First, a covalently crosslinked, enzymatically degradable hydrogel is developed and exploited to study the biophysical dynamics of axon extension and matrix remodeling. It is demonstrated that dispersed motor neurons require a battery of adhesive peptides and growth factors to maintain viability and extend axons while those in contact with supportive neuroglial cells do not. Additionally, cell-degradable crosslinker peptides and a soft modulus mimicking that of the spinal cord are requirements for axon extension. However, because local degradation of the hydrogel results in a cellular environment significantly different than that of the bulk, enzymatically degradable peptide crosslinkers were replaced with reversible covalent hydrazone bonds to study the effect of hydrogel modulus on axon extension. This material is characterized in detail and used to measure forces involved in axon extension. Finally, a hydrogel with photocleavable linkers incorporated into the network structure is exploited to explore motor axon response to physical channels. This system is used to direct the growth of motor axons towards co-cultured myotubes, resulting in the formation of an in vitro neural circuit.

Dedication

This thesis is dedicated to my girlfriend, Christina Murphy, my mother, Genevieve Devaud, and my father Tom McKinnon, all of whom were so supportive in my journey through graduate school.

Acknowledgements

First and foremost, I would like to acknowledge my committee members; Stephanie Bryant, Jennifer Cha, Curt Freed, and Joel Kaar; for all their helpful feedback throughout the years. Without their guidance and support, this thesis could not exist in its present form. I would also like to acknowledge all Anseth group members, past and present, all of whom aided me through this journey. Notably, my first office mate Josh McCall, materials gurus Malar Azagarsamy and Daniel Alge, rheologician Kelly Schultz, statistician Jen Leight, and protégé Tobin Brown were all instrumental in my development as a scientist. In addition, many friends and colleagues outside the Anseth group contributed immensely to my research including Dylan Domaille, Marty Guess, Kevin Dean, Rob Hall, Jeff Gazaille, Tim Read, and Joel Baskin. Finally, I would like to acknowledge my advisor, Kristi Anseth. I am deeply thankful for having had the opportunity to work in her lab and for all the experiences she had provided. Kristi has constructed an unparalleled mentoring environment and has been a tremendous soundboard for scientific ideas over the years. Her input and feedback will be deeply missed as I progress with my career and I will always remember my years in the Anseth lab.

Contents

Chapter

Tables

Table

Figures

Figure

Chapter 1

Introduction

1.1 Background of Neurodegenerative Diseases

The frontiers of medicine have pushed the mean global life expectancy from 31 years old in 1900 to 67 years old today.[13] Medical researchers have unveiled antibiotics, biologics, retroviral inhibitors, and targeted chemotherapeutics that have saved millions of lives, relegating the once mass killers of tuberculosis,[14] diabetes,[15] HIV,[16] and childhood leukemia[17] to largely treatable conditions. However, as the average human lifespan has increased, new classes of disease have begun to ravage our aging population. For example, neurodegenerative diseases like Parkinson's disease, Amyotrophic Lateral Sclerosis, and Alzheimer's disease appear relatively late in life and are caused by the selective deterioration of populations of nerve cells. These cells, called neurons, are considered by many to be the most complex cells found in the body. Neurons transmit electrical messages and assemble into vast networks containing trillions of synaptic connections that enable the complex reasoning behind theses such as this one. However, neurons are some of the most delicate cells in the body and are often the first cell type to succumb to oxidative damage associated with aging.[18–20] The relatively recent appearance of these neurodegenerative diseases coupled with the complexity of the neurons associated with the diseases results renders a poor outlook for patients. In fact, the prognosis for patients afflicted with these conditions is often quite bleak. Patients diagnosed with amyotrophic lateral sclerosis (ALS) suffer from the subtype specific loss of motor neurons and can expect to die of respiratory failure within 3-5 years. Those diagnosed

with Parkinson's and Alzheimer's disease face more positive outcomes, but these patients can suffer for years with severely impaired physical and cognitive abilities. To date, most treatments are sub-optimal and no cure exists.

1.2 Treatment Options for Neurodegenerative Diseases are Limited

While their mechanisms of action are largely unknown and suggested to be disparate, with genetics and environmental factors playing roles in each, the three most common neurodegenerative diseases share a grim outlook for treatment. The one million Americans suffering from Parkinson's disease are commonly treated through initially dosing them with neuroprotective therapies like the drug Selegiline, which inhibits the monoamine oxidase enzyme. However, the efficacy of this drug is still debated and dozens of compounds have been suggested to serve as neuroprotectants. This treatment is commonly combined with treatment by a dopamine agonist, but quickly loses efficacy. After which, L-DOPA, a dopamine precursor that allows remaining cells to produce more dopamine, is introduced with or without a catechol-O-methyl transferase inhibitor. Once these pharmaceutical strategies fail to control the progression of symptoms, surgical options like deep-brain electric stimulation are considered.[21] However, significant debate still exists among clinicians as to the best course of treatment, and while these therapies can delay the progression of the disease, no cure exists.[21] The treatment options for the 5.2 million Americans with Alzheimer's disease are even more limited. While dozens of different drugs are either approved or in development that target almost as many genes, most drugs only marginally reduce or delay some of the symptoms. In fact, large meta-analyses of clinical studies question whether the benefits of these treatments are large enough to justify their use.[22] The 30,000 Americans diagnosed with ALS face perhaps the easiest and yet most difficult treatment decision. While Parkinson's and Alzheimer's patients have the option to consider treatment by a number of different drugs of varying efficacy, ALS patients have only one. Riluzole is known to improve glutamate uptake in early-stage ALS patients and has been shown to extend lifespans by several

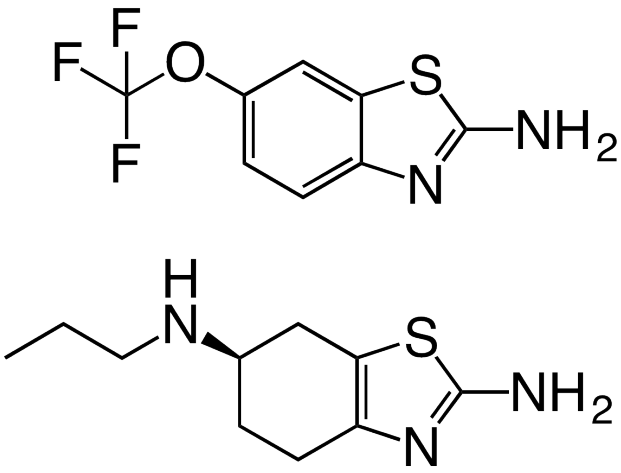

Figure 1.1: Riluzole (left) and Dexpramipexole (right), a structurally similar drug that recently failed in Phase III clinical trials. Riluzole is currently the only drug approved to treat ALS and displays questionable efficacy.

months (Figure 1.1).[23,24] However beyond this compound and several others in clinical trials, ALS patients have no options.

All of these treatments for neurodegeneration serve only to treat some of the symptoms, but do not address the root cause of the underlying disease. While developing drugs and other treatments for these conditions is an active area of medical research, mechanistically neurodegenerative diseases are much more complicated than those already conquered by molecular medicine. Historically, a drug is often designed to target a single gene or mechanism, for example bacterial cell wall synthesis that is disrupted by treatment with antibiotics. However, other than oxidative damage,[19] which appears to be a common theme among neurodegenerative diseases, no single or even collection of genes has been shown to be responsible. This lack of a target makes neurodegeneration extremely difficult to treat using existing medical approaches, even with refinements and improvements in drug delivery and targeting over the last century. The dozens of genes associated with Parkinson's, Alzheimer's, and ALS serve to render existing strategies high ineffectual.[25] Additionally, the gene defects that are most closely associated with the disease states are frequently seen in only a small fraction of the overall population, further reducing the utility of this classical

approaches. For example, the most common gene associated with ALS, SOD1, is linked with only 2% of cases, with similar statistics and variability reported for other neurodegenerative diseases.[26] This genetic diversity makes neurodegenerative diseases tremendously difficult to treat with drugs, and therefore, a prime candidate for exploring new paradigms.

1.3 Cell Replacement Therapy Has Been Used to Treat Parkinson's

Despite the challenges of identifying and delivering drugs to treat neurodegenerative diseases, recent advances in stem cells suggest potentially revolutionary treatment options through cell replacement therapies. While the mechanistic basis for Parkinson's and ALS is largely unknown, both are caused by the specific death of classes of nerve cells. Dopaminergic neurons die in the case of Parkinson's and motor neurons in the case of ALS. Cell replacement therapy focuses on strategies to replace the damaged dopaminergic or motor neurons with new cells that can function in place of their diseased counterparts. Because the damaged cell types are biologically very well understood, if new cells could be generated, implanted, and reintegrated into existing neural circuits, both of these devastating diseases could be potentially cured.

This strategy has already been demonstrated in clinical trials for the treatment of Parkinson's disease. Professor Curt Freed, of the University of Colorado School of Medicine, and colleagues succeeded in transplanting human embryonic dopamine neurons into the brains of patients with severe Parkinson's disease.[1,27] They isolated human embryonic mesencephalic tissue containing dopamine neurons and implanted the tissue into the forebrains of patients receiving treatment. Patients were monitored following the surgery through both functional assessment and PET imaging detecting the uptake of labeled DOPA. Overall, young patients were shown to statistically improve in both functional and dopamine uptake measures (Figure 1.2), and many patients were able to discontinue L-dopa supplementation. Further, the delivered cells were shown to survive and grow, indicating the brain environment of the Parkinson's patient was not toxic to transplanted cells.[1,27,28] Imaging of patient brain

sections post-mortem revealed robust process extension from the transplanted cells into the surrounded brain region, indicating integration and reinvervation.[28]

1.4 Cell Replacement Therapy Has Been Proposed to Treat ALS

Cell replacement strategies may be particularly appropriate for ALS sufferers, as the cellular mechanisms of the disease are very well understood (Figure 1.3).[29] ALS patients lose their motor neurons, the type of neuron that relays signals for motion from the spinal cord to the musculature. Initially, ALS patients show decreased isokinetic strength, with isometric strength falling soon after, as increasing populations of motor neurons die. Eventually, the disease progresses to the motor neurons controlling the diaphragm, leading to loss of control of the muscles related to breathing.[30] If these motor neurons could be replaced in the spinal cord and guided to reconnect to their target muscles, these functions could be restored. However, several hurdles limit this approach. First, human embryonic tissue is limited and difficult to isolate. The human brain contains only 400,000 dopaminergic neurons, and dopaminergic neurons are generally isolated to the *substantia nigra*, so implanting a limited number of cells in this specific area of the brain has the potential to more readily integrate and reverse disease progression.[31,32] In contrast, motor neurons exist in numerous pools spanning the length of the spinal cord rendering this approach more difficult. The location of motor neuron cell bodies varies by up to a meter in the spinal cord where they are organized into complex pools and columns that would be difficult to reproduce through simple cell transplantation methods.[33] Second, dopaminergic neurons enervate limited regions of the brain and can be implanted directly into those regions.[1,32] Because motor neurons have to transmit a signal from a descending input, a cortical neuron, to the muscle, they cannot be simply implanted in the muscle tissue. The motor neurons must be implanted in the spinal cord, be enervated by the descending cortical neurons, and extend axons into the musculature. Each of these individual steps presents a daunting challenge, let alone coordinating all three events.

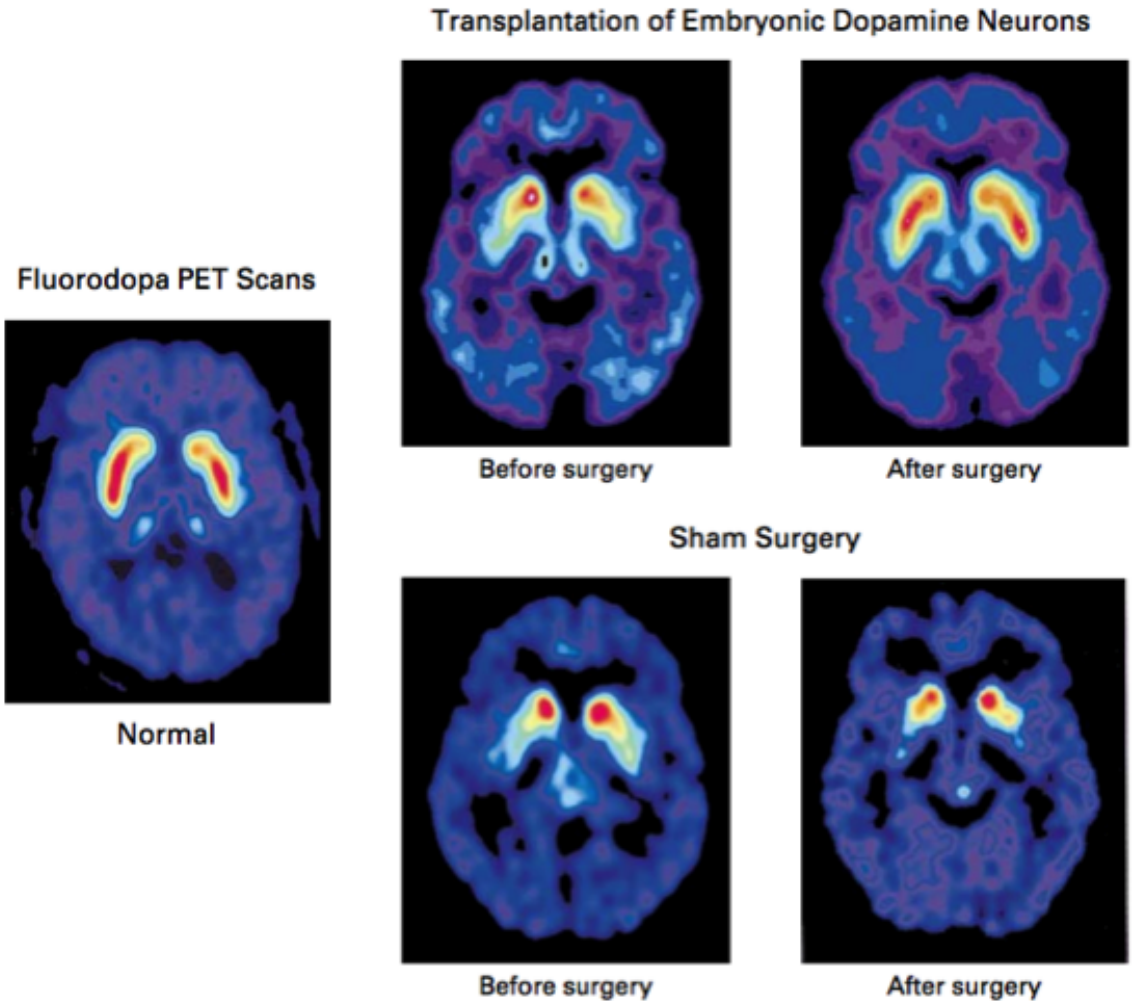

Figure 1.2: Assessment of dopa uptake by patients who received cell transplantation therapy for Parkinson's disease or a sham surgery using ^{18}F-labeled fluorodopa and PET imaging. The images are axial brain scans where red areas indicate a strong PET signal signifying strong uptake of fluorodopa, which is correlated to the progression of Parkinson's disease. Increased uptake is shown after transplantation surgery, but not after the sham surgery. This imaging along with behavioral assessments indicate cell transplantation was successful in treating younger Parkinson's patients.[1]

Despite the complexity of this process of re-innervation, the biology of motor neurons is one of the best understood in the central nervous system.[34] *In vivo*, their cell bodies reside in the spinal cord and during development they extend axons towards muscle groups that is determined by their position in the spinal cord.[33] These axons are able to carry electrical signals from the cell body to its target muscle, allowing the brain atop one's head to fire a muscle at the tip of one's toe.[35] Furthermore, the molecular biology and function of motor neurons has been extensively studied, and many neurotrophins, chemo-attractants, and chemo-repellents have been elucidated using genetic[35–39] and other techniques[40–42] to better understand what guides the formation of functional neuromuscular junctions This strong biological foundation combined with the specificity of ALS to motor neurons suggest that this cell type may be an excellent candidate to study in relation to cell replacement therapy.

Furthermore, while reliable cell sources for embryonic dopaminergic cells are lacking, motor neurons can be easily generated from embryonic stem cells,[2] induced pluripotent stem cells,[43] or even directly from fibroblasts.[44] While research has progressed since Professor Freed and colleagues' early cell transplantation studies and evidence exists that embryonic stem cells can be differentiated *in vivo* and *ex vivo* into dopaminergic neurons,[45,46] the functional properties of motor neurons have been extensively tested both *in vitro* and *in vivo*.[2,43,44,47–50] To generate motor neurons from mouse embryonic stem cells, only one week and two small molecules are required. ES cells are plated on gelatin coated polystyrene dishes, expanded for two days, placed in suspension culture for two days, then treated with 1 μM retinoic acid and 1 μM smoothened agonist (Figure 1.4). Three days later, motor neurons are mature and ready for experimentation.[2,51] Nearly identical processes have been adapted for human embryonic stem cells and human induced pluripotent stem cells.[43,52–55] Very recent advances have led to the direct transdifferentiation of human fibroblasts to motor neurons using viral vectors, which have been used to study *in vitro* behavior of ALS versus normal motor neurons, but, due to the use of viral vectors, this method is currently less

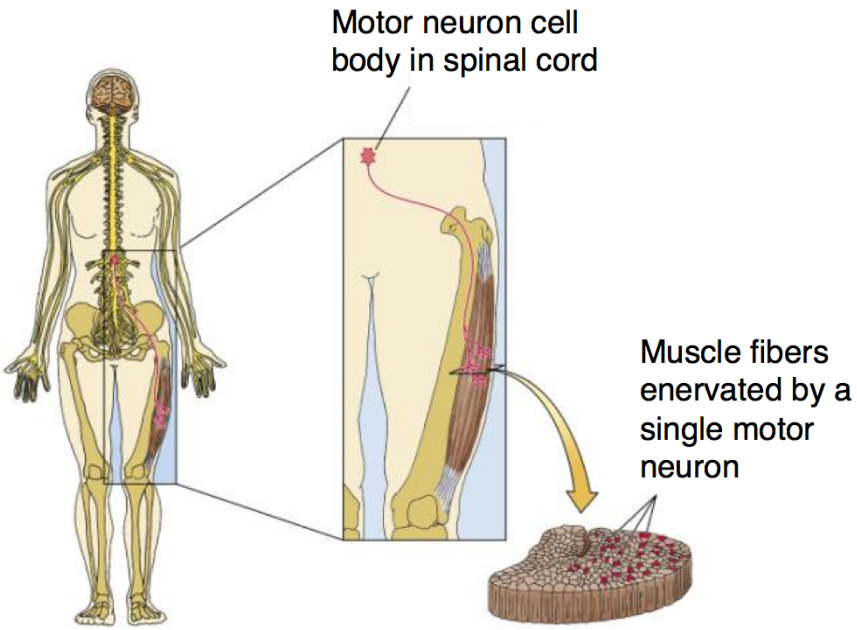

Figure 1.3: The cell bodies of motor neurons reside in the spinal cord from where they project axons toward their targeted muscle fibers. Motor neurons serve as biological wires to connect the brain to the musculature.

interesting for regenerative medicine applications.[44]

For all intents and purposes, embryonic stem cell-derived motor neurons (ESMNs) represent an unlimited source of motor neurons for fundamental studies and applications as a potential cell replacement therapy. This statement has been extended to induced pluripotent stem cells and trans-differentiated cells recently and technology now exists to generate motor neurons whose genetic profile is essentially identical to that of the patient, eliminating potentially serious issues with immune rejection.[43,44,55] Regardless of source, all of these lab-generated motor neurons have been shown to integrate into existing neural circuits in developing embryos in manner that appears identical to primary motor neurons.[2,43,44,47–50] The transplanted cells respond electrically to neurotransmitters, form functional synapses with myotubes, code nearly identical RNAs, and express the same pre- and post-synaptic proteins as their primary counterparts. Additionally, an embryonic cell line that expresses eGFP under control of Hb9, a transcription factor specific to motor neurons, has been generated in the lab of Professor Thomas Jessell and colleagues to allow easy visualization of cell behavior (Figure 1.5).[2] This cell line enables easier and higher-throughput studies of many aspects of motor neuron behavior without time consuming immunostaining to verify the cellular identity. This cell line has been kindly provided to our research group, and has been used as part of this thesis research.

Unfortunately, despite the detailed characterization of motor neuron biology and advances in stem cell culture to provide a robust source for motor neurons, intraspinal delivery of motor neurons in adult animals has thus far been largely unsuccessful.[56,57] In embryonic chick and prenatal mouse animal models, ESMNs transplanted into the spinal cord extend axons towards and form functional synapses with their myotube targets in a subtype-specific manner.[2,49] The transplanted cells seem to behave identically to their primary counterparts. However, when transplanted into the adult central nervous system (CNS), the axons generally fail to exit the spinal cord and enervate the musculature. Rather, the axons grow parallel to the spinal cord without restoring function (Figure 1.6).

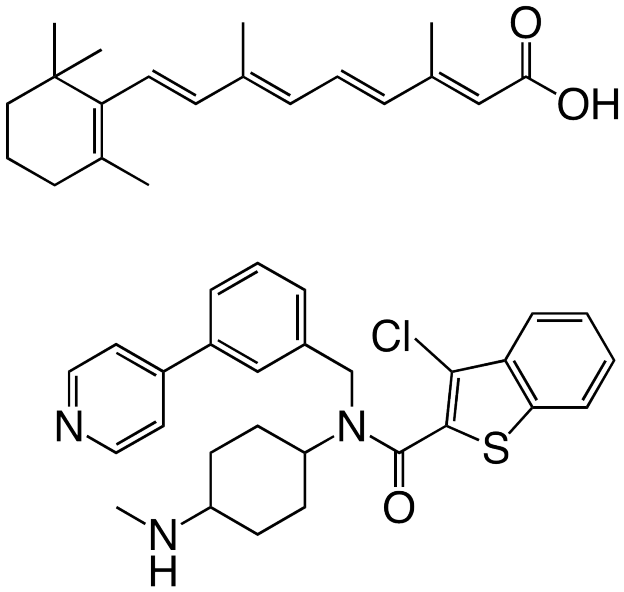

Figure 1.4: Retinoic acid (top) and smoothened agonist (bottom) are two inexpensive, commercially available small molecules used to generate motor neurons from embryonic stem cells easily and efficiently.

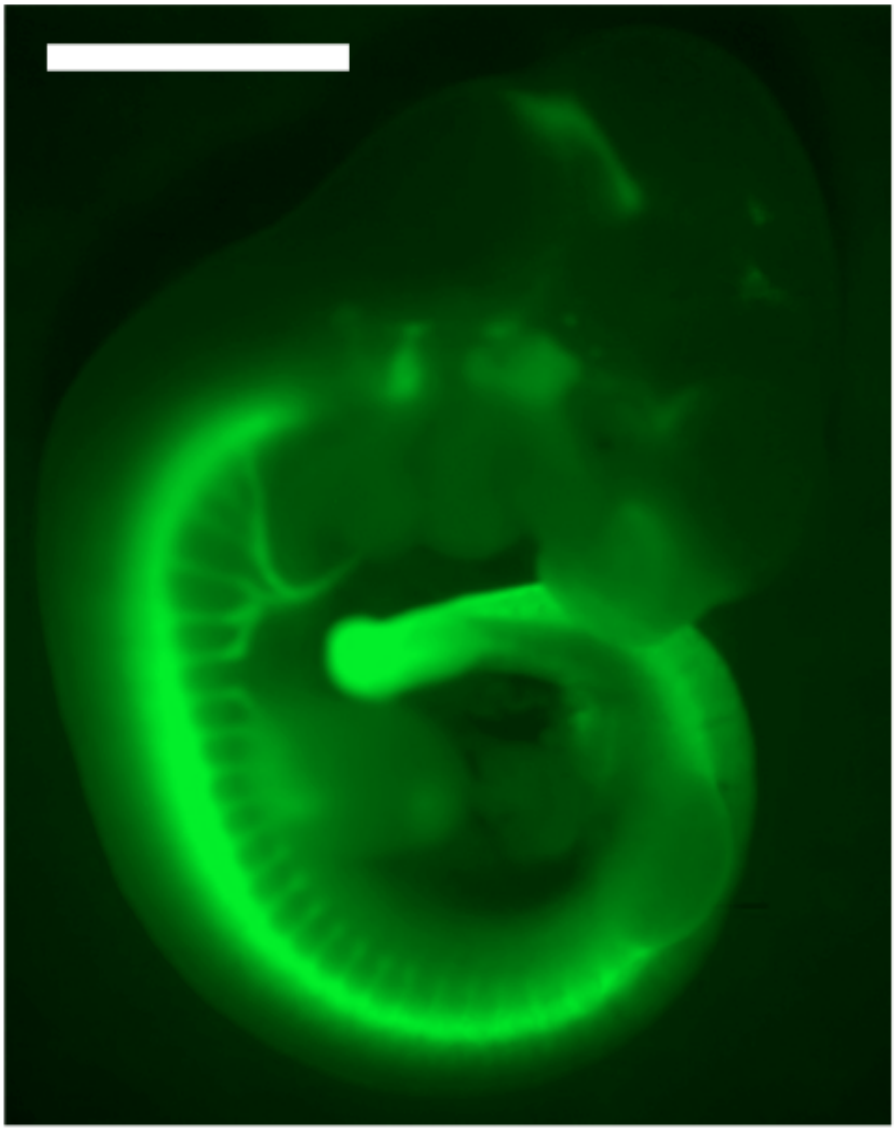

Figure 1.5: Hb9::GFP mouse embryo clearly showing GFP^+ motor neurons. The cell bodies reside in the spinal cord and axons extends into the musculature.[2] Scale bar is 1 mm.

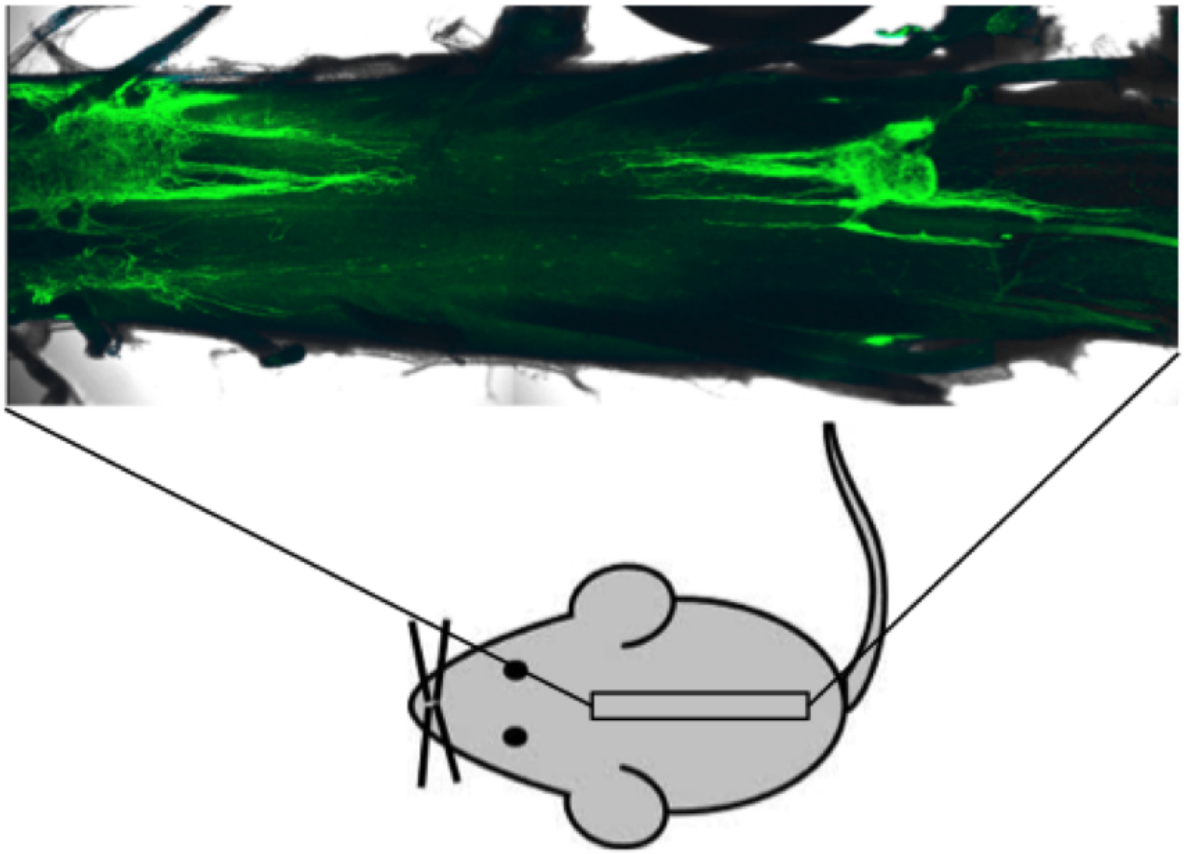

Figure 1.6: ESMNs transplanted into the adult mouse spinal cord, split axially above, extend axons along the axis of the spinal cord, but do not exit and enervate the musculature. Notice the axons travel parallel to the cord, rather than perpendicular as they do during development when they enervate the musculature.

1.5 Transplanted Motor Neurons Largely Fail to Extend Axons into the Musculature

Professor Douglas Kerr and colleagues have reported modest functional improvement upon implantation of motor neurons in paralyzed adult rats in conjunction with several drugs and neurotrophins. His group delivered ESMNs along with Glial-Derived Neurotrophic Factor (GDNF), the most commonly delivered neurotrophin in the motor neuron literature,[58–60] rolipram, an anti-inflammatory and potentially neuroprotective small molecule,[61] and dibutryl cyclic adenosine monophosphate (cAMP), use to inhibit myelin-mediated axon repulsion.[57] Their results showed a modest functional improvement in animals treated with high doses of all four compounds. While these initial experiments are promising, many challenges exist as the vast majority of transplanted cells did not survive, and of the surviving cells, most of their axons did not exit the spinal cord. Each motor neuron extends a single axon, and of the 60,000 cells transplanted, only 80 axons were found in the musculature. With this level of integration, this means roughly that only one tenth of one percent of delivered cells would have the potential to reverse the course of ALS. Furthermore, the paralyzed rat model may or may not reproduce many of the critical aspects of the environment found in ALS patients, as the injury model does not include the assault of the underlying disease.[56,57] Ultimately, the marginal functional improvement of these mice likely correlates with a lack of a better understanding of the conditions that promote axon extension. It is unknown why implanted motor axons reach their targets in embryonic animals and not in adult animals, but clearly differences in the cellular microenvironment is playing a role in the opposing outcomes. This premise relates to the motivation for this thesis research, as I seek to develop a biomaterial culture system for primary motor neurons. In particular, I aim to identify matrix microenvironmental conditions that are favorable to promote axon extension and provide for an improved understanding as to how biophysical and biochemical cues can be engineered to promote or inhibit axon extension.

1.6 Studying Motor Axon Extension Could Lead to a Solution

Several innovative platforms have emerged to culture motor neurons and examine motor axon responses to specific chemical or physical challenges. Specifically, Professor Lance Kam and coworkers developed a compartmentalization chamber to study the effect of several tethered proteins on axon extension in 2D. They confirmed the attractive effect of N-Cadherin, a transmembrane protein involved in cell adhesion, and the repulsive effect of Ephrin B2, a membrane protein implicated in many developmental roles, and quantitatively established the crosstalk between bFGF and N-Cadherin signaling (Figure 1.7).[3] Professor Hynek Wichterle and coworkers employed a similar device to show that ESMN response to ephrin-A5, Sem3f, and Sema3a is dose dependent and reliant upon protein synthesis in the axon compartment at low concentrations, but independent at high concentrations.[62]

When the perspective is broadened to the study of all neurons, however, engineering techniques have been widely employed to study axon extension, primarily of dorsal root ganglia (DRG) explants due to their robustness and ease of isolation. This literature has revealed quantitative information on the dynamics of outgrowth in response to many biochemical and biophysical signals. For example, previous work in the Anseth group has demonstrated the importance of hydrogel crosslinking density on axon extension of neural progenitor cells (NPCs). Hydrolytically degradable chain growth hydrogels, (described in the next section) whose time-dependent degradation behavior was well-characterized, were used to determine how NPC axons would extend in response to changing biophysical properties.[4] The Renaud group has developed elegant microfluidics devices combined with agarose-alginate hydrogels to simulate all six cortical layers and showed that encapsulated cells behave in a layer-specific fashion and extend axons towards neurotrophic B27 supplement.[6,63] The Shoichet group has a long history of contributions to the neural tissue engineering community and, in research related to this thesis, has exploited various photochemistries to show DRG explants follow an RGD channel into an agarose gel and NPCs migrate towards a sonic hedgehog gradi-

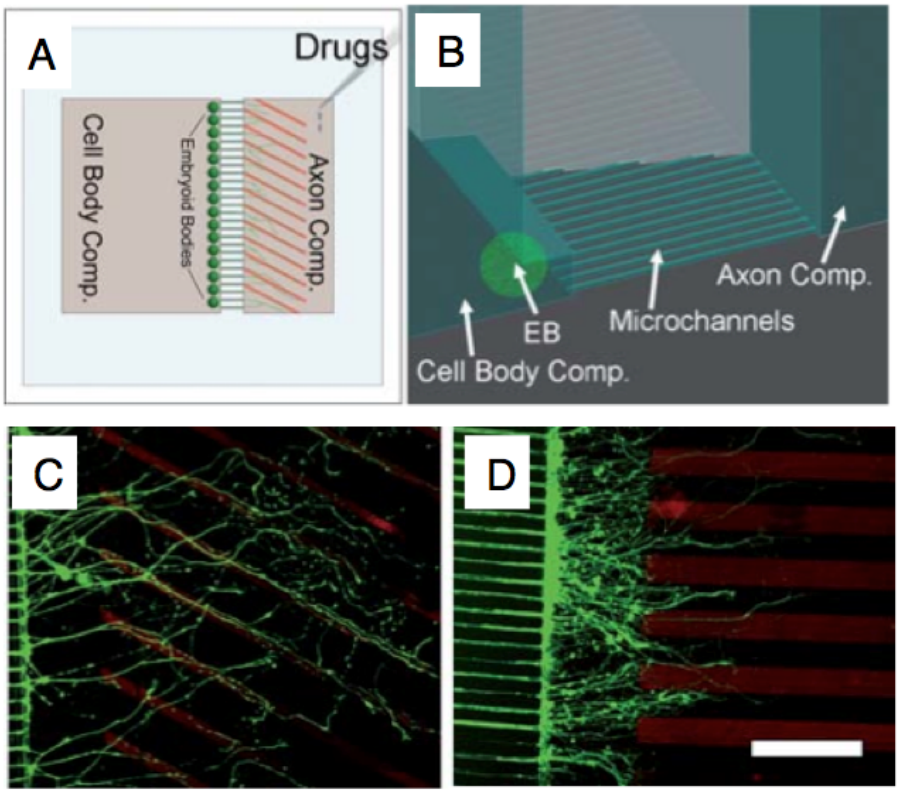

Figure 1.7: A) Schematic of the device designed in the Kam Group to investigate the role of patterned surfaces on motor axon extension. Embryoid bodies were seeded behind a perforated barrier that allowed axons, but not cells to pass through. Proteins of interest with stamped into channels on the other side of the barrier and the interaction between the proteins and the axons were observed through fluorescence microscopy. B) 3D rendering of the same device C) N-cadherin was shown to be attractive as the axons preferentially extend along N-cad tracks, D) while Ephrin-B2 was shown to be respulsive.[3] Scale bar is 200 μm.

ent. Both of these experiments were accomplished through functionalizing agarose gels with caged thiol moieties that became reactive upon exposure to UV light. Biomolecules functionalized with groups that react with the thiol molecules were allowed to swell into the gel, only coupling where light was exposed. Thus, the Shoichet was able to carefully control biochemical environment in three dimensions and monitor the response of DRG explants to RGD peptide and NPCs to a sonic hedgehog protein gradient.[7,8] The Goodhill group has combined diffusion modeling and axon guidance and showed that DRG explants predictably extend axons towards an NGF gradient in a collagen gel.[5,64] Collectively, these contributions demonstrate excellent techniques for culturing neurons and their precursor, and the research indicates that materials and microenvironments can be manipulated to influence axon extension (Figure 1.8. While inspiration and ideas are drawn from this body work, this thesis will focus on the development of new types of hydrogel materials, dynamic and tunable systems, that we hypothesize will be useful for studying and directing the extension of motor axons.

1.7 PEG Hydrogels Will Be Used to Study Conditions Favorable to Motor Axon Extension

To this end, I will develop and characterize a three-dimensional hydrogel system that allows for the encapsulation and culture of motor neurons in a microenvironment that can recapitulate many aspects of that found *in vivo*. Hydrogels have a strong history in regenerative medicine because of their high water content, tissue-like mechanics, wide range of constituents, and strong biocompatibility.[65] In addition, these same characteristics allow the study of fundamental biological processes in a 3D environment that can be imaged using standard microscopy tools. Hydrogels have been used to identify differences in cell behavior in 2D vs. 3D environments,[66] study the effects of tethered or sequestered vs. solubly delivered biochemical signals,[67] and investigate the role of substrate modulus on stem cell differentiation.[68] Additional, the chemical flexibility of hydrogels allows facile incorporation

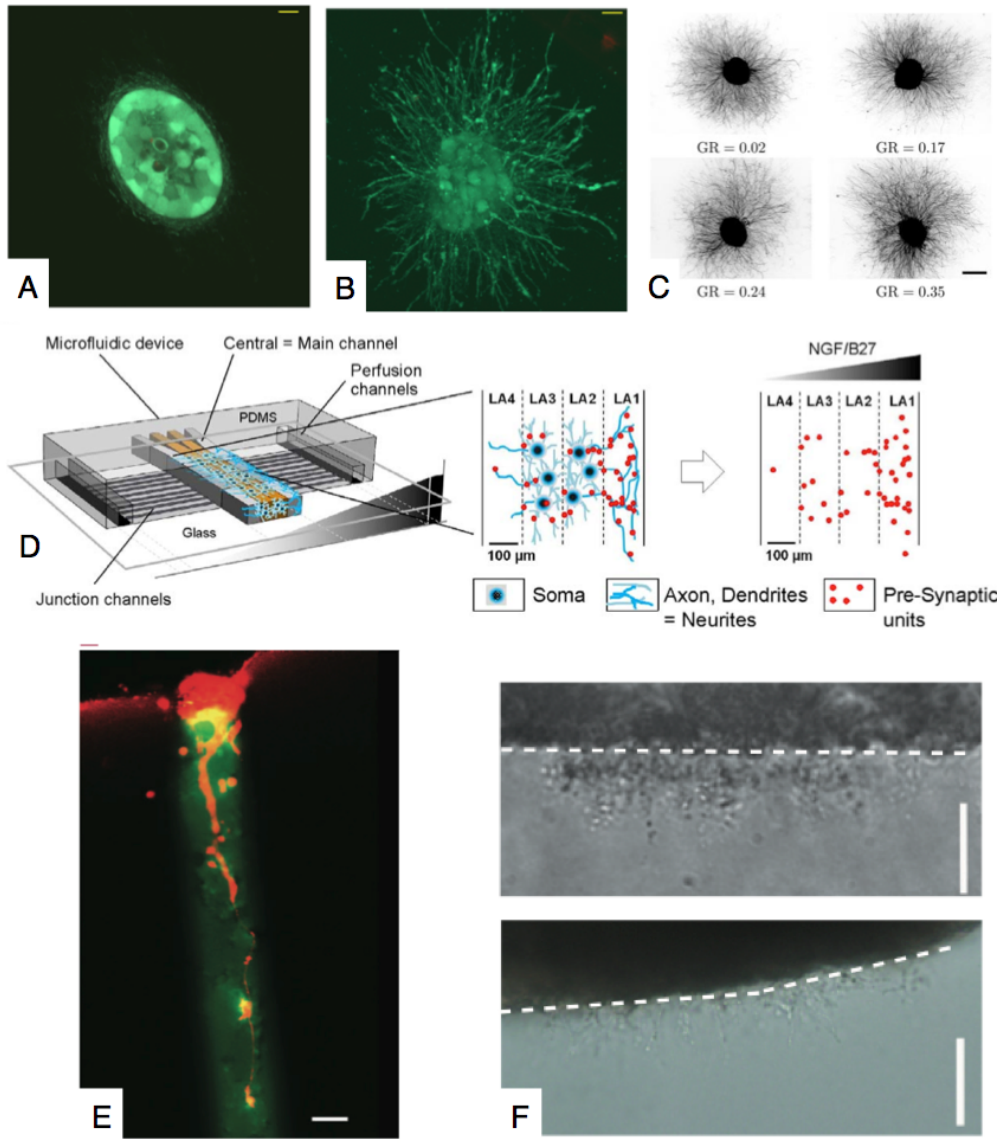

Figure 1.8: A) NPCs encapsulated in hydrolytically degradable PEG hydrogels did not extend axons through the material when the cross linking density was high, but rather when degradation proceeded beyond a critical threshold (B). Scale bar is 20 µm.[4] C) Using collagen gels and Neural Growth Factor (NGF) gradients, the Goodhill group showed control over and predictive ability over DRG axon extension. Scale bar is 400 µm.[5] D) The Renaud group constructed elegant microfluidic devices containing six different regions, one for each layer of the cortex. These devices were used to fabricate an alginate-based microenvironment that recapitulated critical aspects of the connectivity and function of each layer.[6] E) The Shoichet group photo-patterned adhesive fibronectin-based peptide RGDS into an alginate hydrogel, showing DRG cells migrate and extend axons into only the patterned areas (green). Scale bar is 100 µm.[7] F) The Schichet group exploited a more sophisticated technique to pattern sonic hedgehog protein gradients into a similar agarose gel (shown below dotted white line) and demonstrated NPCs migrate towards the gradient (above), but not towards a gel functionalized with only RGDS (below). Scale bar is 50 µm.[7,8]

of stimuli-responsive moieties that can be used to modulate the biochemical environment over time and while quantitatively measuring cell response.[69–72] More specifically, I propose to use poly(ethylene glycol) (PEG) hydrogels as a synthetic analog of the extracellular matrix. PEG has been used for many years as a bioinert polymer in consumer products ranging from shampoos to detergents. PEG is totally synthetic, extremely consistent from batch to batch, has well-defined chemical properties, and can serve as a blank slate for studying cell response to applied cues.

To engineer a PEG hydrogel for 3D cell culture, one must first consider the crosslinking chemistry. Unlike bulk polymer systems with limited chain mobility and strong interactions, PEG dissolves in water in the absence of strong chain-chain interactions. However, PEG chains are often terminated with alcohol functionalities, and these end groups make the installation of reactive chemical moieties to facilitate chemical crosslinking quite straightforward (Figure 1.9). For example, reacting acrylic acid with PEG via a simple ester condensation results in a bifunctional PEG chain with an acrylate group on each end. Because each acrylate group can react with two others through a simple radical-mediated chain reaction, exposing a solution of these bifunctional PEGs to an initiator results in a hydrogel crosslinked through acrylate chains. This simple system has proven quite versatile for the culture of numerous primary cells, such as the early work that allowed researchers to generate and study the formation of cartilage through the encapsulation of chondrocytes.73-75[73–75] However, many cell types require more than a blank-slate matrix to survive and proliferate. Osteoblasts, bone cells, produce significantly more bone when the hydrogel is functionalized with an adhesive moiety like the peptide RGDS, which is derived from fibronectin, a component of the extracellular matrix.[76] By simply functionalizing RGDS with an acrylate group and including it in the gelation solution, an adhesive hydrogel that promotes bone formation can be formed.[77] Therein lies the power of synthetic PEG hydrogels. By exploiting their well-defined chemical properties and ease of modification, it is possible to design materials of increasing complexity and functionality to manipulate and direct desired cellular processes.

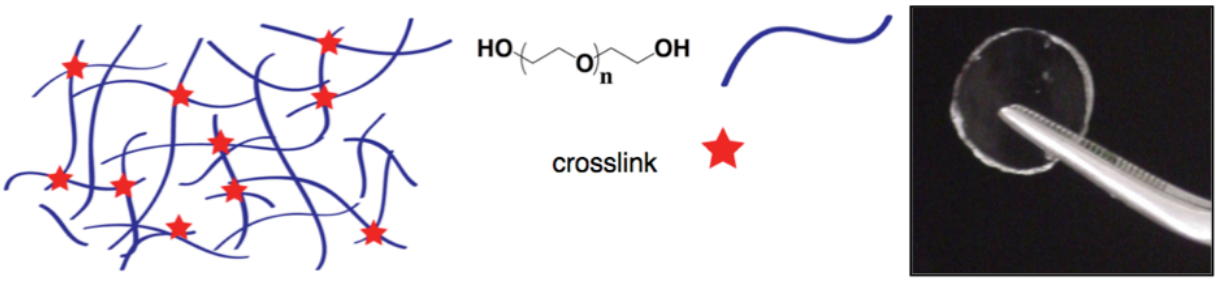

Figure 1.9: The basic anatomy of a PEG hydrogel. PEG chains, show in blue, are connected through some crosslinking reaction that transforms soluble polymer chains into a solid material suitable for biological applications shown with an image of such a PEG hydrogel at right.

In particular, this thesis will investigate how modifying the functionalization and crosslinking of step-growth PEG hydrogels can be used to identify biochemical and biophysical conditions that permit and/or promote motor axon extension. Step-growth hydrogels will be formed by coupling multi-arm PEG macromers through crosslinking chemistries that are easy to design and understand based on the structure of the precursor molecules (Figure 1.10). Mechanical properties will be tuned likewise by changing the density of crosslinks. This level of control will then be applied by demonstrating the translation of the materials into both a potential cell delivery vehicle and a tool to study axon extension.

1.8 Design Parameters for PEG Hydrogels Used to Study Motor Axon Extension

Unlike the primary chondrocytes and osteoblasts mentioned before, motor neurons have very specific matrix requirements for both survival and axon extension. Neurons are easily damaged by oxidative stress, exist both in the central nervous system microenvironment of the spinal cord but also in the peripheral nervous system environment, and extend axons vast distances to fulfill their signaling roles. Thus, a PEG hydrogel designed to study this cell type must incorporate specific design parameters to enable these diverse functions. Fortunately, significant progress has been made in the neuroscience literature to elucidate the

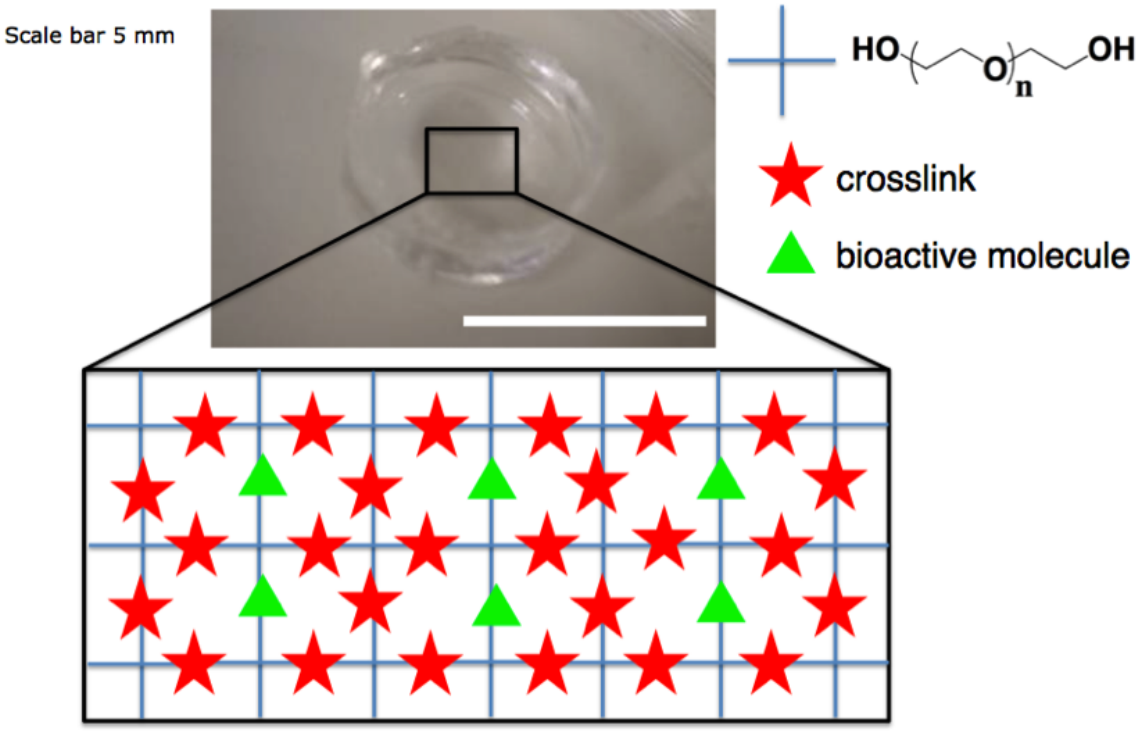

Figure 1.10: A step growth PEG hydrogel is a system of multi-arm PEG molecules crosslinked through some mechanism and generally functionalized with active biomolecules. The scale bar is 5 mm.

conditions required to culture motor neurons *in vitro*. Researchers commonly culture motor neurons on glass coverslips coated with cationic polymers, laminin, and include growth factors like GDNF, CNTF, and BDNF in the media.37,78-80[2,78–80] This collection of literature focused on traditional 2D cultures represents a logical starting point for engineering a PEG hydrogel that would support the viability of motor neurons of 3D. While some cell types can be confined to their initial shape in a polymer network, axon extension is a critical aspect of motor neuron biology to be studied, and the mesh size of a typical PEG polymer network is on the order of ten nanometers, which prevents reptation through the network. For comparison, motor neurons must extend axons, which have a diameter of roughly one micron;[81] therefore, some mechanism for degradation or relaxation must be built into the network crosslinkers. This degradation can be achieved through either engineering hydrolytically, photo-, or enzymatically degradable bonds that can be cleaved on a time scale consistent with axon extension or through reversible chemical or physical crosslinks that yield to advancing axons. Previous work in our group has studied the effect of hydrolytically degradable PEG hydrogels on axon extension from neural stem cells, but these systems lead to bulk material property changes.[4] This thesis aims to complement this work by designing degradable hydrogels with photodegradable linkers (for spatial control), enzymatically degradable linkers (for cellular and local control), or reversible bonds as reversible (de)crosslnking to allow and/or direct axon extension.

1.9 Chapter Summaries

Overall, this thesis focuses on studying the extension of motor axons through synthetic poly(ethylene glycol) PEG hydrogels that have been modified with biochemical functionalities to render them more biologically relevant. Specifically, the research strategy is to encapsulate embryonic stem cell-derived motor neurons (ESMNs) in synthetic PEG hydrogels with dynamically tunable properties through three distinct mechanisms. First, a covalently adaptable hydrogel is developed and exploited to study the biophysical dynamics of axon

extension and matrix remodeling. These results are discussed in Chapter 3, where I employ a cell-degradable peptide crosslinker to allow axon extension. Results show that dispersed motor neurons require a battery of adhesive peptides and growth factors to survive and extend axons, while those in contact with supportive neuroglial cells do not. Additionally, experiments show that the cell-degradable peptide is a requirement for axon extension and a soft modulus that more closely mimics that of the spinal cord results in superior axon extension and cell viability.[81] However, because local degradation of the hydrogel results in a cellular environment significantly different than that of the bulk, an alternative approach is investigated that replaces the cell-degradable peptide with a reversible covalent bond to study the effect of hydrogel modulus on axon extension. These results are presented in Chapters 4 and 5 where the synthesis and characterization of a cytocompatible covalent adaptable network suitable is introduced.[82] In Chapter 6, a strategy is proposed for encapsulating motor neurons into covalently adaptable hydrogels and calculating the force of their axon extension. Finally, a photodegradable hydrogel is exploited to explore motor axon response to physical channels and co-cultured myotubes in a user defined manner. The advantages of this system include a facile and robust biochemical and biophysical control of the matrix properties, spatially controlled degradation, minimal non-specific signaling, consistent material properties, and simplicity of synthesis.[83,84] These results are summarized in Chapters 7 and 8. Chapter 9 summarizes the main conclusions of this thesis and provides my perspective on compelling future directions.

Chapter 2

Objectives

The overall aim of this thesis is to exploit synthetic PEG hydrogels to study motor axon response to varying biochemical and biophysical environments. The hypothesis is that embryonic stem cell-derived motor neurons (ESMNs) encapsulated in synthetic hydrogels will provide fundamental insight into the mechanics of axon extension when challenged with a microenvironment recapitulating critical aspects of that found in vivo. Three material platforms based on three unique crosslinking chemistries will enable the systematic variation of different aspects of the cellular microenvironment and illuminate the role of biochemical environment, biophysical environment, and chemo-attractive factors on axon extension. Specifically, irreversible thiol-ene bonds will be employed to study motor neuron response to changes in biochemical and biophysical microenvironment, adaptable bis-aliphatic hydrazone bonds will be employed to study motor neuron response to varying viscoelastic environments, and degradable nitrobenzyl triazole bonds will be employed to study motor neuron response to physical channels. The specific aims of this thesis are to:

Aim I. Synthesize permissive PEG hydrogel matrices that allow long-term culture and extension of motor axons from ES-cell derived motor neurons and study motor axon extension as a function of the biochemical microenvironment, matrix degradability, and scaffold elasticity.

Aim II. Develop covalently adaptable PEG hydrogels that facilitate the characterization and quantification of axon extension from ESMNs, circumventing large changes in local

crosslinking density that convolutes quantitative analysis. Further, explore the role of matrix biophysical signals on growth cone pathfinding.

Aim III. Develop synthetically accessible photodegradable PEG hydrogels that allow researcher to study motor axon growth and the influence of axon outgrowth as a function of a three-dimensional matrix properties. Finally, demonstrate the ability to understand and manipulate axon guidance to direct outgrowth and facilitate the formation of neural networks *in vitro*. This will be demonstrated through the formation of a simplified neuromuscular junction between an ESMN and myotube.

The first objective focuses on culturing primary embryonic stem cell derived neurons in three-dimensional (3D) microenvironments that more closely recapitulate critical biochemical and biophysical aspects of the developing or adult central nervous system (CNS). Despite years of study, this remains a significant challenge in neurobiological studies and in regenerative medicine. Research associated with the first aim exploits recent advances in PEG hydrogel chemistries to define synthetic niches capable of supporting the culture and axonal outgrowth of both aggregated and dissociated mouse embryonic stem cell-derived motor neurons (ESMNs). Due to the specificity of a thiol-ene click reaction and the relatively low concentration of free radicals generated, thiol-ene crosslinked PEG-peptide hydrogels were engineered to permit neuronal survival and promote axon outgrowth through cell-extracellular matrix interactions, such as those between the laminin-derived YIGSR and its integrin. This material system allows primary neurons to remodel their extracellular environment through matrix metalloproteinase (MMP)-mediated network degradation and was exploited to study the role of the biochemical environment on cell survival and axon extension. Specifically, the role of biochemical functionalization, network crosslinker sequence, and scaffold mechanics on the survival and axon extension of encapsulated ESMNs will be investigated. The hypothesis is that biochemical functionalization of the hydrogel with basement membrane-mimicking peptides will provide sites for cell-matrix interactions and increase viability and axon extension; that matrix degradability will be critical to axon extension as

axon growth cones are two orders of magnitude too large to reptate through the hydrogel mesh; and that a scaffold elasticity that most closely matches the in vivo microenvironment will maximize cell viability and axon extension.

The second objective focuses on developing a reversibly crosslinked biomaterial scaffold that supports complex cell functions like ECM deposition, motility, and spreading, while simultaneously maintaining macroscopic bioscaffold properties. Typically, mechanisms for crosslink degradation must be engineered into hydrogels to enable these cellular functions, which can significantly complicate evaluation of the role of biophysical cues on cell function. For example, in the first objective, the conclusions related to the role of matrix modulus on axon extension must be qualified, as the local modulus in the pericellular environment is likely significantly different than that of the bulk material. However, developing a reversibly crosslinked material addresses aspects of these problems and provides a complementary system to better understand the effects of matrix mechanics on cell function in materials. While many types of reversibly crosslinked materials have been reported in the literature, covalently crosslinked PEG hydrogels are especially suitable as tissue engineering scaffolds due to their well-defined and easily tunable biochemical and biophysical properties. A step-growth PEG hydrogel crosslinked by cytocompatible reversible covalent bonds can provide a versatile matrix suitable for cell culture and capable of mimicking aspects of the viscoelastic properties of native tissues. Cytocompatible and dynamic stress-relaxing crosslinks then permit complex cellular functions to occur while retaining the benefits of traditional covalently crosslinked hydrogels; this thesis exploits this aspect of material design to perform carefully controlled studies of ESMN growth cone response to matrix biophysical properties. While many dynamic covalent chemistries exist that could be used to crosslink these PEG hydrogels, ranging from Diels-Alder to boronic acid esters to macrocyclic assemblies to metal catalyzed rearrangements, the conditions and time scale of reversal vary dramatically over this range of dynamic covalent reactions. More importantly, very few of these chemistries allow dynamic reversal in cytocompatible ranges of temperature, pH, or redox environment. This thesis ex-

plores the hydrazone bond and investigates the ability of this chemistry to maintain integrity of cell-laden hydrogels for weeks of experimentation while reversing rapidly enough to enable critical cellular function. The hydrazone bond has been used previously in bioconjugation reactions, which providing the motivation for this direction of inquiry. The hypothesis is that bis-aliphatic hydrazone crosslinked hydrogels can match the modulus of the ESMN *in vivo* environment and provide stress relaxation at appropriate time constants to support the ability of growth cones to push through the viscoelastic material and enable axon extension.

While the previous aims focus on studying isotropic motor axon outgrowth, the grand challenge is to address the barrier of coaxing axons of transplanted motor neurons to extend out of the spinal cord towards muscular junctions, a process that likely requires axon guidance. In vivo axons must navigate through a complex gamut of physical and chemical environments to arrive at their final synaptic targets. Here, we propose that photodegradable hydrogels can be exploited to explore motor axon response to spatially defined channels, created in situ and used to direct motor axons towards cellular targets of interest. Thus, the final aim of this thesis focuses on developing and characterizing synthetically accessible photodegradable hydrogel from commercially available building blocks. These building blocks, a dibenzyl cyclooctyne acid and an Fmoc-protected nitrobenzyl ether acid, are conjugated to multi-arm PEG macromers to create hydrogel precursors for cell encapsulation. The degradation of the resultant hydrogel will be characterized upon exposure to either single-photon or two-photon light. Furthermore, biochemical functionalization of the gel is explored to enable long-term culture of encapsulated ESMN embryoid bodies, along with two-photon irradiation of these systems to form channels and characterize axon outgrowth as a function of feature dimensions. Finally, C2C12 myotubes, a widely used synaptic target for motor neurons, will be introduced through co-culture with ESMN embryoid bodies, and the guidance of axons through the spatially directed features in photodegradable hydrogel will be studied in vitro. The hypothesis is that an easily accessible photodegradable hydrogel will allow directed motor axon extension and the formation of an in vitro neural network.

Chapter 3

Synthetic Hydrogel Platform for Three-Dimensional Culture of Embryonic Stem Cell-Derived Motor Neurons

3.1 Abstract

Culturing mammalian neurons in three-dimensional (3D) microenvironments that more closely recapitulate critical biochemical and biophysical aspects of the developing or adult central nervous system (CNS) milieu remains a significant challenge in neurobiological studies and in regenerative medicine. Here, we aimed to exploit recent advances in poly(ethylene glycol) (PEG) hydrogel chemistries to define a synthetic niche capable of supporting the culture and axonal outgrowth of both aggregated and dissociated mouse embryonic stem cell-derived motor neurons (ESMNs). Using thiol-ene click chemistry to create peptide crosslinked PEG hydrogels, we identified a hydrogel formulation that promotes neuronal survival and axon outgrowth through cell-extracellular matrix interactions, such as those between the laminin-derived YIGSR and its integrin, and that allows neurons to remodel their extracellular environment through matrix metalloproteinase (MMP)-mediated polymer network degradation. Our results demonstrate a 3D platform for culture of both aggregated and single mammalian motor nerve cells that not only permits cell survival over more than a week of culture, but also allows for the robust extension of motor axons. In addition, the optical transparency of the hydrogel allows simultaneous imaging of live cell functions, and as such, this material system should prove useful for studying fundamental aspects of neuronal development.

3.2 Introduction

Since the initial studies on the CNS pioneered by Santiago Ramon y Cajal[85] at the turn of the twentieth century, there has been an ever-expanding interest in the culture and manipulation of nerve cells *ex vivo*. Specifically, developing culture platforms that mimic cellular microenvironments through which axons navigate to their final target destination in vivo remains a daunting task. Culturing mammalian nerve cells has met significant challenges due to the difficulty of recapitulating many aspects of the intriguing complexities of the CNS milieu and architecture. Nerve cells are traditionally cultured on two-dimensional substrates that do not fully mimic the chemical and mechanical properties of nascent or adult CNS. For example, the shear modulus of glass, a substrate commonly used to culture nerve cells, is 26 GPa, or roughly seven orders of magnitude stiffer than typical *in vivo* neural environments. The bovine spinal cord, which contains spinal motor neurons, the cell type used in these studies, has a shear modulus of only 50 Pa.[86] Moreover, axon guidance cues are usually added to the culture media, but this approach does not reproduce the *in vivo*-like presentation of such molecular cues. *In vivo*, axon guidance cues are generally tethered to cell membranes with which individual axons interact as well as the extracellular matrix.[37,87] In addition, 3D spatial organization of CNS tissues (e.g., cortical layers) is essential to directing axon guidance and neural circuit assembly.

Despite these challenges, several recent studies have raised the possibility of culturing mammalian nerve cells in 3D using synthetic extracellular matrix material systems. Hydrolytically degradable synthetic PEG hydrogels have been used to culture neural progenitor cells (NPCs), where axon extension was observed and correlated strongly with the extent of material degradation.[4] Peptides and proteins have been engineered to assemble into hydrogels that promote neuronal differentiation and axon extension.[88,89] Chemically modified natural material systems have been leveraged to harness some of the benefits of naturally derived macromolecules while enabling selective property tuning. For example,

Figure 3.1: Much of the work described in this chapter appeared in Volume 1, Issue 5 of *Biomaterials Science* where it was also featured as the cover article.

dorsal root ganglia (DRG) cells were shown to extend processes into an agarose gel that was spatially patterned with RGDS peptide to facilitate cell-matrix interactions.[7] Methacrylated hyaluronic acid was used to encapsulate ventral mesencephalic progenitor cells, which preferentially differentiated into neuronal rather than glial lineage in the softest gels.[90] These studies show that neurons respond to biophysical (e.g., modulus) and biochemical (e.g., RGDS) signals presented by their 3D microenvironments in vitro and demonstrate the utility of material-based approaches for directing neural cell function and fate. We sought to gain further control over the 3D cellular milieu by introducing a chemically and physically defined synthetic system that allows for the systematic variation of these signals and subsequent study of cellular response. *In vivo* spinal motor neurons function in a complex environment with cell bodies residing in the spinal cord and motor axons in the periphery, and we aimed to recapitulate aspects of this complexity with a tunable synthetic hydrogel.

While most studies on nerve cells rely on isolation of primary neurons from animals, the excision process results in axotomy (cutting) of neurites and relies on subsequent re-growth of axons. To circumvent this issue, pluripotent embryonic stem (ES) cells have been shown to give rise to distinct types and subtypes of neurons that display characteristic properties and functionalities of their in vivo counterparts.[2,47–49] One of the best-understood types of nerve cells in regards to their diversification and connectivity are spinal cord motor neurons.[91] Importantly, spinal cord motor neurons can be efficiently differentiated from ES cells using developmentally relevant signaling cues, namely retinoic acid (RA) and sonic hedgehog (Shh).[2,51] In all aspects examined, ESMNs appear to be indistinguishable from their primary counterparts.[2,47–49] Importantly, spinal motor neurons are one of the only neurons of the CNS to project into the periphery. Moreover, individual motor neuron subtype loss is an underlying mechanism of ALS and SMA neurodegenerative disorders.[35] In this regard, transplantation of spinal motor neurons could be a feasible strategy for CNS repair. However, intraspinal transplantation into the adult spinal cord generally yields poor outcomes with respect to integration into neural circuits and axon extension.[56,57]

Here, we sought to take advantage of the versatility of thiol-ene reactions and the robustness of ESMN differentiation to define a synthetic niche that permits survival and axonal outgrowth of dissociated and aggregated ESMNs in 3D hydrogels. Specifically, we examined the combinatorial importance of hydrogel mechanical properties, presentation of biochemical cues, and mimicry of axon-ECM interactions in directing survival and axonal outgrowth. As many neurodegenerative disorders result in loss of individual subtypes of nerve cells, studies similar to ours may lead to provision of novel insights into engineering of transplantable biomaterial matrices for future delivery of neural cellular substrates for cell-replacement therapies.

3.3 Background

Neurons are known to be delicate cell types requiring specific growth factors, appropriately functionalized surfaces, and complex growth media to remain viable and extend axons.[92] This sensitivity presents a particular challenge for the 3D culture or delivery of primary neural cells. For example, a large portion of NPCs undergo cell death upon encapsulation[4] within a polymer system that has successfully sustained many primary cell types, including chondrocytes,[73] osteoblasts,[77] smooth muscle cells,[93] fibroblasts,[94] and mesenchymal stem cells.[95,96] Loss of viability during encapsulation is not necessarily an issue for progenitor cells, where rapid divisions can repopulate the hydrogel; however, for post-mitotic primary neurons, such as ESMNs, viability loss presents a serious problem for the encapsulation and delivery of a significant number of cells. Recent advances in thiol-ene chemistry have led to a step-growth hydrogel system that allows the facile incorporation of cell-degradable crosslinks and adhesive peptides, which we hypothesized could be used to rescue neural cell viability and aid in maintaining their function.[97,98] Additionally, this photoinitiated polymerization requires no change in pH, temperature, or chemical environment, and the mild reaction conditions combined with the diverse chemistry motivated us to exploit this system to encapsulate spinal motor neurons.

As illustrated in Figure 3.2, network formation is initiated by photocleavage of a low concentration of visible light photoinitiator (lithium phenyl-2,4,6-trimethylbenzoylphosphonate, LAP), which is water soluble and known to be cytocompatible over a wide range of initiation conditions.[99] The photocleaved fragment of LAP abstracts a proton from a thiol-terminated macromolecule to generate a thiyl radical, which then reacts rapidly and specifically with a norbornene-terminated macromer, forming a thioether bond. The thiyl radical is then regenerated when the reacted norbornene chain transfers to another thiol-terminated macromer. The thiol-ene gels thus form through a radical-mediated step growth process.[97,98]

While radicals are known to cause cell and protein damage, previous studies have shown that the thiol-ene reaction requires fewer radicals to generate a network, and the radicals have shorter lifetimes than more traditional photoinitiated chain polymerizations, leading to higher cell viability and protein activity.[97,98,100,101] Further, thiol-ene reactions are not oxygen inhibited, expanding their utility for bulk polymerization in the presence of cells. For example, a thiol-ene PEG system was shown to support roughly twice the viability of the MIN6 pancreatic β-cell line relative to a methacrylate PEG system.[100] In addition, the activity of a model protein, lysozyme, markedly decreased when encapsulated in an acrylate-based gel, but was virtually unchanged in a thiol-ene system.[101] In addition to the mild polymerization conditions, thiol-ene gels also form near ideal network structures that present a consistent biophysical environment throughout the hydrogel whose modulus can be easily tuned by varying the pre-polymerization functional group concentrations.[102–104] Furthermore, these networks allow for the facile introduction of different crosslinkers or pendant peptides either during or after gelation.[97,105,106] Thus, the cellular environment can be modified initially or sequentially with developmentally relevant and biologically active thiol-containing molecules. Collectively, these prior results suggested that a thiol-ene hydrogel might be suitable for encapsulating a delicate cell type like motor neurons.

In vitro, ESMNs are typically plated either as EBs or dissociated cells on glass slides coated with poly-lysine and laminin, which supports cell adhesion and axon outgrowth.

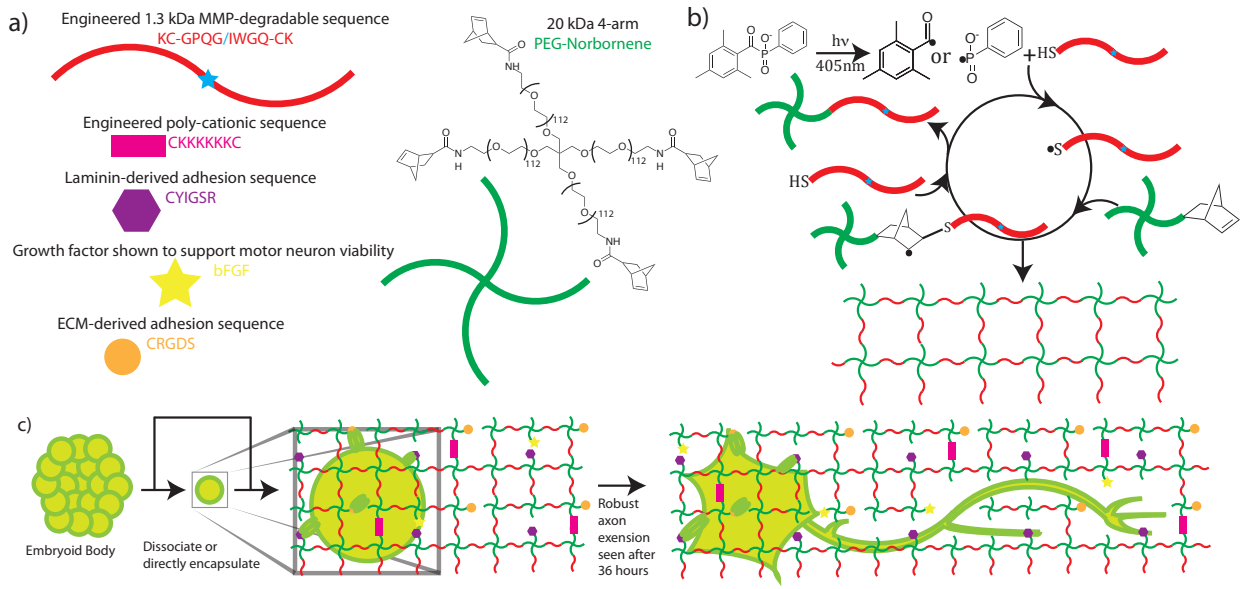

Figure 3.2: Schematic illustrating ESMN encapsulation in degradable peptide crosslinked PEG hydrogels functionalized with ECM-mimic peptides, a cationic peptide, and bFGF. Gels were formed using a thiol-ene click chemistry and LAP as a visible-light photoinitiator. (a) Chemical structures of network components are shown along with schematic representations. (b) The mechanism for gel formation relies on radical-mediated thiol-ene chemistry to produce step growth networks. Free thiols quickly and efficiently initiate chain transfer minimizing radical damage to other species. (c) Motor neurons are encapsulated in the gel formulations and interact with pendent YIGSR and RGDS groups through integrin-mediated binding. Within 36 hours MMPs expressed by the neurons erode defects through the network and allow axons to extend. The diagram is not to scale but has been enlarged to show all of the gel components. The mesh size of the network is on the order of *ca.* 10 nm while an axon is *ca.* 1 μm in diameter.

However, while this surface treatment is critical to dissociated ESMN adhesion, survival, and axon outgrowth, EBs will remain viable for weeks in suspension culture, on tissue culture polystyrene (TCPS), or on treated glass and once adhered will exhibit much more robust axon outgrowth than single cells. After 3 days of culture on poly-lysine and laminin treated glass in media supplemented by neurotrophins, only roughly 20% of dissociated ESMNs survive as compared with nearly all cells cultured in EBs.[2] This dramatic difference is likely due to the tissue like structures formed within EBs during differentiation and the existence of Oligo2$^+$ neural progenitors supporting the viability of ESMNs.[2107] For *in vivo* experimentation, EBs are often deployed because of this robustness.[49] These observations served as a starting point for engineering a synthetic 3D platform for the culture of ESMNs. We postulated that EBs could likely be encapsulated without any survival-promoting matrix interactions, but dissociated ESMNs would require similar signals to those shown to be necessary in 2D. However, while ESMNs maintain higher viability, require fewer signals, and extend longer axons when cultured in EBs, their complex structure creates new challenges associated with deconvoluting the relative contributions of different biophysical and biological cues. A synthetic 3D culture platform for dissociated ESMNs would enable the study of their responses to differing biological cues without the confounding effects of cell-cell contact or naturally derived polymers, and might prove useful to improve upon methods to efficiently differentiate specific motor neuron subtypes.

To rationally design a hydrogel capable of supporting the viability and axon outgrowth of dissociated ESMNs in three dimensions, we began with standard 2D culture platform of poly-lysine and laminin coated glass. Positive charge, which has been shown to promote axon outgrowth,[108] is usually satisfied with poly-lysine in 2D culture. However, cationic polymers are often implicated in cytotoxicity,[109] so we synthesized a hexalysine (CKKKKKKC) sequence to serve in the place of poly-lysine. Further, full laminin protein was replaced by two peptide sequences CRGDS and CYIGSR that have previously been shown to engage the appropriate integrin proteins and promote neuronal adhesion and axon outgrowth.[110]

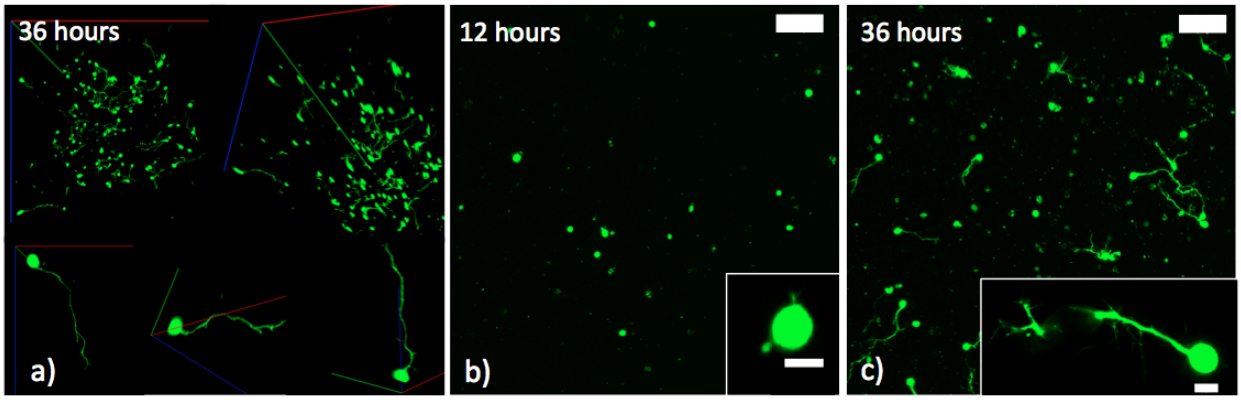

Figure 3.3: (a) ESMNs exhibit robust axonal outgrowth in three-dimensions when encapsulated in the engineered PEG hydrogel (scale bars 100 and 10 μm within inset). (b) Representative image of ESMNs 12 hours post-encapsulation. Small axonal buds are seen in the inset image. (c) Representative image of ESMNs 36 hours post-encapsulation.

Finally bFGF, which exists naturally in its reduced form, has been shown to increase ESMN viability and contains 4 free thiols for facile coupling to the hydrogel.[111,112] We form these biofunctional hydrogels by coupling norbornene-terminated PEG macromers and the cysteine-containing, cell-cleavable peptide sequence[97,113] (KCGPQG↓IWGQCK) using photo-initiated thiol-ene click chemistry, resulting in cytocompatible hydrogel networks that can be locally remodeled by the encapsulated cells (Figure 3.2).

3.4 Results & Discussion

Initial outgrowth of motor axons was observed from the majority of encapsulated cells after 12 hours of culture within 3D hydrogels (Figure 3.3). Embryoid bodies also began budding axons, but early extension was difficult to visualize owing to the size and brightness differential of the thousand-cell aggregates in comparison to the nascent axons (data not shown).

Single ESMNs assumed characteristic polarized shapes of *in vivo* motor neurons with a single axon emanating from the cell body 36 hours post-encapsulation (Figure 3.3). The gels functionalized with integrin binding peptides, cationic hexalysine peptide, and bFGF

maintained dissociated ESMN viability at 21 ± 1% (Figure 3.4, Figure 3.5). This gel formulation also resulted in robust axon outgrowth, with 83 ± 9% of eGFP positive cells extending axons an average of 148 ± 14 μm. In contrast, encapsulation of dissociated ESMNs in unfunctionalized gels lacking biological cues resulted in drastically reduced viability of 4 ± 2% (Figure 3.4, Figure 3.5). The encapsulated EBs, however, did not show a preference for the functionalized material over the unfunctionalized with respect to cell viability as virtually 100% of the cells remained viable after 36 hours in both systems (Figure 3.6). Their axon extension qualitatively appeared more robust in the functionalized gel; however, quantification was not possible due to axon fasciculation and the high density of cell bodies.

By 72 hours, 12 ± 1% of the dissociated cells in the functionalized gels remained viable while only 3 ± 1% of those in the unfunctionalized gels did (Figure 3.4, Figure 3.5). The surviving cells continued to elongate their axons, although not quantifiable owing to eGFP aggregates within the cells and axon extension beyond the field of view. At 72 hours, the cells within EBs still remained nearly 100% viable and extended axons millimeters through the gel (Figure3.6). By this point, every EB in the functionalized gel and many in the unfunctionalized gel exhibited robust axon outgrowth, but interestingly, in the unfunctionalized gel a minority of EBs, approximately 20%, did not extend axons.

While motor neuron differentiation is highly robust and reproducible, only 30%-50% of the cells taken through the differentiation protocol are GFP^+ motor neurons.[51] The remainder is composed of interneurons and $Olig o2^+$ progenitors that can self-renew or further differentiate into oligodendrocytes and other neuroglial cells.[2] Even after 36 hours in these gel cultures, there is a marked difference in viability in dispersed cells and EBs. This difference is likely caused by the supportive effects of these neuroglial cells. While thiol-ene chemistry is a relatively gentle method of cell encapsulation, the process is still stressful to cells, as small changes in osmolarity and other stressers exist over the short timescale required for encapsulation. Remarkably, however, the viability of ESMNs encapsulated in the functional hydrogel is nearly that of cells plated on laminin-coated coverslips. In standard 2D culture,

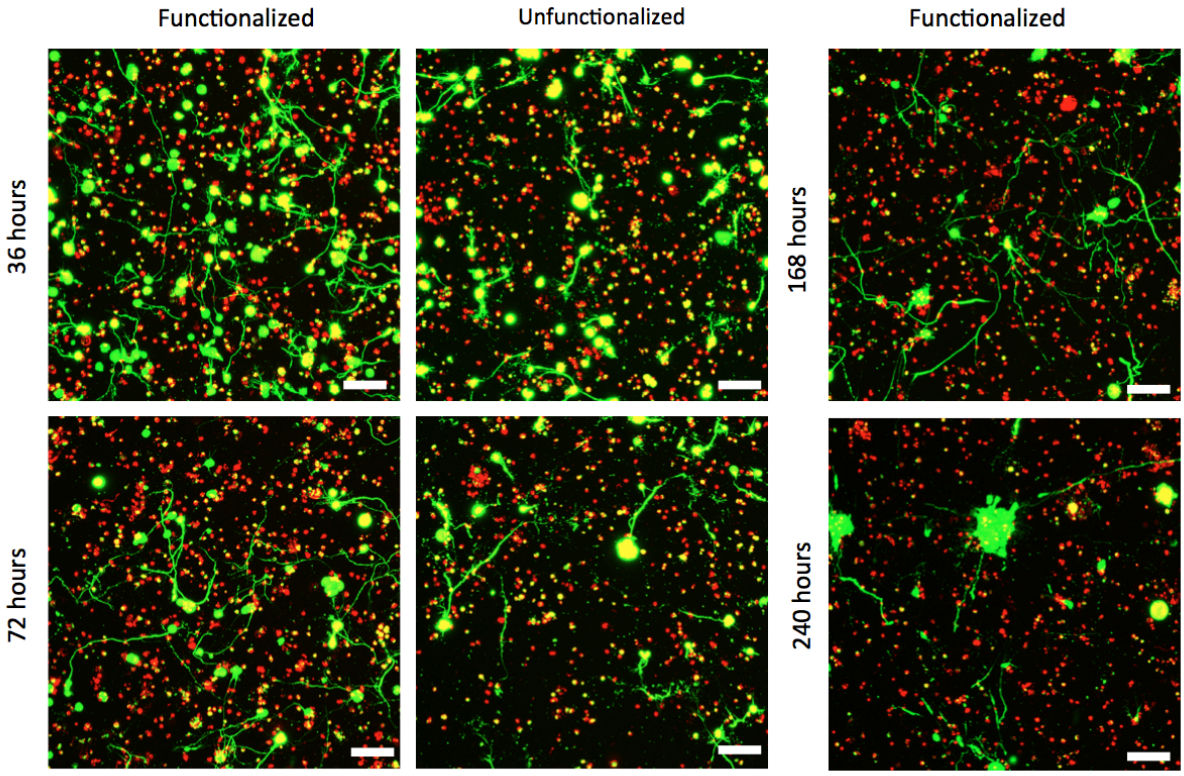

Figure 3.4: Confocal Z-stacks Live (green)/Dead (red) stain of dissociated ESMNs in functionalized and unfunctionalized hydrogels at different time points. The unfunctionalized gels were not imaged after 168 hours. By 240 hours, all live cells existed in multicellular aggregates (scale bar 100 μm).

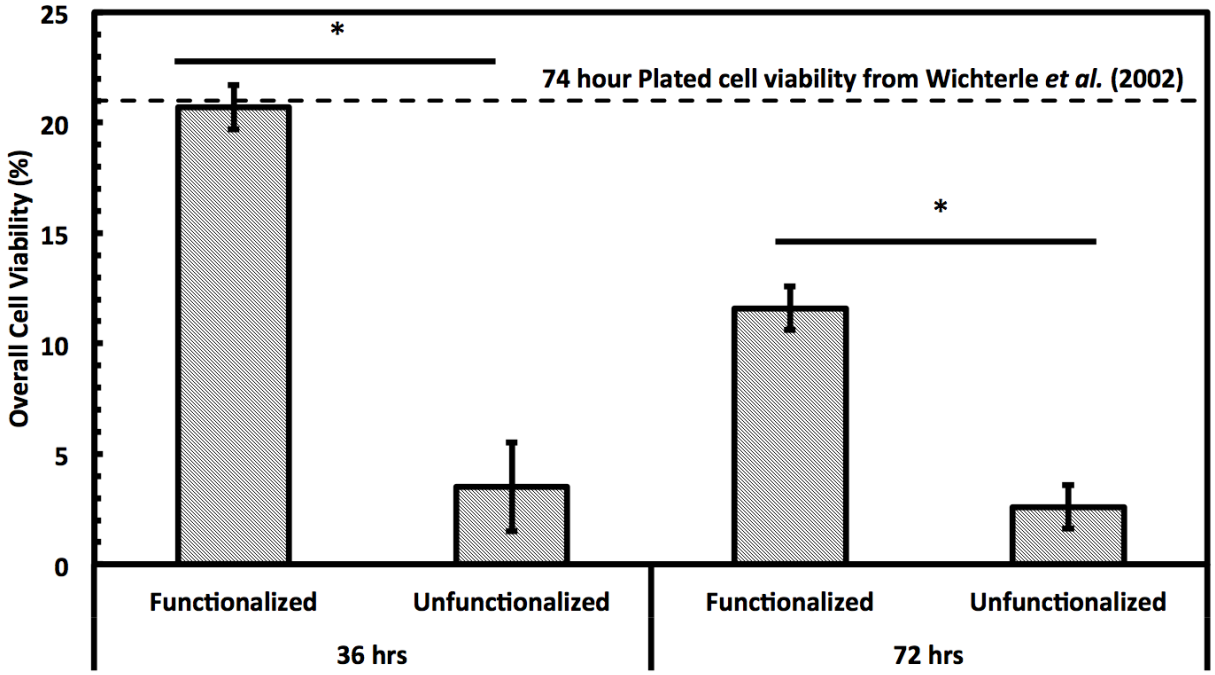

Figure 3.5: Hydrogels functionalized with integrin binding peptides, bFGF, and charged peptide maintain significantly higher dissociated ESMN viability than those lacking these functionalities (mean cells per condition = 422.2, $p<0.001$). The viability of ESMNs encapsulated in the functional hydrogel is nearly that of cells plated on laminin-coated coverslips.[2]

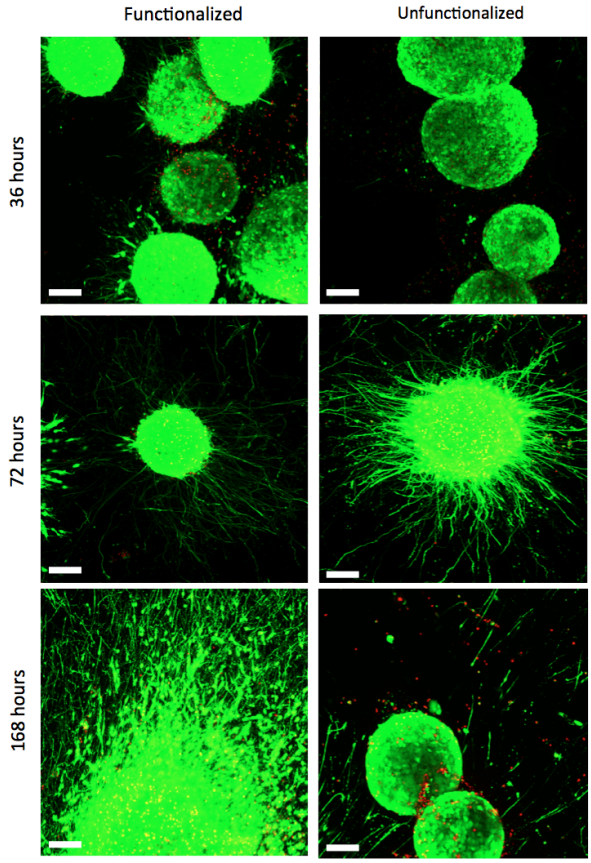

Figure 3.6: Confocal Z-stacks Live (green)/Dead (red) stain of encapsulated EBs in functionalized and unfunctionalized gels at different time points. The image of the EBs in the unfunctionalized gel after 168 hours is not representative, but shows that a subset of EBs failed to extend axons (scale bar 100 μm).

only 5% of ESMNs survive without supportive neurotrophins (NT3, CNTF, BDNF, GDNF) and only 22% survive with these factors after 72 hours.[2] While this is in sharp contrast to the essentially 100% viability of encapsulated EBs, it is congruent with development in vivo in which approximately half of all spinal motor neurons die while competing for a limited pool of neurotrophins.[58,114] This indicates that cell-cell signaling in the EB is extremely important to cell viability within this *in vitro* system.

This conclusion is reinforced by confocal images of the dissociated motor neurons after 168 hours in culture. Dissociated ESMNs encapsulated in the functionalized hydrogel extended axons beyond the field of view of a 10x objective while cell viability drops to 11 ± 4% (Figure 3.4). Interestingly, many of the live cells appeared in small 2-5 cell clusters, suggesting one or two motor neurons surrounded by Oligo2$^+$ neural progenitors as evidenced by the one or two axons emanating from these aggregates and the fact that these aggregates increase in size over time and motor neurons are post-mitotic. This trend increased to the point where every live cell was found in an aggregate by 240 hours (Figure 3.4). The existence of these aggregates lends credence to the idea that that the Oligo2$^+$ progenitors generated during the ESMN differentiation strongly promote ESMN survival. After 168 hours in culture, the EBs encapsulated in both the functionalized and unfunctionalized gels still remained nearly 100% viable, and every EB in the functionalized gel and many in the unfunctionalized gel extended axons from one end of the gel to another, which had swollen to over a centimeter in diameter from its original 5 mm. The entire gel was permeated by axons, even at large distances from encapsulated EBs (Figure 3.7); yet, while in the minority, several EBs (*ca.* 10%) in the unfunctionalized gel failed to extend any axons.

These results indicate that, even at early time points, receptor signaling satisfied by integrin-binding ECM-mimic peptides, bFGF, and charge-coupled interactions are essential for the viability and axon outgrowth of dissociated ESMNs, but are not critical if cell-cell interactions are provided (*i.e.*, cells within an EB). At later time points (>7 days in culture), these ECM-based signals were not sufficient to maintain cell viability and only clusters of

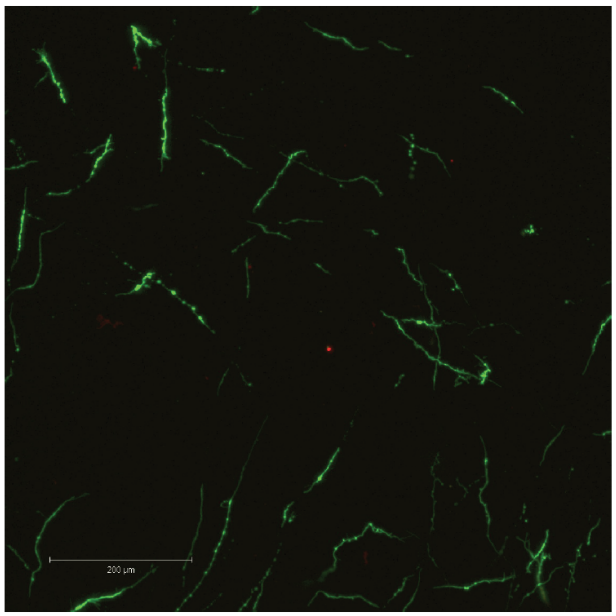

Figure 3.7: Encapsulated EBs extend axons throughout the entire gel after 168 hours. This Z-stack was taken several millimeters from the nearest EB.

cells survive. This observation is consistent with motor neuron behavior in vivo, however, as any cell that does not successfully form a mature synapse with a myotube will apoptose, with only half of the motor neurons generated making it to adulthood20. Future studies will examine this phenomenon through an ESMN/myotube co-culture.

Next, we investigated whether motor axon outgrowth is dependent on the MMP degradable cross-linker peptide KCGPQG↓IWGQCK. We replaced the MMP degradable cross-linker with a 3.4 kDa PEG cross-linker, a macromer containing neither cell-degradable bonds nor cell-interactive domains. Such hydrogels demonstrated similar swollen moduli to those containing the MMP degradable cross-linker. Upon replacement of the MMP degradable cross-linker peptide with PEG-dithiol, many encapsulated ESMNs remained viable, but the vast majority of encapsulated ESMNs failed to extend axons in such a microenvironment (Figure 3.8). Figure 3.9 presents results after quantification of several of these confocal images (N=105 cells for degradable gels, N=118 cells for non-degradable gels). In the non-degradable gel systems, 39 ± 7% of cells extended axons with an average length of 11 ± 4 μm, and no branching was observed. In contrast, in the MMP-degradable gels, 83 ± 9% of cells extended axons with an average length of 148 ± 14 μm. Additionally, individual motor axons branched in MMP-degradable gels, characteristic of their *in vivo* phenotype, and exhibited no branching in non-degradable gels. Furthermore, immunostaining of ESMNs with an antibody specific to MMP2 revealed a strong expression of MMP2 in the cell bodies and growth cones of ESMNs (Figure 3.8). Together, these findings reveal an identification of a peptide functionalized PEG hydrogel formulation which depends on cell-ECM interactions and endogenous MMP2 activity encoded by ESMNs to support ESMN survival and axon outgrowth.

Crosslinking the hydrogel with an inert PEG macromer, rather than an MMP-degradable peptide sequence effectively eliminates axon outgrowth. Unlike naturally-derived and fibrous 3D scaffolds, step-growth PEG networks have a mesh size on the order of 10 nm.[115] An axon is roughly one micron in diameter and is unable to reptate through such a poly-

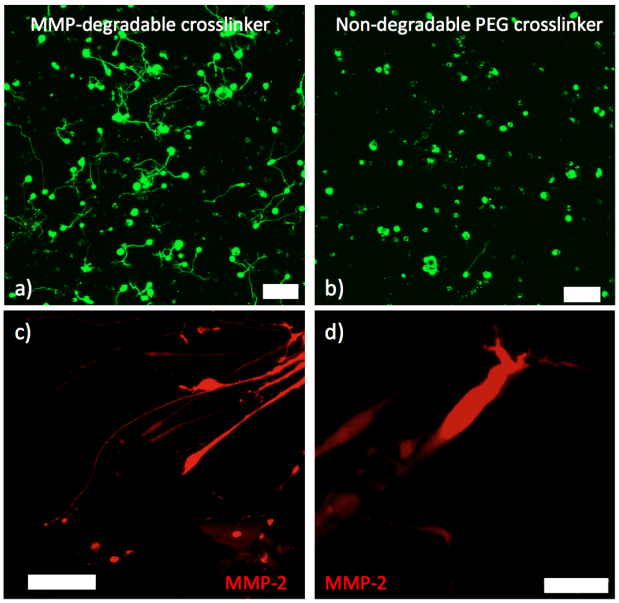

Figure 3.8: (a) Z-projection of motor neurons cultured for 36 hours in gel with MMP-degradable peptide crosslinker (scale bar 100 μm). (b) Z-projection of motor neurons cultured for 36 hours in gel with non-degradable PEG crosslinker. Motor neurons axon extension is limited (scale bar 100 μm). (c) MMP-2 immunostaining showing MMP-2 in growth cone of multiple axons. The cells bodies are contained in an embryoid body to the right of the frame (scale bar 50 μm). (d) Higher magnification image of one growth cone showing MMP-2 staining (scale bar 10 μm).

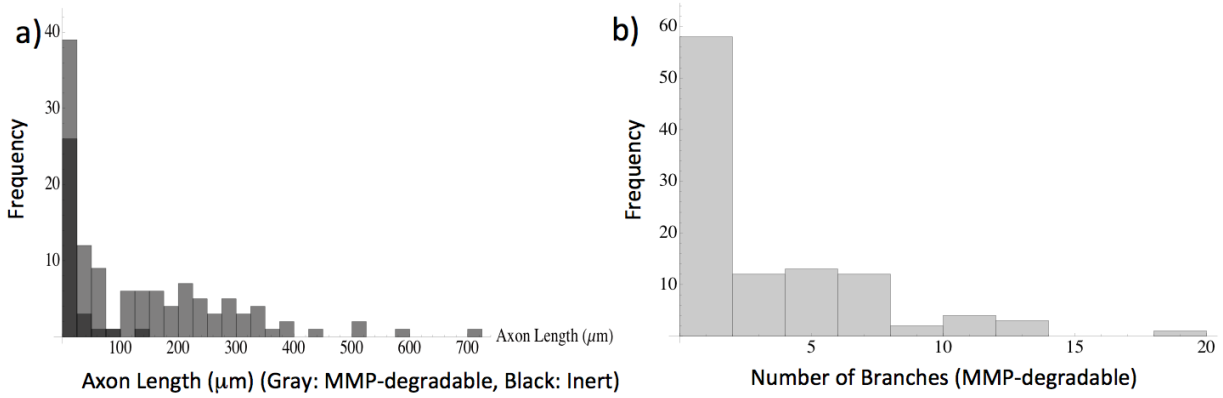

Figure 3.9: Quantification of motor neuron phenotype. Stacks are loaded into Simple Neurite Tracer[9] and axon length and branching are quantified. (a) Histogram of axon length in both non-degradable (black) and MMP-degradable (gray) gels. (b) Number of major axon branches in MMP-degradable gels. None of the axons in the non-degradable gel branched.

mer network unless significant defects are present. Furthermore, ESMNs were shown to express MMP-2 by immunostaining, which has been shown to cleave the peptide crosslinker KCGPQG↓IWGQCK42. While studies in Drosophila have shown a direct requirement for MMP2 in fasciculation of motor axons, whether MMPs play a role in motor axon guidance remains unclear.[116] Our studies provide evidence that motor axon outgrowth in 3D hydrogels relies on the presence of MMP-degradable peptide cross-linkers, removal of which results in reduced axonal outgrowth. Our results also provide evidence that the 3D hydrogel system defined here provides a permissive environment for in vivo-like branching of spinal motor axons shown to be essential for target connectivity.[117]

Finally, we examined whether the elastic modulus of the hydrogel matrix influences the extent of motor axon outgrowth of ESMNs by tracking axonal outgrowth as a function of varying crosslinking densities. We tested this hypothesis by varying the initial PEG-norbornene monomer concentrations from 3.5 to 6.3 wt% while keeping the pendant peptide concentrations constant. Such manipulations resulted in hydrogel matrices with shear elastic moduli that ranged from 350 Pa to 2220 Pa. When ESMNs were encapsulated into hydrogel formulations with the highest modulus of 2220 Pa, ESMNs underwent uniform cell death (Figure 3.10). Interestingly, encapsulation of ESMNs in 780 Pa hydrogels allowed some survival, but motor axons failed to grow in these hydrogels. Finally, robust axon outgrowth was observed in 350 Pa hydrogels.

Hydrogels with an elastic modulus below 350 Pa may provide an even more robust platform for axonal outgrowth. However, hydrogels with moduli below 350 Pa were difficult to manipulate post gelation, making consistent imaging and observations impossible. Despite this, the examined moduli range is consistent with the range of interest for neural microenvironments (50-250 Pa) *in vivo*.[118] These *in vivo* environments, despite being very soft, are distinctly elastic rather than viscous, a trait accurately recapitulated in our hydrogel platform which has a storage modulus roughly one thousand times higher than the loss modulus (Figure 3.11).

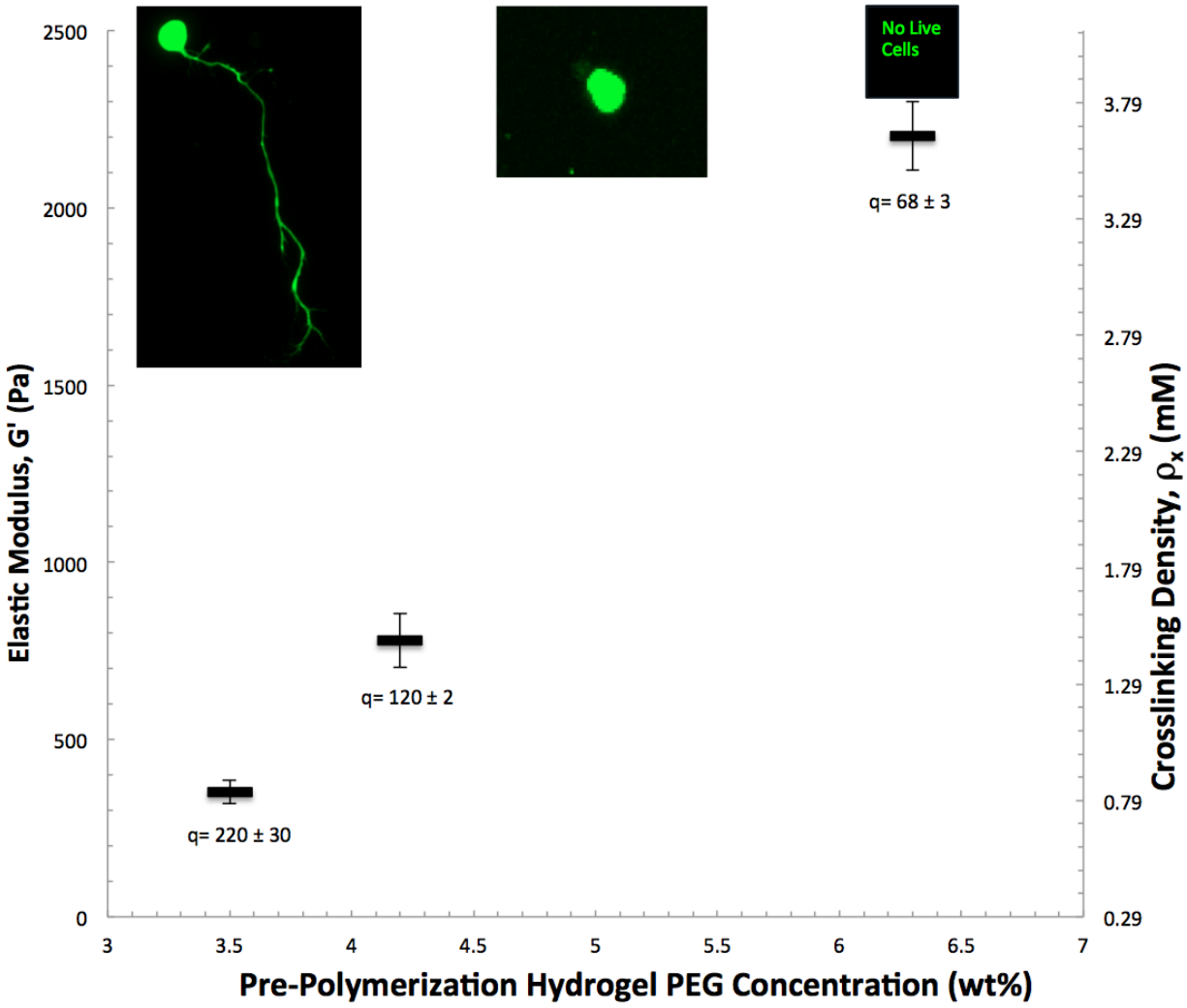

Figure 3.10: 3D ESMN axon outgrowth is highly dependent on the initial gel cross- linking density. At 0.9 mmol crosslinker per liter, axons are able to penetrate through the polymer-network by locally cleaving the collagen-derived peptide crosslinks. However, increasing the crosslinking density to 1.5 mM prevents neurons from extending axons and further increasing the crosslinking density to 3.6 mM results in 100% cell mortality. Mass swelling ratios are shown below and representative cell images are shown close to each data point.

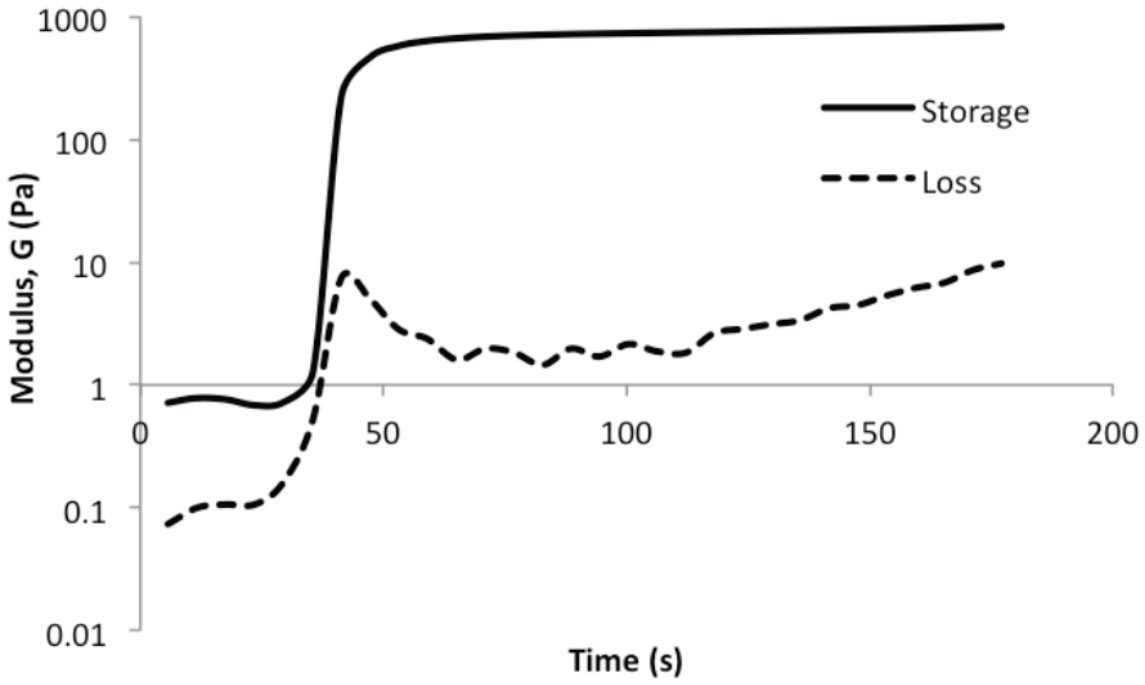

Figure 3.11: Example rheological time sweep of a 6.3 wt% gel initiated with LAP and 405nm light.

3.5 Experimental

ES Cell Culture: ES cells were differentiated into spinal motor neurons as previously described.[51] Briefly, Hb9::GFP mouse embryonic stem cells were plated into ES cell medium (ES DMEM, ES FBS, glutamine, non-essential amino acids, nucleosides, 2-mercaptoethanol, LIF (Life Technologies)) at approximately 5 x 10^5 cells per gelatinized T25 flask. After 24 hours the media was replaced, and on day 2 of culture, ES cells were trypsinized and placed in suspension culture in motor neuron media (Advanced-DMEM/F12, Neurobasal, and Knockout Serum Replacement (Life Technologies)) at 5 x 10^5 cells per untreated 10 cm tissue culture dish. In suspension culture, the cells aggregated into embryoid bodies (EBs). Two days after initial seeding the EBs were split 1:4 and induced into motor neurons with 1 μM retinoic acid (RA) (Sigma) and smoothened agonist (SAG) (Millipore). After 3 days of exposure to RA and SAG, the EBs displayed strong expression of Hb9::GFP transgene.[51]

Peptide synthesis: CRGDS and KCGPQG↓IWGQCK were purchased (American Peptide Company). CKKKKKKC and CYIGSR were synthesized on a Protein Technologies Tribute Peptide Synthesizer using standard Fmoc chemistry and Rink Amide MBHA resin. Peptide cleavage solution was formed by dissolving 250 mg dithiothreitol (DTT) and 250 mg phenol in a solution of 95% trifluoroacetic acid (TFA), 2.5% triisopropylsilane (TIPS), and 2.5% deionized water. Synthesized peptides were cleaved in the solution for 2 hours. Cleaved peptides were precipitated in cold diethyl ether, recovered via centrifugation, desiccated overnight, and then purified by reverse-phase HPLC (Waters Delta Prep 4000) purification on a C18 column using a linear acetonitrile:water gradient. The collected fractions of purified peptides were identified by matrix-assisted laser desorption/ionization-time-of-flight (MALDI-TOF) mass spectrometry (Figure 3.12)

Monomer synthesis: 8 equivalents of 5-norbornene-2-carboxylic acid were dissolved in anhydrous DMF and activated with 7.5 equivalents of HBTU (Sigma). 16 equivalents of N-methylmorpholine (Sigma) were added as base. After activating for 5 minutes, this mixture

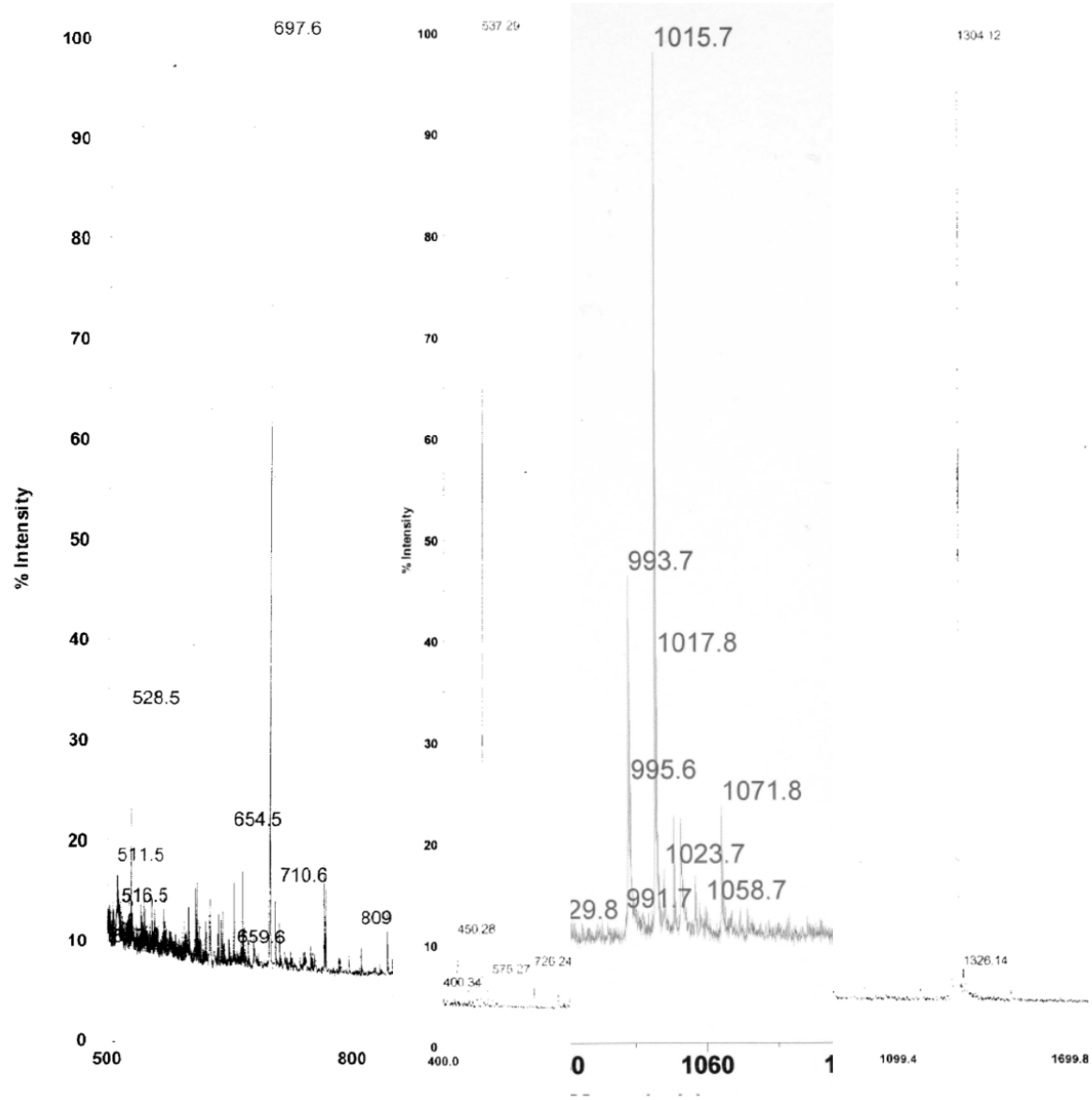

Figure 3.12: MALDI of peptides. Expected masses are 698 for CYIGSR, 537 for CRGDS, 992 (1015 w/Na^+ ion) for CKKKKKKC, and 1305 for KCGPQG↓IWGQCK.

was added to 1 equivalent of 20 kDa 4-arm PEG-amine (JenKem) dissolved in anhydrous DMF and reacted overnight at room temperature. PEG-norbornene was precipitated in diethyl ether, redissolved in DI water, and dialyzed against DI water for 24 h (2,000 MWCO). The product was then lyophilized and used for experimentation (Figure 3.13). LAP was synthesized as previously described.[99]

Cell Encapsulation: Gels were prepared with a total volume of 40 μL from stock solutions of 4-arm 20 kDa PEG-tetra-norbornene, MMP-degradable peptide (KCGPQG↓IWGQCK), ECM-mimic peptides (CRGDS and CYIGSR), cationic peptide (CKKKKKKC), bFGF (R&D Systems), and LAP.[99] The PEG-norbornene was carefully added to the motor neuron medium, followed the MMP-degradable peptide crosslinker or the PEG-dithiol (Sigma), the adhesive peptides, the LAP, and the bFGF. For the unfunctionalized gel, peptides were replaces with equal concentrations of cysteine, and bFGF was replaced with PBS. The mixture was then triturated to evenly mix the polymers. To vary the stiffness, the macromolecular monomer solution weight percent was scaled accordingly, while the total volume was maintained at 40 μL. For gels containing dissociated cells, EBs were exposed to 1 mL of ice-cold trypsin per 10 cm dish for 3 minutes and triturated vigorously to yield single cells. Single neurons were then re-suspended at 10 million cells/mL, and 10 μL of the cell suspension was gently mixed into the prepared gel formulation and polymerized for 1 minute under 40 mW/cm^2 405 nm blue light (Thor Labs Collimated 405nm LED). Gels containing EBs were prepared in an identical manner, but after 1 minute the gel solution was mixed to prevent EB settling. Cell-laden gels were then placed in motor neuron medium supplemented with 10 ng/mL GDNF and N2 and B27 Supplement. Table 3.1 provides a summary of all gel formulations used.

Rheology: The moduli of the hydrogels were measured using a rheometer with an 8 mm parallel plate geometry (AR-G2, TA Instruments), irradiation attachment (UV Light Guide Accessory, TA Instruments), and mercury arc lamp light source with 400-500 nm filter and light guide (Omnicure S2000, Exfo). The samples were formed in situ using a

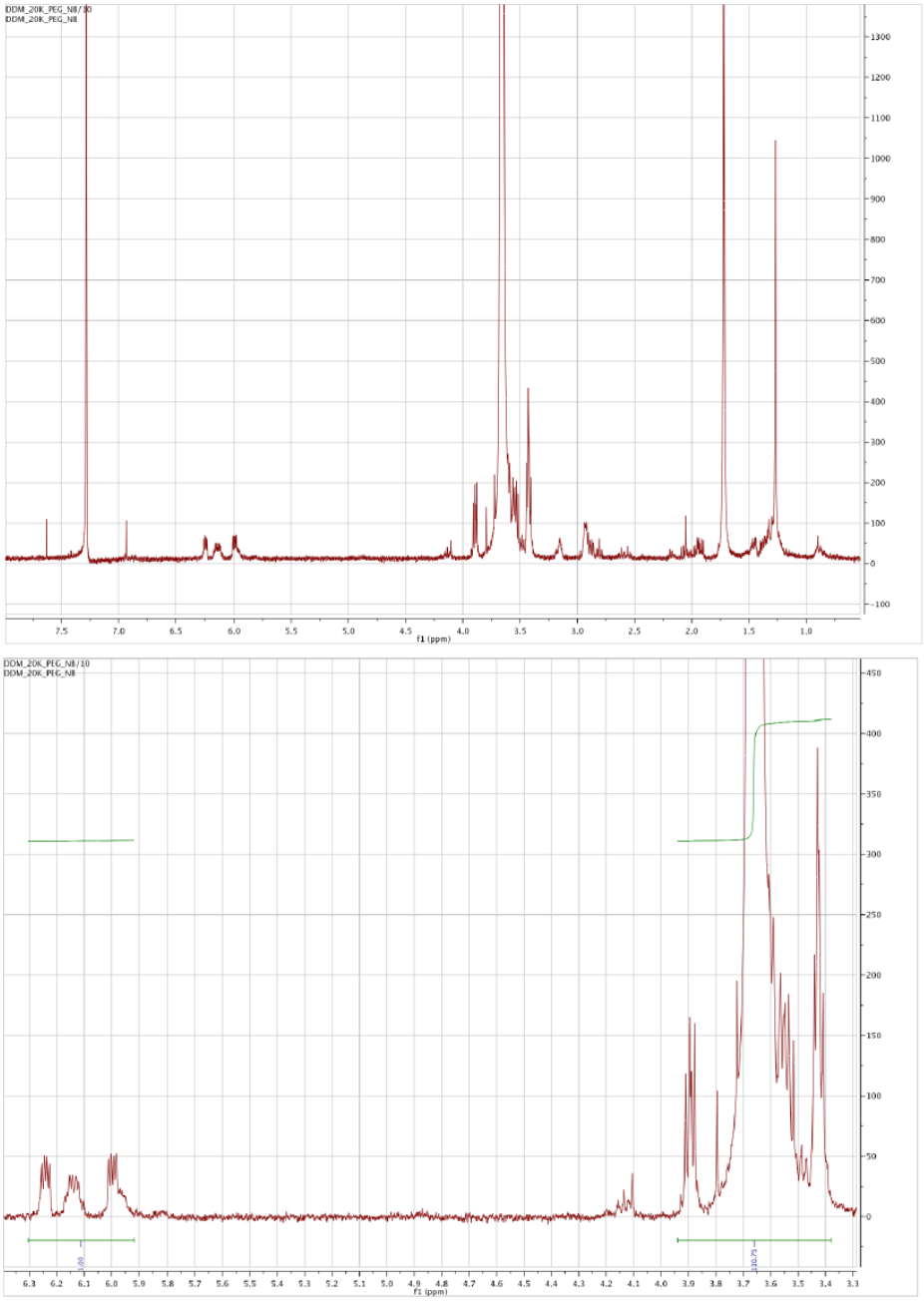

Figure 3.13: ^{1}H NMR of 4-arm PEG-norbornene. The ratio of the integral of the norbornene ene peaks to the PEG backbone peaks shows 88% functionalization after automatic phase and baseline correction.

Table 3.1: Summary of hydrogel formations. For the macromers and peptides, the concentrations refer to the molecular concentration, not the functional group concentration.

Gel	PEG-tetra-norbornene	KCGPQGIWGQCK	HS-PEG-SH	CRGDS	CYIGSR
Soft functionalized (3.5 wt%)	2.1 mM	3.85 mM	0 mM	1.25 mM	1.25 mM
Medium functionalized (4.2 wt%)	2.9 mM	4.50 mM	0 mM	1.25 mM	1.25 mM
Stiff functionalized (6.3 wt%)	3.8 mM	7.20 mM	0 mM	1.25 mM	1.25 mM
Soft unfunctionalized (3.5 wt%)	2.1 mM	3.85 mM	0 mM	0 mM	1.25 mM
Non-degradable functionalized (3.5 wt%)	0 mM	3.85 mM	1.25 mM	1.25 mM	

Gel	CKKKKKKC	Cysteine	LAP	bFGF	ESMNs
Soft functionalized (3.5 wt%)	0.0125 mM	0 mM	0.625 mM	10 nM	2.5M mL^{-1}
Medium functionalized (4.2 wt%)	0.0125 mM	0 mM	0.625 mM	10 nM	2.5M mL^{-1}
Stiff functionalized (6.3 wt%)	0.0125 mM	0 mM	0.625 mM	10 nM	2.5M mL^{-1}
Soft unfunctionalized (3.5 wt%)	0 mM	3.85 mM	0.625 mM	0 nM	2.5M mL^{-1}
Non-degradable functionalized (3.5 wt%)	0.0125 mM	0 mM	0.625 mM	10 nM	2.5M mL^{-1}

modified version of a previously published protocol50. Briefly, monomer solutions for each composition were prepared, and 5-10 L of solution was pipetted on to the bottom plate. The top plate was lowered until the gap was completely filled with solution (approximately 50-100 microns). The irradiation intensity was set to 16 mW/cm2 with the Omnicure shutter fully open (SilverLine Control-cure Radiometer and International Light Radiometer). Owing to this, the irradiation time for sample polymerization was adjusted to ensure that the same irradiation dose used for cell encapsulation (time * intensity) was applied to all samples (time increased from 1 to 2.5 minutes). A dynamic time sweep (10% strain, 5 rad/sec frequency) was used to monitor modulus evolution during polymerization to ensure that all samples reached their fully developed moduli (Figure 3.11). Final moduli were recorded for 3 to 5 replicates of each composition. Moduli of polymerized samples were adjusted to their equilibrium swollen values using measured swelling ratios and rubber elasticity theory.[119]

Confocal Imaging: Gels were placed between a glass slide and a coverslip separated by a rubber gasket and were imaged using a 10x or 20x water immersion objective. A 488nm laser was used to excite eGFP and calcein AM, and a 514nm laser was used to excite ethidium homodimer-1. The Cy3 secondary antibody was excited using a 528nm laser. A Z-stack of 100 images was taken through the entire gel in three different fields of view with approximately 20 μm between images.

Staining: Gels were fixed in a PBS solution containing 4% paraformaldehyde (PFA) for 2 hours at 4°C in the cold room and rinsed 3x with PBS. Gels were then swollen in a solution containing 10% horse serum in PBS overnight. Horse serum was then swollen out for 10 hours into PBS that was periodically changed. The primary antibody (Abcam Rabbit anti-MMP-2 Ab37150) diluted at 100x in 2% horse serum in PBS was then incubated overnight at 4°C on a rocker. In the morning, gels were transferred into PBS solutions and the primary antibody was given 10 hours to swell out in a periodically change PBS well. The secondary (Jackson ImmunoResearch Donkey Anti-Rabbit Cy3) was then diluted 1000x in 2% horse serum and swelled in overnight at 4°C. Finally, the secondary was swelled out for

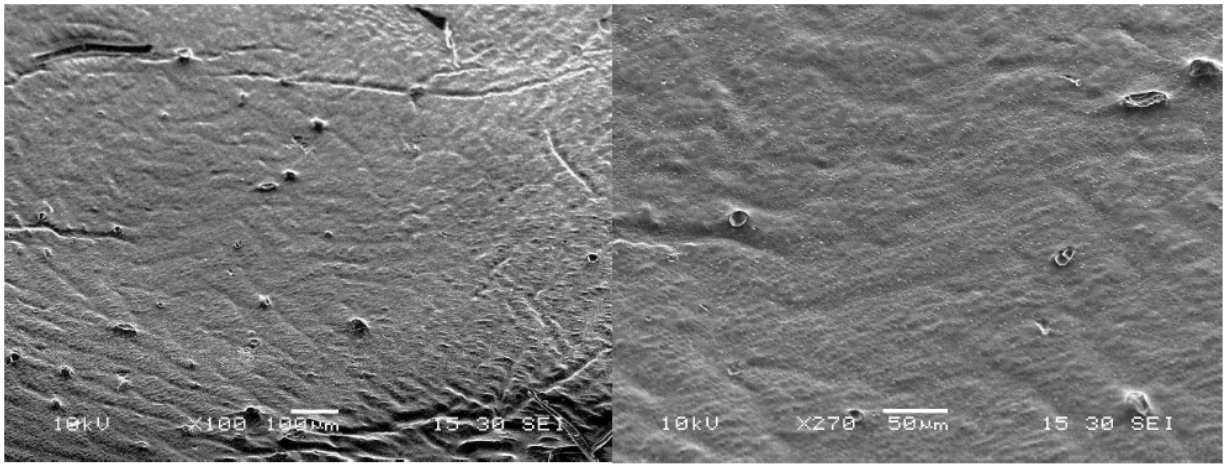

Figure 3.14: SEM images of soft (left) and stiff (right) hydrogels.

24 hours in PBS and the gels were imaged. For Live/Dead imaging, 2 µM of calcein AM and 4 µM of ethidium homodimer-1 stock solutions were diluted in PBS. Gels were incubated in this solution for 30 minutes on a shaker in a cell culture incubator and then imaged.

SEM: Gels were swollen overnight in DI water and dehydrated in ethanol solutions of 20%, 40%, 60%, 80%, 90%, and 100% for 10 minutes each, with the 100% solution being repeated three times. The gels were then dried in hexamethyldisilazane (HDMS), placed under vacuum for 30 minutes, mounted on stubs, and sputter coated with gold.[120] Samples were examined with a JEOL JSM-6480LV (Figure 3.14).

Statistics: Cell viability error is reported as the standard error from three image stacks taken from the same gel. Live cells were manually counted due to their complex shape and overlapping axons, and dead cells were counted using the Analyze Particles tool in ImageJ. More than 400 individual cells were counted for viability experiments. A t-test was performed between the functionalized and unfunctionalized gels at 36 hours and 72 hours to determine significance with $p<0.001$. Axon length was measured using the Simple Neurite Trace plugin for Fiji[9] (Figure 3.15). The error for axon length is reported as the standard error with 105 cells counted for the degradable gel and 118 cells for the non-degradable gels. This experiment was repeated multiple times (>10), and all results were similar. To translate

3D pixel lengths into microns, axons were assumed to have an equal chance of traveling in the x, y, or z directions. The scale in the x- and y-directions was 1.08 microns/pixel and in the z-direction was 3.89 microns/pixel. Therefore, the axon extension in pixels was multiplied by (2/3*1.06+1/3*3.89) to convert to microns.

3.6 Conclusions

Together, our findings emphasize the importance of biochemical and physical microenvironment characteristics in enabling motor axon outgrowth in 3D. In addition, this work highlights the potential of synthetic biomaterials as ECM mimics in the examination of nerve cell biology and axon guidance. Our studies allowed systematic characterization and identification of the chemical and physical properties sufficient for motor axon outgrowth in 3D hydrogel matrices. Such 3D hydrogel matrices may be used to investigate and identify the molecular mechanisms that drive directed axonal outgrowth, as in many cases genetic analysis is confounded by the presence of multiple receptor-ligand signaling systems that operate during axonal pathfinding.

Motor neuron subtype loss is an underlying cause of ALS and SMA disorders. Successful transplantation of nerve cells into the adult CNS for ALS and SMA treatment remains one of the obstacles in utilization of stem cell-based cell-replacement therapy. Fundamental in vitro studies, such as this one, can provide a useful screening tool and may provide novel insights into the requirements for design of transplantable matrices capable of directing axonal outgrowth and suggest improved strategies for cellular delivery vehicles for treatment of neurodegenerative disease states.

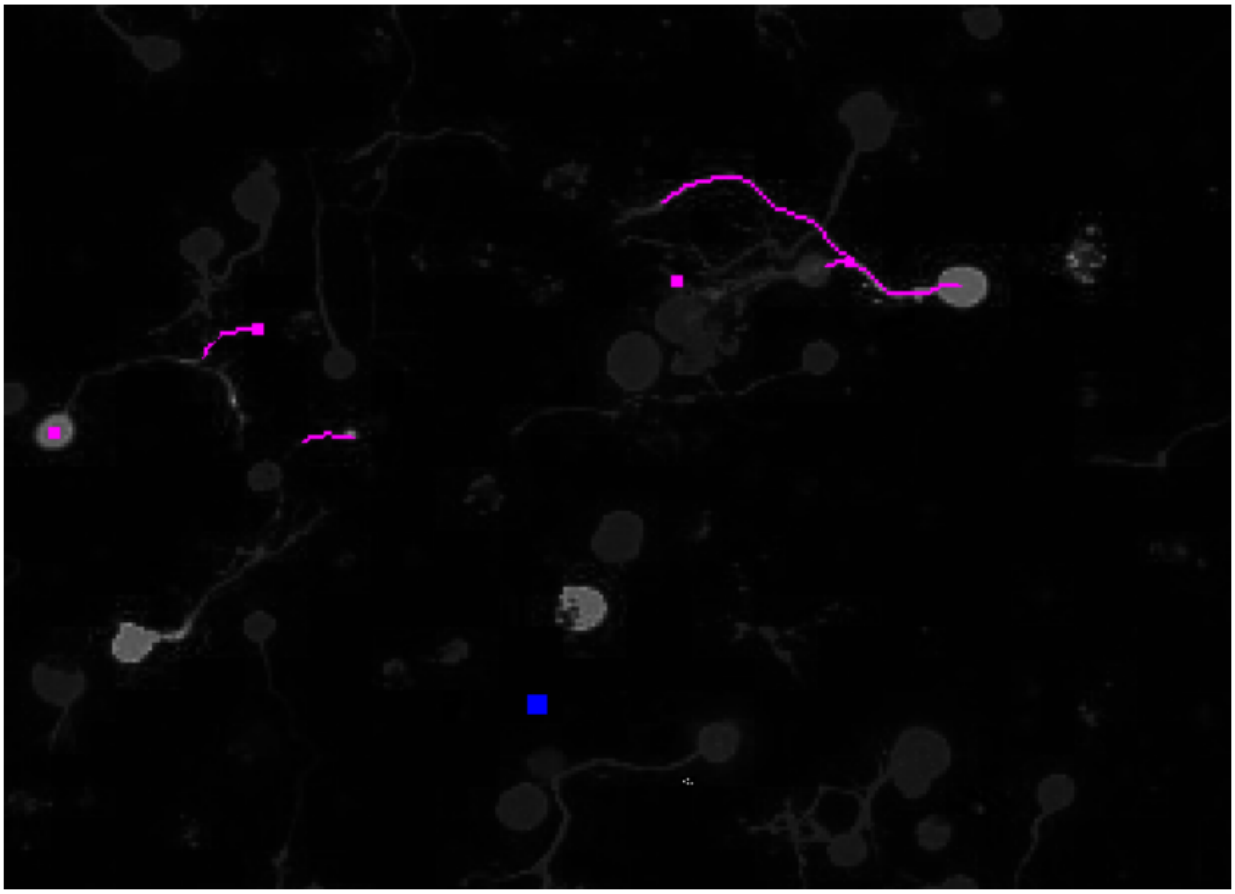

Figure 3.15: Demonstration of the quantification of the ESMN phenotype. Stacks were loaded into Simple Neurite Tracer,[9] a plugin for Fiji, and axon length and branching were quantified. Overlay of Z-projection (20%) opacity, GFP channel (current Z-position), and axon tracks shows high fidelity between each.

Chapter 4

Biophysically defined and cytocompatible covalently adaptable networks as viscoelastic 3D cell culture systems

4.1 Abstract

Covalently crosslinked synthetic hydrogels are especially suitable as tissue engineering scaffolds due to their well-defined and easily tunable biochemical and biophysical properties. In order to enable complex cell functions like ECM deposition, motility, and spreading, a mechanism for crosslink degradation must be engineered into the material; however, the presence of a degradation trigger can complicate the cellular biophysical microenvironment. Furthermore, covalently crosslinked polymers typically produce a predominantly elastic material, while native tissues are complex viscoelastic structures. Here, we present a step-growth poly(ethylene glycol) (PEG) hydrogel crosslinked by reversible hydrazone bonds. The macromer components are readily synthesized from commercially available precursors, and the resulting gels form rapidly under physiological conditions and provide a non-toxic matrix that is suitable for cell culture. This material is capable of mimicking aspects of the viscoelastic properties of native tissues, and the dynamic stress relaxing crosslinks permit complex cellular functions to occur while retaining the benefits of traditional covalently crosslinked hydrogels. Taken together, these attributes make hydrazone crosslinked hydrogels a unique tool for designing viscoelastic scaffolds and studying cellular responses to scaffold elasticity.

4.2 Introduction

Culturing cells in hydrogels for the purpose of regenerating tissue requires that the polymer matrix accommodate numerous cellular functions, beginning with matrix interactions and morphological changes. This initial adaptation allows encapsulated cells to subsequently engage in an external-internal exchange of information that influences critical processes including proliferation, motility, and extracellular matrix (ECM) deposition.[65,121,122] To facilitate improved three-dimensional culture environments, early approaches to hydrogel design often incorporated hydrolytically degradable crosslinks, engineered to degrade at a rate that was matched by the rate of the cellular function under study.[73–75] This strategy allowed for uniform ECM elaboration, but in many instances, only local changes in gel properties are desired (e.g., to promote cell spreading), and pre-engineering the degradation rates is often a complex optimization process. Thus, hampered by artificial constraints of bulk property changes at pre-determined rates, researchers developed complementary strategies based on processes that occur in native ECM, where cells bind, degrade and respond to their local proteinaceous microenvironment. For example, Hubbell *et al.*, pioneered the development of hydrogels crosslinked with cell-degradable and integrin binding peptide sequences, which mimicked critical aspects of the biochemical function of ECM.[97,113,123] Such polymer-peptide gels have permitted researchers to observe and characterize the dynamics of cell spreading,[96,124,125] migration,[125,126] axon extension,[82,127] proliferation,[128,129] and differentiation in a synthetic three-dimensional matrices.[129,130] However, unlike hydrolytically degradable gels, the cellular microenvironment in cellularly remodeled gels can be dramatically different from that of synthetic and hydrolytically degradable materials, which makes it difficult to characterize and draw conclusions about the role of the local biophysical environment on cell function.

In contrast, a covalently adaptable network responds to cell-induced stress by rapidly breaking and reforming elastically active crosslinks while maintaining stable material prop-

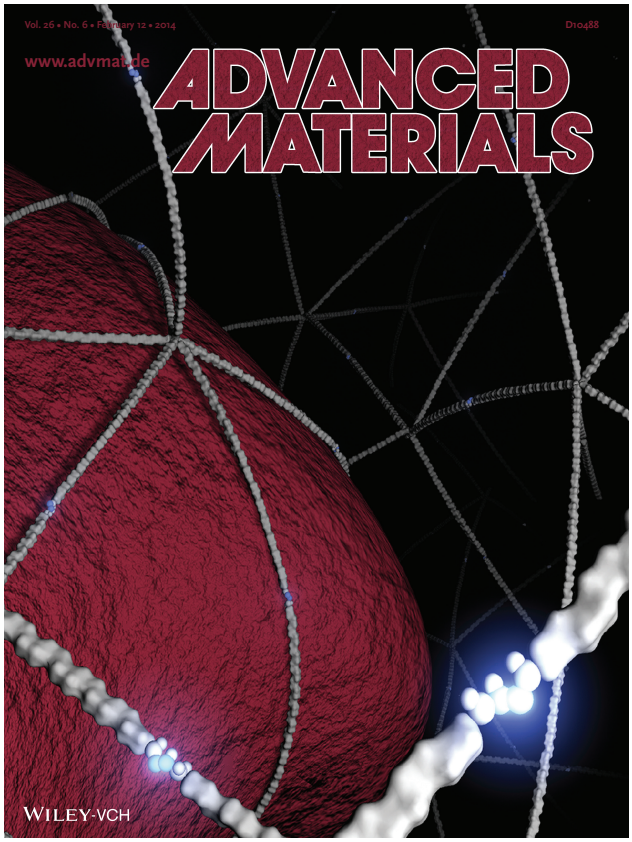

Figure 4.1: The contents of this chapter were awarded the cover of Volume 26, Issue 6 of *Advanced Materials*.

erties over time. This allows the material to respond to cell stresses yet provides a uniform scaffold elasticity to enable the elucidation of the effect of biophysical microenvironment on cell function. Given the increasing use of progenitor cells in biomaterials research and the increasing understanding of the role of biomechanical signaling on cell fate,[131–134] such a material should enable the observation of cell behavior in a biophysically defined scaffold. While dynamic bonds have previously been used in biomaterial scaffolds,[135–139] these linkages are supplemented by additional interactions, which precludes the precise and predictable biophysical control of the hydrogel. We sought to use a linkage that was stable enough to maintain the integrity of a crosslinked PEG network for several weeks of cell culture, but that would be labile enough to relax in response to cell-applied stress and allow for cell spreading, process extension, migration, or axon outgrowth to occur. Furthermore, few dynamic chemistries are compatible with cell encapsulation, and previously published covalently adaptable networks have either relied on high temperatures, low pH, or UV light to trigger covalent adaptability.[140–147]

In order to identify a cytocompatible chemistry that would crosslink hydrogels yet remain dynamic under physiologically relevant conditions, we looked to the field of dynamic covalent chemistry, which is comprised of reversible reactions under thermodynamic control, and include but are not limited to transesterification, acetal exchange, and hydrazone/oxime exchange. We were especially drawn to the hydrazone transimination reaction because it has been used in in vitro biological systems to assemble enzyme substrates[148] and to perform bioconjugations.[10,149–154] Further, the reaction rate between the hydrazine/alkoxyamine nucleophiles and aldehyde electrophiles and the stability of the resulting hydrazone/oxime are highly dependent on the precise chemical structure of the nucleophilic and electrophilic components; stability half-life values range from minutes to months at pH 7.0, depending on the exact functionality.[150,153] Thus, we hypothesized that a hydrazone crosslinked hydrogel would show covalently adaptable behavior, characterized by a frequency-dependent modulus and stress relaxation, under physiological conditions.

4.3 Results & Discussion

The material presented here is a PEG hydrogel formed through the ligation of an aliphatic hydrazine-terminated multi-arm PEG macromer with either a benzaldehyde- or an aliphatic aldehyde-terminated multi-arm PEG macromer. Gel formation occurs rapidly at physiological pH and temperature. The resulting cytocompatible covalently adaptable hydrogel allows a large degree of tunability of the biochemical and biophysical microenvironment, captures both the modulus and adaptability of native tissue, and enables the encapsulation of a diverse array of cell types. We believe that this material system will provide a unique platform to culture cells in three-dimensions, allow for improved reproduction of the stress relaxation found in native ECM, and permit the determination of how dynamic changes in the local biophysical environment influence cellular functions.

In an effort to identify hydrazine and aldehyde constituents that would react on a timescale compatible with hydrogel formation and cell encapsulation, we first investigated the kinetic and thermodynamic properties of small-molecule hydrazones that result from the reaction of a model aliphatic hydrazine, methylhydrazine, with two model aldehydes: an aliphatic aldehyde, butyraldehyde, and an aryl aldehyde, 4-nitrobenzaldehyde. Hydrazone formation was monitored by UV-vis spectroscopy, and the data were fitted to a bimolecular reversible kinetic model.[10] We assume equimolar starting concentrations of reactants and that the concentration of the hydrazone is simply the initial concretion of one reactant less the current concentration of that reactant. These assumptions simplify the rate equation to Equation 4.1,

$$\frac{d[A]}{dt} = -k_1[A]^2 + k_{-1}([A]_0 - [A]) \tag{4.1}$$

where $[A]$ is the concentration of either one of the reactants. The solution to the equation is derived in *Dirksen et al.* and allows the calculation of k_1, k_{-1}, and K_{eq} by monitoring the evolution of the hydrazone bond or the disappearance of one of the reactants.[10] The re-

action between methylhydrazine (25 μM) with butyraldehyde (25 μM) was rapid and reached equilibrium in less than an hour in pH 7.4 buffer (Figure 4.2). In contrast, the reaction of methylhydrazine (25 μM) and 4-nitrobenzaldehyde (25 μM) took several days to reach equilibrium (Figure 4.2). The calculated forward rate constants (k_1), back rate constants (k_{-1}), and equilibrium constants (K_{eq}) are summarized in Figure 4.3.

These data provided convincing evidence that both the aliphatic and aryl hydrazone bonds would form rapidly enough to crosslink a cell-laden hydrogel, as the rate constants for aliphatic and aryl hydrazone formation fall close to the range of reported rate constants for other hydrogel crosslinking chemistry, such as those for dibenzylcyclooctyne-azide (2.1 $M^{-1}s^{-1}$) and vinyl sulfone-thiol couplings ($0.17M^{-1}s^{-1}$).[113,155–158] Thus, we functionalized 4-arm 20 kDa and 8-arm 10 kDa PEG macromers with aliphatic hydrazine end groups (4-H, 8-H) and 4-arm 10 kDa and 8-arm 10 kDa PEG macromers with either benzaldehyde (4-BA, 8-BA) or aliphatic aldehyde (4-AA, 8-AA) end groups. Gram-scale quantities of the macromers are synthetically available in 1-2 steps from inexpensive commercially available precursors, which renders this system accessible to a wide range of biomedical, chemical, and polymer engineering labs. Mixing 18 mM (72 mM functional groups) solutions of either 4-H and 4-AA (Figure 4.3) or 4-H and 4-BA resulted in the formation of a hydrogel at room temperature and pH 7.4. The rheological properties of the gels were investigated under shear, and the results are shown in Figures 4.3 and 4.4. 4-H:4-AA reaches its crossover point in tens of seconds. Evolution of 90% of its final elastic modulus is achieved in 5 minutes, which can be predicted by fitting modulus evolution data to Equation 4.2,

$$G(t) = G_\infty - Ae^{-Bt} \tag{4.2}$$

where G_∞ is the plateau modulus and A and are fit parameters. 4-H:4-BA reaches its final modulus in *ca.* 1 hour at pH 7.4, but this process is highly pH dependent (Figures 4.3 and 4.5.

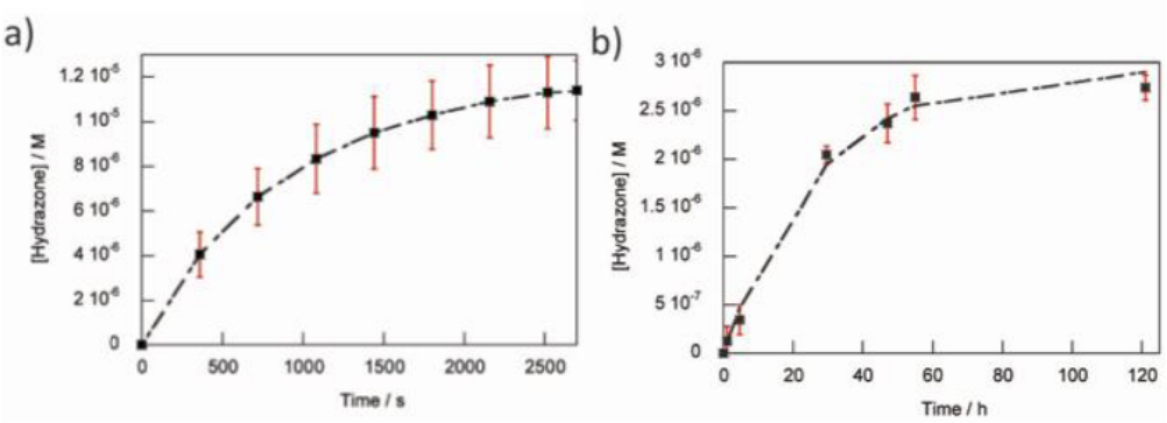

Figure 4.2: Plots showing the rate of hydrazone formation as monitored by UV-visible spectroscopy. a) Plot of hydrazone formation upon reacting N-methylhydrazine (25 μM) and butyraldehyde (25 μM) in PBS, pH 7.4. Each data point represents the mean value from three independent kinetic runs. Error bars represent standard deviation. b) Plot of hydrazone formation upon reacting N-methylhydrazine (25 μM) and 4-nitrobenzaldehyde in PBS, pH 7.4. Each data point represents the mean value from three independent kinetic runs. Error bars represent standard deviation. The dashed grey line represents a fit to a second-order reversible kinetic model.

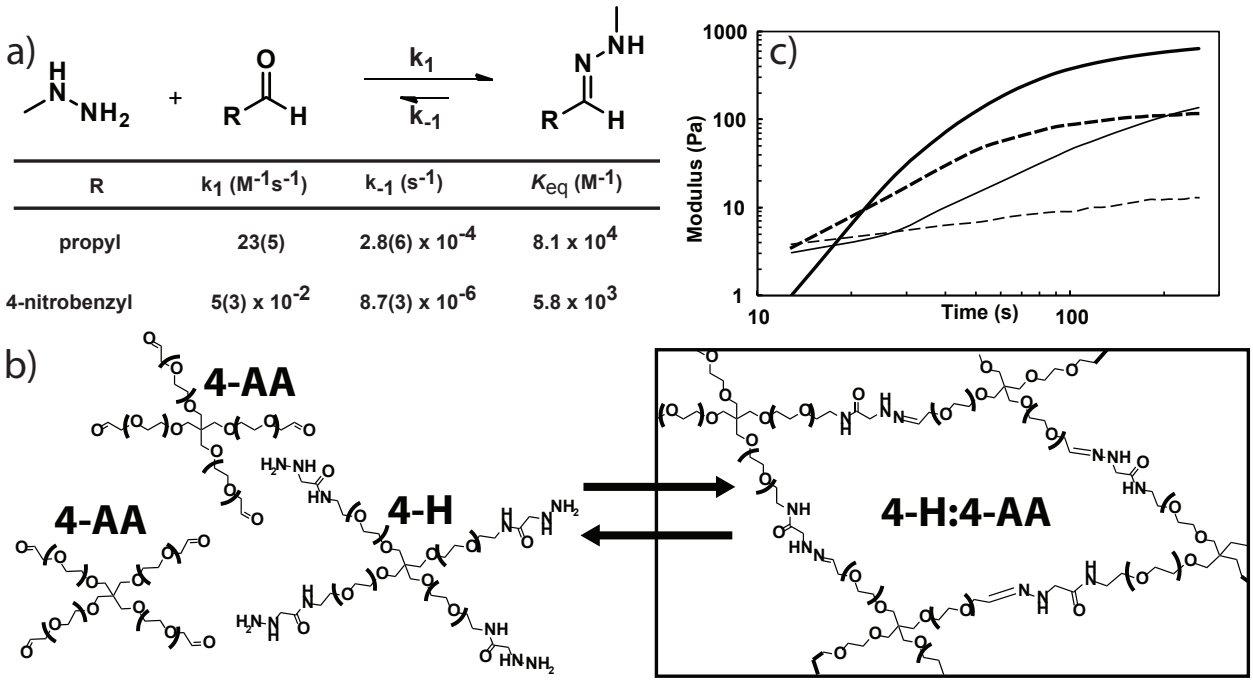

Figure 4.3: a) Table showing the relevant kinetic and thermodynamic information for reactions between N-methyl hydrazine and butyraldehyde or 4-nitrobenzaldehyde at 25°C in pH 7.4 buffer containing 1% DMSO. b) Chemical structures of 4-H and 4-AA showing reversible gelation. c) Rheological time sweep plot showing rates of gelation. Evolution of 90% of G_∞ occurs in 5 minutes for 4-H:4-AA (thick solid line, G′; thick dashed line G″) and *ca.* 1 hour for 4-H:4-BA (thin solid line, G′; thin dashed line G″).

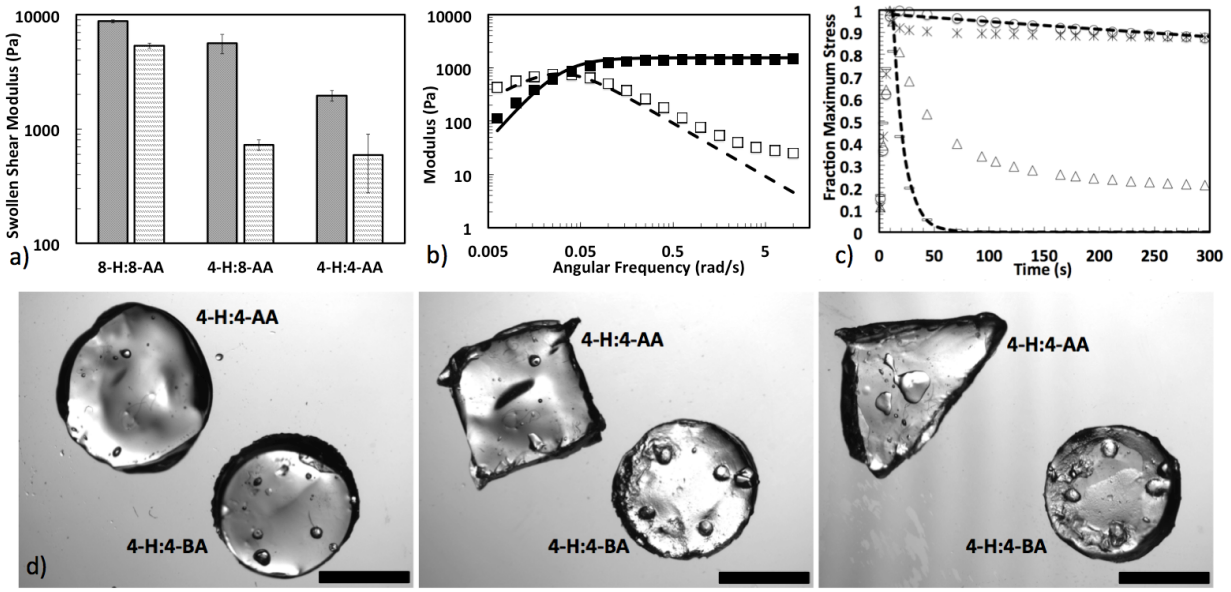

Figure 4.4: a) Hydrogel modulus can be controlled by incorporating crosslinkers of different functionalities or varying the stoichiometry of functional groups (dark bars, on stoichiometry; light bars 50% excess hydrazine, Students t-test, $p<0.05$). b) 4-H:4-AA shows frequency-dependent crossover below 0.03 rad/s, which indicates that it behaves as a Maxwellian viscoelastic fluid (filled squares, G′; empty squares, G″; solid line, G′ Maxwell fit; dashed line, G″ Maxwell fit). c) Stress relaxation is strongly dependent on the ratio of aliphatic to aryl aldehyde crosslinker, with relaxation times ranging from tens of seconds to tens of hours (bars, 100:0 4-AA:4-BA; triangles, 80:20; circles, 0:100). When the mole fraction of 4-BA crosslinker crosses the percolation threshold of the system, the stress relaxation behavior collapses to that of 0:100. Stress relaxation of 4-H:4-AA and 4-H:4-BA are in good agreement with the Maxwell model (dashed lines). Covalent adaptability can be abolished upon treatment by sodium cyanoborohydride, which reduces the hydrazone bond to the corresponding secondary hydrazine (asterisks). d) Stress relaxation can be shown macroscopically through molding. 4-H:4-AA and 4-H:4-BA were pressed into square and triangular molds for 60 s, with 4-H:4-AA adopting the shape of the mold as a viscoelastic fluid and 4-H:4-BA retaining its shape as a more elastic solid (scale bar = 3 mm).

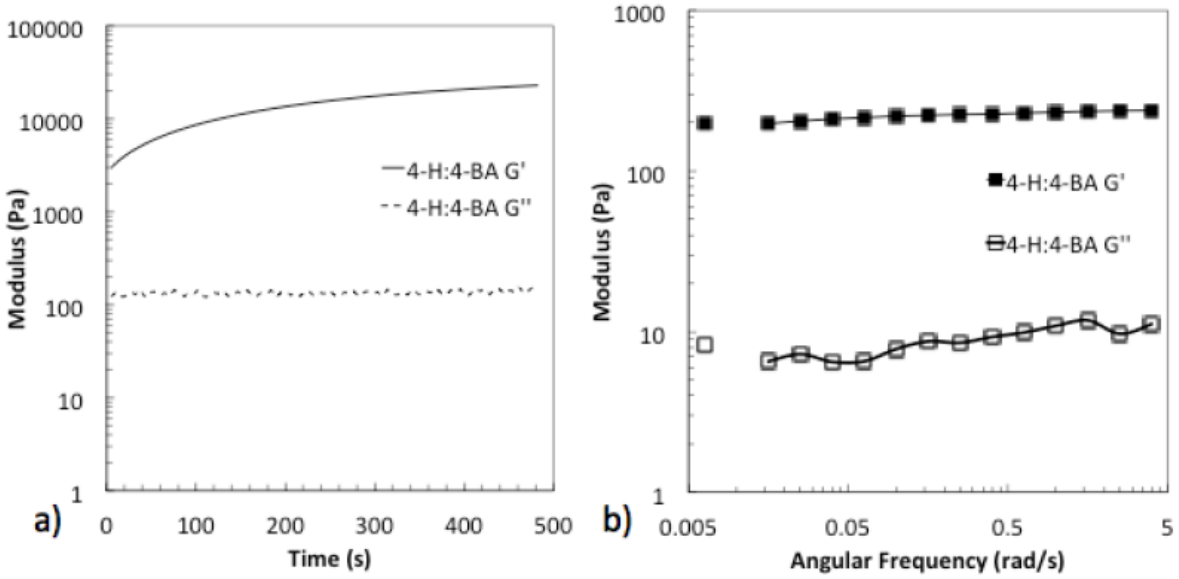

Figure 4.5: a) Slightly lowering the pH dramatically accelerates the gelation of 4-BA and 8-BA crosslinked networks. This 4-H:4-BA gel evolves its final modulus in ten minutes. b) 4-H:4-BA and 8-H:8-BA gels do not display frequency-dependent moduli, indicating the aryl hydrazone bond does not relax on the same time scale of the aliphatic hydrazone.

In addition to exerting control over the stress relaxation characteristics of these materials, we can also control equilibrium modulus by varying the size and functionality of each macromer. Furthermore, because the crosslinking density is linearly related to modulus through Equation 4.3,

$$G = kTQ^{-\frac{1}{3}}\rho_x \tag{4.3}$$

where k is Boltzmann constant, T is the temperature, Q is the volume swelling ratio, and ρ_x is the crosslinking density, the final material modulus can be systematically varied to target a tissue or magnitude of interest. In Figure 4.4, the swollen shear modulus varied from *ca.* 600 Pa (4-H:4-AA, 2:1) to *ca.* 9 kPa (8-H:8-AA), and all of the values are in reasonable agreement with that predicted by rubber elasticity theory. While non-idealities certainly exist, Equations 4.3 and 4.6 enable the rational design of a polymeric viscoelastic material that could serve as a biophysical mimic for complex tissues.

Frequency sweeps of 4-H:4-AA (Figure 4.4) and 4-H:4-BA (Figure 4.5) indicate that the 32-fold difference in k_{-1} dramatically changes the ability of the materials to adapt to strain. 4-H:4-AA exhibits a frequency-dependent modulus that is characteristic of a single-mode Maxwell viscoelastic fluid, whereas 4-H:4-BA exhibits a frequency-independent modulus indicative of a Hookean solid. Presumably, the angular frequency at which G″ crosses G′ is lower than could be accurately measured. Using the Equations 4.4 and 4.5 for a Maxwellian viscoelastic fluid,[159]

$$G'(\omega) = \frac{G_\infty \omega^2 \tau^2}{1 + \omega^2 \tau^2} \tag{4.4}$$

$$G''(\omega) = \frac{G_\infty \omega \tau}{1 + \omega^2 \tau^2} \tag{4.5}$$

where G_∞ is the equilibrium modulus, ω is the angular frequency, and τ is the relaxation time; we find $\tau = 34$ s (Figure 4.4). This agreement with the Maxwell model indicates that

these gels should relax an applied stress on a time scale on the order of tens of seconds and that by varying the ratio of benzaldehyde to aliphatic aldehyde crosslinker, one should retain a great deal of control over the adaptation properties of the material.

Thus, we next polymerized six gels of varying compositions, ranging from 100% 4-AA crosslinks to 100% 4-BA crosslinks and strained them 100% on the rheometer (Figure 4.4). Gels crosslinked by 100% aliphatic aldehyde macromers relaxed 100% of their stress within tens of seconds, while those crosslinked by 100% benzaldehyde macromers took closer to 14 hours to relax 75% of their stress (Figure 4.6). We observed that the stress relaxation profile can be adjusted by changing the ratio of aliphatic aldehyde to benzaldehyde macromer: as the proportion of benzaldehyde macromer increases, the hydrogel relaxes stress more slowly, until a critical point, the percolation threshold (*vide infra*), is reached (Figure 4.4). Thus, by tuning these characteristics the number of arms on the PEG polymer, the choice of either aliphatic aldehyde or benzaldehyde end groups, the ratio of the aliphatic to aryl aldehyde-derivatized macromers, and the relative stoichiometry of hydrazine and aldehyde components it is possible to precisely control the physiological modulus and stress relaxation characteristics of the gel to tailor the gel characteristics specifically to the tissue under study.

Next, we fit the relaxation data to Equation 4.6, a standard Maxwell model for viscoelastic fluids,[160]

$$G(t) = \sum_{k=1}^{N} \frac{\eta_k}{\lambda_k} e^{\frac{t}{\lambda_k}} + G_\infty \tag{4.6}$$

where G_∞ is the elastic modulus, η is the viscosity, and λ is the time constant of relaxation. While all adaptable gels should have a polymer relaxation mode and a bond relaxation mode, the rapid relaxation of the polymer chains (typical $\lambda = 0.05$ s) was not captured in the rheology. The 4-arm-co-4-arm (4-H:4-AA) aliphatic gel fit the model well with a single mode of relaxation ($\lambda = 10.7$ s), as did the 8-arm-co-8-arm (8-H:8-AA) aliphatic gel ($\lambda = 91.0$ s). These numbers are consistent with the fact that at equal weight percent

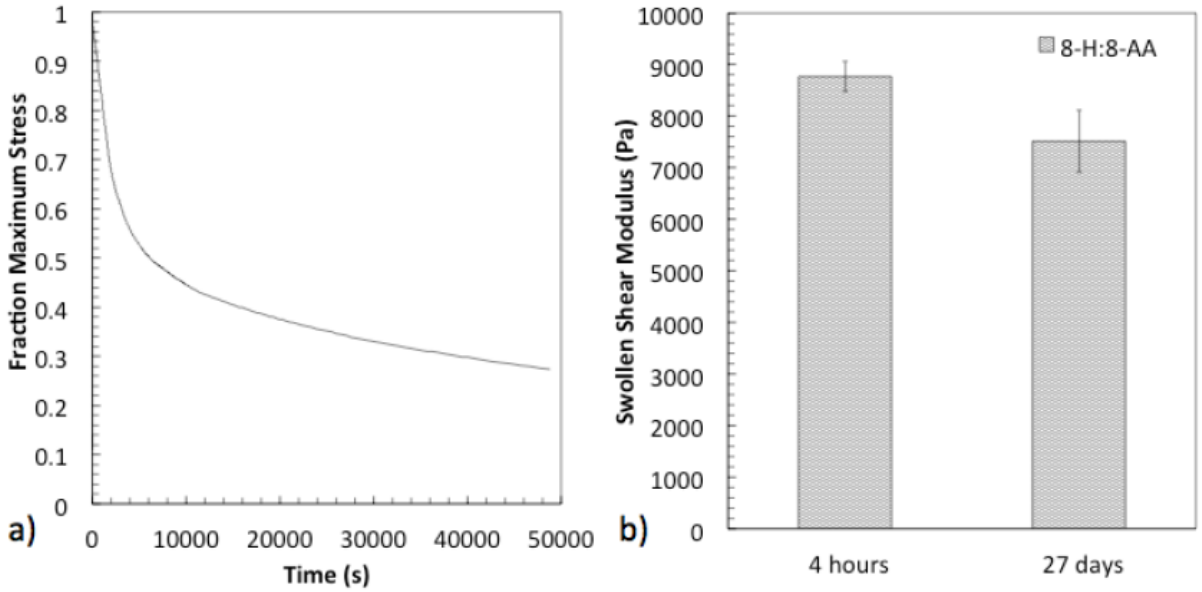

Figure 4.6: a) 8-H:8-BA relaxing from 10% applied stress overnight. It is likely instrument slippage accounts for some of this relaxation. b) The elastic moduli of 8-H:8-AA swollen in PBS at 25°C for 27 days. While 4-H:4-AA dissolves overnight in media at 37°C and within two days in PBS at 25°C, 8-H:8-AA is stable for >2 weeks at 37°C in media and >1 month at 25°C in PBS. Mass loss does occur from the surface and the gels are visibly *ca.* 20% smaller at these time points, but, as evidenced by their bulk moduli, crosslinking density remains fairly constant.

of PEG, the 8-arm-co-8-arm gels contain 8-fold more crosslinks, leading to a roughly 8-fold slower time constant of relaxation. The benzaldehyde crosslinked gels did not fit the model as well, which is likely a result of slow relaxation competing with instrument slip. However, the 4-H:4-BA gel relaxed with a time constant of $\lambda = 2370$ s, while the 8-H:8-BA gel tore before 100% strain could be applied, which precluded accurate measurement of the time constant. Mixed crosslink gels containing a fraction of benzaldehyde crosslinkers below the percolation threshold, calculated using Equations 4.7 and 4.8,[119,161,162]

$$p_c = \frac{1}{\sqrt{\frac{(f_A-1)(f_B-1)}{r}}} \tag{4.7}$$

$$r = \frac{f_B n_B}{f_A n_A} \tag{4.8}$$

which equals 0.33 for 4-H:4-AA and 4-H:4-BA, are modeled reasonably well in their early and late stages by summing both the aliphatic aldehyde and the benzaldehyde modes (Figure 4.7). However, once the gel is comprised of more than 33% 4-BA crosslinks, the stress relaxation behavior of these materials collapses to that of 4-H:4-BA. Finally, when the gel is treated with sodium cyanoborohydride, the hydrazone bond is reduced to the corresponding hydrazine, thus abolishing the dynamic nature of the bond and, consequently, the relaxation behavior (Figure 4.4).

The self-healing, dynamic characteristics of 4-H:4AA and static nature of 4-H:4-BA were also visualized macroscopically. Figure 4.4 shows two disk-shaped hydrogels formed using a syringe mold 5 mm in diameter. Both hydrogels were then pressed into a 4 mm 4 mm square mold for 60 s, re-imaged, pressed into a 6 mm 7mm right triangular mold for 60 s, and imaged again. These qualitative images clearly demonstrate that 4-H:4-AA has the capacity to rearrange its macroscopic network structure to relax stresses applied by the mold within 60 s, allowing it to be re-processed into a new macroscopic shape. On the contrary, 4-H:4-BA is immutable on this time scale and retains its original disk shape throughout the

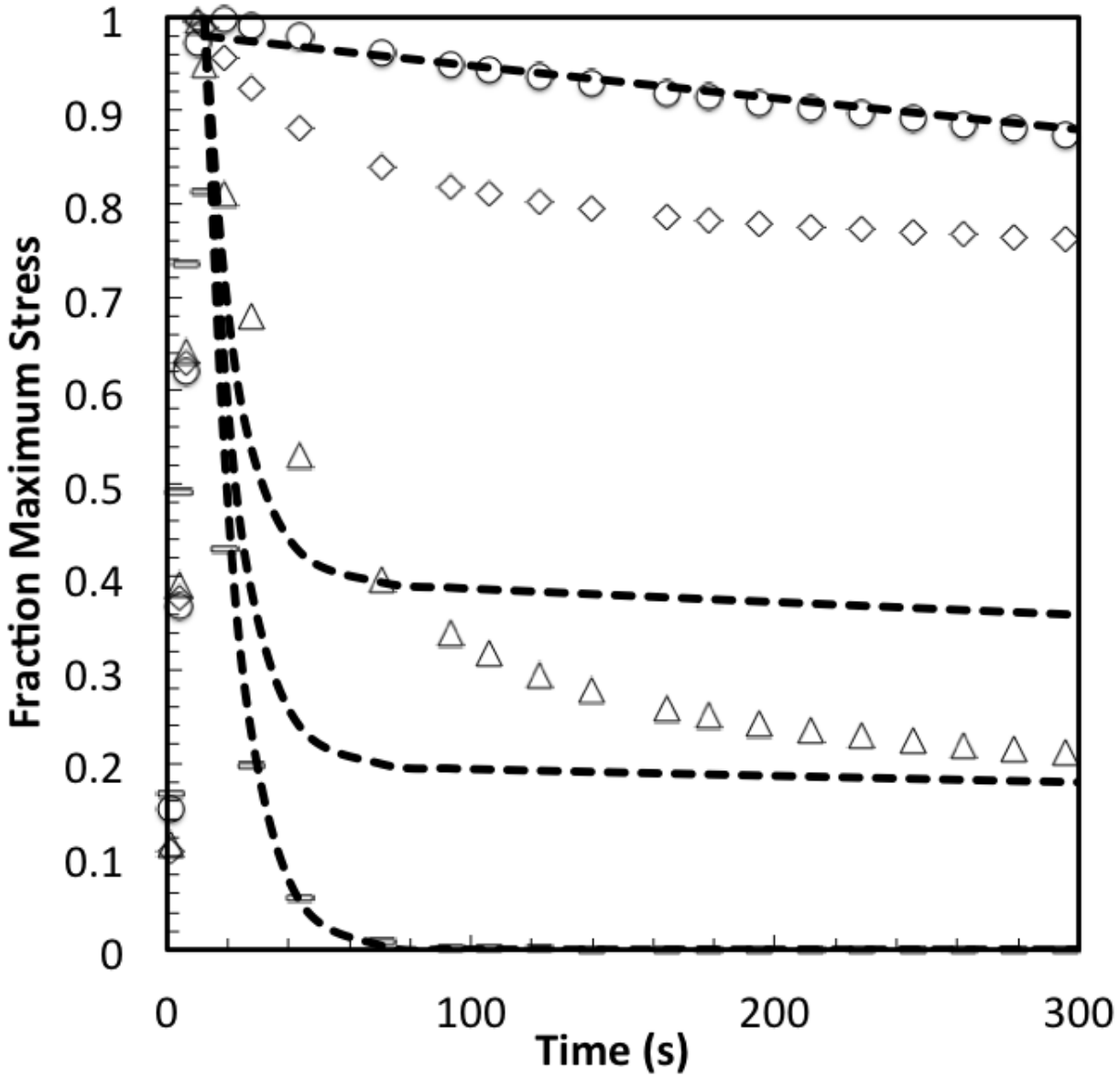

Figure 4.7: Stress relaxation and Maxwell fits for 100:0 4-AA:4-BA (bars), 80:20 (triangles), 60:40 (diamonds), and 0:100 (circles). The intermediate relaxation behavior is smoother than the model predicts for gels containing both 4-AA and 4-BA. This discrepancy is expected, as the Maxwell model assumes that there is no interaction between the modes of relaxation, whereas in this system, a mode of relaxation exists for each combination of 4-arm PEG hydrazine with n aliphatic PEG aldehyde macromers and (4-n) PEG benzaldehyde macromers. Once the fraction of aryl crosslinks exceeds pc (60:40, diamonds), an independent minimally relaxing polymer network is formed, and the material ceases to behave as a viscoelastic fluid, explaining why the Maxwell model ceases to fit the data.

processing. Though the aryl hydrazone bonds can relax stress, albeit on a much longer time scale than the aliphatic hydrazone bonds, we observed no shape change, even after 1 hour. Figure 4.8 further explores these macroscopic demonstrations of stress relaxation and shows the fusion of three gels into a larger shape, their molding into other shapes, and finally their injection through an 18 G needle to form a long extruded fiber.

We next sought to directly compare the viscoelastic properties of these hydrogel networks to that of a complex tissue, namely a mouse gastrocnemius muscle. We selected muscle for comparison, as it is widely known to relax stress in two separate modes, with a fast λ varying from 0.03 s to 8.4 s and a slow λ varying from 2.2 s to 93.8 s, depending on the species.[163] Further, muscle has a Youngs modulus around 10 kPa, which is well within the range of the moduli for the PEG networks that were synthesized here (1.8 27 kPa).[131,163–165] A mouse gastrocnemius muscle was isolated and characterized using shear rheology. The results show a highly frequency-dependent elastic modulus between 2-3 kPa and relaxation of 80% of an applied stress within 600 seconds (Figure 4.9. Consistent with mechanical theories of fiber containing composite materials,[166] we hypothesized that the steep reduction in modulus below 1 rad/s shear was due primarily to the fibrous structure of skeletal muscle, rather than formation and reformation of physical crosslinks. Interestingly, the stress relaxing hydrogels capture aspects of this behavior through breaking and reforming of the material crosslinks, and we observed two discrete modes of relaxation and fit them to a two-mode Maxwell model.[163,164,167] This behavior is readily seen in Figure 4.9, where the applied stress initially decays rapidly and then slows. In contrast, the trace of the 100% 8-H:8-AA gel displays a single mode of relaxation. When fit to the Maxwell model, muscle relaxes with time constants of $\lambda = 7.5$ s and $\lambda = 100$ s with a *ca.* 55% weighting of the slow-relaxing mode and a *ca.* 45% weighting of the fast-relaxing mode. These values are consistent with published measurements of tensile muscle relaxation,[163,164] and they fall within the range of the relaxation time constants of the 4-arm ($\lambda = 10.7$ s) and 8-arm aliphatic gels ($\lambda = 91.0$ s). Collectively, these results suggest that covalently adaptable networks impart

Figure 4.8: The 4-H:4-AA and 8-H:8-AA hydrogels can be easily molded and fused. Here, three puck-shaped gels (two shown) were fused into a star using a simple rubber mold and a pair of glass slides. The star was then remolded into a disc and a triangle, and then extruded into a fiber through an 18-gauge needle using a syringe pump.

unique viscoelastic properties that mimic aspects of native tissue materials that are difficult to capture with traditional synthetic hydrogels. Further, by tuning the initial macromer composition and concentration (8-H:8-AA, 2:1 ratio), gels were formulated with initial and time dependent properties very similar to those of the gastrocnemius.

We next sought to demonstrate the cytocompatibility of the reaction and encapsulation processes and examine how cells would respond to longer-term culture in these covalently adaptable networks. Because of our characterization of mouse skeletal muscle, this compelled us to examine a cell line, C2C12s, a common source of myoblasts that fuse into myotubes under confluent conditions. For cell encapsulation studies, we formulated three hydrogels using the hydrazine- and aldehyde-terminated PEG macromers in combination with a benzaldehyde-terminated KGRGDS peptide, which provides sites for integrin binding and promotes cell survival in PEG gels.[76,77,95,168] Specifically, one gel was synthesized with 100% aliphatic crosslinks (8-H:8-AA), another with 80% aliphatic crosslinks and 20% aryl aldehyde crosslinks (8-H:(80% 8-AA 20% 8-BA)), and a final gel with 100% aryl aldehyde crosslinks (8-H:8-BA). All gels contained 3 mM KGRGDS peptide. We selected these specific compositions to form highly adaptable gels that would remain stable for several weeks of cell culture yet allow a significant variation in stress relaxation properties, from highly relaxing to minimally relaxing. C2C12 myoblasts were encapsulated at a concentration of 106 cells/mL, and the cells were stained and imaged for viability after 24, 72, and 240 hours (Figures 4.10 and 4.11) and cytoskeletal organization at 24, 96, 144, and 264 hours (Figures 4.10 and 4.12).

First, we note high levels of cell survival after encapsulation, thus validating the applicability of this crosslinking chemistry for the conditions studied (Figure 4.10). Calcein-AM and ethidium homodimer staining indicated that viability was higher than 90% in all three conditions after 72 h (Figure 4.10), which confirms that this hydrogel platform is cytocompatible and appropriate for studying cellular responses to dynamic, tissue-mimicking biophysical environments. Furthermore, the significant drop in cell viability in 8-H:8-BA after 10 days in culture implies that matrix dynamism could play an important role in long-term cell via-

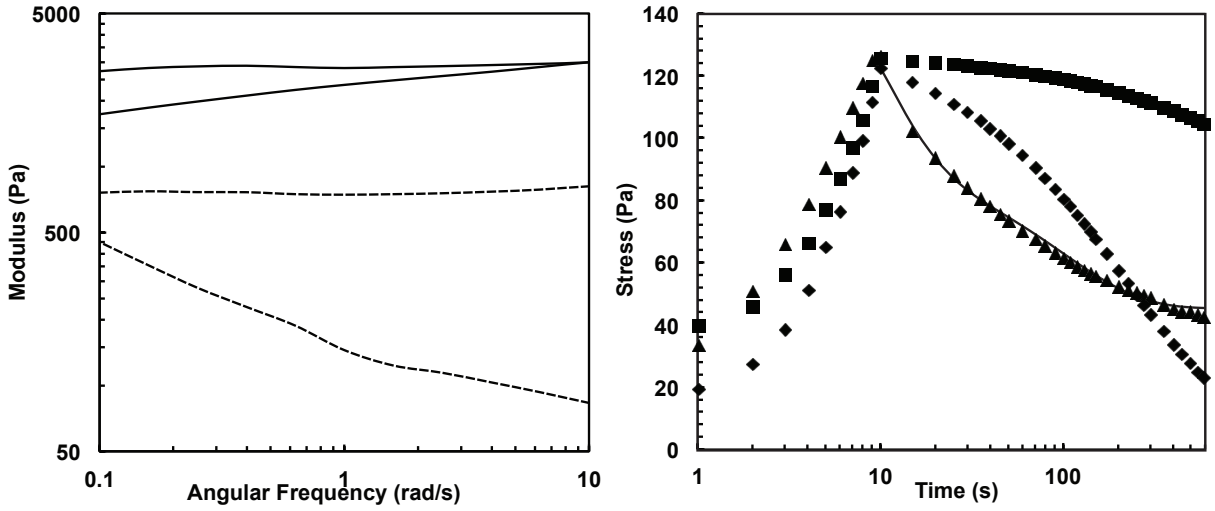

Figure 4.9: The rheological properties of complex tissue can be emulated using covalently adaptable hydrogels. a) The elastic modulus of mouse muscle (thin solid line, G'; thin dashed line, G'') begins to sharply decrease below 1 rad/s, possibly due to the fibrous nature of the tissue, while the 8-H:8-AA (thick solid line, G'; thick dashed line, G'') exhibits this property below 0.05 rad/s. However, G_∞ of the mouse muscle can be exactly matched. b) The mouse muscle (triangles) demonstrates significant stress relaxation over 10 minutes and fits a two-mode Maxwell model (solid line). 8-H:8-AA (diamonds) comes close to reproducing the initial and final stress with just one mode of relaxation. 8-H:8-BA (squares) relaxes much more slowly.

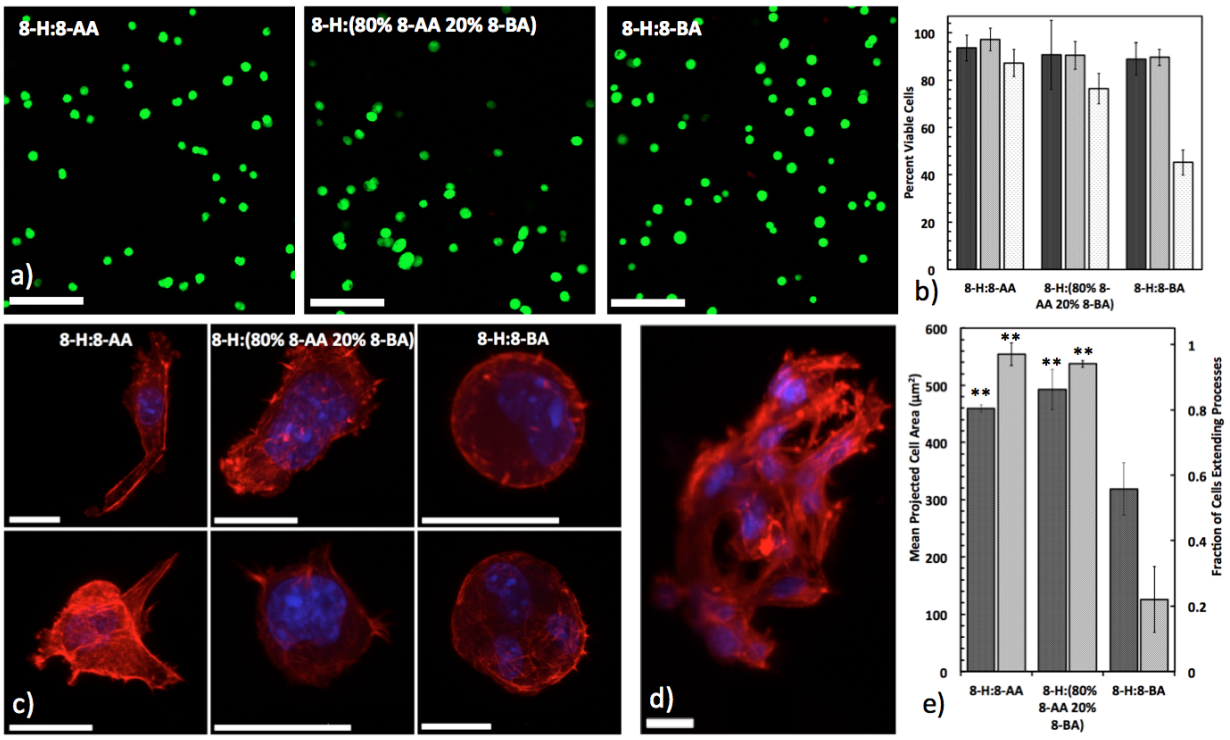

Figure 4.10: a) Images of encapsulated C2C12 myoblasts 72 hours post-encapsulation stained with calcium-AM (green, live) and ethidium homodimer (red, dead; scale bar 200 μm). b) Cell viability quantified at 24 hours (dark bars), 72 hours (medium bars), and 240 hours (light bars). c) Representative images of cells stained for f-actin (red) and the nucleus (blue) are shown (scale bar 20 μm). After 10 days in culture, the cells encapsulated in 8-H:8-AA exhibit significant spreading and robust actin fiber formation. Cells encapsulated in 8-H:(80% 8-AA,20% 8-BA) extend lamellipodia and filopodia and show actin filaments but do not deviate as far from rounded. Cells encapsulated in 8-H:8-BA remain rounded. d) Some cells in the 8-H:8-AA gels fuse into multinuclear structures. e) Quantification of cell spreading (dark bars, left axis) and fraction of cells extending processes (light bars, right axis) by 10 days in culture. Cells in 8-H:8-AA and 8-H:(80% 8-AA,20% 8-BA) both displayed significantly more spreading, as measured by projected cell area and process extension, than those in 8-H:8-BA (Students t-test, $p>0.05$).

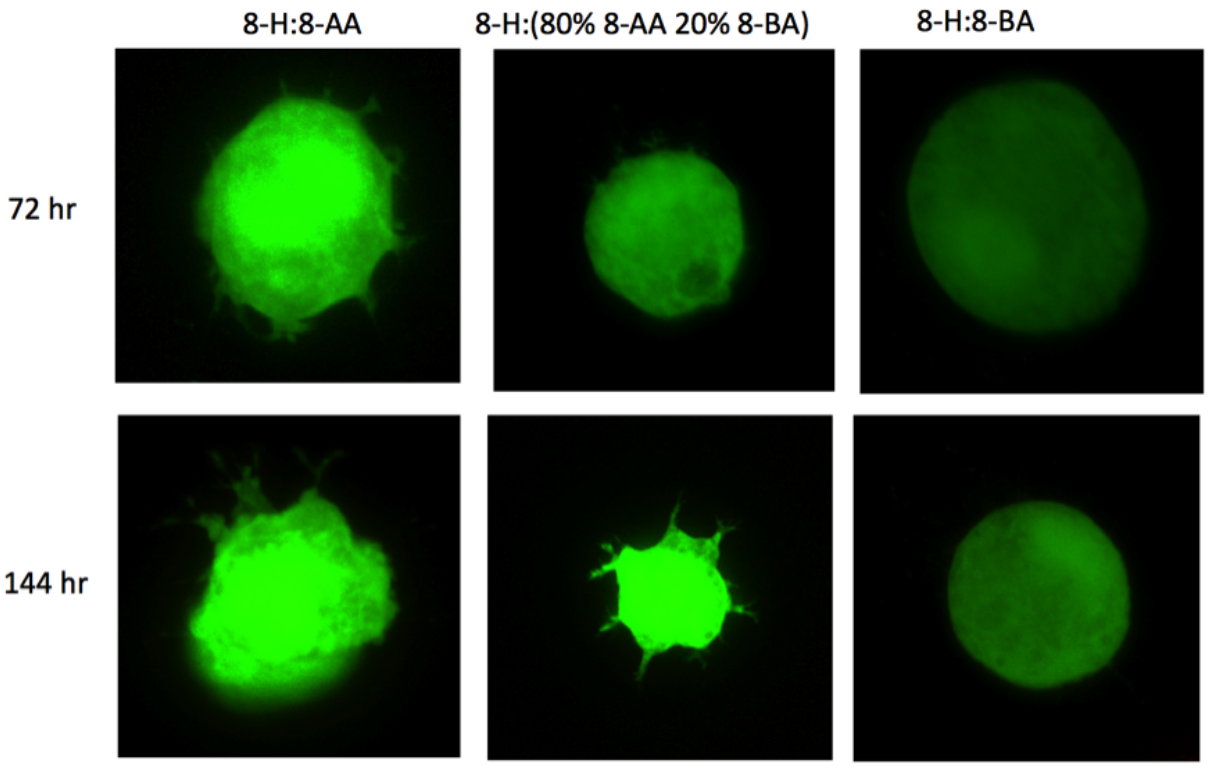

Figure 4.11: Cell morphology as evidenced by a calcein stain through time. By 144 hours, significant spreading did not occur in any of the gels, but nearly every cell in 8-H:8-AA and 8-H:(80% 8-AA 20% 8-BA) was extending processes. Cells in the 8-H:8-BA gels remained rounded.

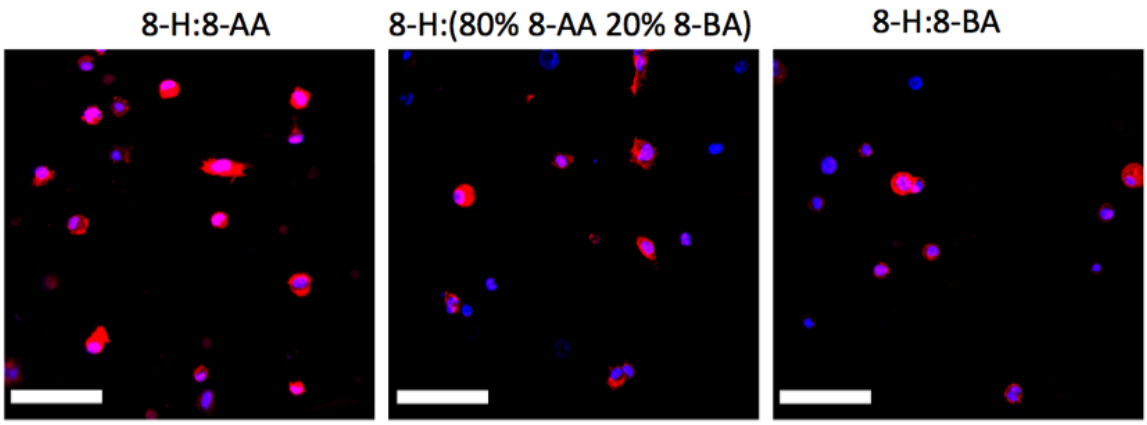

Figure 4.12: After 10 days in culture, gels were stained for f-actin (red) and the nucleus (blue) (scale bar 100 μm). Representative Z-stacks are shown. Cells in 8-H:8-AA and 8-H:(80% 8-AA 20% 8-BA) spread and extended processes over this period, while those in 8-H:8-BA did not.

bility (Figure 4.10). Cells maintain a rounded morphology when encapsulated in covalently crosslinked hydrogels, so we next sought to examine how cells would behave in hydrogels in which the crosslinks dynamically break and re-form.[81,96] Interestingly, we observed that after only 24 hours in culture, a minority of the cells encapsulated in the 8-H:8-AA gels extended small filopodia and lamellipodia, while those in the 8-H:(80% 8-AA 20% 8-BA) and 8-H:8-BA gels retained their circular morphology. By 72 hours, however, nearly all cells in the 8-H:8-AA gels began to extend processes, while those in the 8-H:8-BA gels remained rounded; the 8-H:(80% 8-AA 20% 8-BA) gels contained cells of both phenotypes (Figure 4.11). At later time points, the filopodia and lamellipodia became more pronounced, and essentially all cells in both the 8-H:8-AA and 8-H:(80% 8-AA 20% 8-BA) gels had begun to spread. By 10 days in culture, the cells in the 8-H:8-AA gels demonstrated the spread myoblast phenotype (Figures 4.10 and 4.12), and some cells with close neighbors began to fuse into multinucleated structures demonstrating a myotube-like morphology with continuous actin filaments spanning the entire mass. This myoblast fusion suggests the beginning stages of differniation; this process did not happen to cells in 8-H:8-BA. C2C12s in 8-H:(80% 8-AA 20% 8-BA) displayed significant process extension, but while their mean projected cell area was not significantly different from the cells in 8-H:8-AA, they retained a more rounded morphology. Furthermore, we observed fewer fused multinuclear structures. Cells in the less-dynamic 8-H:8-BA gels remained rounded, even after 10 days with less than 30% of cells extending processes into the material (Figure 4.10). These results were quantified by measuring the mean projected cell area and counting the number of cells extending processes into the material. We found that cells in 8-H:8-AA and 8-H:(80% 8-AA 20% 8-BA) both displayed significantly higher mean cell projected areas and a higher fraction of cells extending processes than cells in 8-H:8-BA (Figure 4.10). Based on these three-dimensional observations, we propose that the dynamic nature of the aliphatic hydrazone linked hydrogel allows the gel to rearrange on a timescale that is compatible with filopodia and lamellipodia extension, and thus, the material can accommodate cytoskeletal outgrowth. In contrast, the more slowly relaxing

gels, such as 8-H:8-BA, produce a much more static matrix that constrains the cells to a circular morphology throughout the course of the experiment. Rheological experiments on cell-laden gels show that the incorporation of cells lowers the equilibrium modulus but does not significantly change the stress relaxation properties (Figure 4.13). SEM imaging reveals that the hydrogels are amorphous solids lacking pores or ordered structure (Figure 4.14). Given the constancy of the stress relaxing properties and the lack of pores or order, it is likely that encapsulated cells apply stress, which leads to a dynamic rearrangement of the hydrazone bonds and allows them to spread out in the material.

4.4 Experimental

General Procedures and Materials: Unless otherwise noted, all chemicals and solvents were of analytical grade and used as received from commercial sources. 4-arm 20 kDa PEG-amine and 8-arm 10 kDa PEG-amine was obtained from JenKem. Water (dd-H2O) used in biological procedures or as a reaction solvent was deionized using Milli-Q Advantage A-10 water purification system (MilliPore, USA). UV-vis spectra were acquired on a DU 730 spectrophotometer (Beckman Coulter, USA) with quartz cuvettes. Peptide synthesis was carried out on a Tribute Peptide Synthesizer (Protein Technologies, USA). Rheology measurements were made with a DH-R3 rheometer (TA Instruments, USA). Confocal images were taken on a Zeiss LSM 710 (Carl Zeiss Microscopy, Germany).

Macromer Synthesis: 8-H and 4-H were synthesized by dissolving tri-Boc-hydrazinoacetic acid (1.372 g, 3.52 mmol, 2.1 equiv. per amine) in anhydrous DMF (10 mL) and was activated with HATU (1.216 g, 3.20 mmol, 2.0 equiv.) and N-methylmorpholine (0.792 mL, 7.2 mmol, 4.5 equiv.). The reaction was stirred for 5 minutes, and then the 4-arm 20 kDa (8.000 g, 0.4 mmol) or 8-arm 10 kDa PEG-amine (2.000 g, 0.2 mmol) was added, and the reaction was allowed to proceed overnight at room temperature. The product was precipitated in ice-cold diethyl ether, dried, treated with a solution of 50:50 DCM:TFA for 4 hours to remove the Boc group. The resulting compound was precipitated in ether, dissolved in DI

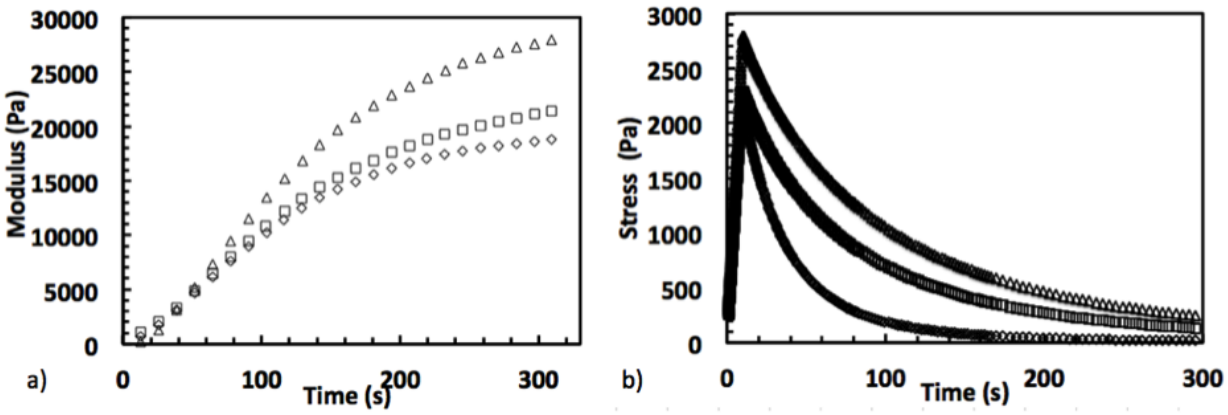

Figure 4.13: a) Sample time sweeps monitoring the polymerization of 8-H:8-AA laden with 10M cells/mL (diamonds), 1M cells/mL (squares), and cell free (triangles). The presence of cells affects the final modulus achieved by 8-H:8-AA but not the kinetics of gelation. The equilibrium unswollen moduli of these gels are 22 kPa, 26 kPa, and 36 kPa as determined by Equation 4.2 in the main text. b) Stress relaxation behavior at 10% strain of 8-H:8-AA laden with 10M cells/mL (diamonds), 1M cells/mL (squares), and cell free (triangles). Behavior is qualitatively similar with time constants of 25 s, 90 s, and 76 s. The lower equilibrium modulus and dramatically faster stress relaxation behavior of the 10M cells/mL gel indicates that the high cell density is disrupting a structurally significant number of crosslinks. These gels all polymerized in the presence of serum containing media, which leads to slightly different material properties than those polymerized in PBS.

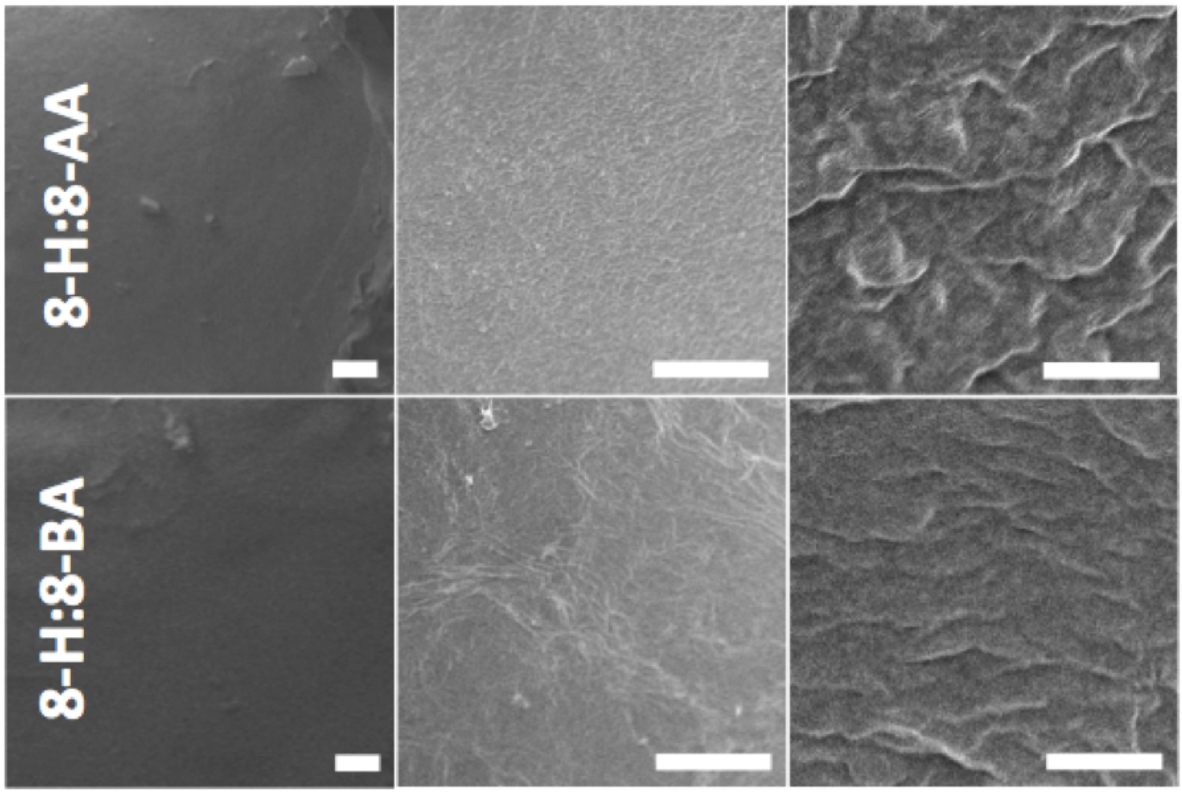

Figure 4.14: SEM images of the surface of 8-H:8-AA (top row) and 8-H:8-BA (bottom row) at three orders of magnitude magnification (scale bar 100 μm, 10 μm, and 1 μm; left to right). The gels are smooth and non-porous but some rippling is introduced in the drying process.

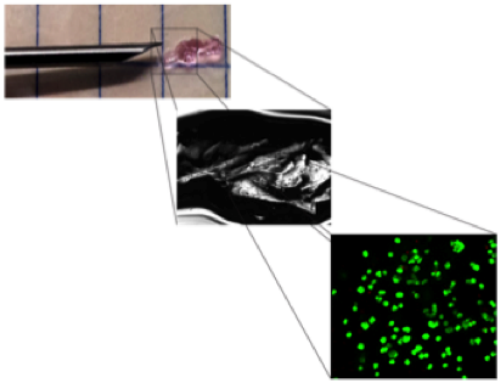

Figure 4.15: C2C12 cells were cultured for 24 hours in 8-H:8-AA, loaded into a syringe, and slowly passed through an 18-gauge needle using a syringe pump set to dispense 100 μL/min. Small muscle fibers were extruded, cultured another 24 hours, and stained for viability. Cell viability remained excellent through the process.

water, dialyzed (2,000 MWCO) against DI water for 24 hours, and lyophilized, after which it was used for experimentation.

8-H and 4-H ^{1}H NMR (D_2O, 400 MHz): δ= 3.59 (s, PEG).

8-AA and 4-AA were synthesized using a Swern oxidation.[169] Oxalyl chloride (1.5 mL, 17.6 mmol, 11 equiv. per hydroxyl) was dissolved in anhydrous DCM (20 mL) in a flame-dried flask purged with argon, and the reaction flask was cooled in an acetone/dry ice bath. DMSO (1.3 mL, 18.5 mmol, 11.5 equiv.) diluted 1:5 in andydrous DCM was added dropwise over the course of 5 minutes. The reaction was allowed to proceed for 10 minutes to ensure formation of the alkoxysulfonium ion intermediate. 8-arm 10 kDa PEG-OH (2 g, 0.2 mmol) or 4-arm 10 kDa PEG-OH (4 g, 0.4 mmol) was dissolved in anhydrous DCM (5 mL) and added dropwise over 10 minutes and allowed to react for 2 hours. Triethylamine (5.6 mL, 40 mmol, 25 equiv.) was added dropwise over 10 minutes and given 20 minutes to react. Finally, the reaction was allowed to warm to room temperature, and the product was precipitated in ether and dialyzed as previously described.

8-AA and 4-AA ^{1}H NMR (D_2O, 400 MHz): δ= 5.04 (t, J = 6 Hz, 1H), δ= 3.76 (t, J = 4 Hz, 2H), δ= 3.59 (s, PEG). Aldehyde exists in the diol form in D_2O.

8-AA and 4-AA ^{1}H NMR (DMSO-d_6, 400 MHz): δ= 9.61 (s, 1H), δ= 4.23 (s, 2H), δ= 3.54 (s, PEG). 8-AA and 4-AA gel in organic solvents therefore NMR peaks were significantly broadened.

8-BA and 4-BA were synthesized by dissolving 4-formyl benzoic acid (0.528 g, 3.52 mmol, 2.1 equiv. per amine) in anhydrous DMF (10 mL) and was activated with HATU (1.216 g, 3.20 mmol, 2.0 equiv.) and N-methylmorpholine (0.792 mL, 7.2 mmol, 4.5 equiv.). The reaction was stirred for 5 minutes, and then the 4-arm 10 kDa (4 g, 0.2 mmol) or 8-arm 10 kDa PEG-amine (2 g, 0.2 mmol) was added, and the reaction was allowed to proceed overnight at room temperature. The product was then precipitated in ether and dialyzed as previously described.

8-BA and 4-BA 1H NMR (D_2O, 400 MHz): δ= 10.01 (s, 1H), δ= 8.03 (d, J = 8 Hz,

2H), δ= 7.93 (d, J = 8 Hz, 2H), δ= 3.59 (s, PEG).

Polymer Functionalization Characterization: The functionalities of 8-BA and 4-BA were determined to be 98% and 96% by integrating the aldehyde and aryl peaks with respect to the PEG backbone peak after automatic phase correction. The functionality of 8-H and 4-H were determined using Flory-Stockmayer Theory, Equations 4.7 and 4.8 and forming gels highly off-stoichiometry between 4-BA and 8-H or 4-H and 4-H and 4-AA or 8-AA. Flory-Stockmayer Theory states that p_c must be greater than 1 for gelation to occur. Thus if 4-BA and 4-H are reacted 9:1 off stoichiometry and gelation still occurs, then 4-H is ideally 100% functionalized and if 4-BA and 8-H are reacted 21:1 off stoichiometry and gelation still occurs, we can conclude the same. Using this method 4-BA and 4-H formed a weak gel of G' = 9 Pa and 4-BA and 8-H a weak gel of $G' = 3$ Pa, indicating the functionalities of 4-BA and 8-H are close to 100%, which is not surprising given HATU couplings are known to proceed to 99% completion in peptide couplings.[170] When 4-H is allowed to react with 8-AA or 4-AA in the same stoichiometric ratios, a soft gel of 206 Pa or 138 Pa, respectively, forms. This is likely due to aldehyde homopolymerization, which is observed at room temperature,[171] in combination with hydrazone bond formation. 8-AA or 4-AA alone do not gel spontaneously. This result convolutes the estimation of 8-AA or 4-AA functionality, but Swern oxidations of primary alcohols have been shown to proceed to 97%-100% completion,[169] so we would expect similar functionalization of 8-AA and 4-AA.

Peptide Synthesis: Benzaldehyde-KGRGDS was synthesized using standard Fmoc chemistry and Rink Amide MBHA resin. Peptide cleavage solution was formed by dissolving 250 mg dithiothreitol (DTT) and 250 mg phenol in a solution of 95% trifluoroacetic acid (TFA), 2.5% triisopropylsilane (TIPS), and 2.5% deionized water. Synthesized peptides were cleaved in the solution for 2 hours. Cleaved peptides were precipitated in cold diethyl ether, recovered via centrifugation, desiccated overnight, and then purified by reverse-phase HPLC (Waters Delta Prep 4000) purification on a C18 column using a linear acetonitrile:water gradient. The collected fractions of purified peptides were identified by matrix-

assisted laser desorption/ionization-time-of-flight (MALDI-TOF) mass spectrometry. Expected mass: 750, found: 751.

Rheology: Samples were formed in situ by pipetting 30 μL monomer solution between the bottom Peltier plate and an 8 mm flat plate, and beginning the experiment as quickly as possible. In order to accurately recapitulate the experimental conditions for cell encapsulation, evolution experiments were done at 25°C, and all others were done at 37°C. Frequency and strain sweeps were performed to ensure measurements were made in the linear region. Evolution experiments were performed at 1% strain and 1 rad/s; frequency sweeps were performed at 1% strain; and stress relaxation experiments were performed at 100% strain for Figure 4.3 and approximately 10% strain for Figure 4.4, although strain had to be adjusted slightly to ensure similar initial stresses.

Kinetics: Rate and equilibrium constants were determined by UV-Vis. The aliphatic hydrazone bond absorbs at 240 nm (ε= 1,986 $M^{-1}cm^{-1}$), and the aryl hydrazone bond absorbs strongly at 340 nm (ε= 13,500 $M^{-1}cm^{-1}$). Stock solutions of the hydrazine and aldehyde (5 mM in DMSO) were diluted into PBS (200 μL), and the hydrazone absorption was monitored. Kinetic parameters were calculated using standard kinetic models.[10]

Cell Encapsulation: Gels were prepared with a total volume of 30 μL from stock solutions of 8-H, 8-AA, 8-BA, and benzaldehyde-KGRGDS, the pH of which had been adjusted to 7.4. Peptide, cells, and 8-H were gently mixed prior to the addition of the 8-AA after which the solution was triturated 10 times and pipeted into a mold. After 3 minutes, the 8-H:8-AA gels were placed in pre-warmed media while the 8-H:8-BA were given 30 minutes.

Staining: For Live/Dead imaging, gels were incubated in a 2 μM calcein AM and 4 μM ethidium homodimer-1 solution for 30 minutes on a shaker in a cell culture incubator and then imaged. For f-actin and nuclear imaging, gels were placed in a 200 mM solution of sodium cyanoborohydride in PBS for 1 hour, a 4% paraformaldehyde solution for 1 hour, and the sodium cyanoborohydride solution again for 1 hour. Gels were then placed in a solution containing 0.1 μg/mL DAPI and 0.3 μg/mL TRITC-phalloidin solution for 3 hours

and imaged.

Confocal Imaging: Gels were placed between a glass slide and a coverslip separated by a rubber gasket and were imaged using a 10x, 20x or 40x water immersion objective. A 488nm laser was used to excite eGFP, calcein AM, and ethidium homodimer. For Live/Dead imaging a Z-stack of 100 images was taken through the first 600 μm of the gel in three different fields of view with 7.75 μm between images. For cytoskeletal imaging, a 405 nm laser was used to excite DAPI, and a 543 nm laser was used to excite TRITC.

Modeling: Stress relaxation data were fit the Maxwell equation for viscoelastic fluids using the *FindFit* function in *Mathematica*. Mixed gels were modeled by adding the aliphatic aldehyde and benzaldehyde decay terms and forcing the pre-exponential values to the aliphatic or benzyl mole fraction.

SEM: Gels were swollen overnight in DI water and dehydrated in ethanol solutions of 20%, 40%, 60%, 80%, 90%, and 100% for 10 minutes each, with the 100% solution being repeated three times. The gels were then dried in hexamethyldisilazane (HDMS), placed under vacuum for 30 minutes, mounted on stubs, and sputter coated with gold. Samples were examined with a JEOL JSM 7401F.[120]

Image Processing: Images were imported into *ImageJ* and process extension was manually counted. Mean cell area was determined by thresholding f-actin channel, computing total cell area using the *Analyze Particles* function, and dividing the total area by number of nuclei.

Statistics: Modulus of hydrogels was determined from three separate gels. Cell viability was determined by taking three random Z-stacks through three gels per condition per time point. Cell process extension and mean cell area were determined by three image stacks through a single gel. All error bars represent the standard deviation. The significance of the difference between conditions in cell area and process extension was determined using a students t-test between 8-H:8-AA or 8-H:(80% 8-AA, 20% 8-BA and 8-H:8-BA with $p<0.5$ in the conditions marked with two stars.

4.5 Conclusions

Here, we examined the simulation of muscle and encapsulation of myoblasts, but this cytocompatible covalently adaptable hydrogel could be applied to other cellular systems where viscoelasticity or careful control of the scaffold biophysical properties is desirable. For instance, it is known that reduced crosslinking in the pericellular environment induces increased proliferation in myofibroblasts,[128] and this covalently adaptable hydrogel could be used to quantify the degree of stress necessary to inhibit proliferation and the kinetics of the associated signaling pathways. Scaffold mechanics and cell shape have both been implicated in progenitor cell differentiation,[131,172,173] but decoupling these two phenomena is challenging in cell degradable gels. Covalently adaptable gels allow the study of progenitor cells in a defined biophysical environment while simultaneously allowing cells to adopt their preferred geometries. Finally traditional covalent gels force secreted ECM molecules into a confined geometry,[74] preluding the assembly of micron-size features like collagen fibers. Covalently adaptable networks may prove a useful system to respond and accommodate the assembly of secreted ECM and subsequent collagen fiber formation.

We have developed a cytocompatible covalent adaptable hydrogel capable of mimicking the modulus and stress relaxation properties of many complex biological tissues. Here, we have described a material that simulates some of the properties of native mouse muscle and demonstrated its utility as a scaffold to culture mouse myoblasts. The modular nature of hydrogel construction and the large number of easily tuned variables provide access to gels with a wide range of modulus and stress relaxation characteristics; the same approach could potentially be applied to nearly any tissue in the body. C2C12 cell encapsulation studies demonstrate that these covalently adaptable hydrogels allow for the development of physiologically relevant morphologies, whereas static, non-adaptable gels prevent cytoskeletal rearrangement and extension. Taken together, these studies show that hydrazone linked hydrogels offer unique advantages in terms of dynamic tunability and should serve as a

valuable complement to existing hydrogel technologies.

Chapter 5

Measuring Forces Using Bis-Aliphatic Hydrazone Crosslinked Stress-Relaxing Hydrogels

5.1 Abstract

Studies focused on understanding the role of matrix biophysical signals on cells, especially those when cells are encapsulated in hydrogels that are locally remodeled, are often complicated by appropriate methods to measure differences between the bulk and local material properties. From this perspective, stress-relaxing materials that allow long-term culture of embedded cells provide an opportunity to elucidate aspects of this biophysical signaling. In particular, rheological characterization of the stress relaxation properties allows one to link this bulk material measurement to local aspects of cellular functions by quantifying the corresponding cellular forces that must be applied locally. Using embryonic stem cell-derived motor neurons encapsulated in a well-characterized covalently adaptable bis-aliphatic hydrazone crosslinked PEG hydrogel,[82,174] axon outgrowth was followed over time and biophysical equations of viscoelasticity were used to calculate the axonal forces and energies involved.

5.2 Introduction

For the past decade, there has been a growing literature devoted to elucidating the effects of matrix modulus on the function of both plated and encapsulated cells.[68,131,134,165,175–177] In two-dimensions, stem cells are routinely seeded on biomaterial surfaces, typically hydrogels of controlled moduli, to investigate the role of mechano-signaling on cell fate. The

Discher group pioneered some of the early efforts in the field and demonstrated that human mesenchymal stem cells (hMSCs) preferentially commit to a lineage based strongly on the mechanics of the surface on which they are seeded.[131] While seemingly intuitive that stem cells plated on hydrogels of modulus comparable to adipose tissue would drive adipogenesis, with corresponding trends observed for osteogenesis, myogenesis, and neurogenesis, this finding provided quantitative evidence that altered many approaches to stem cell culture. Typically, stem cells are plated on polystyrene or glass dishes, both of which have a modulus exceeds that of soft tissues by *ca.* six orders of magnitude. Discher's findings indicated that MSCs cultured on such materials were driven towards osteogenesis. These experiments were repeated with embryonic stem cells, yielding similar results.[133] Thus, great interest arose in better understanding this mechanotransduction, especially in the context of soluble factors often added to media, on cell function.

More recently, many of these hypotheses have been extended to three dimensional culture platforms.8,10-14[81,90,177–180] However, critical differences can arise between two- and three-dimensional culture systems and many biological assays become more difficult in three-dimensions. The in vivo morphology of adhesion dependent cells is typically spread and often connected to neighbors through cadherins, tight junctions, and other interactions. Furthermore, the extracellular matrix found in vivo is both porous and degradable, allowing cells to locally remodel the matrix or maneuver through the matrix to render a native in vivo morphology. Synthetic hydrogels used for many of the original mechanotransduction studies allow neither process, unless some mechanism of degradation is specifically engineered into the crosslinkers. As discussed in the introduction of this thesis, hydrolysis,[73] light,[72] and enzymes[113] have all been employed as triggers for hydrogel degradation. However, enzymatically degradable hydrogels have become increasingly popular, as these can be locally degraded by cells without a priori knowledge of the desired degradation rate, as is required for hydrolysis. While the benefit of cellularly-degraded hydrogels is clear, the disadvantage is that the rate of local degradation is unknown and techniques to characterize the local

modulus in 3D are complex. Efforts include traction force microscopy, pioneered in the Chen group, which involves embedding fluorescent beads into the material and monitoring their displacement both in the presence and in the absence of cells. From the images collected and basic stress-strain calculations, it is possible to infer the amount of force encapsulated cells apply to the material.[181] However, a critical assumption in traction force microscopy is that the local material modulus matches that of the bulk. This is likely not true in the context of the locally degradable gels that have been employed. Additionally, microrheology, using the Brownian motion of probe particles to infer material properties, has also been employed to investigate the local mechanics of hydrogel networks,[182,183] however this technique is limited to very soft materials close to their gel point.

To address some of these complexities, we set out to design a biomaterial for cell culture whose bulk properties would be nearly identical to those found in the local cellular microenvironment. A reversibly crosslinked hydrogel that relaxes in response to stress applied by encapsulated cells or secreted ECM components should allow proper function without having to preprogram degradation rates, while maintaining constant modulus throughout the gel enabling accurate observations of the effect of matrix modulus on encapsulated cells. Such a material was introduced in the previous chapter. Briefly, by crosslinking PEG macromers with rapidly reversible bis-aliphatic hydrazone bonds, a stress-relaxing, viscoelastic, cytocompatible hydrogel allows the observation of cellular function in a highly controlled and characterized biophysical environment. Here, we seek to explore conditions that allow this material to be used to study the biophysical forces involved in axon extension.

5.3 Results & Discussion

Covalently adaptable networks were formed from PEG precursors yielding a hydrazone crosslinked hydrogel,[82] and synthesis and characterization of this material is described in detail in Chapter 4. Briefly, 8-arm 10 kDa PEG macromers were functionalized with either aliphatic aldehyde or aliphatic hydrazine end groups and dissolved in buffered stock

solutions. Upon preparing stoichiometrically balanced solutions, these formulations react in *ca.* 5 minutes to form a hydrogel with an equilibrium swollen shear elastic modulus of *ca.* 10 kPa. Due to the rapid reversibility of the bid-aliphatic hydrazone bond, these materials were able to relax applied stress on the order of minutes. An RGDS peptide coupled to the benzaldehyde moiety was used to confer adhesive functionality to the material for culturing primary ES derived motor neurons. This material was previously shown to be highly compatible for the long-term culture of C2C12 myoblasts;[82] however, initial attempts to encapsulate and culture primary motor neurons results in nearly uniform cell death at the material-embryoid body interface (Figure 5.1).

Perhaps not unexpectedly, primary ESMNs are clearly more sensitive than the C2C12 cell line, and require more stringent regulation of the gel precursors and gelation conditions. Previous studies with 10 mM non-gelling solutions of hydrazine and aldehyde terminated PEG macromers demonstrated that, while hydrazine is a strong nucleophile, and is very toxic as a small molecule, neither PEG-hydrazine nor PEG-hydrazone had a statistically significant impact on cell viability or ATP content in adherent cultures (data not shown). Conversely, treating plated cells with 10 mM solutions of PEG-aldehyde resulted in substantial cell death within hours. Aldehydes can react non-specifically and transiently with amines, alcohols, thiols, and many other functional groups found on the surfaces of the cell, so it is likely that PEG-aldehyde macromer can react non-specifically with biological molecules critical to cell survival. The likelihood of cell death is substantially increased if the PEG-aldehyde can be internalized by the cell where it is exposed to a reducing environment. When this occurs, the transient bonds are reduced to permanent bonds, as in the reduction of an imine to an amine (Figure 5.2).

The equilibrium constant between butyraldehyde and methyl hydrazine, which were chosen as small molecule analogs for the macromolecular system, was previously measured to be 8 x 10^4 M^{-1} s^{-1}. Assuming equimolar starting concentrations and second order kinetics, at the 80 mM functional groups found in a gel prior to swelling, this corresponds to 1 mM

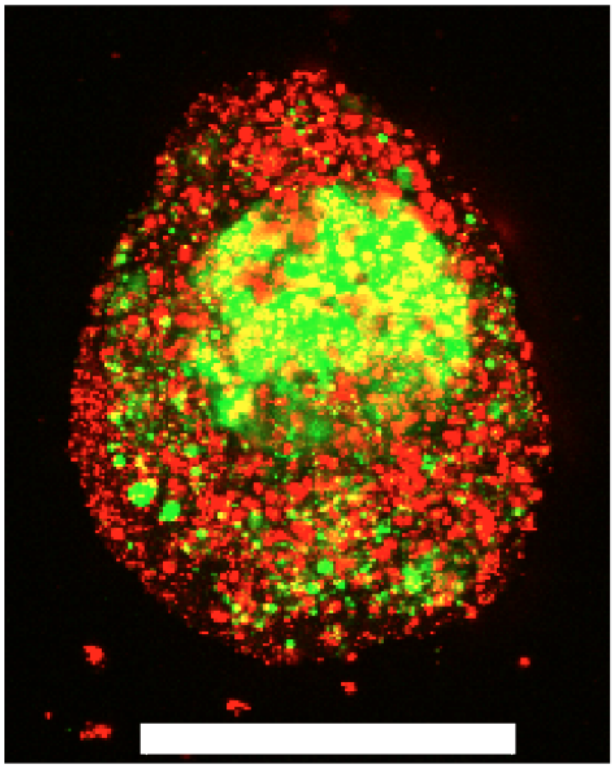

Figure 5.1: An ESMN embryoid body stained with Calcein (green), indicating live cells, and Ethidium Homodimer (red), indicating dead cells, after two days in culture. Note the core of live cells, which do not directly interact with the surrounding material and are surrounded by a shell of dead cells. The aldehyde functionality during gel formation is hypothesized to be cytotoxic via non-specific reactions on the cell surface. Scale bar is 200 μm.

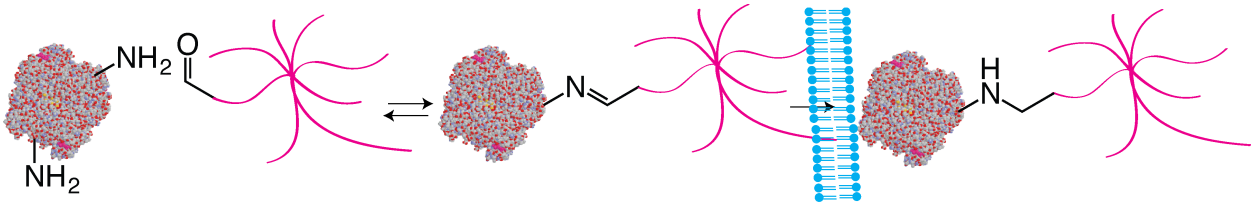

Figure 5.2: One possible mechanism, of PEG-aldehyde toxicity. PEG-aldehyde forms a reversible imine bond with a cell surface amine, which is reduced to the corresponding irreversible amine upon internalization. Both the bonding and steric hindrance introduced by the PEG chains could lead to loss of protein function or membrane permeabilization and thus cytotoxicity.

free aldehyde at any given time in the gel (Equations 5.1 and 5.2, where k_1 is the forward rate constant, k_{-1} is the reverse rate constant, and K_{eq} is the equilibrium constant). 1 mM is a high level of a persistent aldehyde in the gel formulation and likely to have an impact on delicate ESMNs.

$$k_1[Hydrazine][Aldehyde] = k_{-1}[Hydrazone] \tag{5.1}$$

$$K_{eq} = \frac{k_1}{k_{-1}} = \frac{80x10^{-3} - [Aldehyde]}{[Aldehyde]^2} \tag{5.2}$$

However, Le Chatelier's principle informs us that the equilibrium can be driven to towards more benign products (i.e., the hydrazone) by increasing the concentration of one of the reactants. Hydrogels polymerized with an excess of PEG-hydrazine ensure virtually no free aldehyde is available to interact with the cell. By reducing the concentration of PEG-aldehyde by 50%, while maintaining the same concentration of PEG-hydrazine, the predicted concentration of free aldehyde drops by two orders of magnitude to 10 μM. We hypothesized that this reduction would result in dramatically improved ESMN viability. Upon encapsulating ESMN embryoid bodies in this formulation, we observed dramatically improved cell viability and axon extension from many embryoid bodies (Figure 5.3).

After identifying a hydrazone gel formulation that promoteed ESMN viability and axon outgrowth, we next sought to exploit the well-defined mechanical properties to measure the force that axon must exert to extend from their nascent to final positions. Basic mechanics dictates that the energy (E) required to travel through a viscoelastic fluid is the path integral of the stress function ($\sigma(t)$) times the surface area (A) (Equation 5.3).

$$E = \int \sigma(t) * A * dl \tag{5.3}$$

Furthermore, the power (P) exerted during axon extension and the average force (F) over the same period are calculated using Equations 5.4 and 5.5, where l is the path that

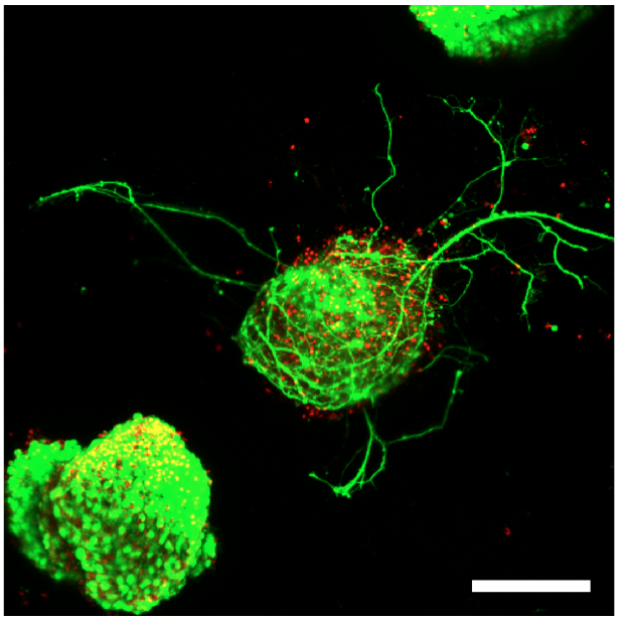

Figure 5.3: ESMN embryoid bodies stained with Calcein (green), indicating live cells, and Ethidium Homodimer (red), indicating dead cells, after two days in culture. The gel formulation was 80 mM PEG-hydrazine with 40 mM PEG-aldehyde, in contrast to the 80 mM of both used for the gels formed in Figure 5.1. High cell viability was observed and many embryoid bodies were observe to extend axons throughout the material. Such extension is possible only in gels with a stress relaxation-mediated mechanism. Scale bar is 200 μm.

was integrated over to calculate the energy (Equation 5.3).

$$P = \frac{E}{t} \tag{5.4}$$

$$F = \frac{E}{l} \tag{5.5}$$

Thus, if the stress function for the material were known and the position of the growth cone could be tracked over time, many fundamental biophysical properties of cells can be readily calculated from these first principles. Exploiting the extensive rheological characterization of the gel formulations (Chapter 4, Figures 4.3-4.9), the hydrazone gels behave as a nearly ideal Maxwellian viscoelastic fluid with an exponentially decaying stress function (Equation 5.6).

$$\sigma(t) = \sigma_0 e^{-t/\tau} \tag{5.6}$$

Here, τ is a time constant of relaxation and σ_0 is the initial stress. Substituting this function into Equation 5.3 renders a path integral over an expression with a time dependence (Equation 5.7).

$$E = A \int_{x_1}^{x_2} \sigma_0 e^{-t/\tau} dl \tag{5.7}$$

However, if the speed of axon extension is relatively constant throughout the experiment (i.e., constant between time steps), then time can be exchanged for position (Equation 5.8).

$$E = A \int_{x_1}^{x_2} \sigma_0 e^{-x/v\tau} dx \tag{5.8}$$

Here v is the mean velocity of the axon growth cone over the time interval. Integration of Equation 5.8 yields the energy required to travel from point x_1 to point x_2 through any viscoelastic fluid given a constant velocity over that period (Equation 5.9).

$$E = A\sigma_0 v\tau(e^{-x_2/v\tau} - e^{-x_2/v\tau}) \tag{5.9}$$

To apply this equation to the analysis of motor axons extending through viscoelastic hydrozone gels, we encapsulated ESMN embryoid bodies in the 2:1 off stoichiometry formulation while simultaneously monitoring axon extension for 48 hours, taking an image every 5 minutes (Figure 5.4). The position of the growth cone was noted at each frame, along with the position and time for 5 axons over 3 hydrogels.

These position data were then plotted with respect to time, generating Figure 5.5. All five axons tracked follow a remarkably similar early trajectory, pushing through the gel at 8.2 ± 1.5 μm per hour. Three then dramatically accelerate to 27 ± 7 μm per hour. This acceleration is likely due to the axons reaching the surface of the gel and switching from extension mechanically inhibited by the gel to simply extending along its surface.

Next, the energies of extension were calculated using Equation 5.9, and the results are plotted versus axon length in Figure 5.6. Axon length and energy appeared linearly correlated, as one might expect based on the results in Figure 5.5, which show that all axons travel approximately the same speed through the material. Using this data, an average force was also calculated from Equation 5.5, which was 800 ± 30 pN for the five axons analyzed. . These result from this analysis compare favorably with existing measures of cellular forces using traction and other methods. For example, fibroblasts seeded in on a surface of a bed of microneedles were shown to exert 1-20 nN of traction force.[184] Fibroblasts seeded on the surface of a hydrogel embedded with fluorescence beads were shown to exert 50-500 Pa of traction force, which corresponds to 500 pN to 5 nN assuming an area under stress of 100 μm^2.[181] Axons extending from PC12 cells, a neuronal cell line, were deflected mechanically and forces of adhesion were measured to be in the 1-5 nN range.[185] Chick sensory neurons were shown to advance with similar forces.[186,187] While all these experiments were performed with cells plated on a surface, rather than encapsulated in a hydrogel, the reported values

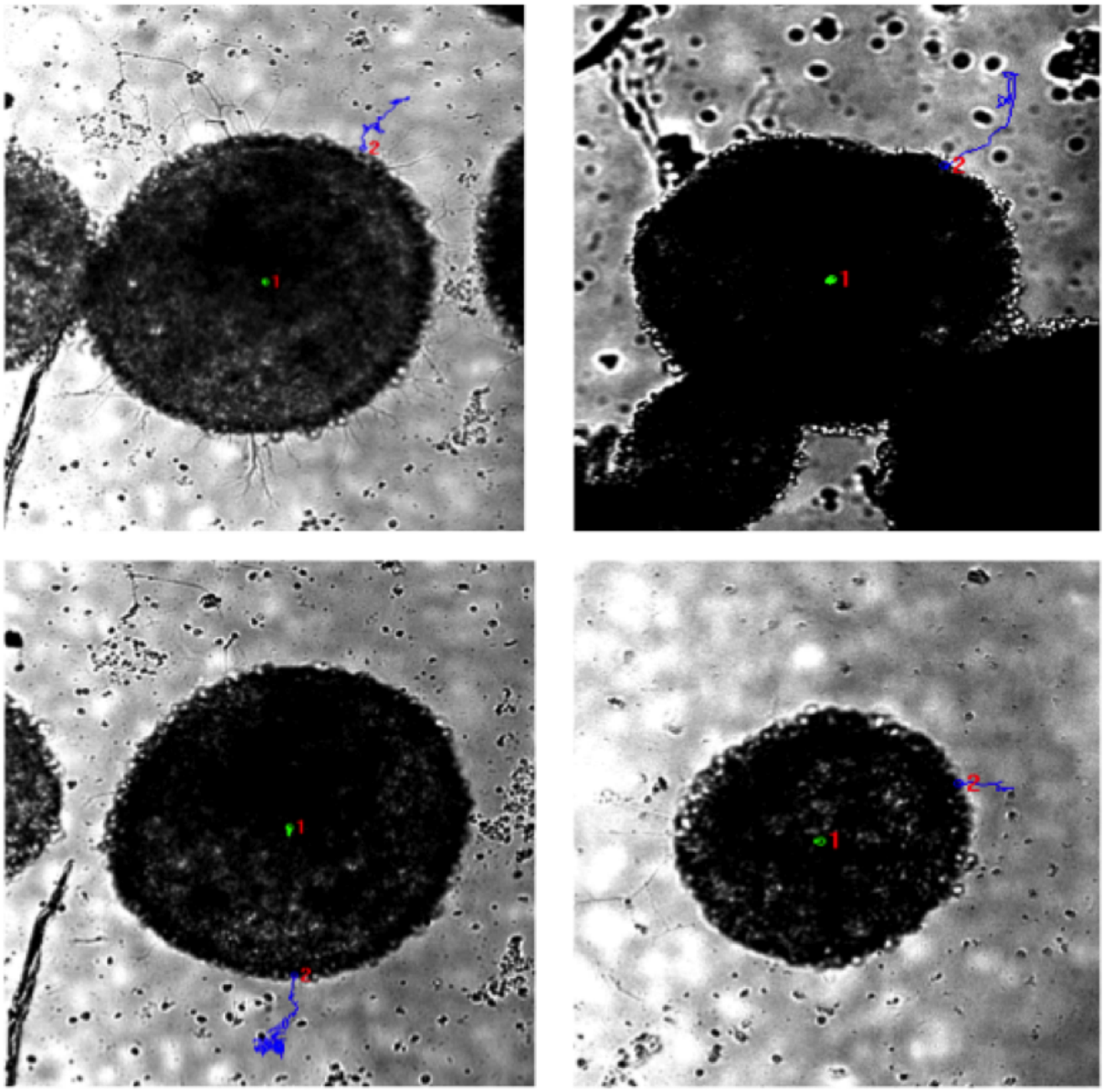

Figure 5.4: Example brightfield images of a ESMN embryoid bodies encapsulated in the hydrazone-crosslinked hydrogel. The blue lines are the paths of axons extending over 24 hours and the green line indicates the extent of sample drift. Scale bar is 100 μm.

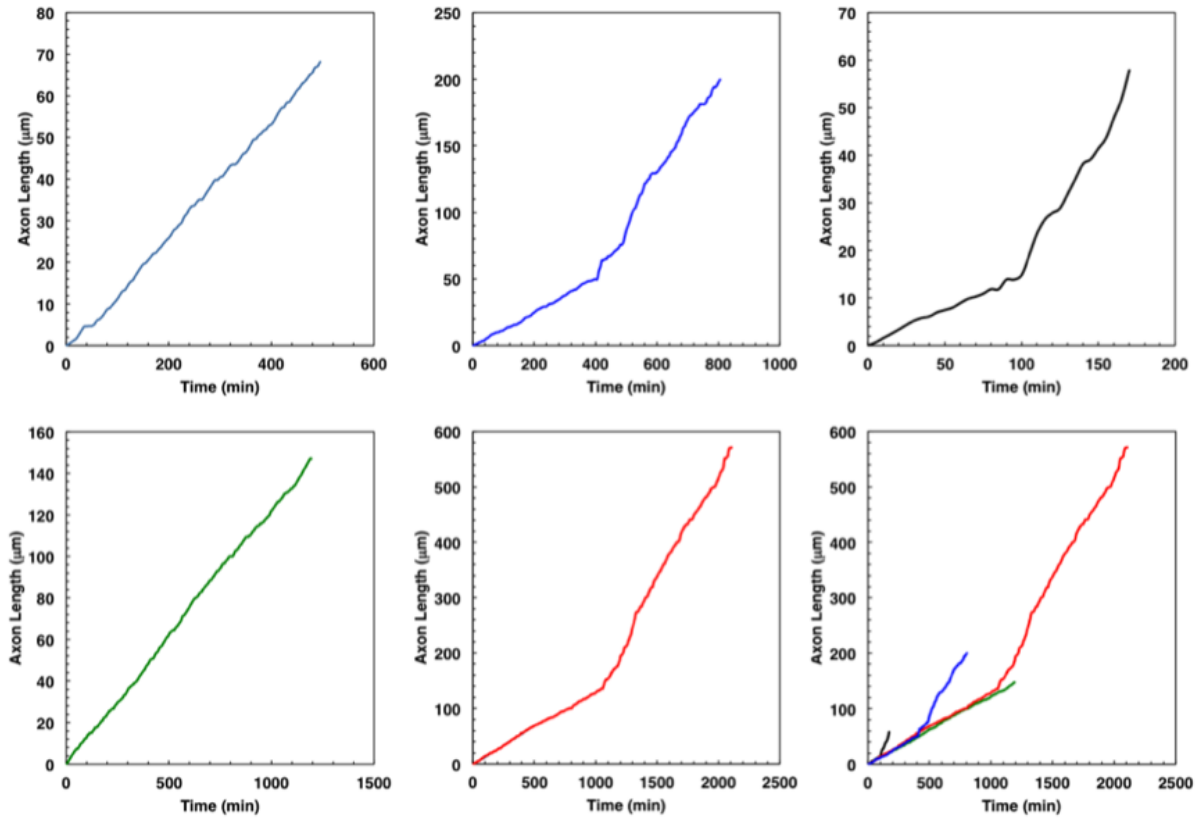

Figure 5.5: Axon displacement as a function of time for five axons extending from five separate embryoid bodies in three different gels. Initial rates of axon extension were 8.2 $\pm$ 1.5 μm per hour. The change in slope of the black, blue, and red traces were likely due to the axon reaching the surface of the gel.

for cellular forces are very similar to those reported here. This is likely the first time the force of an extending motor axon has been measured by any method and work is in progress to validate these results through other experiments.

5.4 Experimental

General Procedures and Methods: Unless otherwise noted, all chemicals and solvents were of analytical grade and used as received from commercial sources. 8-arm 10 kDa PEG-amine and 8-arm 10 kDa PEG-alcohol were obtained from JenKem. Water (dd-H2O) used in biological procedures or as a reaction solvent was deionized using a central system. Peptide synthesis was carried out on a Tribute Peptide Synthesizer (Protein Technologies, USA). Confocal images were taken on a Zeiss LSM 710 (Carl Zeiss Microscopy, Germany).

Macromer Synthesis: 10 kDa PEG-octa-hydrazine (8-H) was synthesized by dissolving tri-Boc-hydrazinoacetic acid (1.372 g, 3.52 mmol, 2.1 equiv. per amine) in anhydrous DMF (10 mL) and was activated with HATU (1.216 g, 3.20 mmol, 2.0 equiv.) and N-methylmorpholine (0.792 mL, 7.2 mmol, 4.5 equiv.). The reaction was stirred for 5 minutes, and then the 4-arm 20 kDa (8.000 g, 0.4 mmol) PEG was added, and the reaction was allowed to proceed overnight at room temperature. The product was precipitated in ice-cold diethyl ether, dried, treated with a solution of 50:50 DCM:TFA for 4 hours to remove the Boc group. The resulting compound was precipitated in ether, dissolved in DI water, dialyzed (2,000 MWCO) against DI water for 24 hours, and lyophilized, after which it was used for experimentation.

8-H ^{1}H NMR (D_2O, 400 MHz): $\delta = 3.59$ (s, PEG).

8-H ^{1}H NMR (DMSO-d_6,400MHz): $\delta = 8.1$ (t, J=4Hz, 1H), $\delta = 4.45$ (m, 2H), $\delta = 3.51$ (s, PEG), $\delta = 3.2$ (m, 1H), $\delta = 2.96$ (m, 2H).

10 kDa PEG-octa-aldehyde (8-AA) was synthesized using a Swern oxidation.18 Oxalyl chloride (1.5 mL, 17.6 mmol, 11 equiv. per hydroxyl) was dissolved in anhydrous DCM (20 mL) in a flame-dried flask purged with argon, and the reaction flask was cooled in an

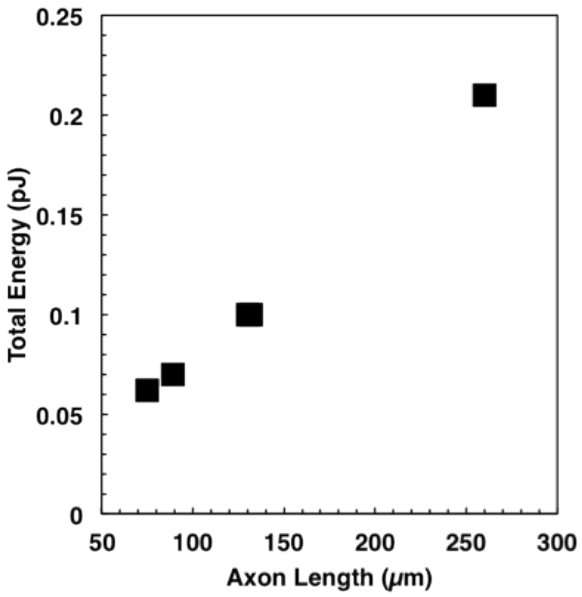

Figure 5.6: Total energy expended over the course of motor axon extension was plotted versus axon length for the five axons measured (two points nearly overlap). Because the axons all travel through the material at nearly the same velocity, we observe a linear relationship between axon length and energy, whose slope represents the force axons exert on the material.

acetone/dry ice bath. DMSO (1.3 mL, 18.5 mmol, 11.5 equiv.) diluted 1:5 in andydrous DCM was added dropwise over the course of 5 minutes. The reaction was allowed to proceed for 10 minutes to ensure formation of the alkoxysulfonium ion intermediate. 8-arm 10 kDa PEG-OH (2 g, 0.2 mmol) or 4-arm 10 kDa PEG-OH (4 g, 0.4 mmol) was dissolved in anhydrous DCM (5 mL) and added dropwise over 10 minutes and allowed to react for 2 hours. Triethylamine (5.6 mL, 40 mmol, 25 equiv.) was added dropwise over 10 minutes and given 20 minutes to react. Finally, the reaction was allowed to warm to room temperature, and the product was precipitated in ether and dialyzed as previously described.

8-AA ^{1}H NMR (D2O, 400 MHz): δ = 5.04 (t, J = 6 Hz, 1H), δ = 3.76 (t, J = 4 Hz, 2H), δ = 3.59 (s, PEG). Aldehyde exists in the diol form in D2O.

8-AA ^{1}H NMR (DMSO-d6, 400 MHz): δ = 9.61 (s, 1H), δ = 4.23 (s, 2H), δ = 3.54 (s, PEG). 8-AA gels in organic solvents; therefore, NMR peaks were significantly broadened.

Cell Encapsulation: Gels were prepared with a total volume of 30 μL from stock solutions of 8-H, 8-AA, and benzaldehyde-KGRGDS, the pH of which had been adjusted to 7.4. Peptide, cells, and 8-H were gently mixed prior to the addition of the 8-AA after which the solution was triturated 10 times and pipeted into a mold. After 3 minutes, the 8-H:8-AA gels were placed in pre-warmed media.

ES Cell Culture: ES cells were differentiated into spinal motor neurons as previously described.[2,51] Briefly, Hb9::GFP mouse embryonic stem cells were plated into ES cell medium (ES DMEM, ES FBS, glutamine, non-essential amino acids, nucleosides, 2-mercaptoethanol, LIF (Life Technologies)) at approximately 5 x 10^5 cells per gelatinized T25 flask. After 24 hours the media was replaced, and on day 2 of culture, ES cells were trypsinized and placed in suspension culture in motor neuron media (Advanced-DMEM/F12, Neurobasal, and Knockout Serum Replacement (Life Technologies)) at 5 x 10^5 cells per untreated 10 cm tissue culture dish. In suspension culture, the cells aggregated into embryoid bodies (EBs). Two days after initial seeding the EBs were split 1:4 and induced into motor neurons with 1 μM retinoic acid (RA) (Sigma) and smoothened agonist (SAG) (Millipore). After 3 days

of exposure to RA and SAG, the EBs displayed strong expression of Hb9::GFP transgene.

Staining: For Live/Dead imaging, gels were incubated in a 2 μM calcein AM and 4 μM ethidium homodimer-1 solution for 30 minutes on a shaker in a cell culture incubator and then imaged.

Confocal Imaging: Gels were placed between a glass slide and a coverslip separated by a rubber gasket and were imaged using a 10x, 20x or 40x water immersion objective. A 488nm laser was used to excite eGFP, calcein AM, and ethidium homodimer.

Real-time Imaging: Cell motility in cell-laden hydrogels was characterized using a Nikon TE 2000-E microscope with a Nikon environmental chamber and an external heater (In vivo Scientific) and CO2 regulator (In vivo Scientific). Hydrogels were polymerized and swollen as described previously, then placed in a 24-well culture insert plate (BD Falcon, Fisher) and held in place by a transwell insert (Becton Dickinson) with the bottom removed by a 5 mm biopsy punch. Fresh experimental medium was placed in the well at the beginning of each experiment. Real-time tracking was performed using Metamorph software for automated stage control, image collecting and positional cell tracking. After 2 hours in culture, cell center tracking was commenced and followed for 24 h.

5.5 Conclusions

Here we have shown that the combination of well-defined viscoelastic materials, fundamental physics, and real-time microscopy allows for the measurement of basic biophysical processes that are extremely difficult to measure by other means. The encapsulation of ESMN embryoid bodies in well-characterized bis-aliphatic hydrazone crosslinked hydrogels has enabled the determination, for the first time, of the forces involved in motor axon extension. However, in principle this technique could be extended to study any dynamic cellular process.

Chapter 6

Bis-Aliphatic Hydrazone-Linked Hydrogels Form Most Rapidly at Physiological pH: Identifying the Origin of Hydrogel Properties with Small Molecule Kinetic Studies

6.1 Abstract

Rheological and small molecule kinetic studies were performed to study the formation and hydrolysis of the bis-aliphatic hydrazone bond. The rate of gelation was found to correspond closely with the rate of bond formation and the rate of gel relaxation with the rate of hydrolysis, indicating that small molecule kinetic studies can play an important role in material design. Furthermore, unlike aryl or acyl hydrazone bonds, the bis-aliphatic hydrazone bond forms rapidly under physiological conditions without requiring aniline catalysis, yet maintains a pH-dependent rate of hydrolysis. These results suggest the bis-aliphatic hydrazone bond should find use alongside existing bioorthogonal click chemistries for bioconjugation, biomaterial synthesis, and controlled release applications.

6.2 Introduction

Materials that behave predictably in response to applied stimuli have been employed in a myriad of advanced applications. For instance, functional materials that release payloads;[188–195] change geometries;[196,197] and alter their optical and mechanical properties in response to light,[72,134,145,177,198] heat,[140,199,200] pH,[142,197,199] electromagnetic fields,[144] and other stimuli[201] have been engineered for diverse applications rang-ing from differentiating

stem cells[175,176] to simulating fracture healing[140] to directing cell migration.[8] Though various design strategies have been employed, organic polymer networks represent an especially utile class of stimuli-responsive materials because their properties can be easily and predictably modeled through established kinetic and polymer physics equations.[119,161,202,203] Furthermore, the defined functionalities of step growth polymer networks provide systems in which theoretical and experimental relationships can be more readily established between macroscopic material properties and crosslinking reaction kinetics.[204–206]

In previous work, we developed a cytocompatible covalently adaptable network formed through dynamically covalent hydrazone linkages, and we used the resulting material to explore the effects of a defined, viscoelastic microenvironment on cell behavior.[82] In the course of these studies, we observed the surprisingly fast gelation of a bis-aliphatic hydrazone crosslinked hydrogel and confirmed these results through a model kinetic study between an aliphatic hydrazine, monomethylhydrazine, and an aliphatic aldehyde, butyraldehyde. While hydrazone reactions have found wide-spread application in the fields of bioconjugation and materials science owing to their stimuli-responsive nature and their rapid formation under physiological conditions, when catalyzed by aniline or one of its derivatives,[10,151,154,207–209] most studies have focused on the reaction of aryl aldehydes with either aryl or acyl hydrazine partners.[10,150–152,207–210] Synthetically, these functionalities are easier to install in biological systems, and, in the case of bis-aryl hydrazones, result in covalent linkages that are resistant to hydrolysis with corresponding equilibrium constants on the order of 10^6 M^{-1}.[150] However, as we and others have reported, the rate of formation and hydrolysis of aryl aldehyde derived hydrazones differ significantly from those of aliphatic aldehyde derived hydrazones, with the aliphatic hydrazone forming at a rate nearly 500-fold faster than a representative aryl hydrazone at neutral pH.[82,209,211] We reasoned that the kinetics of this reaction were heavily influencing the bis-aliphatic hydrazone hydrogel properties and sought to investigate how altering the kinetic and thermodynamic parameters of this chemical bond through changes in pH and temperature would influence the mechanical properties of a bis-aliphatic hydrazone

crosslinked hydrogel.

Here, we present the effects of pH and temperature on the rheological properties of a bis-aliphatic hydrazone crosslinked hydrogel. We observed unexpectedly rapid hydrogel evolution at physiological pH and temperature and, in an effort to understand the origin of these characteristics, further explored this system by analyzing complementary small molecule kinetic studies. By reducing the complexity of the system to the reaction of model aliphatic aldehyde and hydrazine components, we were able to gain molecular insights into the origin of the bulk hydrogel material properties. The forward and back rate constants of the small-molecule bis-aliphatic hydrazone reaction not only accurately describe the hydrogel evolution and stress relaxation properties, but also suggest that the bis-aliphatic hydrazone bond should prove useful in a variety of research areas in which rapid and specific chemical ligation is desired, as the reaction exhibits a second-order rate constant that is competitive with specialized bioconjugation reactions.

6.3 Results & Discussion

Eight-arm 10 kDa and four-arm 20 kDa PEG macromers were functionalized with aliphatic aldehyde and hydrazine end-groups, respectively, using previously reported methods (Scheme 6.1).[82] Briefly, 8-arm PEG-OH was oxidized to its corresponding aliphatic aldehyde (8-AA) with a Swern oxidation procedure; precipitation from an ether solution provided the final material. Four-arm PEG-NH2 was reacted with HATU-activated tri-boc-hydrazinoacetic acid to give the amide-linked aliphatic hydrazine (4-H). Treatment with DCM:TFA removed the Boc protecting groups and subsequent precipitation from diethyl ether provided the final product.

To investigate modulus evolution, bis-aliphatic hydrazone cross-linked hydrogels were formed *in situ* on the rheometer and shear viscous and elastic moduli were monitored as a function of time (Figure 6.7. Because hydrazone formation is canonically acid-catalyzed, we expected that the gels would form most rapidly at acidic pH and evolve more slowly

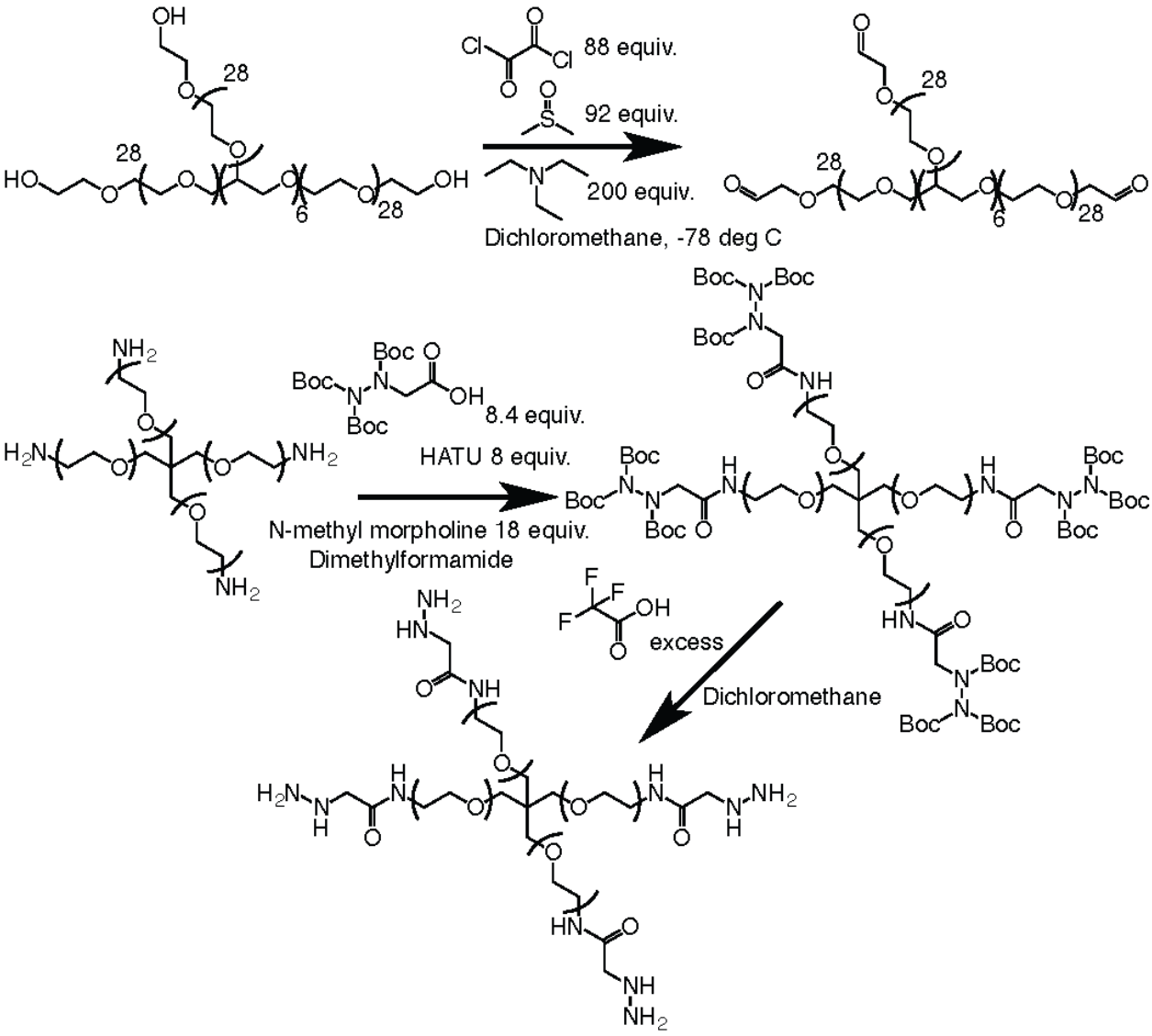

Figure 6.1: Synthetic pathway to 8-arm 10 kDa aliphatic aldehyde (8-AA) and 4-arm 20 kDa aliphatic hydrazine (4-H).

as the pH increased. In contrast to our expectations, we observed relatively slow hydrogel formation at pH 4.2 and a maximal rate of gel evolution at physiological pH. Increasing the pH of the buffer above physiological pH led to a decrease in the rate of gel evolution (Figure 6.3).

Fitting the curves to Equation 6.6, an exponential model of step-growth hydrogel evolution, yielded a half-life of gel evolution with respect to pH (Figure 6.3). These half-lives show clearly that the hydrazone-linked hydrogel forms most rapidly at physiological pH; the rate of hydrogel formation drops off at more acidic and more basic pH values. While hydrogels formed at pH 4.2 require 50 s to reach half their equilibrium moduli, those at pH 7.3 require only 25 s, and those at pH 10.03 require 85 s (Figure 6.3).

In an effort to better understand the unique rheological characteristics of the bis-aliphatic hydrazone hydrogels, we simplified the system to a model reaction between an aliphatic aldehyde, butyraldehyde, and an aliphatic hydrazine, monomethylhydrazine (Scheme 6.4).

We measured the rates of hydrazone formation between butyralde-hyde and monomethyl-hydrazine in buffers identical to those used in the rheological characterization studies. Each kinetic trace was fitted independently to a second-order reversible kinetic model, derived by Dirksen et al.,[10] and this enabled the simultaneous de-termination of the forward (k_1) rate constant of hydrazone for-mation and the back rate constant (k_{-1}) of hydrazone hydrolysis at each pH condition (Figure 6.5).

As the pH of the solution increased from 5.3 to 6.3, we saw an increase in the rate of small molecule hydrazone formation, from 3.9 ± 0.5 M^{-1} s^{-1} at pH 5.3 to 6.5 ± 1.4 M^{-1} s^{-1} at pH 6.3. In excellent agreement with the hydrogel evolution studies, we saw maximal hydrazone formation at pH 7.3, with a corresponding forward rate constant of 15.5 ± 1.3 M^{-1} s^{-1}. Again, in agreement with the hydrogel evolution studies, the rate of hydrazone formation decreased as the pH was increased above physiological pH. Increasing the pH to 8.1 led to a decrease in rate relative to the rate at pH 7.3, but hydrazone formation still proceeded remarkably fast, with a second-order rate constant of 9.5 ± 0.7 M^{-1} s^{-1}. Even

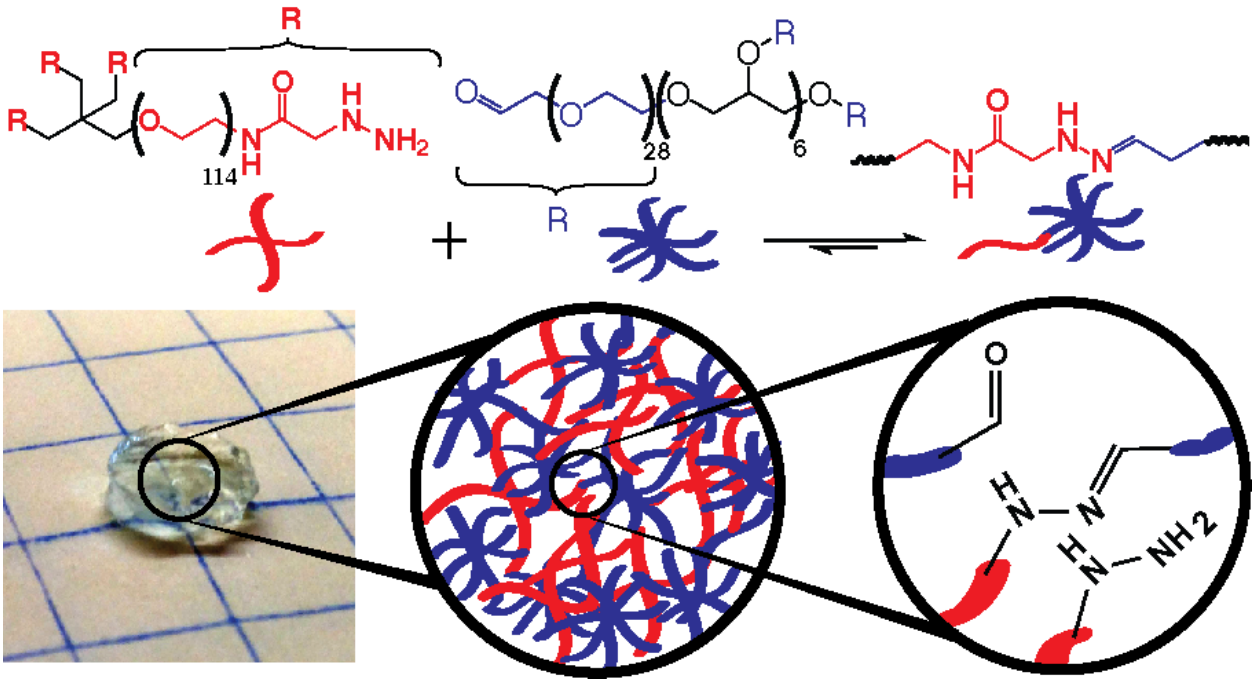

Figure 6.2: Gel formation occurs within minutes when 4-H and 8-AA are mixed due to the formation of the bis-aliphatic hydrazone bond crosslinking the polymer network.

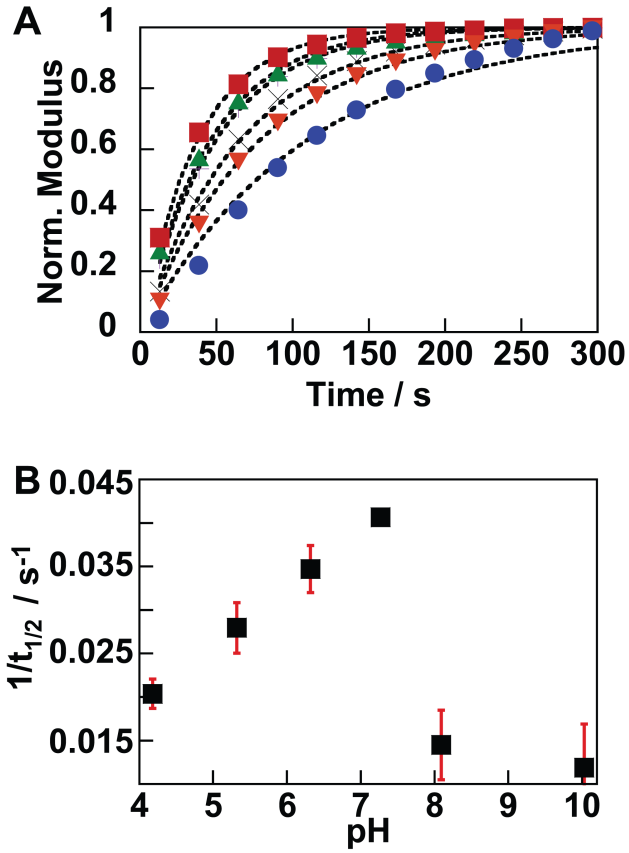

Figure 6.3: A) Bis-aliphatic hydrazone hydrogel evolution traces at pH 4.2 (X), 5.3 (+), 6.3 (triangle), 7.3 (square), 8.1 (del), and 10.0 (circle). Dashed lines represent a fit to an exponential model of step-growth hydrogel evolution. B) Half-life of gel evolution at different pH values. Data points represent the average of two independent measurements. Error bars represent standard deviation.

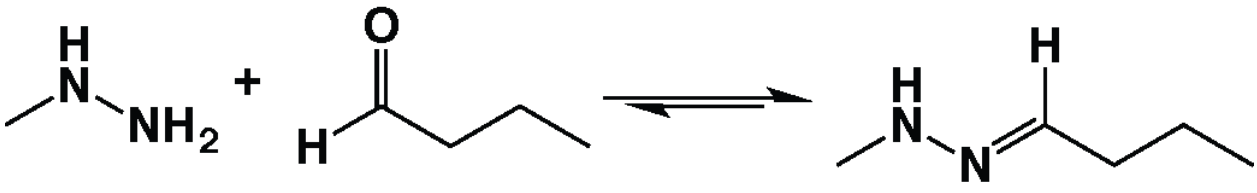

Figure 6.4: The small molecule reaction between monomethylhydrazine and butyraldehyde was used as a model system. Reaction progress was monitored by measuring the absorbance at 240 nm.

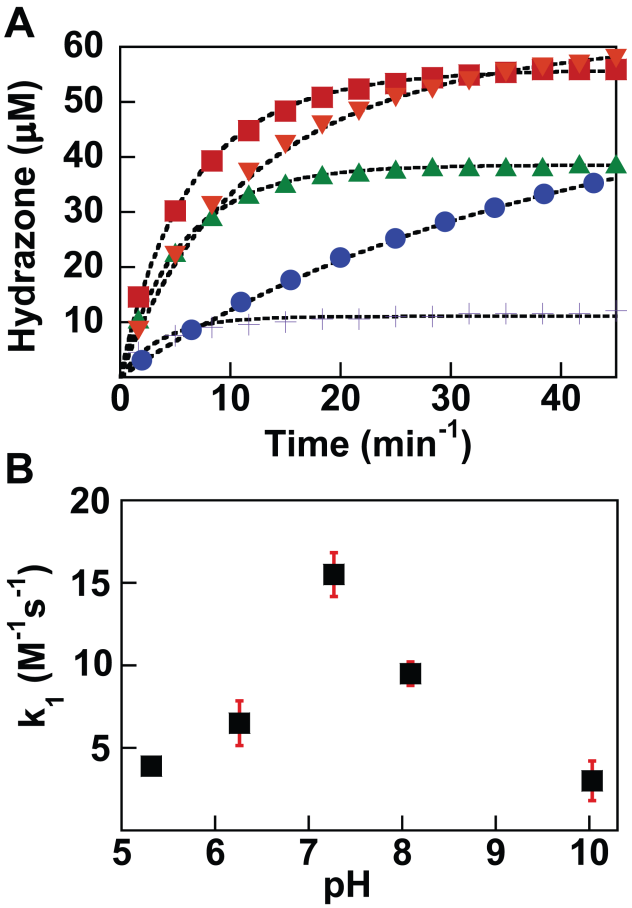

Figure 6.5: (A) Hydrazone formation between butyraldehyde (100 μM) and monomethylhydrazine (100 μM) at pH 5.3 (+), 6.3 (triangle), 7.3 (square), 8.1 (del), and 10.0 (circle). Dashed lines represent a fit to a second-order reversible reaction model.[10] (B) Second-order rate constant for hydrazone formation between butyraldehyde and monomethylhydrazine at different pH values. Each data point represents the average of three independent kinetic measurements. Error bars represent standard deviation.

in pH 10.0 phosphate buffer, we observed rapid hydrazone formation, with a corresponding forward rate constant of 3.0 ± 1.2 M^{-1} s^{-1} (Figure 6.5). The correlation between the small molecule studies and the hydrogel evolution traces strongly suggests that the rate of hydrogel evolution is dominated by the kinetics of the of bis-aliphatic hydrazone formation.

Because the bis-aliphatic hydrazone bond is reversible and the kinetics of the hydrolysis reaction vary significantly with pH, we next sought to investigate the pH-dependent stress relaxation properties of the material. We previously postulated that the stress relaxation properties would be heavily influenced by the rate of hydrazone bond hydrolysis.[82] Thus, by studying the stress relaxation properties over a range of pH values, we sought to directly interrogate the effect of hydrazone hydrolysis on the mechanical properties of the gel. We again formed hydrogels in situ and allowed them to equilibrate for 30 min in a buffered bath before straining to 10% at 25 °C. Stress was recorded as a function of time, and a clear pH-dependent behavior was observed, with the rate of stress relaxation increasing as a function of proton concentration (Figure 6.6).

The relaxation traces were fit to the Maxwell model (Figure 6.12), which assumes the material behaves as an elastic spring placed in series with a viscous dashpot; this represents the simplest model capable of predicting stress relaxation.[11] This fitting provided the time constants of relaxation, τ, which spanned more than an order of magnitude, from 300 s at pH 4.2 to 4000 s at pH 10.0 (Figure 6.5). The fits are shown in Figure 6.5, and the excellent agreement between the model and the data indicate that changes in pH do not introduce network non-idealities and that the relaxation properties can be predictably controlled through pH modulation.

The kinetic treatment of the hydrazone evolution studies between butyraldehyde and monomethylhydrazine also provides the rate of the back reaction, k_{-1}, which corresponds to the hydrolysis of the hydrazone bond. Plotting the rate of the back reaction with respect to pH provided good agreement with the rheological data: more acidic buffers greatly enhances the rate of hydrolysis, an observation in line with previous studies of hydrazone hydrolytic

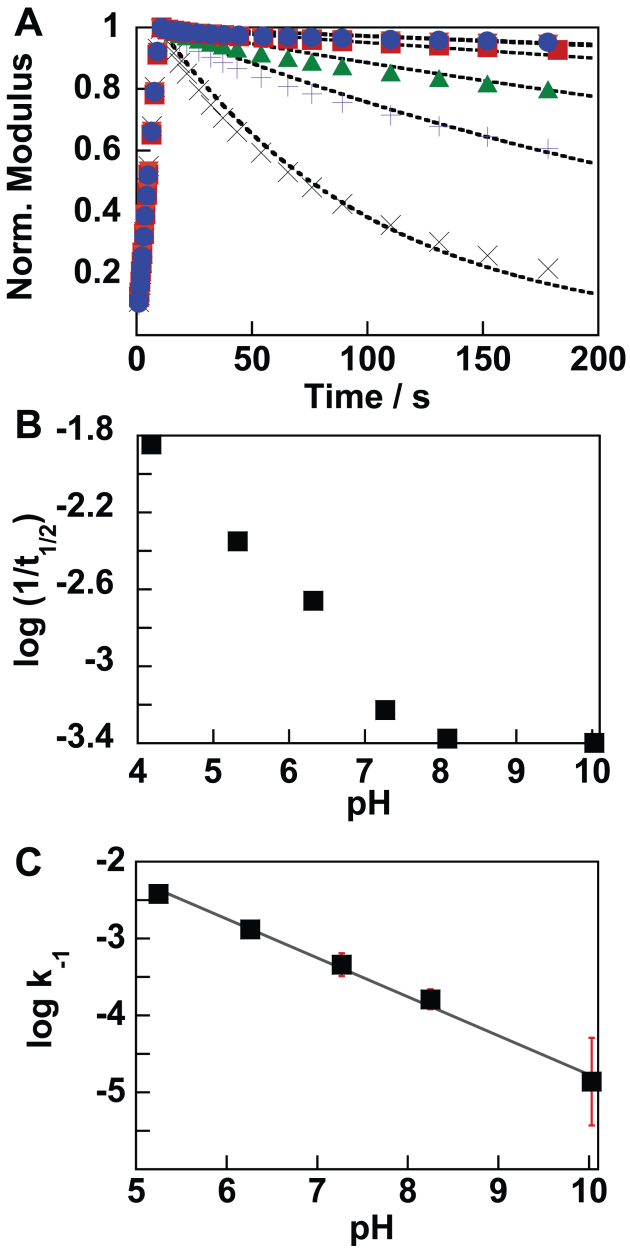

Figure 6.6: (A) Hydrogel stress relaxation at pH 5.3 (+), 6.3 (triangle), 7.3 (square), 8.1 (del), and 10.0 (circle). Dashed lines represent a fit to the Maxwell model.[11] (B) Inverse half-life of gel relaxation at different pH values. (C) Rate of small molecule hydrazone hydrolysis at different pH values. Each data point represents the average of three independent kinetic measurements. Error bars represent standard deviation.

stability (Figure 6.5).[153] As the rate of k_{-1} decreases, a factor that can be precisely altered by increasing the pH, the gels take longer to relax applied stress; at more acidic pH values, the k_{-1} values increase, and correspondingly, the gels relax stress more quickly. Thus, the rate of the back reaction dominates the ability of the material to relax applied stress, an observation that should provide a valuable design principle for the development of next-generation stress relaxation materials.

Taken together, the small molecule kinetic studies provide excellent agreement with the hydrogel evolution and stress relaxation characteristics of bis-aliphatic hydrazone hydrogels. It is notable that the rheological characteristics of a complex PEG hydrogel system can be captured by the characteristics of the kinetics of the reactive end groups. This demonstration provides a versatile strategy for screening of suitable hydrogel-forming reactions through analogous small-molecule studies, and future studies will focus on quantifying the theoretical underpinnings of the relationship be-tween the relaxation properties of the hydrogel and the rate constants of the crosslinking reactions.

6.4 Discussion of the Rapid Formation of the Bis-Aliphatic Hydrazone Bond

An unexpected consequence of this analysis is the observation not only that bis-aliphatic hydrazones form exceptionally quickly at physiological pH, a characteristic observed and reported by us and others,[82,209,211] but also that physiological pH is the point at which this bond forms most rapidly. This is in contrast to established precedence in the literature, which is largely dominated by studies of hydrazone formation with aryl aldehydes. We are currently investigating the mechanistic basis of the bis-aliphatic hydrazone bond formation and hope to apply the discoveries from these studies to the development of next-generation hydrogel materials.

Previous work has shown hydrazone bonds to form and hydrolyze by the mechanism shown in Figure 6.8. We hypothesized that the bis-aliphatic hydrazone bond could have possibly formed by a different mechanism, involving the cleavage of the alpha-C-H bond

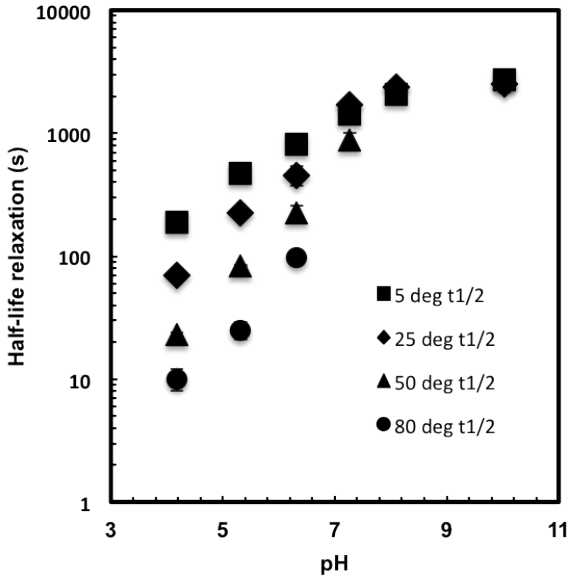

Figure 6.7: The half-life of relaxation is shown as a function of pH and temperature. The gels relaxed much more quickly at higher temperatures and lower pH values. High temperatures combined with high pH values resulted in gel decomposition.

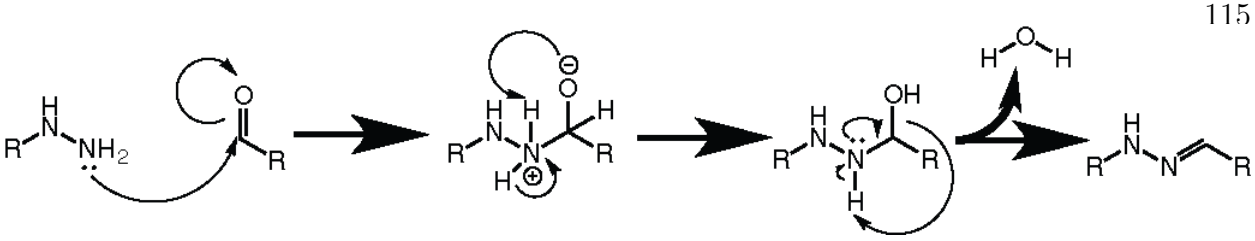

Figure 6.8: Accepted mechanism of hydrazone bond formation.

on the butyraldehyde. However, kinetic studies with deuterated butyraldehyde showed no significant kinetic isotope effect, providing evidence against a shift in mechanism to include a C-H bond breakage event in the rate determining step (Figure 6.9) and indicating a different mechanism is not likely driving the extremely rapid bond formation at physiological pH.

We next hypothesized that the hydration state of the aldehyde may be important to the kinetics of hydrazone bond formation. Previous studies have shown that aryl aldehydes exists almost exclusively in their unhydrated, aldehyde form in water, while aliphatic aldehydes are frequently found in equilibrium with their conjugate diols. Instinct suggests that the diol form would likely be unreactive to-wards a hydrazine attack and perhaps buffer pH affects the equilibrium aldehyde:diol ratio. However, ^{1}H NMR studies showed a similar degree of gem-diol formation at pH 3.2, 7.2, and 11.0, suggesting that the rate differences do not originate as a result of different populations of these two compounds at different pH values (Figure 6.10).

Finally, previous studies have shown that buffer can serve as a general acid catalyst for hydrazone formation.[209,212] These results implicate that hydrazone bonds should form most rapidly in buffers of pH close to the pKa of the buffering molecule. Thus, in acetate buffer it would be expected that the rate of hydrazone formation would peak at pH 4.7 and in phosphate buffer pH 7.2. While we observed a maximum rate of hydrazone bond formation in phosphate buffer at pH 7.3, the corresponding maximum in acetate buffer occurred at 6.3. Additionally, hydrazone formation in 2 M KCl with 1 mM, 5 mM, 20 mM, or 100 mM phosphate does not differ significantly, suggesting that, unlike the reaction between

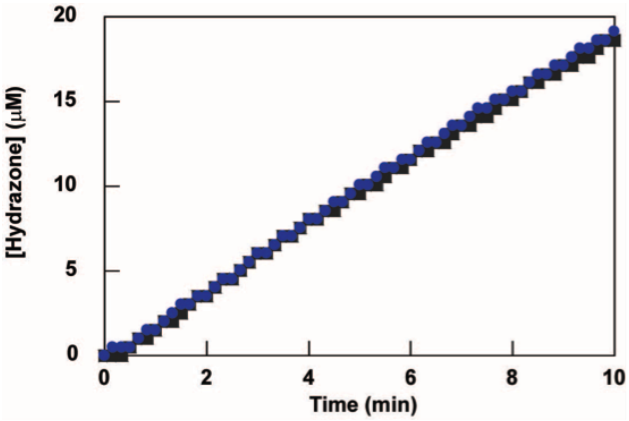

Figure 6.9: Rate of hydrazone formation with n-butyraldehyde-2,2′-d_2 (blue) and methylhydrazine and n-butyraldehyde and methylhydrazine (black) in D_2O. No significant rate difference in product formation is seen between the two substrates.

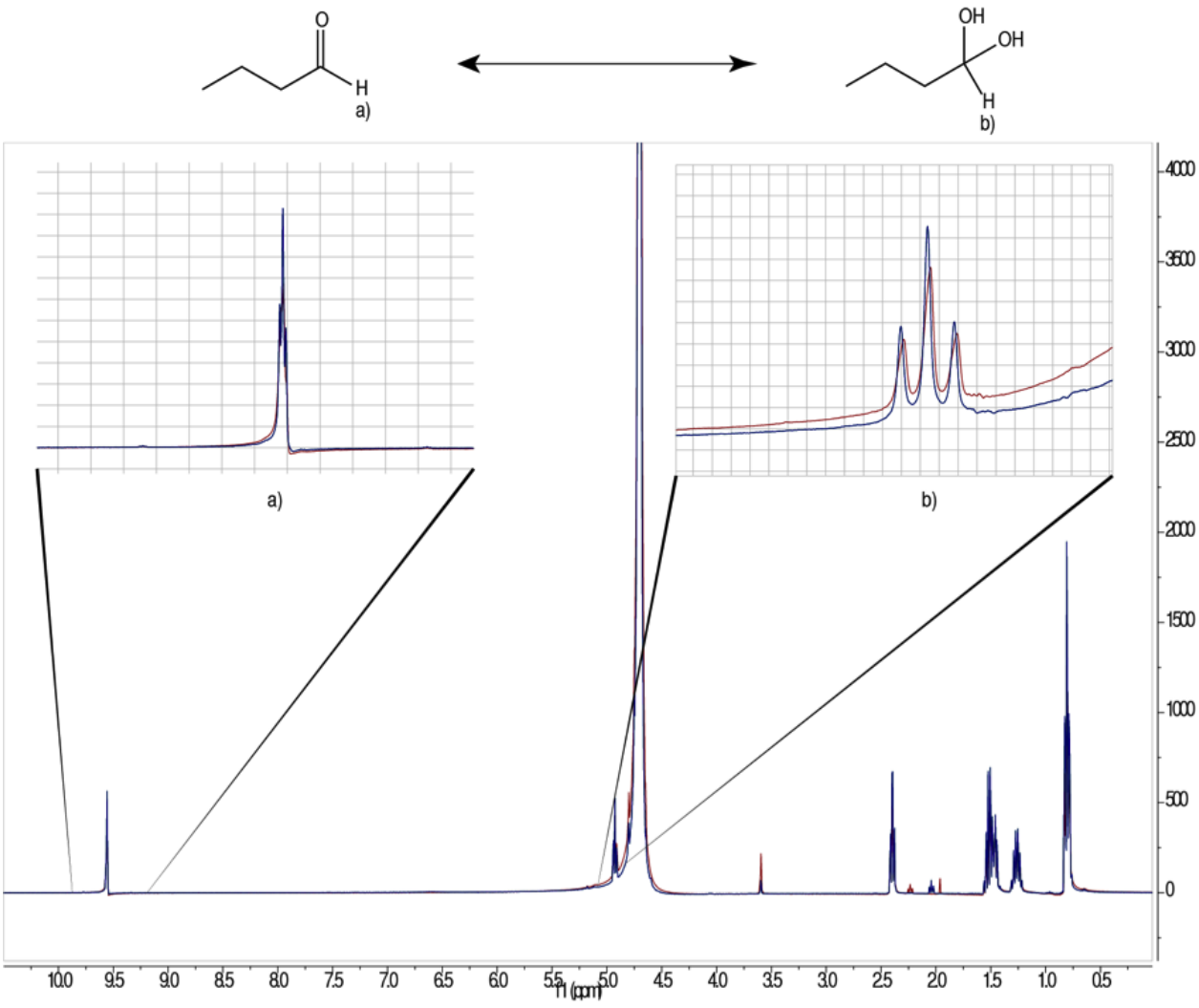

Figure 6.10: ^{1}H NMR traces of butyraldehyde in 90% D2O:10% pH 3.2 acetate buffer (red), pH 7.2 phosphate buffer (green), or pH 11.0 phosphate buffer (blue). The ratio of aldehyde proton a) and gem-diol proton b) remains constant through this pH range (1:1.4) indicating the hydration state of butyraldehyde does not contribute to the pH-dependent kinetics.

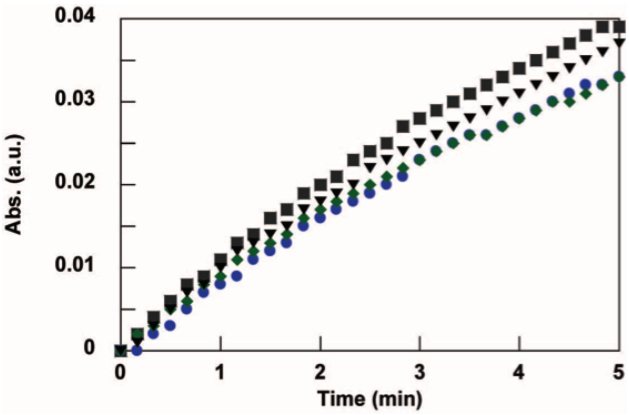

Figure 6.11: Effect of phosphate ion concentration on the rate of hydrazone formation between butyraldehyde and methylhydrazine. Reactions were carried out in 2 M KCl containing 1 mM (diamond), 5 mM (del), 20 mM (circle), and 100 mM (square) of phosphate buffer.

hydroxylamine and acetone, the observed rate differences are not a result of the phosphate ion behaving as a general acid catalyst (Figure 6.11).[212] Future studies are in progress to determine the mechanistic basis for these reaction characteristics.

6.5 Experimental

General Procedures and Materials: Unless otherwise noted, all chemicals and solvents were of analytical grade and were used as received from commercial sources. 4-arm 20 kDa PEG-amine and 8-arm 10 kDa PEG-OH was obtained from JenKem. Water (dd-H_2O) used in biological procedures or as a reaction solvent was deionized using Milli-Q Advantage A-10 water purification system (MilliPore, USA). UV-vis spectra were acquired on a DU 730 spectrophotometer (Beckman Coulter, USA) with quartz cuvettes. Rheological measurements were made with a DH-R3 rheometer (TA Instruments, USA).

Buffer preparation: 100 mM buffers were prepared using either acetate or phosphate stock solutions. Recipes are summarized in Table 6.1 and 6.2.

Macromer synthesis: The 8-arm 10 kDa PEG-aldehyde (8-AA) was synthesized using a Swern oxidation.[169] Oxalyl chloride (88 equiv.) was dissolved in anhydrous DCM in a flame-dried flask purged with argon and immersed in a dry ice/acetone bath at -78° C bath.

Table 6.1: Buffer recipes for pH 4.2, 5.3, and 6.3

pH	Vol 100 mM acetic acid (mL)	Vol 100 mM acetate (mL)
4.2	42	18
5.3	18	32
6.3	3	47

Anhydrous DMSO (92 equiv.) was added dropwise, forming an activated alkoxy sulfonium intermediate. Next, one equivalent of 8-arm 10 kDa PEG-alcohol in a minimal volume of DCM was added dropwise, and the reaction was allowed to proceed for 20 minutes, at which point triethylamine (200 equiv.) was added dropwise. Finally, the reaction was allowed to warm to room temperature, and the product was precipitated with diethyl ether and purified by dialyzing against DI water. The 4-arm 20 kDa PEG-hydrazine (4-H) was synthesized by activating of tri-boc-hydrazinoacetic acid (8.8 equiv.) with HATU (8 equiv.) and N-methyl morpholine (18 equiv.) in DMF. One equivalent of 4-arm 20 kDa PEG-amine dissolved in DMF was added to the activated hydrazinoacetic acid solution, and the reaction was allowed to proceed overnight. Next, the product was precipitated in ether and dissolved in a 50:50 mixture of DCM/TFA to remove the Boc protecting group. After 4 hours, the product was again precipitated in ether, dissolved in water, and dialyzed against DI water for 24 hours. Finally, the product was lyophilized and used for experimentation.

Macromer characterization: Macromers were characterized through ^{1}H NMR and shear rheology.

4-H ^{1}H NMR (D_2O, 400 MHz): δ= 3.59 (s, PEG)

4-H ^{1}H NMR (DMSO-d_6, 400 MHz): δ= 8.1 (t, J = 4 Hz, 1H), δ= 4.45 (m, 2H), δ=

Table 6.2: Buffer recipes for pH 7.3, 8.1, and 10.0

pH	Vol 100 mM disodium phosphate (mL)	Vol 100 mM HCl (mL)	Vol 100 mM NaOH (mL)
7.3	38	12	0
8.1	48	2	0
10.0	48	0	2

3.51 (s, PEG), δ= 3.2 (m, 1H), δ= 2.96 (m, 2H)

8-AA ^{1}H NMR (D_2O, 400 MHz): δ= 5.04 (t, J = 6 Hz, 1H), δ= 3.76 (t, J = 4 Hz, 2H), δ= 3.59 (s, PEG). Aldehyde exists as a diol in D_2O.

8-AA ^{1}H NMR (DMSO-d_6, 400 MHz): δ= 9.61 (s, 1H), δ= 4.23 (s, 2H), δ= 3.54 (s, PEG). 8-AA gels in organic solvents; therefore, NMR peaks were significantly broadened.

To determine functionalization, a four-arm benzaldehyde-terminated macromer of known functionalization were mixed with 4-H highly off-stoichiometrically, and the point at which gelation no longer occurred was noted. This information was combined with Flory-Stockmayer theory (Equation 6.1 and 6.2), which states,

$$p_c = \frac{1}{\sqrt{\frac{(f_A-1)(f_B-1)}{r}}} \tag{6.1}$$

$$r = \frac{f_B n_B}{f_A n_A} \tag{6.2}$$

where f_A is the functionality of the first macromer, f_B is the functionality of the second macromer, n_B and n_A are their concentrations, and p_c is the percolation threshold, which must be greater than one for gelation to occur. For this system studied, f_A is 4 and f_B is 4, so theoretically, gelation should barely occur when the macromers are mixed 1:3.3 off-stoichiometrically. The result was observed, indicating that 4-H was nearly fully functionalized, which is not surprising given HATU-mediated peptide couplings are known to proceed to 99% completion.[170] The experiment was repeated with 4-H and 8-AA and similar results were observed, which is again expected as Swern oxidations are known to proceed to 97%-100% to completion.[169]

Gel formation: The PEG macromers were dissolved in buffered saline to form 30 wt% and 15 wt% stock solutions for the 4-arm PEG-hydrazine and 8-arm PEG-aldehyde, respectively. Solutions were combined stoichiometrically at 10.5 wt% to form hydrogels *in situ* on a temperature-controlled Peltier plate set to 25°C on a shear rheometer, unless

otherwise specified.

Rheology: Samples were formed *in situ* by pipetting 30 μL monomer solutions between the bottom Peltier plate and a flat tool 8 mm in diameter on a shear rheometer. The gap was closed to 500 μas quickly as possible, and the experiment was commenced. All experiments were performed at 25°C. Frequency and strain sweeps were performed to ensure measurements were made in the linear region. Evolution experiments were performed at 1% strain and 1 rad/s,; frequency sweeps were performed at 1% strain; and stress relaxation experiments were performed at 10% strain.

Kinetics: An Eppendorf tube was charged with buffer at the indicated pH (198 μL), and butyraldehyde (1 μL of a 20 mM stock in DMSO) and methylhydrazine (1 μL of a 20 mM stock in DMSO) were added. The contents were quickly transferred to a cuvette, the cuvette was covered with a layer of Parafilm, and the absorbance at 240 nM was monitored (ε= 1,986 M^{-1} cm^{-1}).[82] The data were fit to Equations 6.3, 6.4, and 6.5, a standard kinetic model derived by Dirksen et al.[10]

$$x(t) = \frac{a_+(x_0 - a_-) - a_-(x_0 - a_+)e^{-k_1(a_+ - a_-)t}}{(x_0 - a_-) - (x_0 - a_+)e^{-k_1(a_+ - a_-)t}} \tag{6.3}$$

$$a_+ = \frac{-k_{-1} + \sqrt{k_{-1}^2 + 4k_1k_{-1}x_0}}{2k_1} \tag{6.4}$$

$$a_+ = \frac{-k_{-1} - \sqrt{k_{-1}^2 + 4k_1k_{-1}x_0}}{2k_1} \tag{6.5}$$

Here, x is the concentration of one reactant as a function of time; x_0 is the initial concentration the reactant; k_1 and k_{-1} are the forward and backward rate constants; and a_+ and a_- are defined in terms of these variables. This model assumes a bimolecular reaction with equimolar starting concentrations of the reactants and no side reactions. Each kinetic trace was fitted to the model, and the k_1 and k_{-1} values were recorded. Three independent measurements were made at each pH value. The reported values are the mean value and

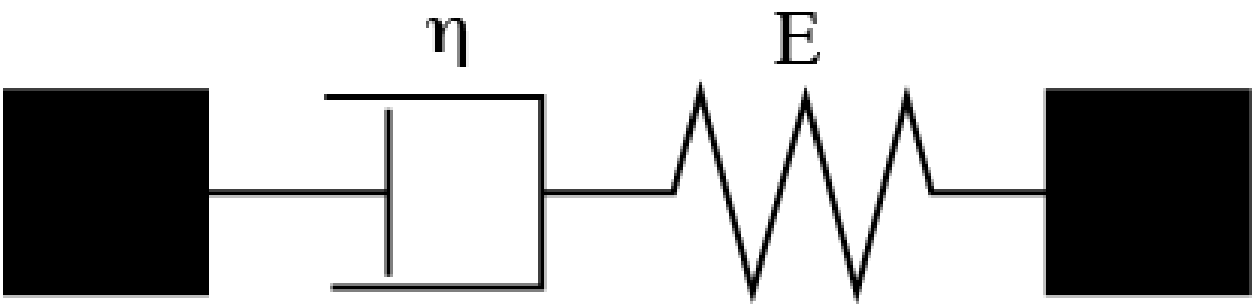

Figure 6.12: A dashpot (damper) with viscosity, η, in series with a spring of elastic modulus, E, is the simplest model for a viscoelastic fluid capable of capturing stress relaxation behavior.

standard deviation for these three calculations. Excellent run-to-run agreement was seen at all pH values.

Rheological Modeling: Gel evolution was fit to an exponential model, as shown in Equation 6.6,

$$G(t) = G_\infty - Ae^{-\tau t} \tag{6.6}$$

where $G(t)$ is the elastic modulus, G_∞ is the equilibrium elastic modulus, A and τ are fit parameters, and t is the time. The half-lives of hydrogel evolution were calculated to compare the effects of different pH values.

Because every bond in the material is reversible, we assumed the material behaved as an ideal Maxwellian viscoelastic fluid, represented by a spring in series with a dashpot, as shown in Figure 6.12.

The total stress on a Maxwell material must equal the stress on each of the individual components, and the total strain is divided between the two with some time dependence. These assumptions are combined into Equation 6.5

$$\frac{d\epsilon}{dt} = \frac{\sigma}{\eta} + \frac{1}{E}\frac{d\sigma}{dt} \tag{6.7}$$

where ϵ is the total strain, σ is the stress, η is the dashpot viscosity, E is the spring

modulus, and t is the time. However, under the conditions used to measure stress relaxation, the material is strained a fixed amount and stress is measured; thus, the time derivative of strain is zero, and the equation simplifies to Equation 6.8,

$$\sigma(t) = \sigma_0 e^{-t/\tau} \tag{6.8}$$

where τ is a characteristic time constant of relaxation equal to the viscosity of the dashpot divided by the modulus of the spring. The stress relaxation data were then fit to this equation using the *FindFit* function in *Mathematica*, and relaxation times were used to quantitatively compare the effects of varying pH values.

Statistics: Small molecule kinetic studies were performed in triplicate and rheological experiments were performed in duplicate. Error bars represent the standard deviation.

6.6 Conclusions

To close, our study demonstrates that a small-molecule model system can capture and describe the origin of bis-aliphatic hydra-zone hydrogel evolution and stress relaxation characteristics. The forward rate constant of the reaction dominates the gel evolution process, while the back rate constant heavily influences the ability of the gel to relax stress, providing a set of rational design principles for the development of next-generation stress relaxation materials. Moreover, the unexpectedly rapid formation of the bis-aliphatic hydra-zone at physiological pH indicates that this reaction may find extensive use in bioconjugation methods and dynamic covalent chemistry applications, especially for use with pH-sensitive proteins and molecules.

Chapter 7

A Coumarin-based Photodegradable Hydrogel: Design, Synthesis, Gelation, and Degradation Kinetics

7.1 Abstract

The design, synthesis, and characterization of a new class of coumarin-based photodegradable hydrogels are reported. Hydrogel formation was achieved rapidly and efficiently under aqueous conditions using copper-catalyzed click chemistry, which afforded excellent control over the rate of network formation. Rapid photodegradation, to the point of reverse gelation, was observed using both 365 nm and 405 nm light, and micron-scale features were eroded using two-photon irradiation at wavelengths as long as 860 nm.

7.2 Introduction

Hydrogels, water-swollen crosslinked polymeric networks, are an important class of polymeric materials in biomedical research. For applications in tissue engineering and regenerative medicine, some of the key properties of hydrogels are their ability to localize and deliver therapeutic proteins in a controlled manner, serve as delivery vehicles for cell transplantation, and allow the culture of stem cells in tissue-like three-dimensional microenvironments in vitro.[65,81,213] Degradable hydrogels are among the most attractive and useful classes of hydrogel scaffolds, as their degradability can be leveraged to control the release and delivery of therapeutic cells and proteins.[74,97,113,198] Conventionally, hydrogel degradation is achieved either hydrolytically or proteolytically; these approaches to degrad-

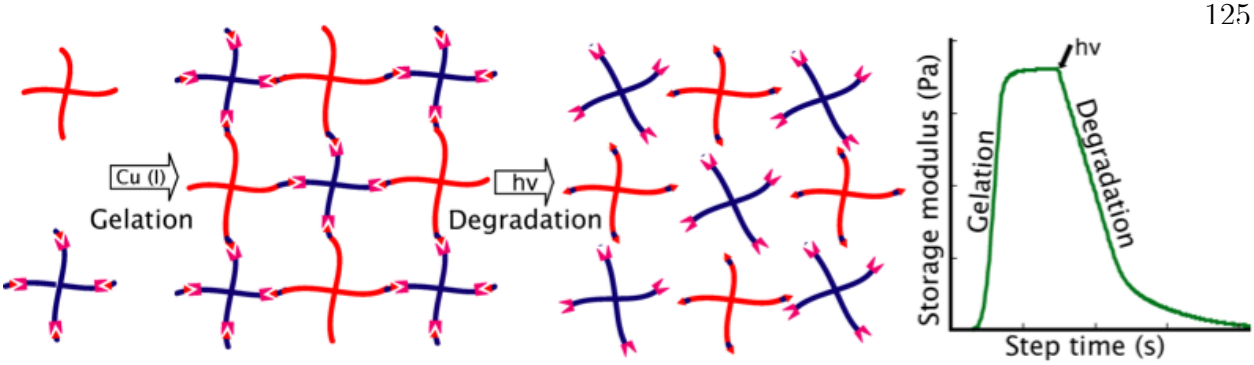

Figure 7.1: Step-growth hydrogels cross linked though copper catalyzed click chemistry form predictably and degrade rapidly upon exposure to ultraviolet, short wavelength visible, and two-photon infrared light.

ability are often mediated by external triggers such as pH, temperature, small molecules, and enzymes.[123,137,174,214] However, there is a growing interest among researchers in developing chemical strategies that allow for spatiotemporal control over the cleavage of gel crosslinks.[82,128,213,215] To this end, photodegradable hydrogels, which allow for precise user-directed degradation of the network structure via light-mediated reactions, have evolved and received enormous attention in recent years.[72,192,216] While these hydrogels have found have numerous applications to date,[132,175,176,190] the majority of the systems reported are based on incorporating a photolabile nitrobenzyl moiety into the network crosslinks.[72,192,217]

In this communication, we introduce a coumarin-based photodegradable hydrogel platform as a potential alternative to the previously reported nitrobenzyl-based systems. Importantly, this chemistry is highly suitable for biological applications, as the photodegradation reaction produces biologically inert by-products.[218,219] Unlike the nitrobenzyl system, which releases an aldehyde or ketone, both of which are reactive towards amine functionalities of proteins,[220,221] the coumarin system exposes an innocuous alcohol.[191,218,219,222] An additional advantage of this coumarin-based platform is that the red shift in its degradation wavelengths, relative to the nitrobenzyl-based systems, provides access to a broader spectrum of cytocompatible wavelengths of light.[191,218,219,222] Here, the synthesis of a new class of coumarin-based hydrogels, which are crosslinked using aqueous copper catalyzed

click chemistry,[102,223–225] is described. In addition, characterization of the gel formation and photo-degradation properties of these hydrogels is presented.

7.3 Results & Discussion

The macromolecular precursors: 4-armed poly(ethylene glycol) (PEG) tetra-alkyne **1** and 4-armed PEG tetra-coumarin azide **2** used in the formation of the photodegradable hydrogels are shown in Figure 7.2. Polymer **1** was synthesized in a straightforward manner upon reacting 4-armed 5 kDa PEG tetra-amine with pentynoic acid. The coumarin based polymeric precursor **2** was obtained by coupling 4-armed 5 kDa PEG tetra-carboxylic acid with an amine terminated coumarin azide **3**. This coumarin azide **3** was synthesized following the synthetic route described in Scheme 7.3. Briefly, 7-amino-methylcoumarin was first diazotized and then treated with sodium azide to obtain 7-azido-methylcoumarin **4**. The methyl functionality of the coumarin was then oxidized to a methylene alcohol using selenium dioxide as an oxidizing agent. The resultant coumarin methyl alcohol **5** was then coupled to Boc-protected beta-alanine and exposed to trifluoroacetic acid to obtain the final amine-containing coumarin azide **3**.

Hydrogel formation was achieved by mixing equimolar (100 mg/mL, 80 mM functional groups) aqueous solutions of **1** and **2** with solutions of sodium ascorbate (316 mg/mL, 1.6M), followed by copper sulfate at varying concentrations. The final concentrations of alkyne and azide functional groups were 36 mM, and the final concentration of sodium ascorbate was 80 mM. The concentration of copper sulfate was varied from 2 mM to 16 mM to investigate the effects of this variable on the gelation characteristics, specifically the kinetics of gel formation and the final modulus reached during *in situ* polymerization on a shear rheometer. As expected, a correlation between the concentration of copper sulfate and the gelation kinetics was observed, where higher concentrations resulted in faster network formation (Figure 7.4). For example, with 0.44 equivalents of copper per alkyne (16 mM), the modulus reached 90% of the final value within two minutes, while reducing the copper

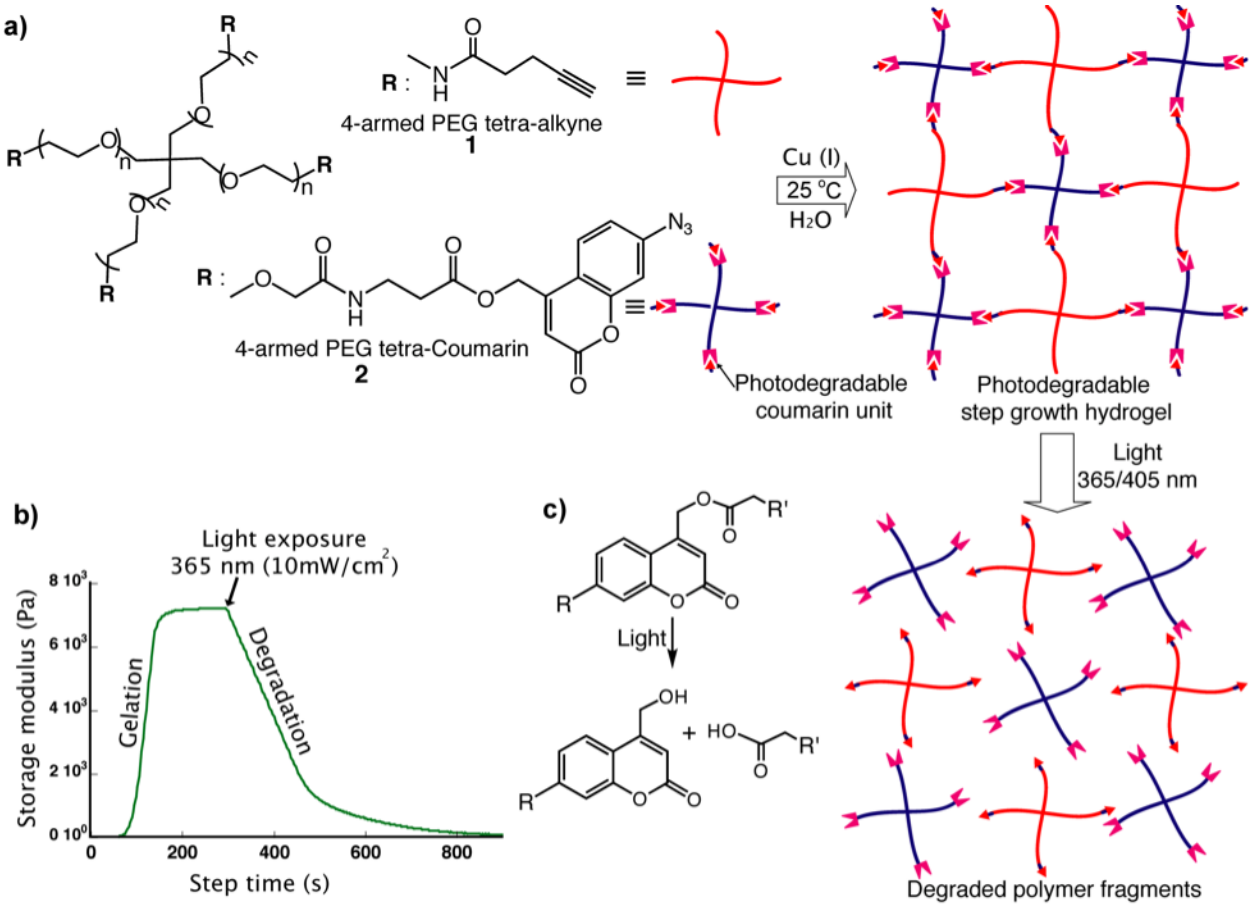

Figure 7.2: Coumarin-based photodegradable hydrogel: a) Chemical structures of 4-arm PEG tetra-alkyne (5 kDa) and 4-arm PEG tetra-azide (5 kDa) and schematic representation of copper (I) catalyzed gel formation and light activated degradation; b) *In-situ* rheology of gelation and degradation of coumarin hydrogels. Gelation and degradation were achieved at 2-16 mM of Cu (I) and at 365 nm (10mW/cm^2) light, respectively, under aqueous conditions at room temperature; c) Photochemistry of coumarin methyl ester degradation, in which coumarin methyl alcohol is produced after degradation.

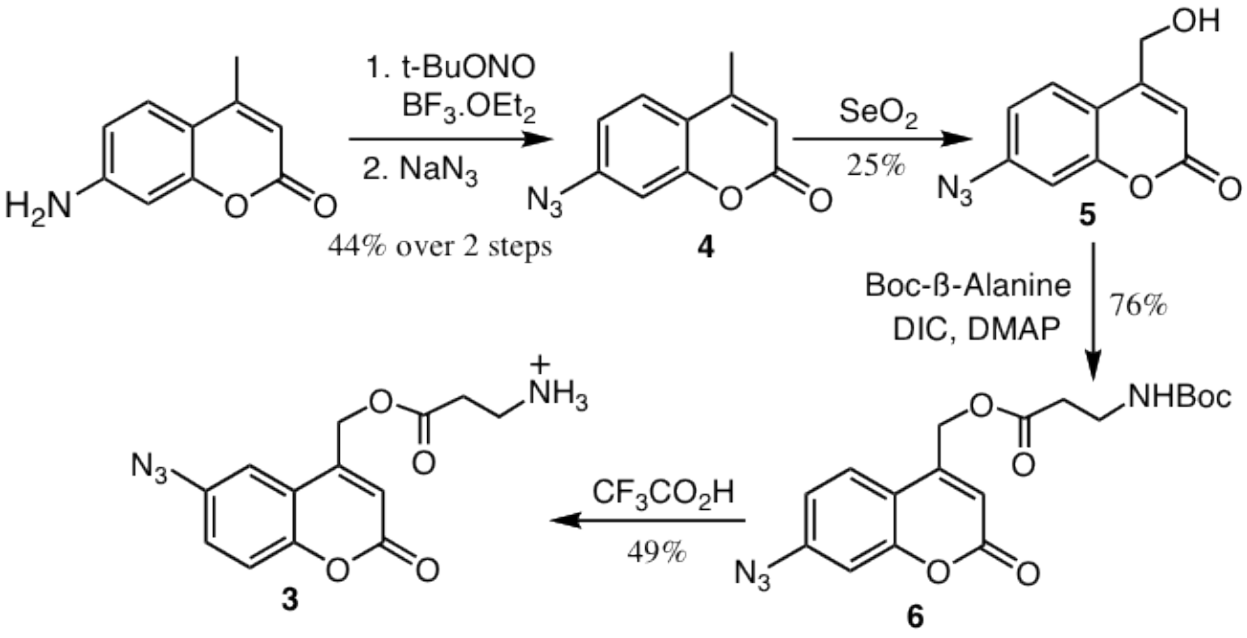

Figure 7.3: Synthesis of amine-terminated coumarin azide **3**.

Table 7.1: Kinetics of coumarin-based photodegradable hydrogel formation.

[Cu]	Time between gel point and 90% G_{eq}	G'_{eq}
16 mM	58(12) s	6500(400) Pa
8 mM	104(18) s	7300(500) Pa
4 mM	344(120) s	9700(500) Pa
2 mM	784(60) s	11,000(1,000) Pa

concentration to 0.05 equivalents (2 mM) delayed this conversion to over 15 minutes. In general, the time required to reach 90% of the final modulus (based on when the macromers were placed on the rheometer) varied over an order of magnitude from ca. 100 s to ca. 1000 s. To quantify the kinetics of gel formation, we measured the time elapsed between the gel point[1] and the gel reaching 90% of its final modulus to avoid errors associated with the time required to initiate measurements (Figure 7.4, Table 7.1). These times were inverted to generate rates of modulus evolution, which are linear with respect to copper concentration (Figure 7.5). This analysis indicates that the copper is involved in the rate limiting step, and the rate of modulus evolution corresponds well with the rate of the click reaction, which is also linear with respect to copper concentration.[224–226]

Interestingly, the copper sulfate concentration also had an effect on the modulus of the final hydrogel, as higher catalyst concentrations resulted in lower final moduli (Figure 7.4). For example, decreasing the copper concentration from 0.44 to 0.05 equivalents per alkyne nearly doubled the final modulus achieved. Previous reports on building polymers using click reactions have shown no change in conversion with respect to the copper concentration. Thus, the effect of copper concentration on final modulus is likely driven by the kinetics of gel formation, leading to different network structures and non-idealities.[224] While the opposite trend was previously observed for thermally initiated thiol-ene step growth gels,[227] we hypothesize that the more complicated mechanism of triazole formation may be responsible for this difference. With this crosslinking chemistry, three collisions are necessary to achieve

[1] Due to the physical characteristics of our rheometer, the exact gel point was not consistently observed, but rather approximated by the time at which the elastic modulus exceeded 1 Pa.

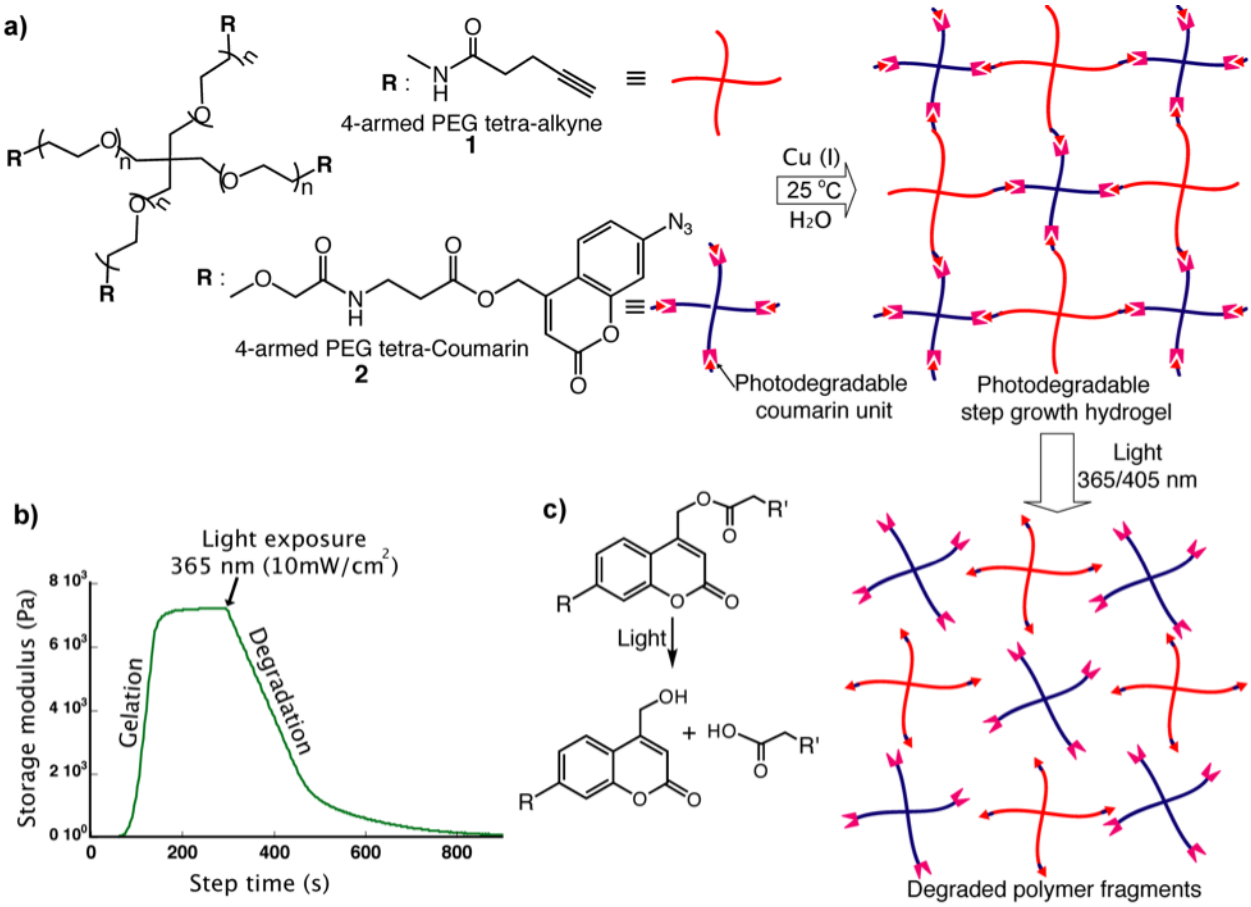

Figure 7.4: Coumarin-based photodegradable hydrogel: a) Chemical structures of 4-arm PEG tetra-alkyne (5 kDa) and 4-arm PEG tetra-azide (5 kDa) and schematic representation of copper (I) catalyzed gel formation and light activated degradation; b) *In-situ* rheology of gelation and degradation of coumarin hydrogels. Gelation and degradation were achieved at 2-16 mM of Cu (I) and at 365 nm (10mW/cm^2) light, respectively, under aqueous conditions at room temperature; c) Photochemistry of coumarin methyl ester degradation, in which coumarin methyl alcohol is produced after degradation.

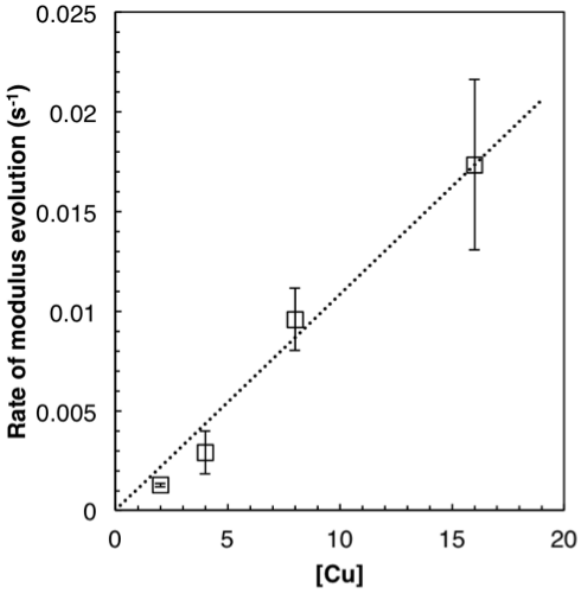

Figure 7.5: Rate of modulus evolution plotted versus copper concentration with linear fit. Because the rate of the cross linking reaction is proportional to each of the reactants, this plot shows that copper is a limited reagent.

bond formation: (i) copper (II) and sodium ascorbate to form copper (I), (ii) copper (I) and alkyne to form the activated copper (I)/alkyne complex, and (iii) copper (I)/alkyne complex and azide for crosslink formation.[226] Consequently, rapid gelation may potentially restrict functional group mobility and lead to network non-idealities (e.g., loops or unreacted end groups), which would likely reduce the crosslink density and modulus. Work is ongoing to elucidate a potential mechanism for the reaction rate dependent modulus observation.

After characterizing the network formation in these step growth hydrogels, detailed characterization of the photodegradation reaction was performed. Previous work has demonstrated that the coumarin moiety cleaves in response to UV (365 nm) and visible (405 nm) light at vastly different rates. Bone morphogenetic proteins (BMPs) tethered to a hydrogel network through a coumarin linker was shown to be released 3.3 times faster than one tethered through a nitrobenzyl linker under 365 nm irradiation and 2.9 times slower under 405 nm irradiation.[191] We sought to investigate and quantify the rates of coumarin cleavage upon exposure to different intensities of 365 nm and 405 nm light through hydrogel degradation kinetic studies. Coumarin crosslinked hydrogels were polymerized *in situ* and exposed to varying intensities of both 365 nm and 405 nm light. We observed significant differences in the time required for crosslink cleavage, as measured by modulus reduction, over the range of intensities and wavelengths investigated. The shear elastic moduli of coumarin crosslinked hydrogels exposed to 1.4 mW/cm^2 of 405 nm irradiation was reduced to only *ca.* 95% of its initial value after 200 s, while hydrogels exposed to 10.4 mW/cm^2 365 nm experienced a modulus reduction of less than 25% of its initial value at the same time point (Figure 7.6, Table 7.2). This behavior was fit to a first order degradation model shown in Equations 7.1 and 7.2 to yield apparent rates of crosslinking cleavage that can be quantified and compared.[72,192]

$$G(t) = G_0 e^{-k_{app} t} \tag{7.1}$$

Table 7.2: Kinetics of coumarin-based photodegradable hydrogel degradation.

Light Intensity	Time to reach $\frac{1}{2}$ G_0	k_{app} x 10^4
1.4 mW/cm^2 365 nm	600(80) s	12(1) s^{-1}
4.0 mW/cm^2 365 nm	270(1) s	25(1) s^{-1}
10.4 mW/cm^2 365 nm	90(30) s	77(16) s^{-1}
1.4 mW/cm^2 405 nm	7000(1200) s	1.0(0.1) s^{-1}
4.0 mW/cm^2 405 nm	1800(200) s	3.8(0.5) s^{-1}a
10.4 mW/cm^2 405 nm	750(160) s	9.2(2) s^{-1}
40.0 mW/cm^2 405 nm	300(100) s	34(10) s^{-1}

$$k_{app} = \frac{\phi\epsilon\lambda_0(2.303x10^{-6}}{N_A hc} \tag{7.2}$$

Here $G(t)$ is the shear elastic modulus as a function of time, G_0 is the initial modulus, and t is the time of exposure. The apparent rate of degradation, k_{app}, has been to shown to depend on the quantum yield, ϕ, the molar absorptivity, ϵ, the incident irradiation, I_0, and the wavelength of light, λ. This relationship is shown in Equation 7.2, where N_A is Avogadro's number, h is Planck's constant, and c is the speed of light. Thus, the rate of gel degradation can be modulated by changing light intensity or wavelength, as the molar absorptivity is a function of wavelength.[72,192]

The shear elastic modulus of coumarin crosslinked hydrogels was monitored during exposure to 40 mW/cm^2, 10.4 mW/cm^2, 4.0 mW/cm^2, and 1.4 mW/cm^2 of 405 nm light and 10.4 mW/cm^2, 4.0 mW/cm^2, and 1.4 mW/cm^2 of 365 nm light. The resulting data were plotted and fit to Equation 7.1 (Figure 7.6). The apparent rate constant, k_{app}, varied by almost two orders of magnitude, from 1.0 x 10^{-4} s^{-1} under exposure to 1.4 mW/cm^2 405 nm light exposure to 79 x 10^{-4} s^{-1} under 10.4 mW/cm^2 365 nm light. Because the degradation is a first-order process, the rates of degradation at each wavelength are expected to collapse to a single point when normalized for light intensity (Figure 7.6, Tables 7.2 and 7.3). In general, we observed excellent agreement with this theory and show consistent kapp/I0 for a given wavelength. Furthermore, based on these calculations, the coumarin crosslinked gel degraded with 365 nm light at a rate comparable to the fastest nitrobenzyl moieties reported.16 While

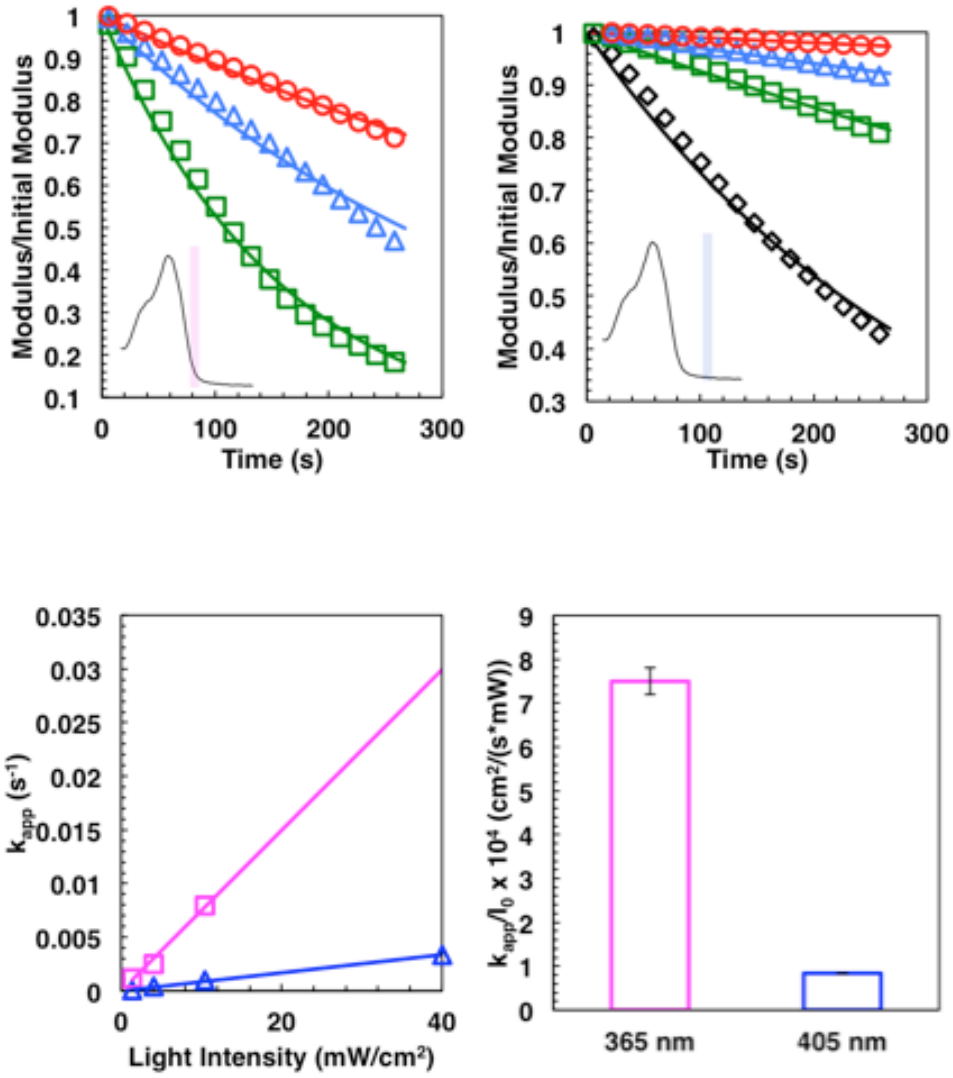

Figure 7.6: Coumarin-based photodegradable hydrogel degradation kinetics: a) *In-situ* rheology of the coumarin gel degrading in response to 365 nm light. The data are shown as points and the fit is shown as a line. Green is 10.4 mW/cm^2, blue is 4.0 mW/cm^2, and red is 1.4 mW/cm^2. The absorbance of the material along with a band representing 365 nm is shown inset. b) *In-situ* rheology of the coumarin gel degrading in response to 405 nm light. Black is 40 mW/cm^2, green is 10.4 mW/cm^2, blue is 4.0 mW/cm^2, and red is 1.4 mW/cm^2. The absorbance of the material along with a band representing 405 nm is shown inset. c) Plot of k_{app} versus light intensity. Across a wavelength, a straight line is expected with data (points) and fits (lines) shown for 365 nm (magenta) and 405 nm (violet). Error bars are smaller than the points. d) k_{app}/I_0 versus light intensity. Both these numbers collapse to $k_{app}/(I_0 * \epsilon)x10^4 = 0.0030 \pm 0.0001 cm^3 * M/(s * mW)$ when normalized to the extinction coefficient, ϵ, of the material at those wavelengths.

Table 7.3: Coumarin hydrogel degradation constants.

Wavelength	k_{app}/I_0 x 10^4
365 nm	7.5(0.3) $cm^2/(s*mW)$
405 nm	0.84(0.01) $cm^2/(s*mW)$

the degradation kinetics were roughly ten times slower at 405 nm, this result is consistent with the absorbance data showing that the PEG-coumarin molecule 2 absorbs slightly less than ten times more light at 365 nm (ϵ = 2480 cm-1 M-1 per functional group) than at 405 nm (ϵ = 280 cm-1 M-1 per functional group). When this difference in molar absorptivity is taken into account, all of the data collapse to a single value, kapp/(I0*ϵ) x 104 = 0.0030 0.0001 cm3*M/(s*mW), indicating that the quantum yield is similar for both wavelengths of light.

Finally, we hypothesized that the coumarin moiety would also cleave in response to longer wavelengths of two-photon light. Using a confocal microscope and a tunable two-photon laser, we observed visible material degradation for wavelengths between 720 and 860 nm (Figure 7.7). While the efficiency of degradation was much higher at 740 nm, requiring only a 1.58 μs pixel dwell at a 110 mW/μm^3 intensity, degradation was observed even out to 860 nm by increasing the pixel dwell time.

7.4 Experimental

General Procedures and Materials: Unless otherwise noted, all chemicals and solvents were of analytical grade and were used as received from commercial sources. 4-arm 5 kDa Poly(ethylene glycol) (PEG) was obtained from JenKem. UV-Vis spectra were acquired on a NanoDrop spectrophotometer. Rheological measurements were made with a DH-R3 rheometer (TA Instruments, USA). ^{1}H NMR spectra were recorded on a 400 MHz Bruker NMR spectrometer using the residual proton resonance of the solvent as the internal standard. Chemical shifts are reported in parts per million (ppm). When peak multiplicities are given, the following abbreviations are used: s, singlet; d, doublet; t, triplet; m, multiplet; bs,

Figure 7.7: Images of two-photon degradation. The coumarin gel is fluorescent in response to 405 nm incident light. Thus, transmitted, fluorescent, and merged images are shown (left, center, and right, respectively). The numbers refer to the two-photon wavelength used to degrade the material. Degradation and gel erosion was tested up to 900 nm of two-photon light. However, degradation at 900 nm was inefficient. Scale bar: 100 μm.

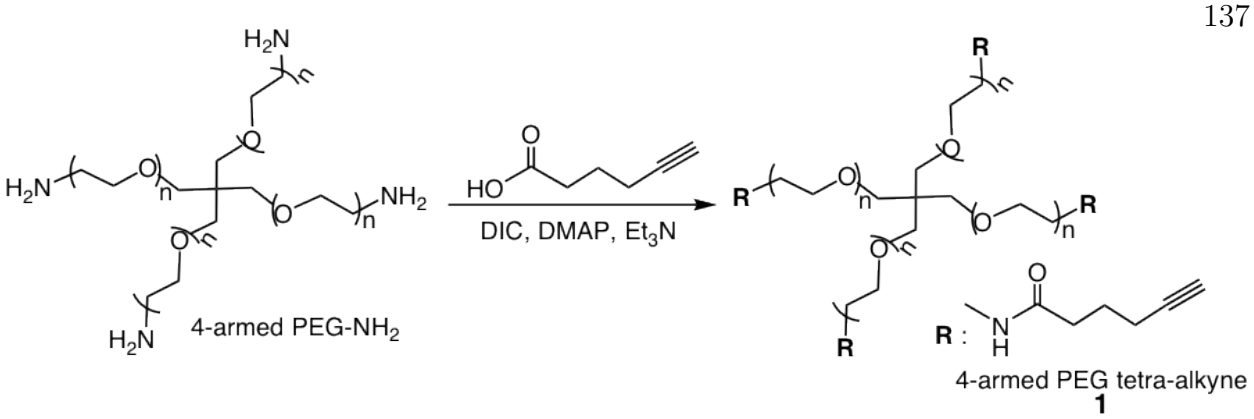

Figure 7.8: Synthesis of compound **1**.

broad singlet.

Macromer synthesis: Compounds **3-6** were synthesized according our previously reported procedures.[191]

Synthesis of 4-armed PEG tetra-alkyne **1**: To a solution of 4-arm PEG amine-HCl (mol. wt. 5 kDa) (1.0 g, 0.2 mmol) in dichloromethane (1.5 mL) was added triethylamine (0.14 mL, 1.0 mmol) and stirred at room temperature (RT) for 15 mins. To the above mixture was added 4-pentynoicacid (0.16 g, 1.6 mmol), diisopropyl carbodiimide (DIC) (0.25 mL, 1.6 mmol) and dimethyl aminopyridine (DMAP) (0.02 g, 0.2 mmol) at ice-bath temperature and the mixture was stirred at RT for 24 hrs. The reaction mixture was then drop-wise added into cold diethyl ether (45.0 mL) in a 50 mL centrifuge tube and the resultant PEG precipitate was centrifuged and the supernatant solutions were decanted. After allowing it to dry for a few hours, the precipitate was dissolved in distilled water and dialyzed against a large volume of water (2 L) for 24 hrs, replacing the water every 12 hrs. The dialyzed solution was then lyophilized to obtain the polymer **1** as a colorless powder (0.8 g, 75%).

^{1}H NMR (400 MHz, DMSO) δ 4.15-4.10 (m, 8H, (terminal-CH_2O)4), 3.65-3.30 (m, 460H, (CH2-CH2O)n), 2.80 (t, J= 4Hz, 4H), 2.52-2.47 (m, 16H), 2.40-2.30 (m, 8H).

Synthesis of 4-armed PEG- tetra coumarin azide **2**: To a solution of 4-arm PEG tetra-carboxylic acid (mol.wt. 5 kDa) (0.18 g, 0.04 mmol) in dichloromethane (0.5 mL) was

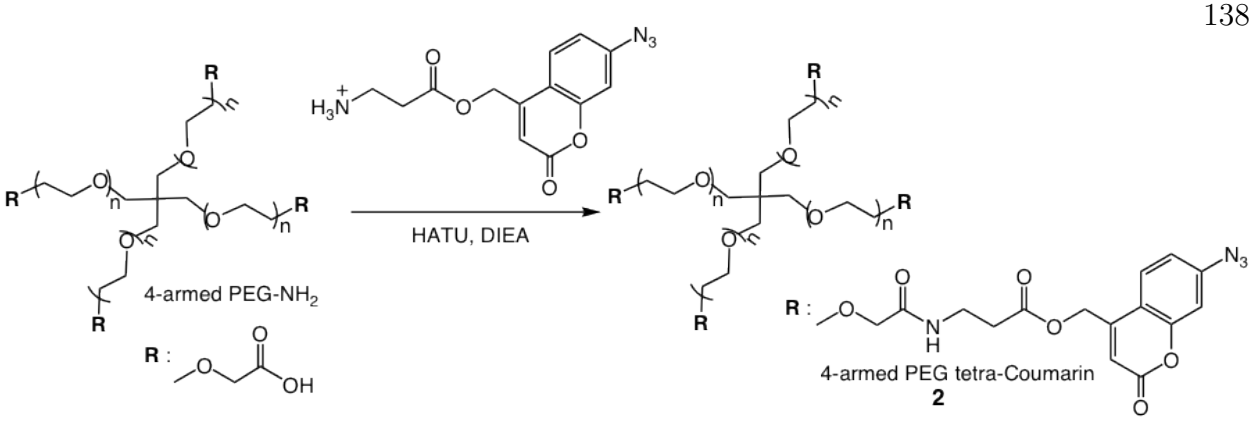

Figure 7.9: Synthesis of compound **3**.

added N,N-diisopropyl ethylamine (DIEA, Hunig's base) (50 μL, 0.3 mmol), followed by 1-[bis(dimethylamino)methylene]-1H-1,2,3-triazolo[4,5-b]pyridinium 3-oxid hexafluorophosphate) (HATU) (0.08 g, 0.22 mmol). To the above mixture was added amine containing coumarin azide **3** and DIEA (50 μL, 0.3 mmol) in dichloromethane (0.5 mL) at ice bath temperature. The reaction mixture was then stirred overnight at RT. The reaction mixture was then added drop-wise into cold diethyl ether (45.0 mL) in a 50 mL centrifuge tube. The resultant PEG precipitate was centrifuged, and the supernatant solutions were decanted. After allowing it to dry for a few hours, the precipitate was dissolved in distilled water and dialyzed against a large volume of water (2 L) for 24 hrs, replacing the water every 12 hrs. The dialyzed solution was then lyophilized to obtain 2 as a slightly brownish powder (0.15 g, 69%).

^{1}H NMR (400 MHz, D2O) δ 7.63-7.50 (bs, 4H), 7.04-6.9 (bs, 8H), 6.40-6.30 (bs, 4H), 5.32-5.21 (bs, 8H), 4.00-3.90 (m, 8H), 3.65-3.30 (m, 450H, (CH_2-CH_2O)n), 2.75 (t, J=4Hz, 8 H).

7.5 Conclusions

In conclusion, our results demonstrate the utility of coumarin-based photodegradable moieties for user-directed manipulation of hydrogel materials. Importantly, this chemistry

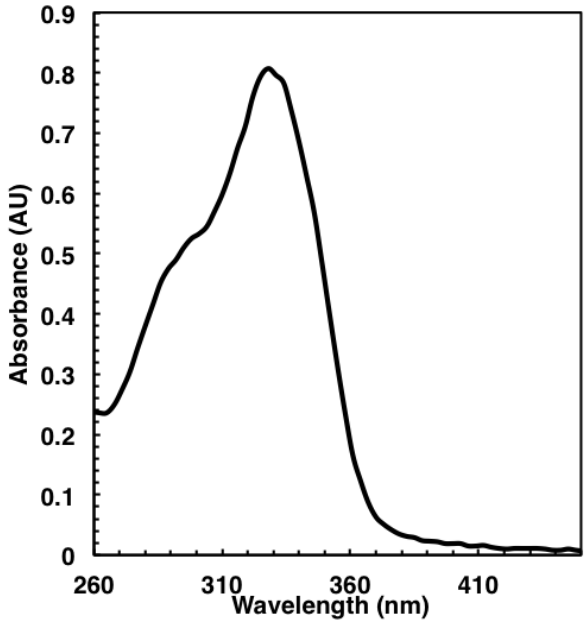

Figure 7.10: Absorbance spectrum of 20 mM **2**.

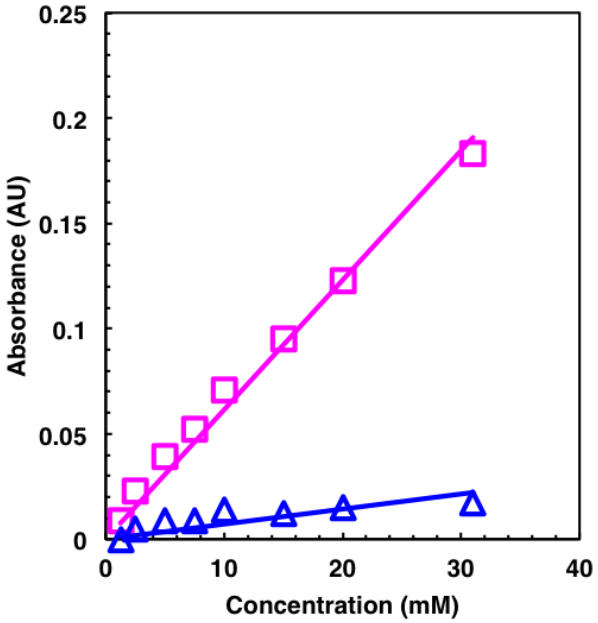

Figure 7.11: Beer's Law fit to determine the extinction coefficient, ϵ, of **2** at 365 nm (magenta) and 405 nm (blue).

is efficient at longer wavelengths of light and produces biologically benign by-products upon photocleavage. Although this characterization has been performed using hydrogels crosslinked by copper catalyzed click chemistry, this coumarin chemistry could easily be adapted to a cytocompatible copper-free hydrogel platform.[82,158,191,228–231] Thus, we anticipate that this versatile new chemistry will prove useful in future tissue engineering studies focused on spatiotemporal patterning of cellular microenvironments.

Chapter 8

Synthetically Accessible Photodegradable Hydrogels for User-Directed Formation of Neural Networks

8.1 Abstract

Hydrogels with photocleavable units incorporated into the crosslinks have provided researchers with ability to control mechanical properties temporally and study the role of matrix signaling on stem cell function and fate. With a growing interesting in dynamically tunable cell culture systems, methods to synthesize photolabile hydrogels from simple precursors would facilitate broader accessibility. Here, a step-growth photodegradable hydrogel system is developed from commercially available precursors in two straightforward synthetic steps with high yields (¿95%). The network evolution and degradation properties are characterized in response to one- and two-photon irradiation. The hydrogel is employed to encapsulate embryonic stem cell-derived motor neurons (ESMNs) and in situ degradation is exploited to gain three-dimensional control over the extension of motor axons using two-photon infrared light. Finally, ESMNs and their in vivo synaptic partners, myotubes, are co-encapsulated, and the formation of user-directed neural networks is demonstrated.

8.2 Introduction

Recent directions in the synthesis of scaffolds for cell culture and tissue regeneration have made tremendous progress in recapitulating aspects of the complex milieu of signals found in in vivo microenvironments.[84,213] This direction represents a significant advance-

ment for the field, but one often considers which features are most important and how much mimicry is required. In some applications, such as cartilage tissue engineering, early efforts found success when focused primarily on mechanical characteristics of the scaffolds, thereby recapitulating the basic tissue properties while simultaneously supporting chondrocyte function (e.g., survival and secretory properties).[73–75] However, other tissue engineering applications necessitated the development of scaffolds that introduced biochemical signals to promote or direct desired cell function, and this led to significant advances in bioconjugation methods to tether proteins and small molecules, conferring functionalization and signaling to embedded cells. Such approaches have been exploited to design materials that preferentially differentiate stem cells into different lineages,[232,233] increase production of extracellular matrix (ECM) components,[67] direct cell migration,[7,234,235] and control extension of axons.[7,8] However, *in vivo* signals are not presented in such a static manner, but rather, complex spatially and temporally regulated presentation of biological cues drive many fundamental processes.[236,237] With this in mind, more recent efforts in scaffold design have exploited advances in polymer chemistry to demonstrate in situ and real time manipulation of cellular microenvironments, thus beginning to recreate the dynamic cellular milieu in vitro. Such approaches have relied on advances of bio-orthogonal reactions and cytocompatible photochemical reactions to render advanced cell culture niches.

Specifically, photopatterned protein-ligand interactions have enabled the spatially controlled presentation of bioactive signaling proteins to drive stem cell migration12,15[8,238] and orthogonal photocleavage reactions have been used to more efficiently differentiate cells by mimicking in vivo pathways.[191] The Shoichet group developed a system exploiting strong protein-ligand interactions to immobilize gradients of sonic hedgehog protein to drive neural progenitor cell migration into an agarose gel.[8] The Lutolf group used developed a photoactivated enzymatic ligation to pattern gradients of VEGF to demonstrate control over mesenchymal stem cell migration.[238] Previous work in the Anseth group identified orthogonal photo-degradation reactions that allowed the sequential release of bone morphogenic

proteins, which enabled more efficient differentiation of human mesenchymal stem cells.[191]

While the above advances have demonstrated the power of controlled biological signaling to cells through regulation of material properties in space and time, complementary materials and simplified systems provide opportunities to expand the accessibility of the chemistry to a broader community of biomaterial researchers.[71,239] Here, recent advances in molecular building blocks are exploited to synthesize a step-growth poly(ethylene glycol) (PEG) hydrogel crosslinked through copper-free click chemistry capable of undergoing degradation upon irradiation by either single- (334 nm and 365 nm) or two-photon light (740 nm). The macromolecular monomer components used to synthesize the hydrogel are readily synthesized in 1-2 steps in gram quantities and at high yields (¿95%) from commercially available precursors. The gel evolution and subsequent photodegradation properties are characterized by shear rheology and confocal microscopy and shown to behave in a predictable way based on step-growth network structure-property relationships (e.g., initial gel modulus) and fundamental photochemical reactions for the cleavage reaction. This predictable behavior and precise control of the initial hydrogel allows design of cell scaffolds with spatiotemporally tunable properties.

McKinnon et al.[81] previously synthesized an MMP-degradable PEG hydrogel system for the culture of embryonic stem cell-derived motor neurons (ESMNs) and identified chemical and physical signals that were critical to promoting long term ESMN survival and axon extension. While this synthetic method allowed facile introduction of multiple biofunctional cues and subsequent control of critical aspects of the cellular microenvironment, the materials render the experimenter a passive observer as the cells dictate and remodel the surrounding environment. Perhaps not surprisingly, axon outgrowth was observed to be isotropic, which then motivates the question as to how one might direct or guide this outgrowth in a spatially regulated manner. Gaining control over the course of motor axon extension using an accessible photodegradable hydrogel platform could allow fundamental and quantitative studies of the effect of neurotrophins and growth factors on these processes. Such informa-

tion may prove useful treating motor neuron injuries or treating neurodegenerative diseases, such amyotrophic lateral sclerosis (ALS), especially in the context of better understanding how to present cues that might guide neuromuscular junctions in vivo.20,21[30,39] Combining a dynamic, accessible hydrogel with embryonic stem cell-derived motor neurons provides a strong platform for further understanding motor axons extension on which to build future research.

8.3 Results & Discussion

4-arm 20 kDa PEG macromers were functionalized with dibenzylcyclooctyne (DBCO) moieties and 8-arm 40 kDa PEG macromers were functionalized with nitrobenzyl azide (NBA) moieties and dissolved into phosphate buffered saline (PBS) at 20 wt% (50 mM functional groups) to form stock solutions. As first reported by the Bertozzi Group,[240] DBCO reacts with NBA quickly and specifically via a strain promoted azide-alkyne cycloaddition (SPAAC), and mixing macromer solutions of 8-NBA and 4-DCBO under physiological conditions results in the formation of a hydrogel, abbreviated by 8-NBA:4-DBCO, with an equilibrium shear elastic modulus of 3600 ± 200 Pa (Figure 8.1). Furthermore, evolution of the network is rapid with a mean time of 240 ± 40 s to achieve 90% of the final modulus (Figure 8.1). While the gelation kinetics and final modulus are acceptable for the experiments discussed herein, both of these parameters can be easily tailored to the application at hand by varying the stoichiometry, molecular weight, or functionality of the initial PEG macromers. The results can be predicted using fundamental theories describing step-growth gelation.[157,231,241]

While SPAAC coupling between DBCO and NBA drives gel formation, the presence of NBA in the final network structure can serve as a photolabile linker, allowing externally directed degradation of the gel by exposure to UV single-photon or NIR two-photon irradiation. Upon absorption of a photon, the NBA cleaves between the nitrogen and the tertiary carbon through an intramolecular reaction into an amide-terminate fragment and an aldehyde ter-

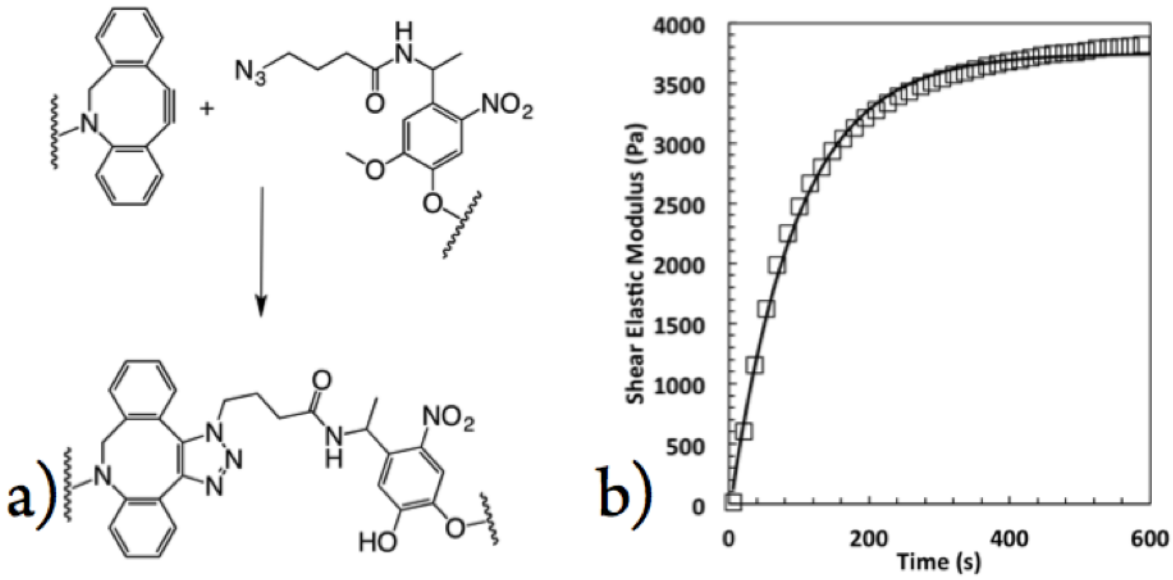

Figure 8.1: a) Chemical structures showing the formation of the triazole bond linking the PEG macromers driving the formation of the hydrogel. b) Evolution, left, of synthetically accessible click hydrogel (open squares) along with exponential fit (line). Gels reached 90% of their equilibrium moduli of 3600 ± 200 Pa after 240 ± 40 s.

minated fragment (Figure 8.2). An important difference between this material system and previously published studies[72,192] is that the nitrobenzyl ether group is linked to the PEG via an amide bond instead of an ester bond. The rationale for choosing the amide-linker is that the small molecule Fmoc-protected photolabile linker is commercially available, which is then readily coupled to PEG-NH_2 through standard peptide coupling conditions. This Fmoc-protected photolabile linker allows the synthesis of photodegradable macromers in 1-2 steps with ¿95% yield. However, the photocleavage properties of amide-linked NBA have not been previously studied and we hypothesized that its degradation properties may differ significantly from the ester-linked nitrobenzyl due to the dramatically different stabilities of ester and amide bonds.

Consistent with previously published degradation studies, hydrogels were formed *in situ* on a rheometer and exposed to varying intensities of UV light derived from a mercury arc lamp coupled to a 320 nm-390 nm bandpass filter. Hydrogel degradation was observed to be much slower than similar ester-linked nitrobenzyl hydrogels. Because hydrogel degradation is a first-order process, plots of decaying shear elastic modulus were fit to Equation 8.1 and 8.2,

$$G(t) = G_0 e^{-k_{app} t} \tag{8.1}$$

$$k_{app} = \frac{\phi \epsilon \lambda I_0 (2.303 \times 10^{-6})}{N_A h c} \tag{8.2}$$

where $G(t)$ is the shear elastic modulus as a function of time, G_0 is the initial shear elastic modulus, t is the time, ϕ is the quantum yield, ϵ is the absorbance, λ is the wavelength, I_0 is the incident light intensity, N_A is Avogadro's number, h is Planck's constant, and c is the speed of light. Hydrogels were exposed to 204 mW/cm^2, 154 mW/cm^2, and 102 mW/cm^2 UV irradiation for 1200 s and, as expected, rates of degradation increased with increasing light intensity. Interestingly, immediately upon exposure to light the hydrogel modulus noticeably

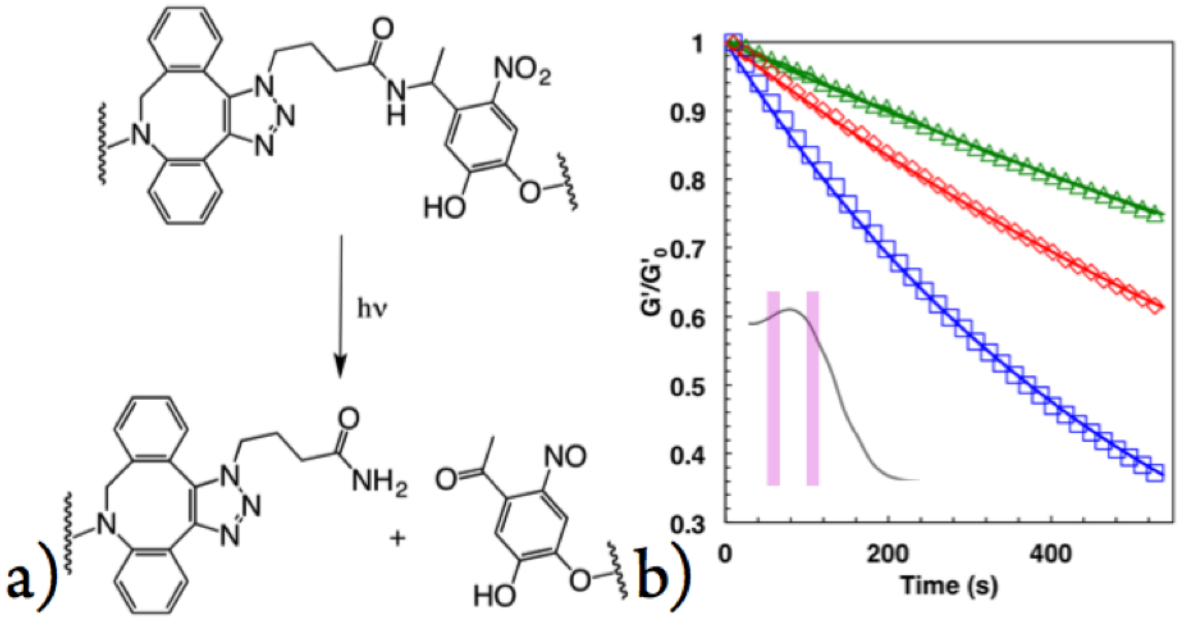

Figure 8.2: a) Chemical structures showing the degradation of the bond crosslinking the hydrogel network. Cleavage occurs between the tertiary carbon and the amide nitrogen in a radical-mediated mechanism. Degradation of the same hydrogels under 204 mW/cm^2 (blue), 154 mW/cm^2 (red), and 102 mW/cm^2 (green) UV irradiation (Mercury arc lamp with 320nm-390nm bandpass filter) along with first-order fits. The absorbance spectrum of the nitrobenzyl cleavable unit is shown inset along with the bands used for degradation (334 nm and 365 nm)

increased, a phenomenon previously observed by Kasko *et al.*[192] However, we eliminated this effect from our rheological traces and fit degradation to a first-order exponential decay model (Figure 8.2).

Upon fitting and analyzing the data, we observed much slower rates of degradation compared to previously published reported values for the ester-linked nitrobenzyl.[192] Apparent rates of degradation varied from 1.6 ± 0.2 x 10^{-3} s^{-1} under 204 mW/cm^2 irradiation to 0.5 ± 0.1 under 102 mW/cm^2. If photodegradation occurs in a thin film and follows a first order process, the apparent kinetic constant of cleavage normalized to the light intensity (k_{app}/I_0 x 10^4) for the amide linked NBA is simply 6.3 ± 1.4 cm^2 mW^{-1} s^{-1}. Note that this value is 5 times slower than kinetic of cleavage of the slowest nitrobenzyl group previously reported and 130 times slower than the fastest.[192]

We then sought to characterize the degradation properties of this material in response to two-photon light. Two-photon light has been used widely in the biomedical sciences due to its limited dispersion and biocompatibility. However, intense two-photon light has been shown to disrupt mitochondrial function,[242] damage the cytoskeleton,[243] and cleave axons.[244] Furthermore, some potential existed that the slow single-photon degradation characteristics would preclude two-photon degradation, due to the intensity of light required cavitating the hydrogel before degrading crosslinks, an effect that was previously observed at high pulse energies.[245] However, the two-photon response of an organic molecule is not necessarily correlated to its single photon response, a phenomenon that is abundantly clear when designing genetically encoded fluorescent proteins.[246]

In using two-photon degradation to introduce topographical features in 3D, we first wanted to ensure that the light dose required for degradation of the material would be within a range tolerated by encapsulated cells and not cause material cavitation before erosion of desired features. As ESMN embryoid bodies are generally between 100 and 500 μm in diameter, a 0.3 NA 10x water objective was selected to erode mesoscale features relevant to the length scales of axon extension. Since the focal volumes of lenses used for focusing

2-photon light are well understood, we estimated that the 10X water immersion lens with 740 nm light would have a focal volume of 2.5 μm^3, and at the maximum laser power of 279 mW, only 0.25 nJ/μm^3 is delivered per pulse. This is several orders of magnitude lower than doses known to damage cells in the literature.[242] For example, axotomy has been reported at 400 nJ/μm^3,[244] mitochondrial damage at 77 nJ/μm^3,[243] and the lowest threshold for cellular damage reported as 58 nJ/μm^3.[242]

Next, we sought to estimate the minimum time of irradiation to erode gel features as a function of the gel connectivity and exposure parameters. Specifically, the time for reverse gelation, t_c, was estimated as a function of the percolation threshold (p_c), the average power of irradiation (P_{avg}), the two-photon cross section of the nitrobenzyl unit ($\phi_u\delta_u$), the period of the laser pulses (T, 12.5 ns), the duration of the laser pulses (τ_p, 140 fs), the wavelength (λ, 740 nm), the focal area (ω_{xy}, 532 nm), and the focal volume (VF, 2.5 μm^3) (Equations 8.3 and 8.4). h and c are Planck's constant and the speed of light.

$$t_c = -\frac{\ln p_c}{\alpha P_{avg}^2} \tag{8.3}$$

$$\alpha = 1.17\phi_u\delta_u\frac{T}{\tau_p}\left(\frac{\lambda}{\pi hc\omega_{xy}^2}\right)^2 VF \tag{8.4}$$

Equations 8.3 and 8.4 define a curve combining photodegradation kinetics, two-photon physics, and statistical models of reverse gelation to define what combination of light intensity and exposure time will result in total material erosion.[245] Thus, the extent of photodegradation can be controlled by varying light exposure, connectivity of the hydrogel, objective lens, and quantum yield of photodegradable crosslinker. Given *ca.* 25% overlap in pixel size and the 8 μm z-resolution of the 0.3 NA 10x objective, the light exposure is effectively increased by a factor of 8 when eroding planes separated by 1 μm, which is a typical spacing used in these studies. With these assumptions and equations, we calculated expected critical exposure times for different laser powers using previously published quantum efficiencies of

a similar nitrobenzyl moiety (Figure 8.3).[12] Using these plots, we calculated the theoretical minimum power and exposure time required for complete gel degradation.

To test the validity of these estimates and their relevance to the experimental samples, wildtype ESMN embryoid bodies were encapsulated in gel formulations identical to those characterized on the rheometer (6.3 wt%, 8.3 mM functional groups) aside from the addition of 0.7 mM YIGSR adhesive peptide and 3 μm Alexa-594 to enable hydrogel visualization. The cell-laden gels were placed in motor neuron media and stained for markers of viability at 72 hours (Figure 8.4). Note, ESMNs lacking the Hb9::GFP transgene were used to avoid convolution with the viability staining and imaging. Since primary motor neurons are highly sensitive to oxidative damage,[20] it is important to note that the SPAAC crosslinking allows gelation in the presence of ESMNs and leads to high levels of cell survival (>95%). These results are very similar to our previously reported thiol-ene hydrogel system,[81] but in this case, we added an azide-terminated YIGSR peptide as an adhesive cue and also incorporated the photolabile linker to create topographical features for guidance of axon extension in 3D.

Next, ESMN embryoid bodies were encapsulated in the same hydrogel formulations, and ten 10 x 10 x 300 μm channels were eroded in proximity to the embryoid bodies, scanning each pixel 3.16 μs and using laser powers varying from 10-100%, corresponding to 15-110 mW/μm^3. Theoretically, the critical threshold for reverse gelation should be crossed at 40% laser power (50 mW/μm^3), if the quantum yield for the amide-linked nitrobenzyl crosslinker is similar to that of the ester-linked version.[12] Experimentally, axon extension was observed in channels created at only 20%, 28 mW/μm^3, laser power, indicating efficient two-photon degradation (Figure 8.5).

After experimentally confirming exposure conditions necessary to erode gel features and allow axon extension, the effects of channel dimensions on this extension were investigated. In contrast to literature reported of cell migration as a function of channel dimensions,[247,248] the speed and extent of axon outgrowth were found to be relatively independent of channel width, except when the channel dimensions (2 x 2 μm) approached those of extending axons

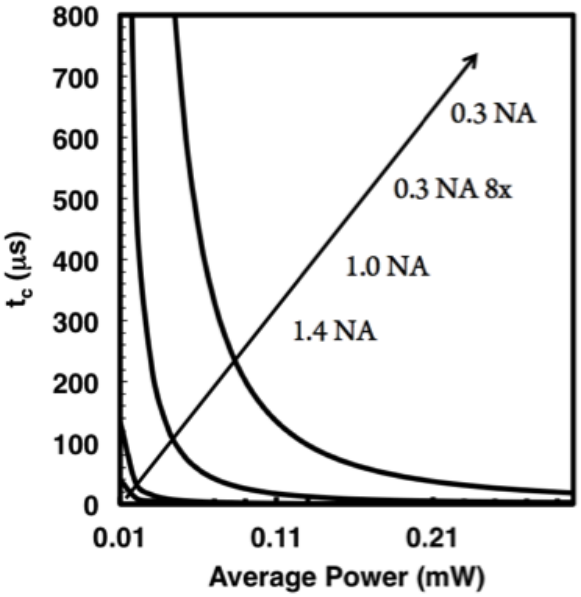

Figure 8.3: Theoretical plots of critical exposure time versus power with curves representing lenses of several common numerical apertures. The critical exposure time decreases dramatically for a given power as the numerical aperture increases.

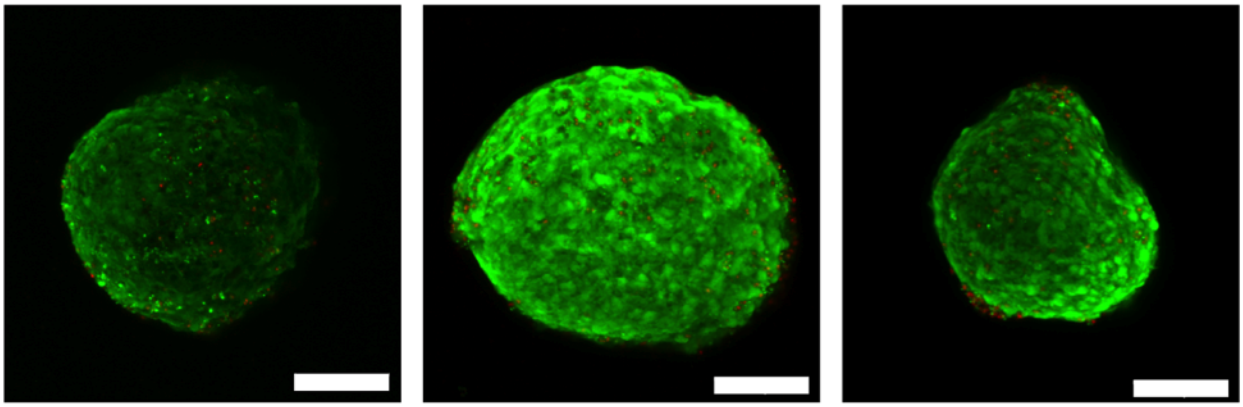

Figure 8.4: Images of ESMN embryoid bodies encapsulated in synthetically accessible photodegradable click hydrogel 72 hours after encapsulation. 6.3 wt% (8.3 mM functional groups) SPAAC crosslinked PEG gels were functionalized with 0.7 mM YIGSR peptide and 3 µm Alexa-594 to allow hydrogel visualization. Cells are stained with calcein (green) and ethidium homodimer (read) indicated live and dead cells, respectively. Cell viability is excellent in all cases, although difficult to quantify based on the tight packing of cells into embryoid bodies. Scale bar is 100 µm.

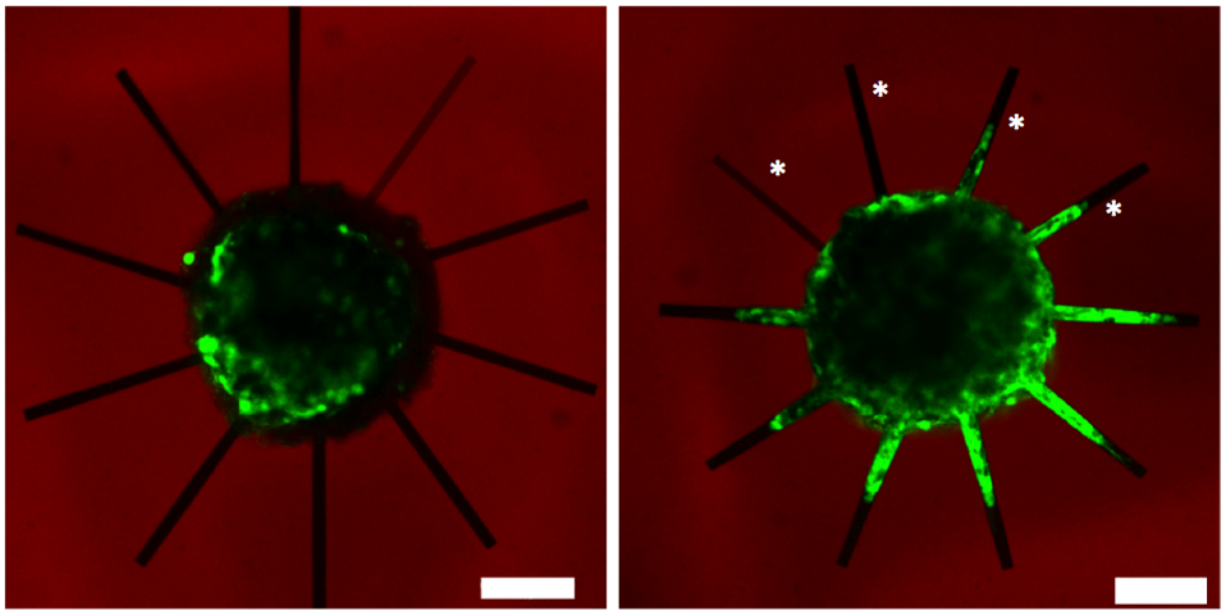

Figure 8.5: ESMN embryoid body encapsulated in the 6.3 wt% 8-NBA:4-DBCO hydrogel immediately after encapsulation and erosion of channels (left) and 48 hours after. Axons extend into channels that have been exposed to sufficient light to erode the material. Channels represent varying erosion where the exposure time was held constant at 3.16 μs and the power was varied from 15-110 mW/μm^3. These powers correspond to a t_c from 815-0.90 μs, based on a $\delta_u\phi_u$ value of 0.20 GM. Channels marked with an asterisks were exposed to light under conditions that do not theoretically lead to complete gel erosion, which is theoretically crossed at $<$ 63 mW/μm^{3}3 and the ray at 3 o'clock. In all of these conditions, axon growth is not observed. Because axons extend through channels exposed to 39 mW/μm^3, it is likely the quantum efficiency, $\delta_u\phi_u$, of the nitrobenzyl linker under study is actually higher than the previously reported value of a similar compound.[12] Scale bar is 100 μm.

(*ca.* 1 μm x 1 μm in cross section) where hindered outgrowth was observed (Figure 8.6).

After identifying conditions for channel erosion and physiologically relevant channel dimensions that promote axon extension, we next sought to conduct experiments to explore aspects of motor axon path-finding and decision-making. *In vivo*, motor axons must follow a complex array of signal gradients to reach their final synaptic destination. Numerous proteins implicated in this process have been identified, but few quantitative methods exist to explore their role *in vitro* or to study aspects of competing signals. Thus, to develop an *in vitro* model of this, we engineered a patterned hydrogel system to present extending axons with pathway options, specifically physical channels of varying orientation to the initial axon extension (Figure 8.7). In the absence of externally presented biochemical stimuli, motor axons prefer to extend in a persistent manner through channels that are in the direction of the extension (i.e., straight or at $\pm$ 45° to the this line). From this baseline characterization, experiments are currently underway to present gradients of attractive cues through unfavorable forks at 135° angles or repulsive cues through favorable forks. Through such experiments, we seek to quantification the relative role of biophysical versus biochemical signals on axon guidance with the goal of providing fundamental insight into competing and synergistic mechanisms of axon guidance.

The rationale of studying and manipulating axon guidance is to maintain functionality of neuromuscular junctions after traumatic injury or chronic disease. Towards the first step of a model *in vitro* system of physiological interest, we aimed to demonstrate the ability of photodegradable and patternable hydrogel systems to allow user-directed axon outgrowth -and formation of a simplified neural network. ESMNs have been shown to spontaneously form functional synapses with C2C12 myotubes *in vitro*,[47,48] so we sought to demonstrate matrix control over motor axon extension and assemble a neural circuit in this hydrogel. Specifically, C2C12 were differentiated myoblasts into myotubes using established literature techniques.[249,250] Briefly, myoblasts were allowed to become confluent and then switched to a low-serum media, which drives fusion and myotube formation. The resulting myotubes were

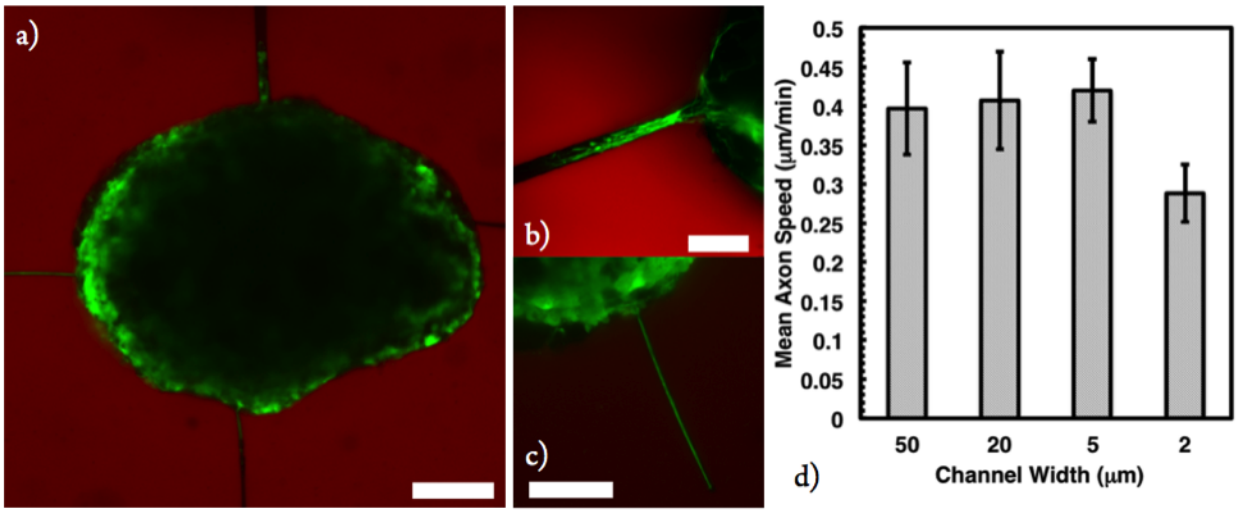

Figure 8.6: Square channels of 50 μm x 50 μm, 20 μm x 20 μm, 5 μm x 5 μm, and 2 μm x 2 μm cross sectional area were eroded proximal to encapsulated ESMN embryoid bodies in 6.3 wt% 8-NBA:4-DBCO hydrogels. Axon growth rates were then monitored using a real-time microscope. Axon extension rates were found to be independent of channel size, until the size of the channel cross-sectional area approached 2 μm, which is close to the size of the axon, and progress is physically impeded. a) ESMN embryoid body extending axons through channels of interest. b) Motor axons extending through a 20 μm x 20 μm channel. c) Motor axons extending through a 2 μm x 2 μm channel. Scale bar is 100 μm for a) and 50 μm for b) and c).

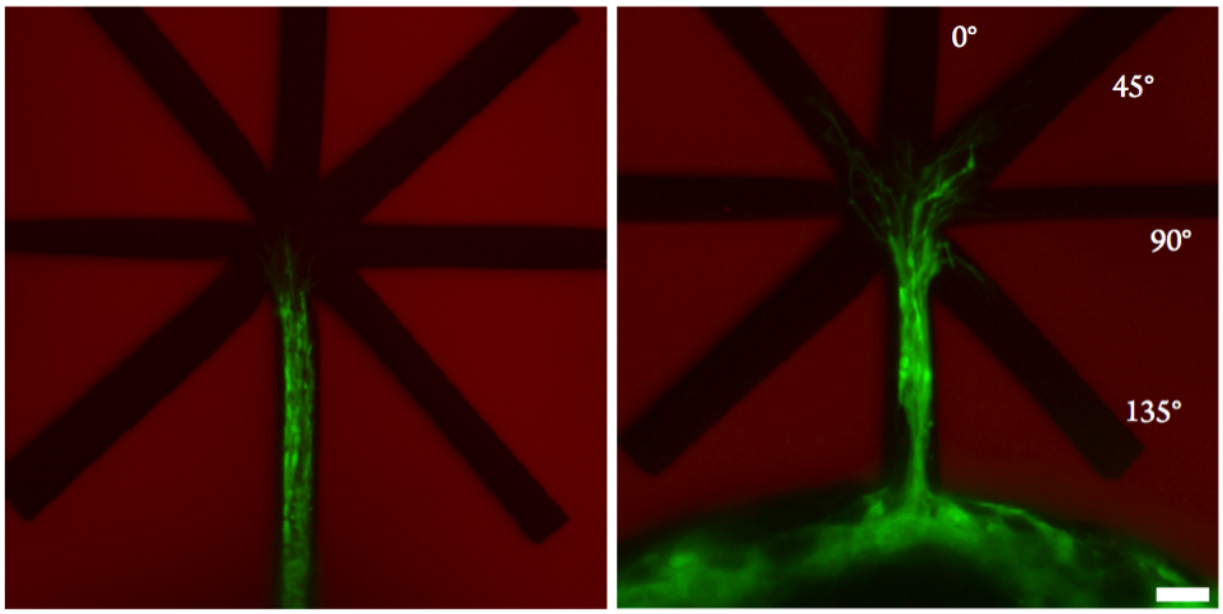

Figure 8.7: Fork-shaped patterns were eroded into the the 6.3 wt% 8-NBA:4-DBCO using 740 nm two-photon light providing extending motor axons with decisions regarding their direction of extension. The image on the left shows axons hours before reaching the fork and the image on the left shows axons shortly after selecting a direction. We observed that the vast majority of axons entered the 0° or ± 45° forks, indicating persistence in axon outgrowth when no external stimulus is applied. Scale bar is 10 μm.

then mechanically removed from culture plates through gentle scraping, forming myotube bundles that were roughly the same size as the ESMN embryoid bodies. These myotube bundles were then co-encapsulated with ESMN embryoid bodies at roughly one dozen aggregates per hydrogel. The gels were then imaged to identify spatial location of the two cell types, and then eroded via two-photon process to create channels connecting the two cell types. Images captured motor axon extension towards their synaptic targets within two days, as well as observation of synaptic markers between the two via staining with alpha bungarotoxin (Figure 8.8). Specially, significant axon branching and interrogation of the myotube surface were observed, and evidence of the formation of functional junctions was characterized by staining for acetylcholine receptor clustering using alpha-bungarotoxin.

8.4 Experimental

Macromer synthesis: Eight-arm 40 kDa PEG-nitrobenzyl-azide (8-NBA) macromers were synthesized by first coupling a Fmoc-photolabile linker (16.8 equivalents, Advanced ChemTech, RT1095) with 8-arm 40 kDa PEG-amine (1 equivalent, JenKem, A8012) using 1-[Bis(dimethylamino)methylene]-1H-1,2,3-triazolo[4,5-b]pyridinium 3-oxid hexafluorophosphate (HATU, ChemPep, 120801) (16 equivalents) as an activator and 4-methyl morpholine (32 equivalents, Aldrich, M56557) as a base. The reaction was allowed to proceed overnight, after which the product was precipitated in ice cold ether, collected via centrifugation, and dissolved in 80% DMF 20% piperidine to remove the Fmoc protecting group. After 4 hours of deprotection, the product was again precipitated in ice cold ether, dissolved in DMF, and coupled to azido butanoic acid (16.8 equivalents), which was synthesized as previously described,[71] again using HATU (16 equivalents) as an activator and 4-methyl morpholine at a base (32 equivalents). The final product was precipitated in diethyl ether for a third time, dissolved in a minimal volume of DI water, and dialyzed for 24 hours, after which it was lyophilized and used for experimentation.

Four-arm 20 kDa PEG-dibenzylcyclooctyne (4-DBCO) macromers were synthesized by

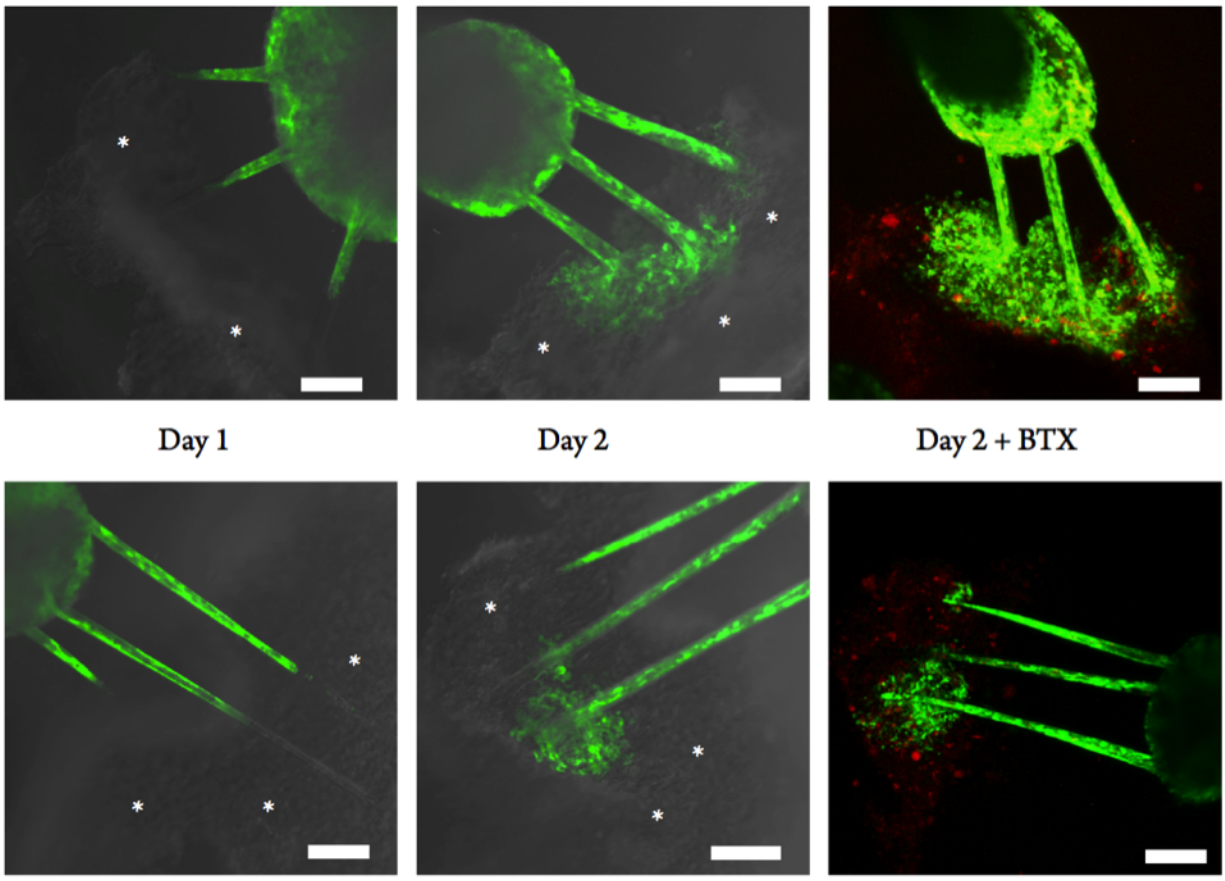

Figure 8.8: User-directed *in vitro* assembly of neural circuits. ESMN embryoid bodies expressing eGFP (green) were cultured with myotube bundles (grey, marked with asterisks) and connected using a 740 nm two-photon laser to erode 10 μm x 10 μm channels between the two cell types. Multiple channels were eroded to increase the chances of axons extending from the embryoid body to the myotube aggregate. Within two days, motor axons extended up to millimeters to reach the myotubes. Bungarotoxin stain (red) suggests the formation of functional synapses. Asterisks are added to mark the location of myotube bundles. Scale bar is 100 μm.

coupling 4-arm 20 kDa PEG-amine (1 equivalent, JenKem, A7026) with DBCO-acid (8.8 equivalents, Click Chemistry Tools, A101) using HATU (8 equivalents) as an activator and 4-methyl morpholine (18 equivalents) as a base. The product was precipitated in ice-cold diethyl ether, dissolved in DI water, dialyzed for 24 hours, lyophilized, and finally used for experimentation (Scheme 8.9).

Peptide synthesis: N_3-YIGSR and N_3-RGDS were synthesized on a Protein Technologies Tribute Peptide Synthesizer using standard Fmoc chemistry and Rink Amide MBHA resin. The final azide reside was incorporated onto the N-terminus by including azidobutanoic acid in the final cartridge. Peptide cleavage solution was prepared by dissolving 250 mg dithiothreitol (DTT) and 250 mg phenol in a solution of 95% trifluoroacetic acid (TFA), 2.5% triisopropylsilane (TIPS), and 2.5% deionized water. Synthesized peptides were cleaved in the solution for 2 hours. Cleaved peptides were precipitated in cold diethyl ether, recovered via centrifugation, desiccated overnight, and then purified by reverse-phase HPLC (Waters Delta Prep 4000) purification on a C_{18} column using a linear acetonitrile:water gradient. The collected fractions of purified peptides were identified by matrix-assisted laser desorption/ ionization-time-of-flight (MALDI-TOF) mass spectrometry.

Gel formation: The PEG macromers were dissolved in PBS to form 20 wt% (50 mM functional groups) stock solutions for the 4-DBCO and 8-NBA. Solutions were combined stoichiometrically at 6.7 wt% (8.3 mM functional groups) to form hydrogels (8-NBA:4-DBCO) *in situ* on a temperature-controlled Peltier plate set to 25 °C.

Rheology: Hydrogels were formed *in situ* by pipetting 12 μL monomer solutions (2 μL 4-DBCO, 2 μL 8-NBA, 8μL PBS) between the bottom quartz plate and a flat tool 8mm in diameter on a shear rheometer (TA DH-R3). This yielded a stoichiometrically balanced 6.7 wt% (8.3 mM functional group concentration) gel. The gap was closed to 100 μm and the experiments were commenced as quickly as possible, typically in less than one minute. Frequency and strain sweeps were performed to ensure measurements were made in the linear region. Experiments designed to monitor the hydrogel evolution and its subsequent

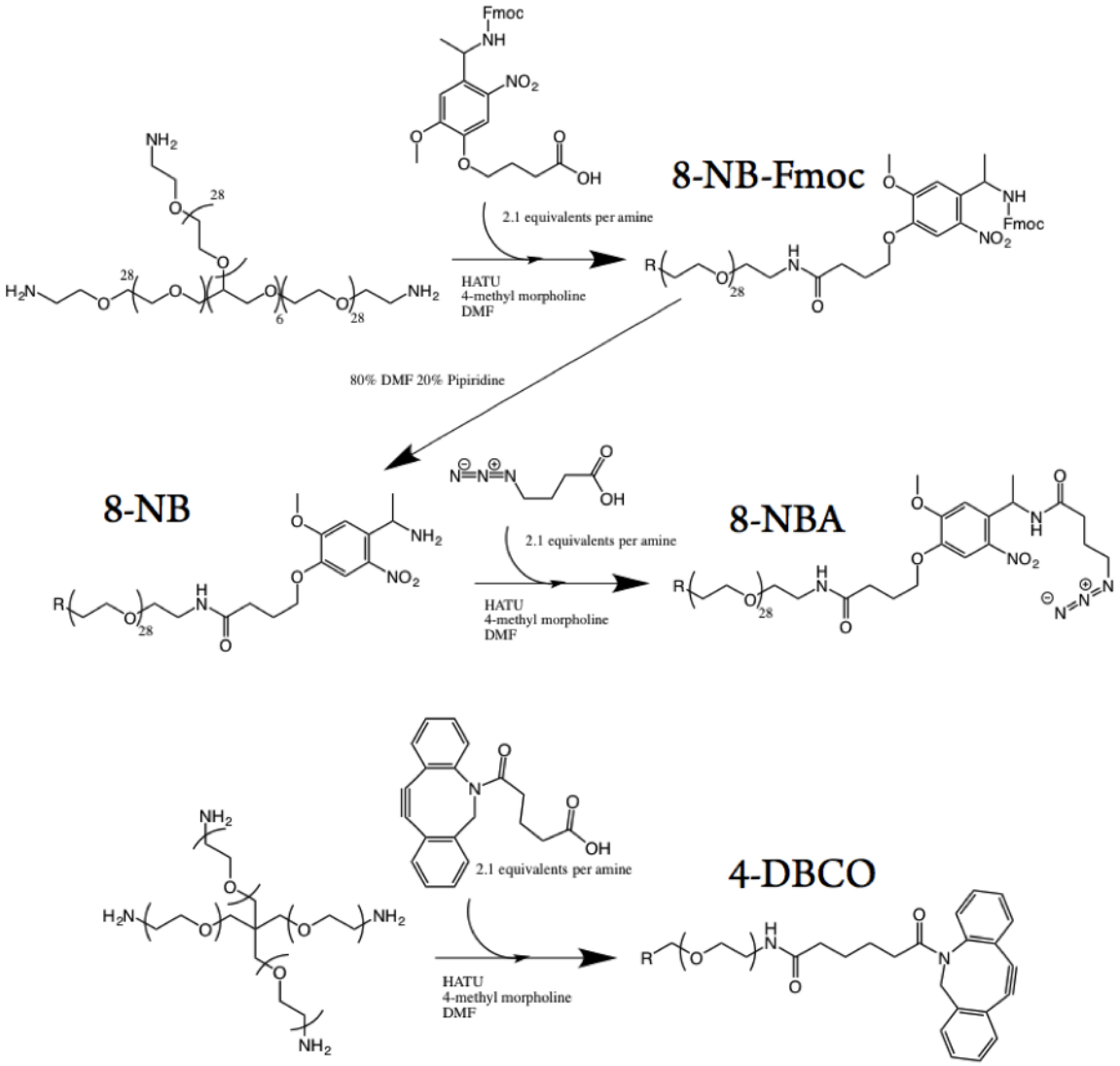

Figure 8.9: Facile, one or two step syntheses of starting materials for copper-free click chemistry crosslinked photodegradable hydrogels. 8-NBA is synthesized through coupling commmericially available Fmoc-protected photolabile group to 8-arm 40 kDa PEG-amine, deprotecting the Fmoc group with piperidine, and coupling azido butanoic acid. 4-DBCO is synthesized by simply coupling DBCO-acid to 4-arm 20 kDa PEG-amine.

photodegradation were performed at 1% strain and 1 rad/s, and frequency sweeps were performed at 1% strain. The light source used for the photodegradation experiments was an EXFO Actacure with a 320-390 nm filter in between the mercury lamp and the rheometer, allowing the 365 nm and 334 nm bands to erode the material. Light intensities between 102 and 204 mW/cm^2 were used and based on initial functional group concentrations, 40% of the light was attenuated through the hydrogel.

ES Cell Culture: ES cells were differentiated into spinal motor neurons as previously described.[2,51] Briefly, Hb9::GFP mouse embryonic stem cells were plated into ES cell medium (ES DMEM, ES FBS, glutamine, non-essential amino acids, nucleosides, 2-mercaptoethanol, LIF (Life Technologies)) at approximately 5 x 10^5 cells per gelatinized T25 flask. After 24 hours the media was replaced, and on day 2 of culture, ES cells were trypsinized and placed in suspension culture in motor neuron media (Advanced-DMEM/F12, Neurobasal, and Knockout Serum Replacement (Life Technologies)) at 5 x 10^5 cells per untreated 10 cm tissue culture dish. In suspension culture, the cells aggregated into embryoid bodies (EBs). Two days after initial seeding the EBs were split 1:4 and induced into motor neurons with 1 μM retinoic acid (RA) (Sigma) and smoothened agonist (SAG) (Millipore). After 3 days of exposure to RA and SAG, the EBs displayed strong expression of Hb9::GFP transgene.

Cell Encapsulation: Gels were prepared with a total volume of 30 μL from stock solutions of 4-DBCO (50 mM functional groups), 8-NBA (50 mM functional groups), N3-YIGSR (20 mM), N3-RGDS (20 mM), and N3-Alexa 594 (0.1 mM). 4-DBCO was pre-reacted for 5 minutes with peptides and dye to minimize cellular uptake of small molecules. Dozens of EBs were then gently mixed into the solution and 8-NBA was added. The solution was then quickly, but carefully, transferred into a mold 5 mm in diameter and 1.5 mm tall and allowed to polymerize for 5 minutes before transferring into motor neuron media.

Confocal Microscopy Imaging and Gel Degradation: Gels were placed between a glass slide and a coverslip separated by a rubber gasket and were imaged using a NA 0.3 10x water immersion objective on a Zeiss LSM 710 confocal microscope. Hydrogel features were

eroded using a 2-photon laser tuned to 740nm emitting a total averaged power of 300 mW. This power was achieved through a 1.58 μs scan speed. A 488nm laser was used to excite eGFP, calcein AM, and ethidium homodimer-1.

Axon growth videomicroscopy and tracking: Dynamic axon growth in photodegraded channels was observed using a Nikon TE 2000-E microscope with a Nikon environmental chamber, an external heater (InVivo Scientific), and a CO2 regulator (InVivo Scientific). Hydrogels were degraded as described previously, and imaged within a 24-well culture insert plate (BD Falcon, Fisher). The gels were held stationary by the addition of a modified transwell insert that lacked a bottom filter to allow for clear visualization of the axon growth. Immediately following photodegradation, images were taken at a 5 minute interval for 36 hours using Metamorph software for automated stage control, image collecting, and post-experiment axon tracking. Specifically, the axon growth cone was tracked from the initial distinction from the embryoid body until reaching the end of the channel. Axonal growth speed was then calculated from positional information over time.

C2C12 culture conditions: C2C12 mouse myoblasts were plated on TCPS and cultured in myoblast growth medium (high glucose DMEM with 20% FBS and P/S). When the cells reached confluency, the media was changed to differentiation medium (high glucose DMEM with 2% FBS and P/S) to induce myotube formation. After 7-10 days in differentiation medium, myoblast fusion and myotube alignment was observed.

Co-culture: Differentiated C2C12 myotubes were mechanically removed from TCPS, triturated until clusters were similar in size to EBs, and washed twice to remove single cells. Encapsulation was performed as before, except myotubes and EBs were encapsulated together in the same gel. The medium used for co-culture was motor neuron media supplemented with 10 ng/ml Glial Cell-Derived Neurotrophic Factor (GDNF).

Bungarotoxin staining: Once axons had reached the muscle cells and begun to innervate the cell mass, α-Bungarotoxin (α-BTX) conjugated with Alexa Fluor 594 was introduced to the culture media at 10 ng/ml and allowed to swell into the gel for 3 hours on a shaker.

The media was then replaced with PBS to allow excess α-BTX to diffuse out for 3 hours, changing the PBS each hour.

8.5 Conclusions

The synthesis and characterization of a photodegradable hydrogel formed through bioorthogonal click chemistries is reported. Gelation characteristics were characterized via rheological methods, and found to be appropriate primary ESMN cultures and to yield a wide range of properties for biomaterial applications. Cell-laden gels can be modified in real time and user defined time points by single and multi-photon degradation. While single photon degradation was significantly slower than previously reported systems two-photon degradation occurred at cytocompatible rates, namely conditions below the threshold exposure that can lead to possible cell damage or material cavitation. This hydrogel was then functionalized with laminin-derived peptide to enable the culture of ESMN embryoid bodies. These cells were shown to remain nearly 100% viable in the material and two-photon degradation was employed to gain control over their axon extension. Speed and degree of axon extension was observed to be independent of eroded-channel width and axons were observed to generally extend in a persistent manner. Finally, ESMNs and C2C12 myotubes were co-cultured in the gel and channels were eroded connecting aggregates of both cell types. Motor axons extended from the embryoid bodies to the myotube aggregates and branched over their surface. Strong, punctate alpha bungarotoxin staining indicated the formation of functional neuromuscular junctions. These results suggest that dynamic materials can be used to direct the formation of neural networks in vitro and should have broad implications in the biomaterials, neuroscience, and neural engineering communities.

Chapter 9

Conclusions & Future Directions

9.1 Thesis Conclusions

This thesis has demonstrated the importance in biochemical and biophysical signals on motor axon viability and extension while engineering and characterizing a cytocompatible covalently adaptable network worthy of further study. In Chapter 3, I showed that the integrating binding peptides RGDS and YIGSR, the cationic peptide CKKKKKKC, and the growth factor bFGF are essential to supporting the viability of dispersed motor neurons, but nonessential for those cultured in embryoid bodies, likely due to the presence of supportive neuroglial cells. Furthermore, I showed that axon extension was reliant on crosslinking the polymer network using the degradable peptide KCGPQG↓IWGQCK and that the mechanical properties of the gel can be using to either inhibit or promote axon extension.[81] However, because axon extension is enables in this system through local material degradation, it is likely that in these experiments the bulk modulus differed significantly from the pericellular modulus.[251] Because bulk rheological measurements were used to characterize gel properties, this system does not represent the most ideal way to study how cells respond to differing biophysical environments.

To improve upon this system, I developed a hydrogel crosslinked by reversible hydrazone bonds that allowed axon extension through yielding in response to stress rather than local degradation. I showed this material behaved as an ideal viscoelastic fluid and its properties could be modeled by existing polymer physics theories. C2C12 muscle cells were then

used to show the cytocompatibility of this hydrogel and we observed to spread in the material, demonstrating its ability to respond to biophysical stimuli.[81] These results are shown discussed in Chapter 4.

Next the material had to be optimized for motor neuron culture. Initial attempt to encapsulated motor neurons in the hydrazone crosslinked material resulted in nearly universal cell death the embryoid body-hydrogel interface. However, I reasoned that the toxicity was likely due to the presence of unreacted aliphatic aldehydes, which could be detrimental to protein function and result in cell death.[136,252] To test this hypothesis, I encapsulated motor neuron embryoid bodies in hydrogels formed with a 100% excess of hydrazine functionalities with respect to the aldehyde functionalities, thus decreasing the likelihood that a motor neuron would encounter a free aldehyde. This solution dramatically increased cell viability and axons were observed to extend through these gels. By tracking the position of the growth cone over time and applying some fundamental physics equations, I determined the both the forces the axons applied to the material and the energy expended in the process. This type of analysis should allow the measurement of essentially any type of cell force and the procedures are detailed in Chapter 5.

While characterizing the bis-aliphatic hydrazone crosslinked hydrogel for cell culture applications, we observed it had very unexpected properties with regards to its rapid evolution under physiological pH. Canonically, hydrazone bonds are acid catalyzed and should form extremely slowly at pH 7.4, which we observed with hydrazones formed from both aryl- and acyl-aldehyde partners. However, a hydrogel crosslinked with the bis-aliphatic hydrazone bond reaches is final modulus in minutes and relaxes stress on a similar time scale. Interestingly, this phenomenon has been only scarcely studied and virtually no literature exists on the subject. Given this gap in the literature, we sought to study both the formation of the bond and the behavior of the hydrogel in response to environments of different pH. We found that the kinetics of the small molecule reaction correspond very closely to those of hydrogel evolution and relaxation. As expected, hydrazone hydrolysis and hydrogel relax-

ation occurred most rapidly at acidic pH values, but surprisingly the rate of bond formation and hydrogel evolution was maximized at physiological pH. This finding is contrary to much of the established hydrazone literature and, in an attempt to uncover the mechanism, we investigated buffer catalysis, the hydration state of the aldehyde, and the possibility that the bis-aliphatic hydrazone forms through a separate mechanism. Unfortunately, all three of these pathways revealed a negative result and the mechanism behind these mysterious kinetics is still unknown.[174] These results are discussed further in Chapter 6.

Finally two photodegradable hydrogels were developed to enable the erosion of physical channels to direct motor axon extension. The first exploits a coumarin functionality to enable photodegradation. We show that gels formed through this chemistry degrade quickly in response to UV, visible, and long wavelength 2-photon irradiation and their behavior can be modeled through established theories of hydrogel erosion. These results are discussed in Chapter 7. Next, advances in commercially available molecular building blocks were exploited to develop a photodegradable synthetically tractable click hydrogel. The macromers from this hydrogel were available in gram scale after only three simple synthetic steps and the hydrogel was shown to behave predictably in response to one- and two-photon irradiation. The hydrogel was then functionalized with laminin-derived peptides to enable motor neurons to interact with its surface and, using calculated doses of two-photon light, channels were eroded in three dimensions. Motor neurons were shown to respond to channel width only in the case where the channel physically hindered axon extension and axon decision making was explored using forked paths. Finally, motor axons were directed toward co-encapsulated myotubes to form neural circuits between motor neurons and C2C12 myotubes. These results are discussed in Chapter 8.

While the origins in this thesis lie in developing synthetic hydrogels to study motor axon extension, the development of a hydrazone-crosslinked cytocompatible covalently adaptable network opened two distinct future directions.

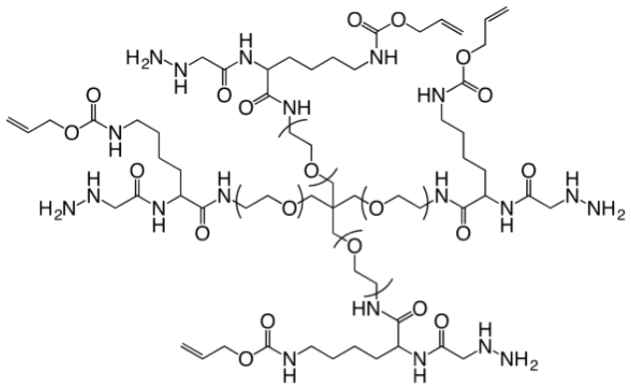

Figure 9.1: Chemical structure of 4-arm hydrazine-terminated PEG macromer functionalized with ene groups to enable thiol-ene photochemical patterning.

9.2 Investigating Fundamental Properties of Hydrazone Gels

9.2.1 Incorporate photo patterning in bis-aliphatic hydrazone crosslinked hydrogel

A core focus of the Anseth group lies in photochemical patterning.[97,106] Significant works exists showing the value of controlling material properties spatially and temporally with light.[71,132] If the dynamic properties of the hydrazone gel could be controlled spatially and temporally with light, valuable insights could be gained in exploring cellular response to viscoelastic environments. This material could be designed by simply incorporating a lysine-alloc amino acid into the macromer backbone, providing a free ene with which to perform photoinitiated thiol-ene reactions (Figure 9.1).

9.2.2 Incorporate cytocompatible catalysts to control material properties

While we showed control over material properties using pH and temperature, neither of these can be varied significantly in the presence of cells, limiting their use in biomaterials applications. However, researchers in the Kool group at Stanford have recently synthesized a whole suite of aniline-derivatives capable of catalyzing the formation and hydrolysis of hydrazone bonds.[207–209]Preliminary data show that anthranilic acid derivatives are well tolerated by both C2C12 and ES cells and could be used to dynamically change the stress

relaxation properties a hydrazone crosslinked hydrogel (Figure 9.2).

9.2.3 Investigate the origin of the kinetics of the bis-aliphatic bond

Upon discovering the unexpected rate of bond formation and its rate surprisingly maximized at physiological pH, we sought to mechanistically explain this behavior. Three obvious hypotheses exists in the possibility of buffer catalysis, the possibility of the hydration state of the aldehyde determining rate, and the possibility of the reaction proceeding by a totally different mechanisms. Each possibility was rigorously tested and disproved, although the reaction rate does vary slightly in different buffer concentrations, suggesting buffer catalysis plays a minor role. However, the bis-aliphatic hydrazone bond forms roughly three orders of magnitude faster than essentially any other hydrazone bond under physiological conditions. This rate is remarkable and more investigation into its mechanism would represent a valuable contribution to the hydrazone, bioconjugations, and materials communities.

9.2.4 Investigate effects of aryl, acyl, and aliphatic partners

Another unanswered question lies in characterizing the small molecule kinetics of all the main classes of hydrazone bonds. While many minor substituent modifications could be synthesized, hydrazines and aldehydes are readily commercially available in benzyl, acyl, and aliphatic forms. Each type of hydrazine could be coupled with each type of aldehyde to form nine different types of hydrazone bonds. To date, a rigorous investigation comparing the properties of these bonds is absent from the literature. The comparison made between the kinetic of formation of the bis-aliphatic and aliphatic-benzyl hydrazone discussed earlier in this thesis are actually counterintuitive from the standpoint of physical organic chemistry. One would expect a large electron-withdrawing group like a benzyl ring adjacent to the aldehyde would increase rather than decrease reaction rate. This effect could be explained away by stearic hindrance, but a more detailed investigation into the different types of hydrazone bonds is needed (Figure 9.3).

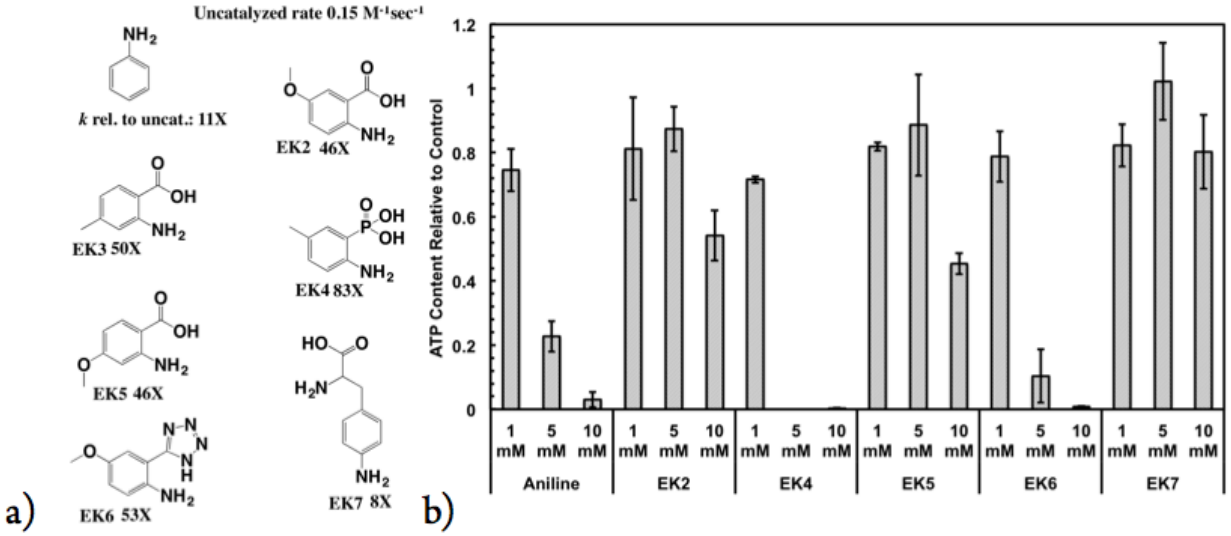

Figure 9.2: a) Structures of charged aniline-derivatives designed to increase cytocompatibility. b) ATP content of C2C12 cells exposed to varying concentrations of catalyst for 4 days. The anthranilic acid derivatives are both very effective at catalyzing the hydrazone reaction and very well tolerated by cells in culture.

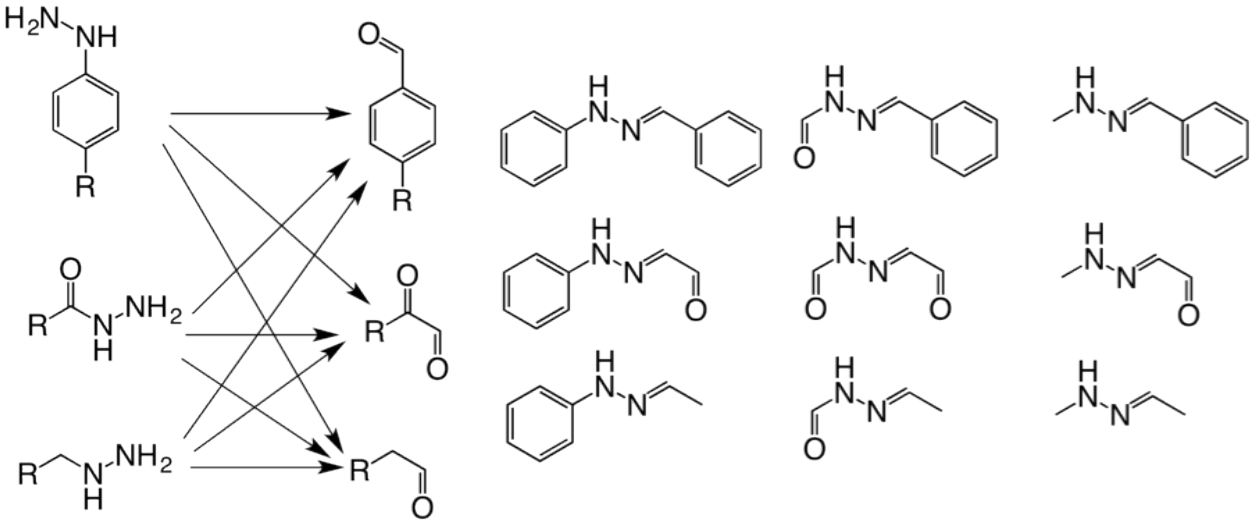

Figure 9.3: Three classes of hydrazines shown with three classes of aldehydes and the nine hydrazone bonds they form.

9.2.5 Accurately measure cellular forces

The basic ideas are explored in Chapter 5, but a well-defined stress relaxing hydrogel combined with fundamental mechanics equations could be used to measure nearly any dynamic cellular force. While the notion of force behind axon extension was discussed in detail, the hydrazone material could be used to measure forces of migration, spreading, division, and many other cellular phenomena. This technique could provide a complement and validation of existing techniques like traction force microscopy and enable many fundamental biophysical measurements.[177,181,184]

9.3 Exploring Motor Axon Behavior in Hydrogels

9.3.1 Present gradients of molecules forcing decision-making

The chemically and physically dynamic nature of synthetic hydrogels makes them excellent platforms for exploring cellular decision-making. A simple example of axons given a choice between fork tongs was discussed in Chapter 8, but this simple example could be coupled with dozens of different interesting tethered or soluble signals to investigate their effect on motor axon extension. For example, many genetic and other techniques have been used to elucidate the effect of many growth factors and neurotrophins, but little quantitative information is available about their relative strengths or effective concentrations.[37,40,253] The tight control over functionalization afforded by a synthetic hydrogel would enable the quantification of the effect of many signals on motor axon outgrowth, while currently only qualitative information is available (Figure 9.4).

9.3.2 Synergies in contact vs. chemical guidance

The guidance detailed in Chapter 8 is limited to contact guidance. Many experiments were attempted to encourage or discourage axon growth through channels, but speed and density of axon outgrowth remained amazingly constant. However, addition investigation

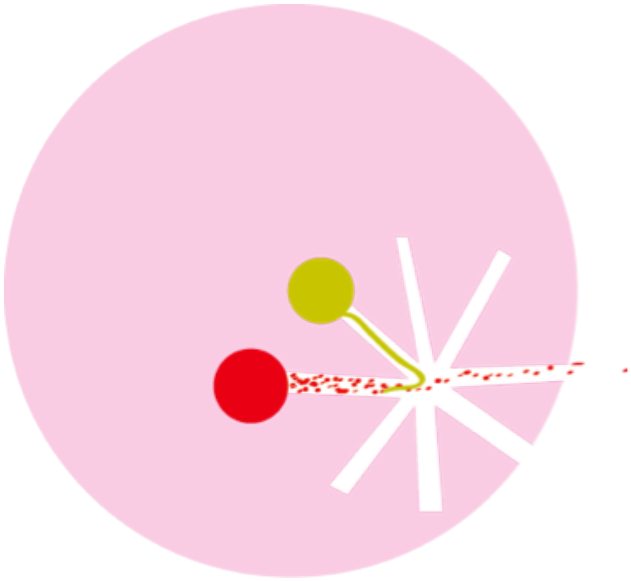

Figure 9.4: A fork degraded through the hydrogel allows chemoattractants to be released driving axons down an unfavorable path.

could determine synergies between contact and chemical guidance to develop next generation nerve guides.

9.3.3 Density of neuromuscular junctions

ESMNs implanted into the spinal cords of adult animals form an extremely low density of neuromuscular junctions. Thus, developing in vitro strategies to increase this density could lead to techniques to increase this density in vivo. Hydrogels encapsulating ESMN-myotube cocultures could be developed to investigate whether infusing the myotubes with bFGF, GDNF, and CNTF increased the density of enervation. These findings should prove valuable to both fundamental motor neuron biologists as little quantitative work exists in motor axon guidance and translational lab interested in cell transplantation strategies for the treatment of ALS.

9.3.4 Functional neural circuits

Finally, while preliminary evidence was shown in Chapter 8, the guided formation of a functional neural circuit in a hydrogel in three dimensions would represent a tremendous step forward in neural engineering. A motor neuron wired to a muscle cell that could be shown to contract upon stimulation of the neuron would open many research directions regarding ALS and many other neuromuscular diseases.

Bibliography

[1] Curt R Freed, Paul E Greene, Robert E Breeze, Wei-Yann Tsai, William DuMouchel, Richard Kao, Sandra Dillon, Howard Winfield, Sharon Culver, John Q Trojanowski, David Eidelberg, and Stanley Fahn. Transplantation of Embryonic Dopamine Neurons for Severe Parkinson's Disease. New England Journal of Medicine, 344(10):710–719, March 2001.

[2] H Wichterle, I Lieberam, JA Porter, and Thomas M Jessell. Directed Differentiation of Embryonic Stem Cells into Motor Neurons. Cell, 110:385–397, 2002.

[3] Peng Shi, Stephane Nedelec, Hynek Wichterle, and Lance C Kam. Combined microfluidics/protein patterning platform for pharmacological interrogation of axon pathfinding. Lab on a Chip, 10(8):1005–1010, 2010.

[4] MJ Mahoney and Kristi S Anseth. Three-dimensional growth and function of neural tissue in degradable polyethylene glycol hydrogels. Biomaterials, 27:2265–2274, 2006.

[5] Duncan Mortimer, Julia Feldner, Timothy Vaughan, Irina Vetter, Zac Pujic, William J Rosoff, Kevin Burrage, Peter Dayan, Linda J Richards, and Geoffrey J Goodhill. A Bayesian model predicts the response of axons to molecular gradients. Proceedings of the National Academy of Sciences, 106(25):10296–10301, 2009.

[6] Anja Kunze, Ana Valero, Dominique Zosso, and Philippe Renaud. Synergistic NGF/B27 Gradients Position Synapses Heterogeneously in 3D Micropatterned Neural Cultures. PLoS ONE, 6(10):e26187, October 2011.

[7] Ying Luo and Molly S Shoichet. A photolabile hydrogel for guided three-dimensional cell growth and migration. Nature Materials, 3(4):249–253, March 2004.

[8] Ryan G Wylie, Shoeb Ahsan, Yukie Aizawa, Karen L Maxwell, Cindi M Morshead, and Molly S Shoichet. Spatially controlled simultaneous patterning of multiple growth factors in three-dimensional hydrogels. Nature Materials, (10):799–806, August 2011.

[9] M H Longair, D A Baker, and J D Armstrong. Simple Neurite Tracer: open source software for reconstruction, visualization and analysis of neuronal processes. Bioinformatics, 27(17):2453–2454, August 2011.

[10] Anouk Dirksen, Sjoerd Dirksen, Tilman M Hackeng, and Philip E Dawson. Nucleophilic Catalysis of Hydrazone Formation and Transimination: Implications for Dynamic Covalent Chemistry. Journal of the American Chemical Society, 128(49):15602–15603, December 2006.

[11] Michael Rubinstein and Ralph H Colby. Polymer Physics. Oxford University Press, USA, 2003.

[12] Isabelle Aujard, Chouaha Benbrahim, Marine Gouget, Odile Ruel, Jean-Bernard Baudin, Pierre Neveu, and Ludovic Jullien. o-Nitrobenzyl Photolabile Protecting Groups with Red-Shifted Absorption: Syntheses and Uncaging Cross-Sections for One- and Two-Photon Excitation. Chemistry - A European Journal, 12(26):6865–6879, September 2006.

[13] Health, History, and Hard Choices: Funding Dilemmas in a Fast-Changing World . Technical report, June 2006.

[14] Tracy Kidder. Mountains Beyond Mountains: The Quest of Dr. Paul Farmer, a Man Who Would Cure Random House, September 2009.

[15] Gary Pisano. Science Business: The Promise, the Reality, and the Future of Biotech. Harvard Business School Press, November 2006.

[16] Is HIV Managable?

[17] Siddhartha Mukherjee. The Emperor of All Maladies: A Biography of Cancer. Scribner, August 2011.

[18] Nick Lane. Power, Sex, Suicide: Mitochondria and the Meaning of Life. Oxford University Press, USA, December 2006.

[19] Bayani Uttara, Ajay Singh, Paolo Zamboni, and R Mahajan. Oxidative Stress and Neurodegenerative Diseases: A Review of Upstream and Downstream Antioxidant Therapeutic Options. Current Neuropharmacology, 7(1):65–74, March 2009.

[20] G C Higgins, P M Beart, Y S Shin, and M J Chen. Oxidative Stress: Emerging Mitochondrial and Cellular Themes and Variations in Neuronal Injury. Journal of Alzheimer's Disease, 2010.

[21] C Warren Olanow, Ray L Watts, and William C Koller. An algorithm (decision tree) for the management of Parkinson's disease (2001):. Neurology, 2001.

[22] Krista L Lanctôt, Ryan D Rajaram, and Nathan Herrmann. Review: Therapy for Alzheimer's disease: how effective are current treatments? Therapeutic advances in Neurological Disorders, 163(2):163–180, 2009.

[23] John Dunlop, H Beal McIlvain, Yijin She, and David S Howland. Impaired Spinal Cord Glutamate Transport Capacity and Reduced Sensitivity to Riluzole in a Transgenic Superoxide Dismutase Mutant Rat Model of Amyotrophic Lateral Sclerosis. The Journal of Neuroscience, 23(5):1688–1696, 2003.

[24] Ettore Beghi, Adriano Chiò, Philippe Couratier, Jesùs Esteban, Orla Hardiman, Giancarlo Logroscino, Andrea Millul, Douglas Mitchell, Pierre-Marie Preux, Elisabetta Pupillo, Zorica Stevic, Robert Swingler, Bryan J Traynor, Leonard H Van den Berg, Jan H Veldink, and Stefano Zoccolella. The epidemiology and treatment of ALS: Focus on the heterogeneity of the disease and critical appraisal of therapeutic trials. Amyotrophic Lateral Sclerosis, 12(1):1–10, January 2011.

[25] Katrina Gwinn. Genetics and Parkinson's Disease: What Have We Learned.

[26] S Battistini, C Ricci, E M Lotti, M Benigni, S Gagliardi, R Zucco, M Bondavalli, N Marcello, M Ceroni, and C Cereda. Severe familial ALS with a novel exon 4 mutation (L106F) in the SOD1 gene. Journal of the neurological sciences, (293):112–115, 2010.

[27] C R Freed, R E Breeze, N L Rosenberg, S A Schneck, E Kriek, J X Qi, T Lone, Y B Zhang, J A Snyder, T H Wells, L O Ramig, L T Thompson, J C Mazziotta, Huang S C, S T Grafton, D Brooks, G Sawle, G Schroter, and A A Ansari. Survival of implanted fetal dopamine cells and neurologic improvement 12 to 46 months after transplantation for Parkinson's disease. New England Journal of Medicine, 327(22):1549–1555, 1992.

[28] C R Freed. Will embryonic stem cells be a useful source of dopamine neurons for transplant into patients with Parkinson's disease? Proceedings of the National Academy of Sciences, 99(4):1755–1757, February 2002.

[29] Wim Robberecht and Thomas Philips. The changing scene of amyotrophic lateral sclerosis. Nature Reviews Neuroscience, 14(4):248–264, March 2013.

[30] Benjamin Rix Brooks. Natural history of ALS. Neurology, 1996.

[31] Wolfram Schultz. Multiple Dopamine Functions at Different Time Courses. Annual Review of Neuroscience, 30:259–522, 2007.

[32] S J Chinta and J K Andersen. Dopaminergic neurons. The International Journal of Biochemistry & Cell Biology, 37:942–946, 2005.

[33] R V Routal and G P Pal. A study of motoneuron groups and motor columns of the human spinal cord. Journal of anatomy, 195(2):211–224, 1999.

[34] O de Lapeyrière and C E Henderson. Motoneuron differentiation, survival and synaptogenesis. Current Opinion in Genetics and Development, 7:642–650, 1997.

[35] Kevin C Kanning, A Kaplan, and Christopher E Henderson. Motor neuron diversity in development and disease. Annual Review of Neuroscience, 33:409–440, 2010.

[36] J L Elliott and W D Snider. Motor neuron growth factors. Neurology, 47(Issue 4, Supplement 2):47S–53S, October 1996.

[37] B J Dickson. Molecular Mechanisms of Axon Guidance. Science, 298(5600):1959–1964, December 2002.

[38] M Tessier-Lavigne and Corey S Goodman. The molecular biology of axon guidance. Science, 274(5290):1123–1133, 1996.

[39] Thomas M Jessell, Gülşen Sürmeli, and John S Kelly. Motor Neurons and the Sense of Place. Neuron, 72(3):419–424, November 2011.

[40] I Dudanova, G Gatto, and R Klein. GDNF Acts as a Chemoattractant to Support ephrinA-Induced Repulsion of Limb Motor Axons. Current Biology, 2010.

[41] VH Hopker, D Shewan, M Tessier-Lavigne, MM Poo, and C Holt. Growth-cone attraction to netrin-1 is converted to repulsion by laminin-1. Nature, 401(6748):69–73, 1999.

[42] A Varela-Echavarría, A Tucker, AW Püschel, and Sarah Guthrie. Motor Axon Subpopulations Respond Differentially to the Chemorepellents Netrin-1 and Semaphorin D. Neuron, 18:193–207, 1997.

[43] Gabriella L Boulting, Evangelos Kiskinis, Gist F Croft, Mackenzie W Amoroso, Derek H Oakley, Brian J Wainger, Damian J Williams, David J Kahler, Mariko Yamaki, Lance Davidow, Christopher T Rodolfa, John T Dimos, Shravani Mikkilineni, Amy B MacDermott, Clifford J Woolf, Christopher E Henderson, Hynek Wichterle, and Kevin Eggan. A functionally characterized test set of human induced pluripotent stem cells. Nature Biotechnology, 29(3):279–286, February 2011.

[44] EY Son, JK Ichida, BJ Wainger, JS Toma, Victor F Rafuse, Clifford J Woolf, and Kevin Eggan. Conversion of Mouse and Human Fibroblasts into Functional Spinal Motor Neurons. Cell stem cell, (9):205–218, 2011.

[45] K A Buytaert-Hoefen, Enrique Alvarez, and Curt R Freed. Generation of Tyrosine Hydroxylase Positive Neurons from Human Embryonic Stem Cells after Coculture with Cellular Substrates and Exposure to GDNF. Stem Cells, 22(5):669–674, September 2004.

[46] L M Bjorklund, R Sanchez-Pernaute, S Chung, T Andersson, I Y C Chen, K S P McNaught, A L Brownell, B G Jenkins, C Wahlestedt, K S Kim, and O Isacson. Embryonic stem cells develop into functional dopaminergic neurons after transplantation in a Parkinson rat model. Proceedings of the National Academy of Sciences, 99(4):2344–2349, January 2002.

[47] Joy A Umbach, Katrina L Adams, Cameron B Gundersen, and Bennett G Novitch. Functional Neuromuscular Junctions Formed by Embryonic Stem Cell-Derived Motor Neurons. PLoS ONE, 7(5):e36049, May 2012.

[48] G B Miles, Damien C Yohn, Hynek Wichterle, Thomas M Jessell, Victor F Rafuse, and Robert M Brownstone. Functional Properties of Motoneurons Derived from Mouse Embryonic Stem Cells. Journal of Neuroscience, 24(36):7848–7858, September 2004.

[49] Mirza Peljto, Jeremy S Dasen, Esteban O Mazzoni, Thomas M Jessell, and Hynek Wichterle. Functional Diversity of ESC-Derived Motor Neuron Subtypes Revealed through Intraspinal Transplantation. Cell stem cell, 7(3):355–366, September 2010.

[50] R Goland, H Wichterle, CE Henderson, and K Eggan. Induced Pluripotent Stem Cells Generated from Patients with ALS Can Be Differentiated into Motor Neurons. Science, 2008.

[51] Hynek Wichterle and M Peljto. Differentiation of mouse embryonic stem cells to spinal motor neurons. Current protocols in stem cell biology, 2008.

[52] Francesco Paolo Di Giorgio, GL Boulting, S Bobrowicz, and KC Eggan. Human Embryonic Stem Cell-Derived Motor Neurons Are Sensitive to the Toxic Effect of Glial Cells Carrying an ALS-Causing Mutation. Cell stem cell, 3:637–648, 2008.

[53] Neeta Singh Roy, Takahiro Nakano, Li Xuing, Jian Kang, Maiken Nedergaard, and Steven A Goldman. Enhancer-specified GFP-based FACS purification of human spinal motor neurons from embryonic stem cells. Experimental Neurology, 196(2):224–234, December 2005.

[54] Saravanan Karumbayaram, Bennett G Novitch, Michaela Patterson, Joy A Umbach, Laura Richter, Anne Lindgren, Anne E Conway, Amander T Clark, Steve A Goldman, Kathrin Plath, Martina Wiedau-pazos, Harley I Kornblum, and William E Lowry. Directed Differentiation of Human-Induced Pluripotent Stem Cells Generates Active Motor Neurons. Stem Cells, 27(4):806–811, April 2009.

[55] Kevin Eggan Evangelos Kiskinis. Progress toward the clinical application of patient-specific pluripotent stem cells. The Journal of Clinical Investigation, 120(1):51, January 2010.

[56] J M Harper, Chitra Krishnan, Jessica S Darman, DM Deshpande, Schonze Peck, Irina Shats, Stephanie Backovic, JD Rothstein, and Douglas A Kerr. Axonal growth of embryonic stem cell-derived motoneurons in vitro and in motoneuron-injured adult rats. Proceedings of the National Academy of Sciences, 101(18):7123–7128, April 2004.

[57] DM Deshpande, YS Kim, T Martinez, Jessica Carmen, Sonny Dike, Irina Shats, Lee L Rubin, Jennifer Drummond, Chitra Krishnan, Ahmet Hoke, Nicholas Maragakis, Jeremy Shefner, JD Rothstein, and Douglas A Kerr. Recovery from paralysis in adult rats using embryonic stem cells. Annals of Neurology, 60:32–44, 2006.

[58] Ronald W Oppenheim, Lucien J Houenou, James E Johnson, Leu-Fen H Lin, Linxi Li, Albert C Lo, Ann L Newsome, David M Prevette, and Siwei Wang. Developing motor neurons rescued from programmed and axotomy-induced cell death by GDNF. Nature, 373(6512):344–346, January 1995.

[59] Robert H Baloh, Hideki Enomoto, Eugene M Johnson Jr, and Jeffrey Milbrandt. The GDNF family ligands and receptors — implications for neural development. Current opinion in neurobiology, 10(1):103–110, February 2000.

[60] Qiao Yan, Christine Matheson, and Oscar T Lopez. In vivo neurotrophic effects of GDNF on neonatal and adult facial motor neurons. Nature, 373(6512):341–344, January 1995.

[61] R W Chen, A J Williams, Z Liao, C Yao, and F C Tortella. Broad spectrum neuroprotection profile of phosphodiesterase inhibitors as related to modulation of cell-cycle elements and caspase-3 activation. Neuroscience Letters, 418:165–169, 2007.

[62] Stephane Nedelec, Mirza Peljto, Peng Shi, Mackenzie W Amoroso, Lance C Kam, and Hynek Wichterle. Concentration-Dependent Requirement for Local Protein Synthesis in Motor Neuron Subtype-Specific Response to Axon Guidance Cues. Journal of Neuroscience, 32(4):1496–1506, January 2012.

[63] A Kunze, M Giugliano, A Valero, and Philippe Renaud. Micropatterning neural cell cultures in 3D with a multi-layered scaffold. Biomaterials, 32:2088–2098, 2011.

[64] D Mortimer, Z Pujic, T Vaughan, A W Thompson, J Feldner, I Vetter, and G J Goodhill. Axon guidance by growth-rate modulation. Proceedings of the National Academy of Sciences, 107(11):5202–5207, March 2010.

[65] B V Slaughter, S S Khurshid, O Z Fisher, Ali Khademhosseini, and Nicholas A Peppas. Hydrogels in Regenerative Medicine. Advanced Materials, 21:3307–3329, 2009.

[66] Mark W Tibbitt and Kristi S Anseth. Hydrogels as extracellular matrix mimics for 3D cell culture. Biotechnology and Bioengineering, 103(4):655–663, July 2009.

[67] Joshua D McCall, Jacob E Luoma, and Kristi S Anseth. Covalently tethered transforming growth factor beta in PEG hydrogels promotes chondrogenic differentiation of encapsulated human mesenchymal stem cells. Drug Delivery and Translational Research, 2(5):305–312, September 2012.

[68] Chun Yang, Mark W Tibbitt, Lena Basta, and Kristi S Anseth. Mechanical memory and dosing influence stem cell fate. Nature Materials, March 2014.

[69] Mark W Tibbitt and Kristi S Anseth. Dynamic Microenvironments: The Fourth Dimension. Science Translational Medicine, 4(160):1–4, November 2012.

[70] CA DeForest and Kristi S Anseth. Photoreversible Patterning of Biomolecules within Click-Based Hydrogels. Angew Chemie, 124:1852–1855, 2012.

[71] C.A. DeForest and K.S. Anseth. Cytocompatible click-based hydrogels with dynamically tunable properties through orthogonal photoconjugation and photocleavage reactions. Nature Chemistry, 3(12):925–931, 2011.

[72] April M. Kloxin, Andrea M. Kasko, Chelsea N. Salinas, and Kristi S Anseth. Photodegradable Hydrogels for Dynamic Tuning of Physical and Chemical Properties. Science, 324(5923):59–63, 2009.

[73] Stephanie J Bryant and Kristi S Anseth. Hydrogel properties influence ECM production by chondrocytes photoencapsulated in poly(ethylene glycol) hydrogels. Journal of Biomedical Materials Research Part A, 59(1):63–72, October 2001.

[74] Stephanie J Bryant and Kristi S Anseth. Controlling the spatial distribution of ECM components in degradable PEG hydrogels for tissue engineering cartilage. Journal of Biomedical Materials Research Part A, 64A(1):70–79, December 2002.

[75] Stephanie J Bryant, Kevin L Durand, and Kristi S Anseth. Manipulations in hydrogel chemistry control photoencapsulated chondrocyte behavior and their extracellular matrix production. Journal of Biomedical Materials Research Part A, 67A(4):1430–1436, November 2003.

[76] Michael D Pierschbacher and Erkki Ruoslahti. Cell attachment activity of fibronectin can be duplicated by small synthetic fragments of the molecule. Nature, 309(5963):30–33, May 1984.

[77] Jason A Burdick and Kristi S Anseth. Photoencapsulation of osteoblasts in injectable RGD-modified PEG hydrogels for bone tissue engineering. Biomaterials, 23(22):4315–4323, November 2002.

[78] Mirza Peljto and Hynek Wichterle. Programming embryonic stem cells to neuronal subtypes. Current opinion in neurobiology, 21:43–51, 2011.

[79] L Luckenbill-Edds. Laminin and the mechanism of neuronal outgrowth. Brain Research Reviews, 1997.

[80] Millet LJ and Gillette MU. Over a Century of Neuron Culture: From the Hanging Drop to Microfluidic Devices. The Yale Journal of Biology and Medicine, 85(4):501–521, December 2012.

[81] Daniel D McKinnon, April M. Kloxin, and Kristi S Anseth. Synthetic hydrogel platform for three-dimensional culture of embryonic stem cell-derived motor neurons. Biomaterials Science, 1(5):460–469, 2013.

[82] Daniel D McKinnon, Dylan W Domaille, Jennifer N Cha, and Kristi S Anseth. Biophysically Defined and Cytocompatible Covalently Adaptable Networks as Viscoelastic 3D Cell Culture Systems. Advanced Materials, 26(6):865–872, October 2013.

[83] Cole A DeForest and Kristi S Anseth. Advances in Bioactive Hydrogels to Probe and Direct Cell Fate. Annual Review of Chemical and Biomolecular Engineering, 3(1):421–444, July 2012.

[84] Chelsea M Kirschner and Kristi S Anseth. Hydrogels in healthcare: From static to dynamic material microenvironments. Acta Materialia, 61(3):931–944, February 2013.

[85] Santiago Ramon Cajal. Texture of the Nervous System of Man and the Vertebrates, 1999.

[86] Lisa A Flanagan, Yo-El Ju, Beatrice Marg, Miriam Osterfield, and Paul A Janmey. Neurite branching on deformable substrates. Neuroreport, 13(18):2411–2415, December 2002.

[87] C Manitt, MA Colicos, KM Thompson, E Rousselle, AC Peterson, and TE Kennedy. Widespread expression of netrin-1 by neurons and oligodendrocytes in the adult mammalian spinal cord. Journal of Neuroscience, 21(11):3911–3922, 2001.

[88] G A Silva, C Czeisler, K L Niece, E Beniash, and Samuel I Stupp. Selective Differentiation of Neural Progenitor Cells by High-Epitope Density Nanofibers. Science, 303:1352–1355, 2004.

[89] C T S Wong Po Foo, J S Lee, W Mulyasasmita, A Parisi-Amon, and S.C Heilshorn. Two-component protein-engineered physical hydrogels for cell encapsulation. Proceedings of the National Academy of Sciences, 106(52):22067–22072, December 2009.

[90] SK Seidlits, ZZ Khaing, RR Petersen, JD Nickels, Jennifer E Vanscoy, Jason B Shear, and Christine E Schmidt. The effects of hyaluronic acid hydrogels with tunable mechanical properties on neural progenitor cell differentiation. Biomaterials, 31:3930–3940, 2010.

[91] Jeremy S Dasen, Alessandro De Camilli, Bin Wang, Philip W Tucker, and Thomas M Jessell. Hox Repertoires for Motor Neuron Diversity and Connectivity Gated by a Single Accessory Factor, FoxP1. Cell, 134(2):304–316, July 2008.

[92] Christopher E Henderson, William Camu, Clément Mettling, Annie Gouin, Kristian Poulsen, Mona Karihaloo, Janette Ruilamas, Tony Evans, Stephen B McMahon, Mark P Armanini, Lucy Berkemeier, Heidi S Phillips, and Arnon Rosenthal. Neurotrophins promote motor neuron survival and are present in embryonic limb bud. Nature, 363(6426):266–270, May 1993.

[93] Brenda K Mann, Andrea S Gobin, Annabel T Tsai, Rachael H Schmedlen, and Jennifer L West. Smooth muscle cell growth in photopolymerized hydrogels with cell adhesive and proteolytically degradable domains: synthetic ECM analogs for tissue engineering. Biomaterials, 22(22):3045–3051, November 2001.

[94] Stephanie J Bryant, Charles R Nuttelman, and Kristi S Anseth. Cytocompatibility of UV and visible light photoinitiating systems on cultured NIH/3T3 fibroblasts in vitro. Journal of Biomaterials Science, Polymer Edition, 11(5):439–457, January 2000.

[95] C R Nuttelman, M C Tripodi, and K.S. Anseth. Synthetic hydrogel niches that promote hMSC viability. Matrix Biology, 24:208–218, 2005.

[96] S B Anderson, C C Lin, D V Kuntzler, and K.S. Anseth. The performance of human mesenchymal stem cells encapsulated in cell-degradable polymer-peptide hydrogels. Biomaterials, (32):3564–3574, 2011.

[97] Benjamin D Fairbanks, Michael P Schwartz, Alexandra E Halevi, Charles R Nuttelman, Christopher N Bowman, and Kristi S Anseth. A Versatile Synthetic Extracellular Matrix Mimic via Thiol-Norbornene Photopolymerization. Advanced Materials, 21(48):5005–5010, December 2009.

[98] Charles E Hoyle and Christopher N Bowman. Thiol-Ene Click Chemistry. Angewandte Chemie International Edition, 49(9):1540–1573, February 2010.

[99] Benjamin D Fairbanks, Michael P Schwartz, Christopher N Bowman, and Kristi S Anseth. Photoinitiated polymerization of PEG-diacrylate with lithium phenyl-2,4,6-trimethylbenzoylphosphinate: polymerization rate and cytocompatibility. Biomaterials, 30:6702–6707, 2009.

[100] CC Lin, A Raza, and Han Shih. PEG hydrogels formed by thiol-ene photo-click chemistry and their effect on the formation and recovery of insulin-secreting cell spheroids. Biomaterials, 32:9685–9695, 2011.

[101] Joshua D McCall and Kristi S Anseth. Thiol–Ene Photopolymerizations Provide a Facile Method To Encapsulate Proteins and Maintain Their Bioactivity. Biomacromolecules, 13(8):2410–2417, July 2012.

[102] Michael Malkoch, Robert Vestberg, Nalini Gupta, Laetitia Mespouille, Philipe Dubois, Andrew F Mason, James L Hedrick, Qi Liao, Curtis W Frank, Kevin Kingsbury, and Craig J Hawker. Synthesis of well-defined hydrogel networks using Click chemistry. Chemical Communications, (26):2774–2776, 2006.

[103] Takamasa Sakai, Takuro Matsunaga, Yuji Yamamoto, Chika Ito, Ryo Yoshida, Shigeki Suzuki, Nobuo Sasaki, Mitsuhiro Shibayama, and Ung-il Chung. Design and fabrication of a high-strength hydrogel with ideally homogeneous network structure from tetrahedron-like macromonomers. Macromolecules, 41(14):5379–5384, 2008.

[104] Takuro Matsunaga, Takamasa Sakai, Yuki Akagi, Ung-il Chung, and Mitsuhiro Shibayama. Structure Characterization of Tetra-PEG Gel by Small-Angle Neutron Scattering. Macromolecules, 42(4):1344–1351, February 2009.

[105] Cole A DeForest, Brian D Polizzotti, and Kristi S Anseth. Sequential click reactions for synthesizing and patterning three-dimensional cell microenvironments. Nature Materials, 8(8):659–664, June 2009.

[106] Brian D Polizzotti, Benjiman D Fairbanks, and Kristi S Anseth. Three-Dimensional Biochemical Patterning of Click-Based Composite Hydrogels via Thiolene Photopolymerization. Biomacromolecules, 9(4):1084–1087, April 2008.

[107] Thomas C Doetschman, Harald Eistetter, Margot Katz, Werner Schmidt, and Rolf Kemler. The in vitro development of blastocyst-derived embryonic stem cell lines: formation of visceral yolk sac, blood islands and myocardium. Journal of Embryology and Experimental Morphology, (87):27–45, 1985.

[108] Mahrokh Dadsetan, Andrew M Knight, Lichun Lu, Anthony J Windebank, and Michael J Yaszemski. Stimulation of neurite outgrowth using positively charged hydrogels. Biomaterials, 30(23-24):3874–3881, August 2009.

[109] Ji Hoon Jeong and Tae Gwan Park. Poly(l-lysine)-g-poly(d,l-lactic-co-glycolic acid) micelles for low cytotoxic biodegradable gene delivery carriers. Journal of controlled release, 82:159–166, 2002.

[110] Ken-ichiro Tashiro, Gregory C Sephel, Benjamin Weeks, Makoto Sasaki, George R Martin, Hynda K Kleinman, and Yoshihiko Yamada. A Synthetic Peptide Containing the Ikvav Sequence From the a-Chain of Laminin Mediates Cell Attachment, Migration, and Neurite Outgrowth. Journal of Biological Chemistry, 264(27):16174–16182, 1989.

[111] S A Thompson. The disulfide structure of bovine pituitary basic fibroblast growth factor. Journal of Biological Chemistry, 267(4):2269–2273, 1992.

[112] Richard A Hughes, Michael Sendtner, Mitchell Goldfarb, Dan Lindholm, and Hans Thoenen. Evidence that fibroblast growth factor 5 is a major muscle-derived survival factor for cultured spinal motoneurons. Neuron, 10(3):369–377, March 1993.

[113] M P Lutolf and J A Hubbell. Synthesis and Physicochemical Characterization of End-Linked Poly(ethylene glycol)- co-peptide Hydrogels Formed by Michael-Type Addition. Biomacromolecules, 4(3):713–722, May 2003.

[114] P Vanderhaeghen and H J Cheng. Guidance Molecules in Axon Pruning and Cell Death. Cold Spring Harbor Perspectives in Biology, 2(6):a001859–a001859, June 2010.

[115] Ferdinand Brandl, Fritz Kastner, Ruth M Gschwind, Torsten Blunk, Jörg Teßmar, and Achim Göpferich. Hydrogel-based drug delivery systems: Comparison of drug diffusivity and release kinetics. Journal of controlled release, 142(2):221–228, March 2010.

[116] Crystal M. Miller, Andrea Page-McCaw, and Heather T. Broihier. Matrix metalloproteinases promote motor axon fasciculation in the Drosophila embryo. Development, 135(1):95–109, 2008.

[117] Jean Livet, Markus Sigrist, Simon Stroebel, Vincenzo De Paola, Stephen R Price, Christopher E Henderson, Thomas M Jessell, and Silvia Arber. ETS Gene Pea3 Controls the Central Position and Terminal Arborization of Specific Motor Neuron Pools. Neuron, 35(5):877–892, August 2002.

[118] YB Lu, K Franze, G Seifert, Christian Steinhauser, Frank Kirchhoff, Hartwig Wolburg, Jochen Guck, Paul A Janmey, Er-Qing Wei, Josef Kas, and Andreas Reichenbach. Viscoelastic properties of individual glial cells and neurons in the CNS. In Proceedings of the National Academy of Sciences, pages 17759–17764, 2006.

[119] Paul J Flory. Constitution of three-dimensional polymers and the theory of gelation. Journal of Physical Chemistry, 46(1):132–140, 1942.

[120] F Braet, R De Zanger, and E Wisse. Drying cells for SEM, AFM and TEM by hexamethyldisilazane: a study on hepatic endothelial cells. Journal of Microscopy, 186(1):84–87, April 1997.

[121] Jeanie L Drury and David J Mooney. Hydrogels for tissue engineering: scaffold design variables and applications. Biomaterials, 24(24):4337–4351, November 2003.

[122] Orane Guillame-Gentil, Oleg Semenov, Ana Sala Roca, Thomas Groth, Raphael Zahn, Janos Vörös, and Marcy Zenobi-Wong. Engineering the Extracellular Environment: Strategies for Building 2D and 3D Cellular Structures. Advanced Materials, 22(48):5443–5462, September 2010.

[123] M P Lutolf, J L Lauer-Fields, H G Schmoekel, Andrew T Metters, F E Weber, G B Fields, and Jeffrey A Hubbell. Synthetic matrix metalloproteinase-sensitive hydrogels for the conduction of tissue regeneration: Engineering cell-invasion characteristics. Proceedings of the National Academy of Sciences, 100(9):5413–5418, April 2003.

[124] JA Benton, BD Fairbanks, and Kristi S Anseth. Characterization of valvular interstitial cell function in three dimensional matrix metalloproteinase degradable PEG hydrogels. Biomaterials, 30:6593–6603, 2009.

[125] Kyle A Kyburz and Kristi S Anseth. Three-dimensional hMSC motility within peptide-functionalized PEG-based hydrogels of varying adhesivity and crosslinking density. Acta Biomaterialia, January 2013.

[126] M P Schwartz, B D Fairbanks, R E Rogers, R Rangarajan, M H Zaman, and K.S. Anseth. A synthetic strategy for mimicking the extracellular matrix provides new insight about tumor cell migration. Integr Biol, 2010.

[127] JA Shepard, AC Stevans, S Holland, Christine E Wang, Ariella Shikanov, and Lonnie D Shea. Hydrogel design for supporting neurite outgrowth and promoting gene delivery to maximize neurite extension. Biotechnology and Bioengineering, 109(3):830–839, 2012.

[128] J Patterson and J A Hubbell. Enhanced proteolytic degradation of molecularly engineered PEG hydrogels in response to MMP-1 and MMP-2. Biomaterials, 31(30):7836–7845, October 2010.

[129] Thomas P Kraehenbuehl, Prisca Zammaretti, Andre J van der Vlies, Ronald G Schoenmakers, Matthias P Lutolf, Marisa E Jaconi, and Jeffrey A Hubbell. Three-dimensional extracellular matrix-directed cardioprogenitor differentiation: Systematic modulation of a synthetic cell-responsive PEG-hydrogel. Biomaterials, 29(18):2757–2766, June 2008.

[130] Seung Tae Lee, Jung Im Yun, Yun Suk Jo, Mayumi Mochizuki, Andre J van der Vlies, Stephan Kontos, Jong Eun Ihm, Jeong M Lim, and Jeffrey A Hubbell. Engineering integrin signaling for promoting embryonic stem cell self-renewal in a precisely defined niche. Biomaterials, 31(6):1219–1226, February 2010.

[131] AJ Engler, S Sen, HL Sweeney, and Dennis E Discher. Matrix Elasticity Directs Stem Cell Lineage Specification. Cell, 126:677–689, 2006.

[132] A M Kloxin, J A Benton, and K.S. Anseth. In situ elasticity modulation with dynamic substrates to direct cell phenotype. Biomaterials, 31:1–8, 2010.

[133] J Zoldan, E D Karagiannis, C Y Lee, D G Anderson, Robert Langer, and S Levenberg. The influence of scaffold elasticity on germ layer specification of human embryonic stem cells. Biomaterials, 32:9612–9621, 2011.

[134] Murat Guvendiren and Jason A Burdick. Stiffening hydrogels to probe short- and long-term cellular responses to dynamic mechanics. Nature Communications, 3:792, April 2012.

[135] Lihui Weng, Xuming Chen, and Weiliam Chen. Rheological Characterization of in Situ Crosslinkable Hydrogels Formulated from Oxidized Dextran and N-Carboxyethyl Chitosan. Biomacromolecules, 8(4):1109–1115, April 2007.

[136] Lihui Weng, Alexander Romanov, Jean Rooney, and Weiliam Chen. Non-cytotoxic, in situ gelable hydrogels composed of N-carboxyethyl chitosan and oxidized dextran. Biomaterials, 29(29):3905–3913, October 2008.

[137] Hanwei Zhang, Aisha Qadeer, and Weiliam Chen. In Situ Gelable Interpenetrating Double Network Hydrogel Formulated from Binary Components: Thiolated Chitosan and Oxidized Dextran. Biomacromolecules, 12(5):1428–1437, May 2011.

[138] Sujata K Bhatia, Samuel D Arthur, H Keith Chenault, and George K Kodokian. Interactions of polysaccharide-based tissue adhesives with clinically relevant fibroblast and macrophage cell lines. Biotechnology Letters, 29(11):1645–1649, July 2007.

[139] Julia Dahlmann, Andreas Krause, Lena Möller, George Kensah, Markus Möwes, Astrid Diekmann, Ulrich Martin, Andreas Kirschning, Ina Gruh, and Gerald Dräger. Fully defined in situ cross-linkable alginate and hyaluronic acid hydrogels for myocardial tissue engineering. Biomaterials, 34(4):940–951, January 2013.

[140] Xiangxu Chen, Matheus A Dam, Kanji Ono, Ajit Mal, Hongbin Shen, Steven R Nutt, Kevin Sheran, and Fred Wudl. A Thermally Re-mendable Cross-Linked Polymeric Material. Science, 295(5560):1698–1702, March 2002.

[141] C N Bowman and C J Kloxin. Covalent Adaptable Networks: Reversible Bond Structures Incorporated in Polymer Networks. Angewandte Chemie International Edition, (51):4272–4274, 2012.

[142] Guohua Deng, Chuanmei Tang, Fuya Li, Huanfeng Jiang, and Yongming Chen. Covalent Cross-Linked Polymer Gels with Reversible SolGel Transition and Self-Healing Properties. Macromolecules, 43(3):1191–1194, February 2010.

[143] Christopher J Kloxin, Timothy F Scott, Brian J Adzima, and Christopher N Bowman. Covalent Adaptable Networks (CANs): A Unique Paradigm in Cross-Linked Polymers. Macromolecules, 43(6):2643–2653, March 2010.

[144] Brian J Adzima, Christopher J Kloxin, and Christopher N Bowman. Externally Triggered Healing of a Thermoreversible Covalent Network via Self-Limited Hysteresis Heating. Advanced Materials, 22(25):2784–2787, April 2010.

[145] T F Scott, Andrew D Schneider, Wayne D Cook, and Christopher N Bowman. Photoinduced Plasticity in Cross-Linked Polymers. Science, 308(5728):1615–1617, June 2005.

[146] Christopher J Kloxin, Timothy F Scott, Hee Young Park, and Christopher N Bowman. Mechanophotopatterning on a Photoresponsive Elastomer. Advanced Materials, 23(17):1977–1981, March 2011.

[147] M C Roberts, M C Hanson, A P Massey, E A Karren, and P F Kiser. Dynamically Restructuring Hydrogel Networks Formed with Reversible Covalent Crosslinks. Advanced Materials, 19(18):2503–2507, September 2007.

[148] Venugopal T Bhat, Anne M Caniard, Torsten Luksch, Ruth Brenk, Dominic J Campopiano, and Michael F Greaney. Nucleophilic catalysis of acylhydrazone equilibration for protein-directed dynamic covalent chemistry. Nature Chemistry, 2(6):490–497, May 2010.

[149] G Iyer, F Pinaud, J Xu, Y Ebenstein, J Li, J Chang, D Maxime, and S Weiss. Aromatic Aldehyde and Hydrazine Activated Peptide Coated Quantum Dots for Easy Bioconjugation and Live Cell Imaging. Bioconjugate Chemistry, 22:1006–1011, 2011.

[150] A Dirksen, S Yegneswaran, and Philip E Dawson. Bisaryl Hydrazones as Exchangeable Biocompatible Linkers. Angewandte Chemie International Edition, 49:2023–2027, 2010.

[151] Anouk Dirksen and Philip E Dawson. Rapid Oxime and Hydrazone Ligations with Aromatic Aldehydes for Biomolecular Labeling. Bioconjugate Chemistry, 19(12):2543–2548, December 2008.

[152] Adam R Blanden, Kamalika Mukherjee, Ozlem Dilek, Maura Loew, and Susan L Bane. 4-Aminophenylalanine as a Biocompatible Nucleophilic Catalyst for Hydrazone Ligations at Low Temperature and Neutral pH. Bioconjugate Chemistry, 22(10):1954–1961, October 2011.

[153] Jeet Kalia and Ronald T Raines. Hydrolytic Stability of Hydrazones and Oximes. Angewandte Chemie International Edition, 47(39):7523–7526, September 2008.

[154] Dylan W Domaille, Ju Hun Lee, and Jennifer N Cha. High density DNA loading on the M13 bacteriophage provides access to colorimetric and fluorescent protein microarray biosensors. Chemical Communications, 49:1759–1761, 2013.

[155] MR Karver and R Weissleder. Bioorthogonal Reaction Pairs Enable Simultaneous, Selective, Multi-Target Imaging. Angewandte Chemie International Edition, 51(4):920–922, 2012.

[156] J W Bae, E Lee, K M Park, and K D Park. Vinyl Sulfone-Terminated PEGPLLA Diblock Copolymer for Thiol-Reactive Polymeric Micelle - Macromolecules (ACS Publications). Macromolecules, 2009.

[157] Jianwen Xu, Tera M Filion, Fioleda Prifti, and Jie Song. Cytocompatible Poly(ethylene glycol)-co-polycarbonate Hydrogels Cross-Linked by Copper-Free, Strain-Promoted Click Chemistry. Chemistry - An Asian Journal, 6(10):2730–2737, August 2011.

[158] Jukuan Zheng, Laura A Smith Callahan, Jinkun Hao, Kai Guo, Chrys Wesdemiotis, R A Weiss, and Matthew L Becker. Strain-Promoted Cross-Linking of PEG-Based Hydrogels via Copper-Free Cycloaddition. ACS Macro Letters, 1(8):1071–1073, August 2012.

[159] Tom Annable. The rheology of solutions of associating polymers: Comparison of experimental behavior with transient network theory. Journal of Rheology, 37(4):695–726, July 1993.

[160] Faith A Morrison. Understanding Rheology. Oxford University Press, USA, 2001.

[161] Paul J Flory. Molecular Size Distribution in Three Dimensional Polymers. I. Gelation. Journal of the American Chemical Society, 63(11):3083–3090, November 1941.

[162] Walter H Stockmayer. Theory of Molecular Size Distribution and Gel Formation in Branched-Chain Polymers. The Journal of Chemical Physics, 11(2):45, 1943.

[163] B C Abbott and J Lowy. Stress Relaxation in Muscle. Proceedings of the Royal Society B: Biological Sciences, 146(923):281–288, March 1957.

[164] A Magid and D J Law. Myofibrils bear most of the resting tension in frog skeletal muscle. Science, 1985.

[165] Adam J Engler, Maureen A Griffin, Shamik Sen, Carsten G Bönnemann, H Lee Sweeney, and Dennis E Discher. Myotubes differentiate optimally on substrates with tissue-like stiffness: pathological implications for soft or stiff microenvironments. The Journal of Cell Biology, 166(6):877–887, September 2004.

[166] S Onogi and K Ui. Frequency and temperature dispersions of high polymers. Journal of Colloid Science, 11:214–225, 1956.

[167] K W Ranatunga. Sarcomeric visco-elasticity of chemically skinned skeletal muscle fibres of the rabbit at rest - Springer. Journal of Muscle Research and Cell Motility, 22(5):399–414, 2001.

[168] Edward A Phelps, Nduka O Enemchukwu, Vincent F Fiore, Jay C Sy, Niren Murthy, Todd A Sulchek, Thomas H Barker, and Andrés J García. Maleimide Cross-Linked Bioactive PEG Hydrogel Exhibits Improved Reaction Kinetics and Cross-Linking for Cell Encapsulation and In Situ Delivery. Advanced Materials, 24(1):64–70, December 2011.

[169] K Omura and D Swern. Oxidation of alcohols by "activated" dimethyl sulfoxide. a preparative, steric and mechanistic study. Tetrahedron, 34:1651–1660, 1978.

[170] Louis A Carpino, Ayman El-Faham, Charles A Minor, and Fernando Albericio. Advantageous applications of azabenzotriazole (triazolopyridine)-based coupling reagents to solid-phase peptide synthesis. Journal of the Chemical Society, Chemical Communications, 0(2):201–203, 1994.

[171] P Kubisa, K Neeld, J Starr, and O Vogl. Polymerization of higher aldehydes. Polymer, 21:1433–1447, 1980.

[172] Rowena McBeath, Dana M Pirone, Celeste M Nelson, Kiran Bhadriraju, and Christopher S Chen. Cell Shape, Cytoskeletal Tension, and RhoA Regulate Stem Cell Lineage Commitment. Developmental Cell, 6(4):483–495, April 2004.

[173] K A Kilian, B Bugarija, B T Lahn, and M Mrksich. Geometric cues for directing the differentiation of mesenchymal stem cells. Proceedings of the National Academy of Sciences, 107(11):4872–4877, March 2010.

[174] Daniel D McKinnon, Dylan W Domaille, Jennifer N Cha, and Kristi S Anseth. Bis-Aliphatic Hydrazone-Linked Hydrogels Form Most Rapidly at Physiological pH: Identifying the Origin of Hydrogel Properties with Small Molecule Kinetic Studies. Chemistry of Materials, page 140331065644009, March 2014.

[175] Huan Wang, Sarah M Haeger, April M. Kloxin, Leslie A Leinwand, and Kristi S Anseth. Redirecting Valvular Myofibroblasts into Dormant Fibroblasts through Light-mediated Reduction in Substrate Modulus. PLoS ONE, 7(7):e39969, July 2012.

[176] Huan Wang, Mark W Tibbitt, Stephen J Langer, Leslie A Leinwand, and Kristi S Anseth. Hydrogels preserve native phenotypes of valvular fibroblasts through an elasticity-regulatedPI3K/AKT pathway. Proceedings of the National Academy of Sciences, November 2013.

[177] S Khetan, M Guvendiren, W R Legant, D M Cohen, C S Chen, and Jason A Burdick. Degradation-mediated cellular traction directs stem cell fate in covalently crosslinked three-dimensional hydrogels. Nature Materials, 2013.

[178] AP Balgude, X Yu, and A Szymanski. Agarose gel stiffness determines rate of DRG neurite extension in 3D cultures. Biomaterials, 2001.

[179] Kaushik Chatterjee, Sheng Lin-Gibson, William E Wallace, Sapun H Parekh, Young Jong Lee, Marcus T Cicerone, Marian F Young, and Carl G Simon, Jr. The effect of 3D hydrogel scaffold modulus on osteoblast differentiation and mineralization revealed by combinatorial screening. Biomaterials, 31(19):5051–5062, July 2010.

[180] Sapun H Parekh, Kaushik Chatterjee, Sheng Lin-Gibson, Nicole M Moore, Marcus T Cicerone, Marian F Young, and Carl G Simon, Jr. Modulus-driven differentiation of marrow stromal cells in 3D scaffolds that is independent of myosin-based cytoskeletal tension. Biomaterials, 32(9):2256–2264, March 2011.

[181] Wesley R Legant, Colin K Choi, Jordan S Miller, Lin Shao, Liang Gao, Eric Betzig, and Christopher S Chen. Multidimensional traction force microscopy reveals out-of-plane rotational moments about focal adhesions. Proceedings of the National Academy of Sciences, 110(3):881–886, January 2013.

[182] Kelly M Schultz and Eric M Furst. Microrheology of biomaterial hydrogelators. Soft Matter, 8(23):6198, 2012.

[183] Kelly M Schultz and Kristi S Anseth. Monitoring degradation of matrix metalloproteinases-cleavable PEG hydrogels via multiple particle tracking microrheology. Soft Matter, 2013.

[184] J L Tan, J Tien, D M Pirone, D S Gray, K Bhadriraju, and C S Chen. Cells lying on a bed of microneedles: An approach to isolate mechanical force. Proceedings of the National Academy of Sciences, 100(4):1484–1489, January 2003.

[185] T J Dennerll. The cytomechanics of axonal elongation and retraction. The Journal of Cell Biology, 109(6):3073–3083, December 1989.

[186] Steven R Heidemann, Phillip Lamoureux, and R E Buxbaum. Cytomechanics of axonal development. Cell Biochemistry and Biophysics, 27(3):135–155, October 1997.

[187] J Zheng, P Lamoureux, V Santiago, T Dennerll, R E Buxbaum, and S R Heidemann. Tensile regulation of axonal elongation and initiation. 1991.

[188] Elizabeth R Gillies and Jean M J Fréchet. pH-Responsive Copolymer Assemblies for Controlled Release of Doxorubicin. Bioconjugate Chemistry, 16(2):361–368, March 2005.

[189] Elizabeth R Gillies, Thomas B Jonsson, and Jean M J Fréchet. Stimuli-Responsive Supramolecular Assemblies of Linear-Dendritic Copolymers. Journal of the American Chemical Society, 126(38):11936–11943, September 2004.

[190] M A Azagarsamy, D L Alge, S J Radhakrishnan, Mark W Tibbitt, and Kristi S Anseth. Photocontrolled Nanoparticles for On-Demand Release of Proteins. Biomacromolecules, 13:2219–2224, 2012.

[191] Malar A Azagarsamy and Kristi S Anseth. Wavelength-Controlled Photocleavage for the Orthogonal and Sequential Release of Multiple Proteins. Angewandte Chemie International Edition, pages n/a–n/a, October 2013.

[192] Donald R. Griffin and Andrea M. Kasko. Photodegradable Macromers and Hydrogels for Live Cell Encapsulation and Release. Journal of the American Chemical Society, 134(31):13103–13107, August 2012.

[193] Donald R. Griffin and Andrea M. Kasko. Photoselective Delivery of Model Therapeutics from Hydrogels. ACS Macro Letters, 1(11):1330–1334, November 2012.

[194] Baisong Chang, Dan Chen, Yang Wang, Yanzuo Chen, Yunfeng Jiao, Xianyi Sha, and Wuli Yang. Bioresponsive Controlled Drug Release Based on Mesoporous Silica Nanoparticles Coated with Reductively Sheddable Polymer Shell. Chemistry of Materials, 25(4):574–585, February 2013.

[195] Jing Jing, Anna Szarpak-Jankowska, Raphael Guillot, Isabelle Pignot-Paintrand, Catherine Picart, and Rachel Auzély-Velty. Cyclodextrin/Paclitaxel Complex in Biodegradable Capsules for Breast Cancer Treatment. Chemistry of Materials, 25(19):3867–3873, October 2013.

[196] J Kim, J A Hanna, M Byun, C D Santangelo, and R C Hayward. Designing Responsive Buckled Surfaces by Halftone Gel Lithography. Science, 335(6073):1201–1205, March 2012.

[197] Juan Rodríguez-Hernández and Sébastien Lecommandoux. Reversible InsideOut Micellization of pH-responsive and Water-Soluble Vesicles Based on Polypeptide Diblock Copolymers. Journal of the American Chemical Society, 127(7):2026–2027, February 2005.

[198] Patricia Gumbley, Damla Koylu, Robert H Pawle, Bond Umezuruike, Elise Spedden, Cristian Staii, and Samuel W Thomas, III. Wavelength-Selective Disruption and Triggered Release with Photolabile Polyelectrolyte Multilayers. Chemistry of Materials, 26(3):1450–1456, February 2014.

[199] Jing Zhang and Nicholas A Peppas. Synthesis and Characterization of pH- and Temperature-Sensitive Poly(methacrylic acid)/Poly(N-isopropylacrylamide) Interpenetrating Polymeric Networks. Macromolecules, 33(1):102–107, January 2000.

[200] Hongchen Dong, Venkat Mantha, and Krzysztof Matyjaszewski. Thermally Responsive PM(EO) 2MA Magnetic Microgels via Activators Generated by Electron Transfer Atom Transfer Radical Polymerization in Miniemulsion. Chemistry of Materials, 21(17):3965–3972, September 2009.

[201] A Sidorenko, T Krupenkin, A Taylor, P Fratzl, and J Aizenberg. Reversible Switching of Hydrogel-Actuated Nanostructures into Complex Micropatterns. Science, 315(5811):487–490, January 2007.

[202] PJ Flory. Molecular theory of rubber elasticity. Polymer, 20:1317–1320, 1979.

[203] L G Baxandall. Dynamics of reversibly crosslinked chains. Macromolecules, 22(4):1982–1988, July 1989.

[204] Andrew T Metters, Christopher N Bowman, and Kristi S Anseth. A Statistical Kinetic Model for the Bulk Degradation of PLA- b-PEG- b-PLA Hydrogel Networks. The Journal of Physical Chemistry B, 104(30):7043–7049, August 2000.

[205] Andrew T Metters, Kristi S Anseth, and Christopher N Bowman. A Statistical Kinetic Model for the Bulk Degradation of PLA- b-PEG- b-PLA Hydrogel Networks: Incorporating Network Non-Idealities. The Journal of Physical Chemistry B, 105(34):8069–8076, August 2001.

[206] Andrew Metters and Jeffrey Hubbell. Network Formation and Degradation Behavior of Hydrogels Formed by Michael-Type Addition Reactions. Biomacromolecules, 6(1):290–301, January 2005.

[207] Pete Crisalli and Eric T Kool. Water-soluble organocatalysts for hydrazone and oxime formation. Journal of Organic Chemistry, 78(3):1184–1189, 2013.

[208] Pete Crisalli and Eric T Kool. Importance of orthoProton Donors in Catalysis of Hydrazone Formation. Organic Letters, 15(7):1646–1649, April 2013.

[209] Eric T Kool, Do-Hyoung Park, and Pete Crisalli. Fast Hydrazone Reactants: Electronic and Acid/Base Effects Strongly Influence Rate at Biological pH. Journal of the American Chemical Society, November 2013.

[210] Pete Crisalli, Armando R Hernández, and Eric T Kool. Fluorescence Quenchers for Hydrazone and Oxime Orthogonal Bioconjugation. Bioconjugate Chemistry, 23(9):1969–1980, September 2012.

[211] R Nguyen and I Huc. Optimizing the reversibility of hydrazone formation for dynamic combinatorial chemistry. Chemical Communications, pages 942–943, 2003.

[212] William P Jencks. Studies on the mechanism of oxime and semicarbazone formation. Journal of the American Chemical Society, 81(2):475–481, 1959.

[213] M A Azagarsamy and K.S. Anseth. Bioorthogonal Click Chemistry: An Indispensable Tool to Create Multifaceted Cell Culture Scaffolds. ACS Macro Letters, 2012.

[214] M Ehrbar, R Schoenmakers, Erik H Christen, Martin Fussenegger, and Wilfried Weber. Drug-sensing hydrogels for the inducible release of biopharmaceuticals. Nature Materials, 7:800–804, 2008.

[215] Kuen Yong Lee, Kamal H Bouhadir, and David J Mooney. Controlled degradation of hydrogels using multi-functional cross-linking molecules. Biomaterials, 25(13):2461–2466, June 2004.

[216] Darice Y. Wong, Donald R. Griffin, Jason Reed, and Andrea M. Kasko. Photodegradable Hydrogels to Generate Positive and Negative Features over Multiple Length Scales. Macromolecules, 43(6):2824–2831, 2010.

[217] F Ercole, H Thissen, K Tsang, R A Evans, and John S Forsy. Photodegradable Hydrogels Made via RAFT. Macromolecules, 45:8387–8400, 2012.

[218] Jérôme Babin, Maxime Pelletier, Martin Lepage, Jean-François Allard, Denis Morris, and Yue Zhao. A New Two-Photon-Sensitive Block Copolymer Nanocarrier. Angewandte Chemie International Edition, 48(18):3329–3332, April 2009.

[219] YuRui Zhao, Quan Zheng, Kenneth Dakin, Ke Xu, Manuel L Martinez, and Wen-Hong Li. New Caged Coumarin Fluorophores with Extraordinary Uncaging Cross Sections Suitable for Biological Imaging Applications. Journal of the American Chemical Society, 126(14):4653–4663, April 2004.

[220] R S Givens, M Rubina, and J Wirz. Applications of p-hydroxyphenacyl (pHP) and coumarin-4-ylmethyl photoremovable protecting groups. Photochemical & Photobiological Sciences, 11:472–488, 2012.

[221] Xinlin Du, Heinz Frei, and Sung-Hou Kim. Comparison of nitrophenylethyl and hydroxyphenacyl caging groups. Biopolymers, 62(3):147–149, 2001.

[222] Toshiaki Furuta, Samuel S H Wang, Jami L Dantzker, Timothy M Dore, Wendy J Bybee, Edward M Callaway, Winfried Denk, and Roger Y Tsien. Brominated 7-hydroxycoumarin-4-ylmethyls: Photolabile protecting groups with biologically useful cross-sections for two photon photolysis. Proceedings of the National Academy of Sciences, 1999.

[223] Jason M Spruell, Martin Wolffs, Frank A Leibfarth, Brian C Stahl, Jinhwa Heo, Luke A Connal, Jerry Hu, and Craig J Hawker. Reactive, Multifunctional Polymer Films through Thermal Cross-linking of Orthogonal Click Groups. Journal of the American Chemical Society, 133(41):16698–16706, October 2011.

[224] Sandra Binauld, Fernande Boisson, Thierry Hamaide, Jean Pierre Pascault, Eric Drockenmuller, and Etienne Fleury. Kinetic study of copper(I)catalyzed click chemistry stepgrowth polymerization. Journal of Polymer Science Part A: Polymer Chemistry, 46(16):5506–5517, August 2008.

[225] V D Bock and H Hiemstra. CuI-Catalyzed Alkyne–Azide "Click" Cycloadditions from a Mechanistic and Synthetic Perspective - Bock - 2005 - European Journal of Organic Chemistry - Wiley Online Library. European Journal of Organic Chemistry, pages 51–68, 2006.

[226] VV Rostovtsev, LG Green, VV Fokin, and K Barry Sharpless. A stepwise huisgen cycloaddition process: copper (I)catalyzed regioselective "ligation" of azides and terminal alkynes. Angewandte Chemie International Edition, 41(14):2596–2599, 2002.

[227] W D Cook, F Chen, D W Pattison, P Hopson, and Mathieu Beaujon. Thermal polymerization of thiol–ene network-forming systems. Polymer, 56:1572–1579, 2007.

[228] Daniel L Alge, Malar A Azagarsamy, Dillon F Donohue, and Kristi S Anseth. Synthetically Tractable Click Hydrogels for Three-Dimensional Cell Culture Formed Using Tetrazine–Norbornene Chemistry. Biomacromolecules, page 130308093851004, March 2013.

[229] Gregory N Grover, Jonathan Lam, Thi H Nguyen, Tatiana Segura, and Heather D Maynard. Biocompatible Hydrogels by Oxime Click Chemistry. Biomacromolecules, 13(10):3013–3017, October 2012.

[230] V X Truong, M P Ablett, HTJ Gilbert, J Bowen, Stephen M Richardson, Judith A Hoyland, and Andrew P Dove. In situ -forming robust chitosan-poly(ethylene glycol) hydrogels prepared by copper-free azide–alkyne click reaction for tissue engineering. Biomaterials Science, 2:167–175, 2014.

[231] Yaping Fan, Chao Deng, Ru Cheng, Fenghua Meng, and Zhiyuan Zhong. In SituForming Hydrogels via Catalyst-Free and Bioorthogonal "Tetrazole–Alkene" Photo-Click Chemistry. Biomacromolecules, 14(8):2814–2821, August 2013.

[232] Benjamin G Keselowsky, David M Collard, and Andrés J García. Integrin binding specificity regulates biomaterial surface chemistry effects on cell differentiation. 2005.

[233] Danielle S W Benoit, Michael P Schwartz, Andrew R Durney, and Kristi S Anseth. Small functional groups for controlled differentiation of hydrogel-encapsulated human mesenchymal stem cells. Nature Materials, 7(10):816–823, August 2008.

[234] Solitaire A DeLong, James J Moon, and Jennifer L West. Covalently immobilized gradients of bFGF on hydrogel scaffolds for directed cell migration. Biomaterials, 26(16):3227–3234, June 2005.

[235] D Guarnieri, A De Capua, M Ventre, A Borzacchiello, C Pedone, D Marasco, M Ruvo, and P A Netti. Covalently immobilized RGD gradient on PEG hydrogel scaffold influences cell migration parameters. Acta Biomaterialia, 6(7):2532–2539, July 2010.

[236] Hilary L Ashe and James Briscoe. The interpretation of morphogen gradients. Development, 2006.

[237] G Weng, U S Bhalla, and R Iyengar. Complexity in biological signaling systems. Science, 284:92–96, 1999.

[238] Katarzyna A Mosiewicz, Laura Kolb, Andre J van der Vlies, Mikaël M Martino, Philipp S Lienemann, Jeffrey A Hubbell, Martin Ehrbar, and Matthias P Lutolf. In situ cell manipulation through enzymatic hydrogel photopatterning. Nature Materials, 12(11):1072–1078, October 2013.

[239] April M. Kloxin, Mark W Tibbitt, and Kristi S Anseth. Synthesis of photodegradable hydrogels as dynamically tunable cell culture platforms. Nature Protocols, 5(12):1867–1887, November 2010.

[240] JC Jewett, EM Sletten, and Carolyn R Bertozzi. Rapid Cu-Free Click Chemistry with Readily Synthesized Biarylazacyclooctynones. Journal of the American Chemical Society, 132:3688–3390, 2010.

[241] Cole A DeForest, Evan A Sims, and Kristi S Anseth. Peptide-Functionalized Click Hydrogels with Independently Tunable Mechanics and Chemical Functionality for 3D Cell Culture. Chemistry of Materials, 22(16):4783–4790, August 2010.

[242] N Shen, D Datta, and C B Schaffer. Ablation of cytoskeletal filaments and mitochondria in live cells using a femtosecond laser nanoscissor. MCB, 2(1):17–25, 2005.

[243] W Watanabe, N Arakawa, S Matsunaga, and T Higashi. Femtosecond laser disruption of subcellular organelles in a living cell. Opt Express, 2004.

[244] Mehmet Fatih Yanik, Hulusi Cinar, Hediye Nese Cinar, Andrew D Chisholm, Yishi Jin, and Adela Ben-Yakar. Neurosurgery: Functional regeneration after laser axotomy. Nature, 432(7019):822–822, December 2004.

[245] Mark W Tibbitt, April M. Kloxin, Kiran U Dyamenahalli, and Kristi S Anseth. Controlled two-photon photodegradation of PEG hydrogels to study and manipulate subcellular interactions on soft materials. Soft Matter, 6(20):5100–5108, 2010.

[246] Mikhail Drobizhev, Nikolay S Makarov, Shane E Tillo, Thomas E Hughes, and Aleksander Rebane. Two-photon absorption properties of fluorescent proteins. Nature Methods, 8(5):393–399, April 2011.

[247] T Q Huang, X Qu, J Liu, and S Chen. 3D printing of biomimetic microstructures for cancer cell migration. Biomedical microdevices, 2013.

[248] Wei Tan and Tejal A Desai. Microfluidic Patterning of Cells in Extracellular Matrix Biopolymers: Effects of Channel Size, Cell Type, and Matrix Composition on Pattern Integrity. Tissue Engineering, 9(2):255–267, April 2003.

[249] D Yaffe. Retention of differentiation potentialities during prolonged cultivation of myogenic cells. Proceedings of the National Academy of Sciences of the United States of America, 61(2):477, October 1968.

[250] H M Blau, G K Pavlath, E C Hardeman, and C P Chiu. Plasticity of the differentiated state. Science, 1985.

[251] J L Leight, D L Alge, A J Maier, and K.S. Anseth. Direct measurement of matrix metalloproteinase activity in 3D cellular microenvironments using a fluorogenic peptide substrate. Biomaterials, 2013.

[252] Ying Zeng, T N C Ramya, Anouk Dirksen, Philip E Dawson, and James C Paulson. High-efficiency labeling of sialylated glycoproteins on living cells. Nature Methods, 6(3):207–209, February 2009.

[253] TE Kennedy, H Wang, and W Marshall. Axon Guidance by Diffusible Chemoattractants: A Gradient of Netrin Protein in the Developing Spinal Cord. The Journal of Neuroscience, 26(34):8866–8874, 2006.